2014

Tests of Horizontally Curved Tubular Flange Girder System

Kourosh Mahvashmohammadi
Lehigh University

Recommended Citation

Mahvashmohammadi, Kourosh, "Tests of Horizontally Curved Tubular Flange Girder System" (2014). *Theses and Dissertations.* Paper 1552.

Tests of Horizontally Curved Tubular Flange Girder System

by

Kourosh Mahvashmohammadi

Presented to the Graduate and Research Committee
of Lehigh University
in Candidacy for the Degree of
Master of Science
in
Structural Engineering

Lehigh University
September 2014

This thesis is accepted and approved in partial fulfillment of the requirements for the Master of Science.

Date

Dr. Richard Sause
Thesis Advisor

Dr. Panos Diplas
Department of Civil & Environmental Engineering

ACKNOWLEDGEMENTS

The research presented herein was conducted at the Advanced Technology for Large Structural Systems (ATLSS) Research Center at Lehigh University in Bethlehem, PA, USA. Research funding and financial support provided by the Federal Highway Administration (FHWA) and the Pennsylvania Department of Community and Economic Development through the Pennsylvania Infrastructure Technology Alliance (PITA) is gratefully acknowledged.

First, I would like to sincerely thank my research advisor, Dr. Richard Sause, for his support, guidance, and mentorship during my research. I would like to thank Darrick Fritchman, the Laboratory Operations Manager at ATLSS, and Carl Bowman, ATLSS Instrumentation Manager for the time they spent providing insight and suggestions to improve the test planning for my research. The computer technical support provided by Peter Bryan is much appreciated. I would also like to thank all of the ATLSS laboratory staff and technicians, especially Edward Tomlinson, Jeffrey Sampson, Gilberto Perez, Todd Anthony and Roger Moyer for their invaluable help in conducting the tests for this research. Thank you to my fellow student researchers, especially Haiying Ma, for her help throughout the project, and to Kayla Hampe and Eric Putnam, who did the prior researches on this project and passed them to me.

Finally, thank you to my family and friends for their continued love, support, and encouragement

TABLE OF CONTENTS

LIST OF TABLES

LIST OF FIGURES

ABSTRACT

Tubular flange girders (TFG) are an innovative I-shaped steel bridge girder proposed for horizontally curved bridge systems. The I-shaped TFG has a steel tube flanges rather than a conventional flat plate flange for one or both flanges. The closed tube section significantly increases the torsional stiffness of the section and the open I-shaped section provides flexural stiffness. The increased torsional stiffness of the TFG significantly reduces the warping stresses, total normal stresses, vertical displacements, and cross section rotations for an individual curved TFG relative to a conventional curved I-girder.

In this study, a type of tubular flange girder, called TFG1, with a rectangular hollow steel tube as the top flange and a flat plat as the bottom flange was studied. A two-thirds scale TFG1 bridge girder test specimen with two girders connected with diaphragms was studied. The specimen was designed by Ma (2014) and Putnam (2011) based on AASHTO LRFD Bridge Design Specifications (2005) and TFG design recommendations by Dong (2008). The test specimen was constructed, erected, and assembled in 2010. Ma (2014) investigated the expected behavior of the test specimen based on the FE models, and Hampe (2012) designed the loading fixtures for the tests of the specimen. This thesis reviews the test setup and designed loading fixtures, and presents plans for conducting of the tests, as well as the final test results.

The design of the two-thirds scaled two-TFG1 bridge test specimen and the corresponding full-size twp-TFG1 bridge are reviewed. The full-size bridge has a 90 ft span, and a curvature ratio of 0.45. The scaled test specimen has same curvature ratio, but

all dimensions are scaled by two-thirds. The test setup location and layout, and the expected behavior of the test specimen are summarized. Test loading fixtures designed by Hampe (2012) to simulate a uniformly distributed load condition are reviewed. Then, a study on the effect of alternate boundary conditions is presented and the design of the final set of bearing assemblies is described.

The instrumentation plan developed for measuring the test specimen response is described. Geometric calculations required to obtain displacement components from the measured data are discussed. The loading plan, including the load control plan and jack re-stroking plan, is discussed. The instrumentation and loading plan were based on the expected behavior of the test specimen and loading fixtures, with focus on the conditions of the inelastic test which loads the test specimen up to and beyond its maximum load capacity.

The data from tests on the test specimen were collected and analyzed and the processed test results are presented. The test specimen material properties from tensile tests of the test specimen materials are presented. An investigation of geometric imperfections of the tube flange at a tube splice location, near the region where the test specimen failed, is also presented.

The results of the study show that the test loading fixtures, instrumentation, loading equipment, and load control plan performed well and produced reliable test data. The results of the tests have been used to validate FE models and design criteria for TFG1 bridge girders (Ma,2014).

1 INTRODUCTION

1.1 Overview

Horizontally curved bridges are increasingly required in new more complex highway infrastructure systems. The curvature in a horizontally curved bridge adds a significant torsional response to the primary bending response of the supporting bridge girder system. A system of I-shaped steel plate girders (i.e., conventional steel I-girders) connected by cross frames (or diaphragms) is often used to resist the curved bridge torsional effects in current U.S highway bridge design practice. An individual curved conventional steel I-girder is torsionally flexible and weak, and may develop large displacements, cross section rotations, and normal warping stresses under its own self-weight. Therefore, temporary shoring is often required during erection of curved conventional steel I-girder bridge systems to stabilize the I-girders until the cross frames (or diaphragms) are installed.

Wassef et al. (1997) first proposed the use of a steel I-shaped girder with a tube for the flange (i.e., tubular flange girder or TFG) in straight highway bridges. Kim and Sause (2008) investigated the behavior of TFGs with a round concrete-filled tube as the compression flange and a flat plate as the tension flange in straight bridges. Fan (2007) and Dong and Sause (2010a, b) proposed the use of TFGs in curved bridges, to take advantage of the torsional stiffness and strength of a closed cross section (the tube) and the easy fabrication and flexural efficiency of the open cross section of an I-girder. Dong and Sause (2008) presented several example curved bridge systems with one rectangular tube as the top flange and a second rectangular tube as the bottom flange (i.e., a TFG2 cross section) and showed that for longer spans, a cover plate is needed for the bottom tubular flange. In addition, concrete infill or an internal diaphragm is needed inside the bottom tubular flange at the bearings to resist the reactions and avoid local deformations of the tube.

The curved TFG test specimen studied in this research has girder cross sections with a hollow rectangular steel tube as the top flange and a flat steel plate as the bottom flange (i.e., a TFG1 cross section). A 2/3-scale test specimen with two curved TFG1s braced by three internal diaphragms (instead of cross frames) and two end diaphragms has been designed, fabricated, and erected. The design of the test specimen was completed by Ma (2012) and Putnam (2011). AASHTO LRFD Bridge Design Specifications (2005) and design recommendations by Dong (2008) were used to design the full scale bridge and scaled test specimen. Hampe (2012) designed the loading fixtures for the test to simulate uniform loading of the test specimen.

This thesis explains the tests conducted on the test specimen. The expected behavior of the test specimen based on analysis of FE models (Ma, 2014) is discussed and kinematics of the loading fixtures are explained. A study of alternate simply-supported boundary conditions for the test specimen and the selected feasible set of boundary conditions are presented. The set of appropriate bearing assemblies that were designed, fabricated, and placed in the test setup, are described. A plan for instrumentation that was developed to measure the complex behavior of the test specimen during the tests is described. A hydraulic loading plan and control plan that were developed for loading the tests specimen up to (and beyond) maximum capacity are presented. Finally, the supplementary material testing on coupons cut from the test specimen is presented.

1.2 Research Objectives

The overall goal of this research is to develop and conduct tests of a curved TFG1 bridge girder test specimen. The following objectives were established:

1. To gather and review information on the test specimen and the test setup, including the expected behavior of the test specimen, the method of loading of the test specimen, and the design of loading fixtures.
2. To study the effects of alternate boundary conditions and to design a set of bearing assemblies for the test specimen.
3. To study the expected response of the test specimen and to develop an instrumentation plan to measure the response of the test specimen and loading fixtures.
4. To develop a hydraulic loading system and load control procedure for the tests.
5. To conduct elastic and inelastic tests, and present the test results; to conduct tests to obtain material properties of coupons cut from the test specimen.

1.3 Thesis Scope

To understand the expected behavior of the test specimen and loading fixtures, previous work by Putnam (2011), Hampe (2012), and Ma (2014) was studied. The physical conditions of the test setup were considered, and the FE displacement results for the test specimen and corresponding displacements of the loading fixture were studied to develop an instrumentation plan. The load and kinematic results were used develop a hydraulic loading plan and load control procedure. Finally, the tests were conducted and test data (from measurements during the tests) were processed for presentation and discussion.

1.4 Thesis Organization

The thesis consists of eight chapters as follows:

Chapter 1 introduces the research, and provides a general overview, the research objectives, and the organization of the thesis.

Chapter 2 presents background information on previous research related to straight and curved TFGs. Also an explanation of the current test setup and a short review of the design of the two-third scale TFG1 test specimen is presented in this chapter.

Chapter 3 reviews the test specimen loading. The expected behavior of the test specimen based on analysis of FE models under loading up to (and beyond) the maximum load capacity is explained in this chapter. Also, the loading fixtures for the tests are described.

Chapter 4 describes the effects of different possible boundary condition combinations on the response of the test specimen. Also, the bearing assemblies used for the tests are discussed in this chapter.

Chapter 5 describes the instrumentation plan developed to measure the response of the test specimen and loading fixtures. Combinations of displacement transducers, rotation transducers, strain transducers, and force transducers were used in the tests and are discussed in this chapter.

Chapter 6 explains the procedure for the elastic tests and the final inelastic test up to (and beyond) the maximum load capacity of the test specimen. Different aspects of the test plan, including the load control plan and the plan to re-stroke the jacks during the tests are discussed in this chapter.

Chapter 7 presents the test data obtained from instrumentation during the elastic and inelastic tests. The failure mode of the test specimen is also discussed in this chapter.

Chapter 8 describes material testing performed on coupons cut from the test specimen after the tests. Different sections of plates and tubes were cut from parts of the test specimen that did not yield during the tests. Tensile coupons were machined from these plate and tube sections, and were tested to obtain actual material properties. Also observations on the local buckled region of the test specimen are presented in this chapter.

Chapter 9 presents a summary of the thesis, conclusions, and possible future work.

2 BACKGROUND REVIEW

2.1 Introduction

Tubular flange girders (TFG) with different cross sections for straight and curved bridges have been studied and compared with conventional steel I-girders. Section 2.2 reviews previous theoretical, analytical, and experimental research. Section 2.3 to Section 2.5 discuss the 2/3-scale test specimen design, modeling, fabrication, and erection/assembly. The test specimen consists of two curved TFGs with a rectangular hollow tube as the top flange and a flat plat as the bottom flange (TFG1) and three interim diaphragms (instead of cross frames) and two end diaphragms. Section 2.6 describes test setup.

2.2 Previous Work on TFGs

Steel girders with tubular flanges filled with concrete were first proposed by Wassef et al. (1997) for straight highway bridges. Increased local buckling resistance, large torsional stiffness, and reduced web slenderness were identified as potential advantages of these girders. A study of straight concrete-filled TFGs was conducted by Wimer and Sause (2004). A test specimen was fabricated (Figure 2.1) and tested at a 0.45 scale. The tests were conducted at the Advanced Technology for Large Structural Systems (ATLSS) Engineering Research Center at Lehigh University in Bethlehem, PA. The tests examined the test specimen for two conditions: (1) TFGs non-composite with a concrete deck simulating construction conditions when the lateral-torsional buckling (LTB) strength controls the flexural capacity and (2) TFGs composite with a concrete deck simulating the final construction condition when the TFG cross section flexural strength controls the flexural capacity. The test specimen was loaded with precast concrete deck panels and additional concrete blocks to reach the factored design loads. The maximum load capacity of the test specimen was not determined from the tests because the test specimen could not safely be loaded to the maximum load capacity using the loading method that was adopted for the tests.

Kim and Sause (2005a, b) studied straight concrete-filled TFGs with a round steel tube as the top flange and a flat steel plate as the bottom flange. A 0.45-scale test specimen with two straight TFGs with round concrete-filled steel tubes as the top flanges was designed and fabricated (Figure 2.2). The specimen was tested under two conditions: (1) construction conditions when the LTB strength controls the flexural capacity and (2) service conditions when the TFG cross section flexural strength controls the flexural capacity. The test specimen was loaded with a concrete deck and additional concrete and steel blocks. The concrete deck, however, was not composite with the TFGs. For the construction conditions, the concrete-filled TFGs were not braced by the concrete deck, but for the service conditions, the TFGs were braced by the concrete deck. The test specimen carried loads exceeding the factored design loads for both conditions. No unexpected lateral or vertical displacements were observed. The experimental results were compared with FE analysis results, which indicated that FE models can estimate accurately the response of the test specimen.

Dong and Sause (2009) studied straight TFGs with hollow, rectangular steel tubes for both flanges. An FE parametric study was conducted. The study showed the effects of stiffeners, cross section dimensions, residual stresses, initial geometric imperfections, and bending moment distribution on the LTB flexural strength of straight TFGs. The study was used to validate the flexural strength formulas developed by Kim and Sause (2005a, b). Dong and Sause (2010a, b) also studied curved TFGs with one hollow rectangular steel tube for the top flange and second hollow rectangular tube for the bottom flange (i.e., TFG2). FE studies were done on individual girders and simply supported three-girder systems of curved TFG2s and conventional I-girders. A comparative study (Dong and Sause, 2010a) of individual girders under self-weight demonstrated that the curved TFG2s develop less warping normal stress due to the larger torsional rigidity, smaller vertical displacement, and smaller cross section rotation than a corresponding I-girder

Putnam (2010) studied a 1/2-scale individual curved TFG2 test specimen (

Figure 2.3 2.3). Putnam used the test results to validate FE models. The behavior of the curved TFG2 under vertical loads was examined and the results showed that an FE model can accurately predict vertical displacements, cross section rotations, normal strains, and shear strains away from the ends of the curved TFG2.

Dong (2008) applied the design criteria from the 2004 AASHTO LRFD Bridge Design Specifications for conventional curved I-girders to curved TFG2s. Constructability, Service II, and Strength I limit states were considered. The FE results showed that these equations could be used to safely design curved TFG2s for highway bridges.

The advantages of a curved TFG2 system in comparison to a corresponding curved I-girder system are summarized by Sause (2012) as follows:

- Under the same load, the curved TFG2s develop less total normal stress than the corresponding curved I-girders.
- The forces in the cross-frames of the TFG2 systems are smaller than in the corresponding I-girder systems, and thus lighter cross-frame members can be used for the TFG2 systems.
- Fewer cross-frames are needed for the TFG systems.
- The TFG2 system can carry its own weight (plus the weight of a concrete deck) without any support within the span and without interior cross frames (or diaphragms), and, therefore, temporary support for the TFG2 system during construction (before the concrete deck is composite with the girders) may not be needed, which makes bridge erection faster and less expensive

2.3 Curved TFG1 Test Specimen

Tests on the 2/3-scale test specimen were needed to validate the FE results and design criteria equations developed by Dong (2008). A TFG with only one hollow tube as the top flange (TFG1) was studied by Ma (2014) and was chosen instead of a TFG2 with two tubular hollow flanges for multiple reasons. The first reason is that local deformations of the bottom hollow tube flange may occur at the bearings due to the compressive force from the reactions. To prevent these deformations, the tube would need an internal steel diaphragm or concrete infill. The second reason is that when the girder is composite with a concrete deck (in the final constructed condition), a larger girder flexural strength can be achieved using a flat plate of the appropriate width and thickness rather than a tube as the bottom flange, because the tubes are provided at limited depth and width. The third reason is that the unit cost of steel plates is less than the unit cost of steel tubes.

A 2/3-scale test specimen with two curved TFG1s (top flange is a tube and bottom flange is a plate) braced by three intermediate diaphragms was designed (Ma, 2014; Putnam, 2011), fabricated, and erected/assembled. The tubes were not filled with concrete. Figure 2.4 shows the assembled test specimen studied in this research. Figure 2.5 shows the plan view of the test specimen including diaphragms and stiffeners. The TFG1s have a span length to radius ratio of 0.45. Table 2.1 gives the arc length of the span and radius along the centerlines of G1, the test specimen, and G2. The distance between the girder centerlines is 8 ft. Table 2.2 provides a summary of the nominal dimensions of the TFGs. The top flanges of the test specimen girders are HSS12x8x3/8 tube sections fabricated from ASTM A500-B. The tubes were cold bent into the required curvature. The cold bending process for the tubes led to distortions in the cross sections. Table 2.3 gives the nominal and actual dimensions of the 2/3-scale TFG tubes after cold bending. The webs and bottom flanges were fabricated from ASTM A709 grade 50 steel plates. High Steel Structures, Inc. in Lancaster, PA, fabricated the girders in 2009.

The 2/3 scale was chosen to accommodate the available test setup area and to reduce cost. The TFG bridge design was based on design criteria developed by Dong (2008) using the AASHTO Load and Resistance Factor Design (LRFD) Bridge Design Specifications (AASHTO, 2005). The design criteria are described in the following section. Figure 2.6 shows the design process for the 2/3-scale TFG1s (test specimen) and the corresponding full-scale TFG1s. Proper scale factors and associated loading were used to ensure that the stress in the reduced-scaled specimen would be equal to the stress in a full-scale specimen Putnam (2012).

2.4 Detailed FE Models

FE models of the test specimen were developed by Ma (2014) to validate the design criteria from Dong (2008) for the Constructibility, Service II, and Strength I limit states (AASHTO, 2005), and to study the anticipated actual behavior of a curved girder bridge system. In the detailed FE models, shell elements are used to model the top tube flanges, webs, bottom flanges, tube end diaphragms, and stiffeners of the girders. For all detailed FE models, 16 shell elements are used across the width of the top tube flange, 6 shell elements are used across the depth web of the top tube flange, 12 shell elements are used across the depth of the plate web, and 16 shell elements are used across the width of the bottom plate flange. 360 elements are used along the span length of the girders. Beam elements are used to model the diaphragms (Ma, 2014).

Model-D1 is used to validate previous simplified models for the design of the curved girder bridge system. Model-D2 was used to generate the forces and displacements needed to design the loading fixture used for the test specimen. Model-D3 was developed as the bearing assemblies for the test specimen were designed (see Chapter 4). As a result, Model-D3 has boundary conditions based on the bearings designed for the tests. Model-D3 is used to develop the loading procedure and to make a pretest prediction of the test specimen response. Figure 2.6 and Figure 2.7 show detailed FE models of the test specimen with and without the concrete deck.

2.5 Design Criteria

Dong and Sause (2008) showed that the design criteria for conventional curved I-girders from the AASHTO LRFD Bridge Design Specifications (2004) can be adapted and effectively used to safely design TFG2s for curved bridges. Ma (2014) investigated the same criteria (AASHTO, 2010) for TFG1s for curved bridges. Three limits states from AASHTO (2010) were considered in the design criteria for curved conventional I-girder bridges and for curved TFG1 bridges by Ma (2014) as follows:

(1) Constructibility limit states;
(2) Service II limit state;
(3) Strength I limit state.

The design loads, load factors, and load combinations for the limit states above are listed in Table 2.4. The design loads are applied in different combinations with different load factors. The design loads are as follows (Ma, 2014):

D_C = weight of the structural components and attachments

D_W = weight of future wearing surfaces and utilities supported by the bridge girders

LL = live load including both the design truck load and design lane load

S_W = weight of steel girders

LL_C = construction live load

According to AASHTO (2010), both of the following girder compression flange stress criteria must be satisfied for the Constructability limit state:

$$f_{bu} + f_l \leq \phi_f R_h F_{yc} \tag{2.1}$$

$$f_{bu} + \frac{1}{3} f_l \leq \phi_f F_{nc} \tag{2.2}$$

Where

f_{bu} = flange stress from the primary bending moment

f_l = flange stress from the flange lateral bending moment

F_{yc} = specified minimum yield stress of the compression flange steel

F_{nc}= nominal flexural resistance of the compression flange based on the local buckling or lateral torsional buckling resistance of the flange

ϕ_f = resistance factor for flexure

R_h = hybrid factor

To prevent objectionable permanent deflections, AASHTO (2010) limits flexural stresses in steel girder flanges due to dead and live loads using the following criteria for the Service II limit state (Ma, 2014):

For the top steel flange of composite sections:

$$f_f \leq 0.95 R_h F_{yf} \tag{2.3}$$

For the bottom steel flange of composite sections:

$$f_f + \frac{f_l}{2} \leq 0.95 R_h F_{yf} \tag{2.4}$$

For both steel flanges of non-composite sections:

$$f_f + \frac{f_l}{2} \leq 0.80 R_h F_{yf} \tag{2.5}$$

Where

f_f = flange stress from the primary bending moment

f_l = flange stress from the flange lateral bending moment

F_{yf} = specified minimum yield strength of the flange steel

To ensure that adequate strength and stability are provided to resist the maximum loads expected during the normal use of the bridge, AASHTO (2010) requires composite sections in positive flexure to satisfy the following criteria for the Strength I limit state (Ma, 2014):

$$M_u + \frac{1}{3} f_l S_{xt} \leq \phi_f M_n \tag{2.6}$$

Where

M_u = primary bending moment

f_l = flange stress from the flange lateral bending moment

S_{xt} = elastic section modulus for the tension flange about the major axis of the section

M_n = nominal moment capacity of the section

The above AASHTO (2010) design criteria consider only the flange normal stresses and do not consider shear stresses in tubular flanges. Results presented by Dong and Sause (2008) show that the shear stresses in the tube do not have a significant contribution at critical cross sections to the total stresses as evaluated using the Von Mises stress criterion.

2.6 Test Setup Area

The location for the tests is at the Advanced Technology for Large Structural Systems (ATLSS) Engineering Research Center at Lehigh University in Bethlehem, PA. Figure 2.9 is a plan view of the test setup area showing the test setup. The test setup is singly symmetric about the mid-span of the test specimen. Seven parallel cross sections of four types divide up the test specimen. Section A is located at mid-span, Sections BE and BW are 7.5 ft away from mid-span in east and west directions, Sections CE and CW are 15 ft away from mid-span in east and west directions, and Sections DE and DW are 22.5 ft away from mid-span in east and west directions.

Two coordinate systems are used to describe the test setup. The first coordinate system is a cylindrical coordinate system, which corresponds to the geometry of the test specimen. The curved test specimen can be described in terms of a circumferential plane along the centerline of the test specimen, and radial planes perpendicular to the circumferential plane. The second coordinate system is a Cartesian coordinate system, which corresponds to the test setup area. The parallel planes of the test setup area are in the north-south direction and the longitudinal planes of the test setup area are in the east-west direction. The vertical direction is the same for both coordinate systems and is parallel to the direction of gravity.

In the test setup, the diaphragms and stiffeners of the test specimen are located in radial planes, while the ground anchor rods (see Figure 2.11) and loading fixtures are located in parallel planes. The radial plane and parallel plane are identical at mid span plane, but the radial planes and parallel planes intersect at other locations as shown in Figure 2.11. Therefore the parallel plane load fixtures do not line up with the diaphragms and stiffeners (except mid span) and there are offsets between the radial plane intersections with G1 and G2, and the parallel plane intersections with G1 and G2. Figure 2.10 shows the parallel and radial planes, and the intersections between them.

Table 2.1 Test specimen radii and arc lengths (Hampe, 2012)

Location	Radius		Arc Length	
	in.	ft	in.	ft
G1	1552.0	129.3	698.4	58.2
CL Test Specimen	1600.0	133.3	720.0	60.0
G2	1648.0	137.3	741.6	61.8

Table 2.2 TFG cross section and geometry summary (Sause et al., 2014)

Girder	Depth (in.)	Tube (in.)	Plate (in.)	Web (in.)	Area (in.^{2})
G1	36	12x8x0.349	12x0.75	27.25x0.375	32.7
G2	36	12x8x0.349	12x1.5	26.5x0.375	41.4

Table 2.3 Tube distortion from cold curving process (Hampe, 2012)

Location	Nominal Dimensions (in.)	Actual Dimensions After Curving					
		G1			G2		
		Inside Depth (in.)	Outside Depth (in.)	Tube Width (in.)	Inside Depth (in.)	Outside Depth (in.)	Tube Width (in.)
East End	12 x 8	8.450	8.116	11.708	8.328	8.160	11.746
Section A		8.506	8.157	11.642	8.499	8.123	11.678
West End		8.325	8.157	11.689	8.501	8.124	11.633

Table 2.4 Load factors and load combinations for different limit states (Ma, 2014)

Limit State	D_C	LL_C	D_W	LL
Constructability	1.25	1.75	-	-
Service II	1.00	-	1.00	1.30
Strength I	1.25	-	1.50	1.75

Figure 2.1 Straight TFGs with concrete-filled rectangular steel tube top flange (Wimer and Sause, 2004)

Figure 2.2 Straight TFGs with concrete-filled round steel tube top flange (Kim and Sause, 2005a, b)

Figure 2.3 Curved TFG with hollow steel tube flanges and concrete infilled ends (Putnam, 2010)

Figure 2.4 Assembled test specimen studied in this thesis

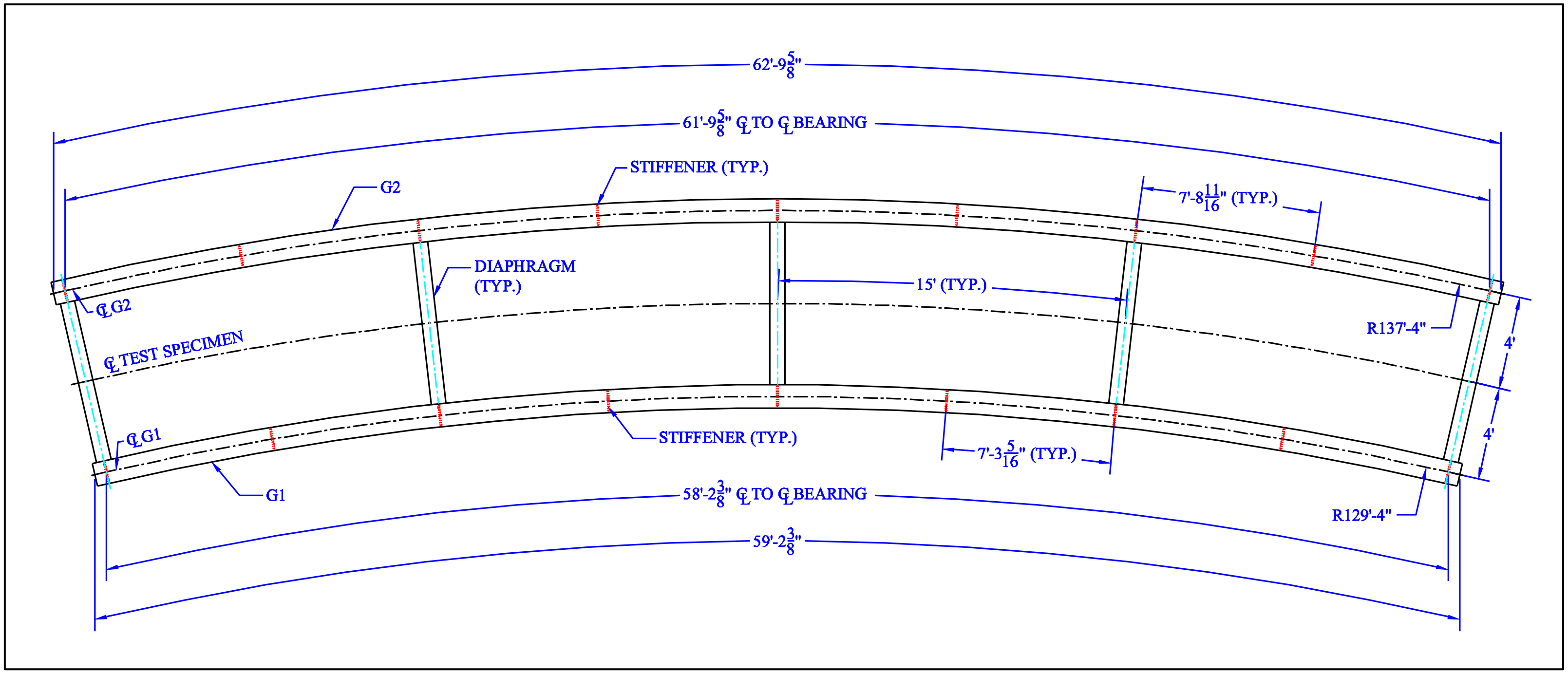

Figure 2.5 Test specimen plan view including diaphragms and stiffeners (Putnam, 2011)

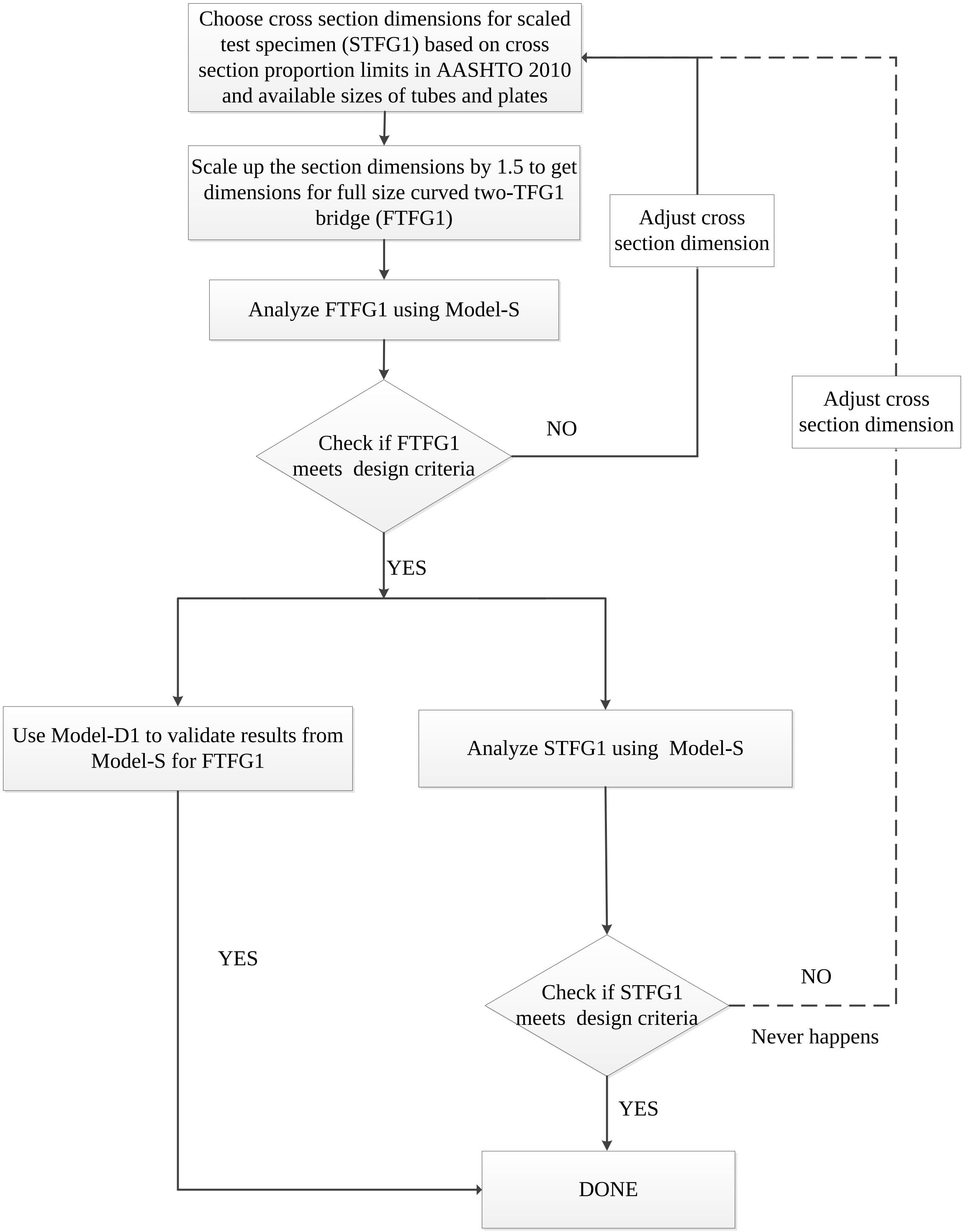

Figure 2.6 Design process for full-scale TFG1 and scaled TFG1 (Sause et al., 2014)

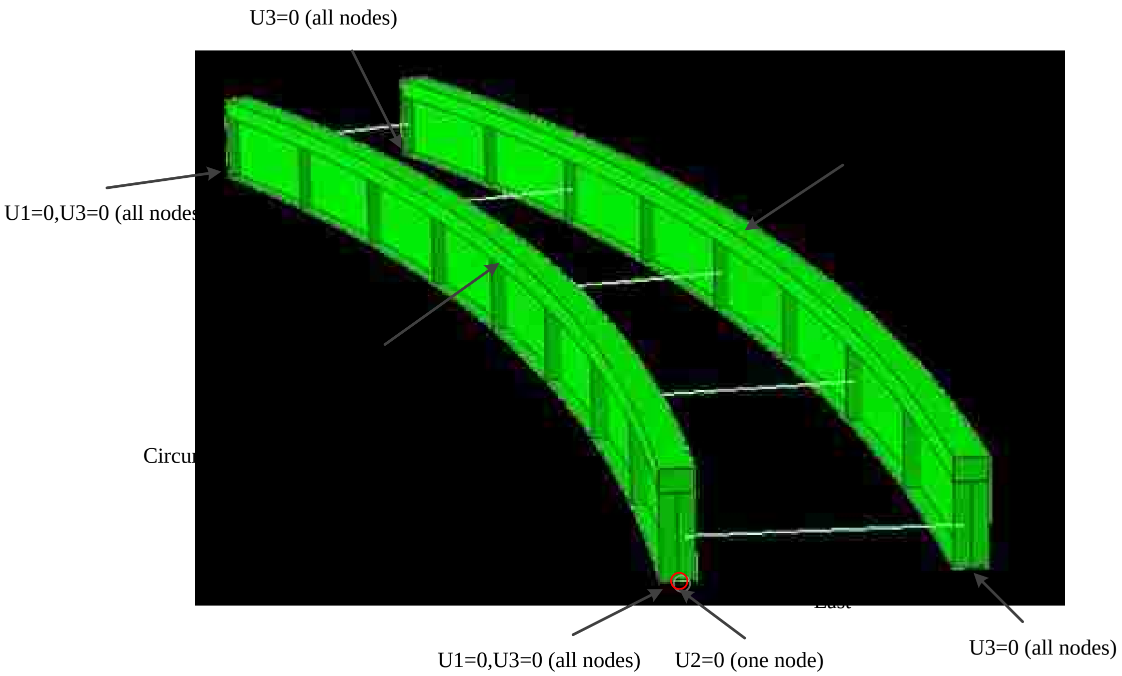

Figure 2.7 Detailed FE model (Model-D1) without concrete deck (Ma, 2014)

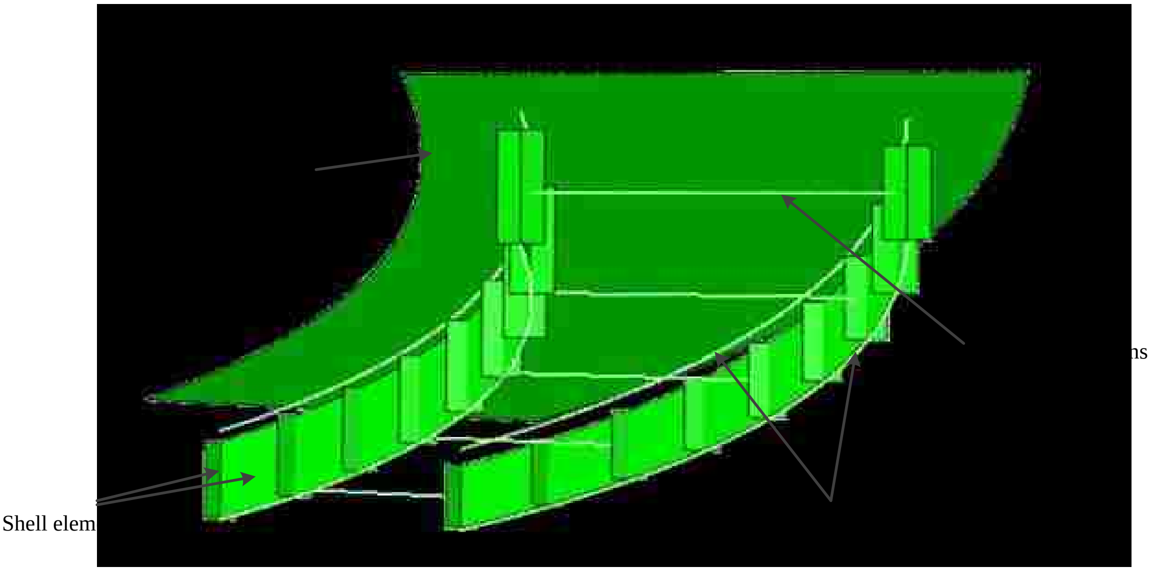

Figure 2.8 Detailed FE model (Model-D1) with concrete deck (Ma, 2014)

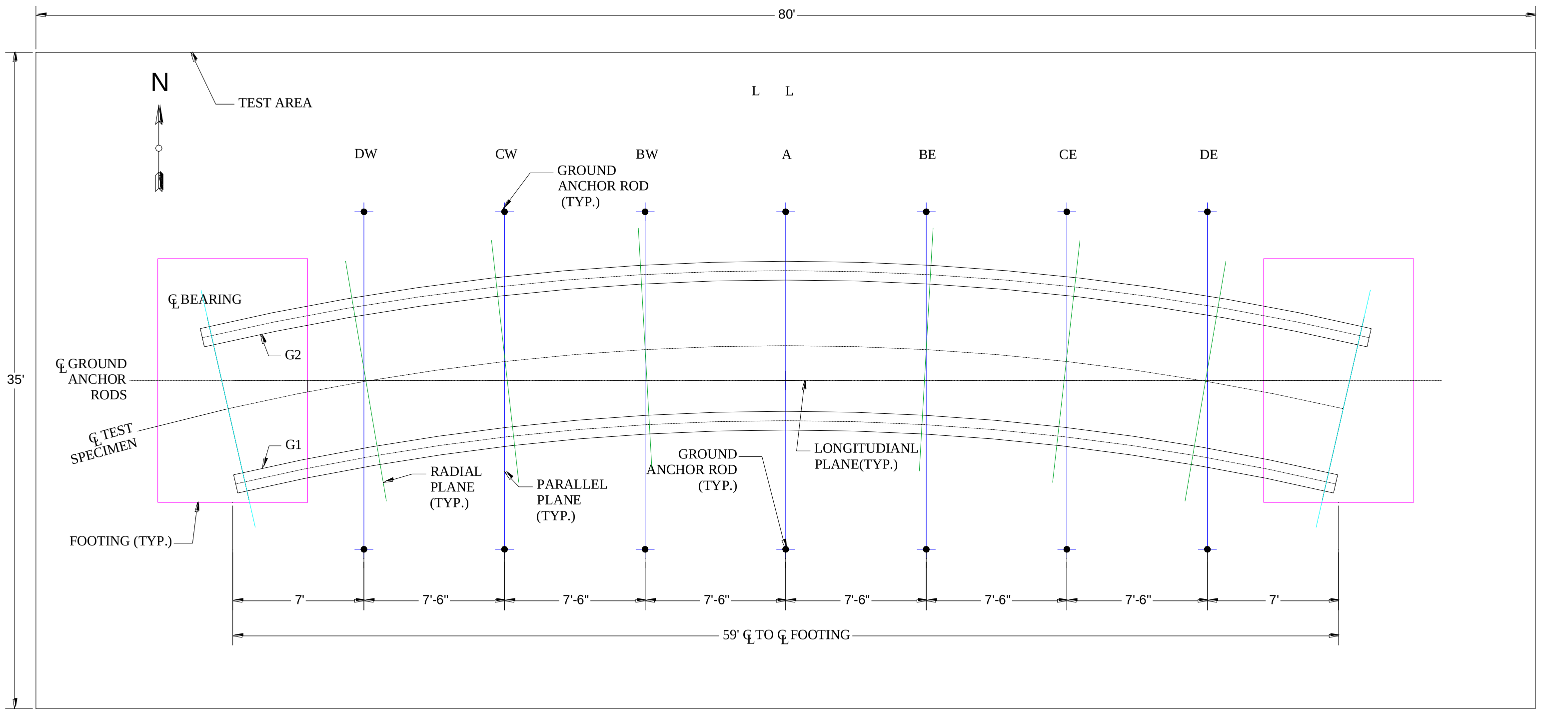

Figure 2.9 Plan view of test setup area (Sause et al.,2012)

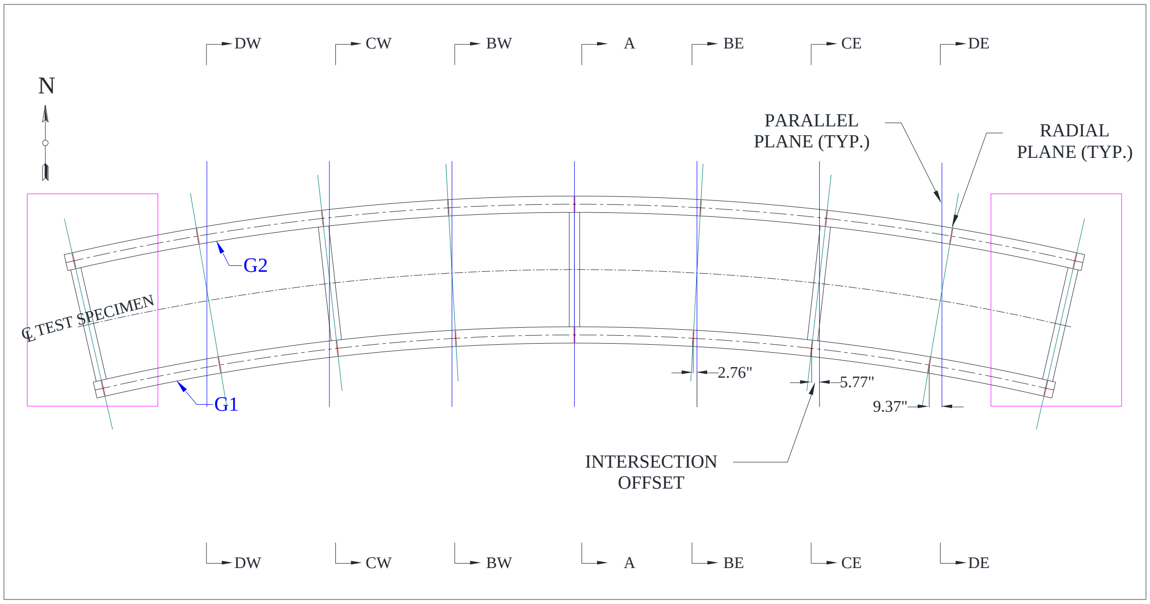

Figure 2.10 Plan view of the test specimen showing parallel planes and radial planes and the intersection offsets between them


[redacted]
[redacted]

Figure 2.11 Installed ground anchor rods covered by plastic pipes (Sause et al., 2009)

3 LOADING AND KINEMATICS OF THE TEST SPECIMEN

3.1 Introduction

This chapter reviews the test specimen loading and the expected behavior of the test specimen and the loading fixtures under loading to (and beyond) the maximum load capacity. Section 3.2 describes the load conditions, idealization, and modeling of the test specimen. Section 3.3 reviews test specimen response based on analysis of FE models. Section 3.4 explains the loading fixtures for the tests, designed by Hampe (2012). A parallel plane cross section view of the test specimen and a loading fixture is shown in Figure 3.1, and the main parts of the loading fixture are shown.

3.2 Test Specimen Loading

The test specimen was loaded using seven loading fixtures (Figure 3.1). Each loading fixture applies two concentrated loads on the test specimen. The loading fixtures were located in the seven parallel planes shown in Figure 3.2. This section explains the loads applied to the test specimen. Section 3.2.1 describes the load conditions for the tests and Section 3.2.2 discusses the idealization and modeling of the loads applied to the test specimen.

3.2.1 Load conditions

Two load conditions were applied to the test specimen. The first load condition is the Constructability limit state design load for the deck placement condition. In this load condition, the test specimen is expected to be in the elastic range and during the tests the load may be several times. The second load condition applied to the test specimen takes it to its maximum load capacity (and displaces it beyond the point of maximum load capacity). In this second load condition, the deck placement condition is of concern, so the test specimen is not composite with a concrete deck. The expected failure mode is yielding in the top tube flange where the stress is expected to be dominated by bending normal stress (Dong, 2008).

3.2.2 Idealization and modeling of loads

During deck placement stage of the steel girder bridge construction process, the non-composite girders support the weight of the concrete deck, the construction live load, and the formwork required to cast the deck. In this study, the deck placement loads are idealized as a uniformly distributed load, which is constant over the deck area. In the tests, it was not possible to apply a uniformly distributed load since the tests required the load to be applied and removed several times; Also, in the final test, the test specimen was to be loaded beyond its maximum load capacity, and test safety is a primary concern.

Therefore, the test specimen was loaded with concentrated loads instead of a uniformly distributed load. For a simply supported straight girder, the same mid span moment can be developed by a uniformly distributed load or a set of concentrated loads. For a simply supported curved girder bridge, this may not be true because of the torsional load effects caused by the horizontal curvature. Therefore, FE Model-D2 was developed to determine if concentrated loads on the test specimen could produce similar load effects as a uniformly distributed load on the test specimen. Finally, as shown in Figure 6.1 and

Figure 6.2, the tests used seven concentrated loads distributed along the span of each curved TFG1 between the bearings to simulate the idealized uniformly distributed load.

Model-D2 (see Section 2.4) includes one concentrated point load at mid span and concentrated patch loads on the tube of the TFG1 at 6 other locations, along the span of each girder of the test specimen. The patch loads are applied over a 12 in. by 12 in. bearing plate at the six locations. At mid span, the concentrated point load is applied on the edge of the mid span stiffener to simulate the load applied to the mid span diaphragm, as discussed later. The seven concentrated loads are applied at sections near the interior diaphragms and at the sections approximately halfway between the diaphragms. The loads do not align precisely with the interior diaphragms and stiffeners because of the differences between the parallel planes and radial planes (as discussed in Section 2.6). In the test setup, sufficient space was needed to work around the loading fixtures and using seven equally-spaced loading fixtures allowed for about 6.5 ft. (clear) spacing between adjacent loading fixtures.

Ideally, each loading fixture would load the test specimen in a radial plane and each concentrated load would represent an idealized tributary area of the bridge deck. However, the ground anchor rods are located in parallel planes as discussed in Section 2.6. Therefore the loads were applied to the test specimen in the parallel planes. The G2 patch loads are larger than the G1 patch loads because the G2 patch loads simulate the load on a larger bridge deck area as shown in Figure 6.4. The difference is caused by the curvature of the test specimen and the resulting bridge deck area that each girder supports. Assuming that each TFG1 supports half of the width of the deck, G2 supports a total area of 399.5 ft^2 and G1 supports a total area of 380.5 ft^2, resulting in a 1.05 ratio of G2 patch loads to G1 patch loads.

The parallel planes are labeled section A, BE, BW, CE, CW, DE and DW as discussed in Section 2.6. Figure 3.3 (a) shows a cross section view of the test specimen with the applied loads at Section A. Figure 3.3 (b) shows a cross section view at Section Type B (representing Sections BE and BW), Section Type C (representing Sections CE and CW), and Section Type D (representing Section DE and DW). The cross section view at Section Type C (representing Sections CE and CW) differs from the view shown in Figure 3.3 (b) because a diaphragm should be shown. In these figures, p represents the concentrated patch loads (such as p_{5_2}) and P represents a concentrated point load (such as P_{5_1}). Each point load equals the patch pressure load multiplied by the patch area it replaces. As shown in Figure 3.3 (a) the point loads, $\mathrm{P}_{5\text{-}1}$ and P_{5_2}, were applied to the inside top edge of the stiffeners in Model-D2.

These point loads simulate the loads applied to the mid span diaphragm of the test specimen. The load was applied to the diaphragm in the test (and to the stiffener in Model-D2) because a point load directly on the tube of the TFG1s at mid span, where failure due to flexural yielding of the tube is expected, would affect the test specimen capacity. Therefore, the concentrated loads at mid span are applied to the mid span diaphragm (test specimen) or stiffeners (Model-D2).

3.3 FE Prediction

The predicted kinematics behavior of the test specimen and the loading fixtures is based on the results from analysis of different FE models conducted by Ma (2014) in ABAQUS. Two types of loading conditions were studied: conditions that produce linear elastic response and conditions that produce inelastic response up to and beyond the maximum load capacity (Ma, 2014).

The vertical and radial displacements of the top tube flanges at the seven parallel cross sections where the loading fixtures are located from FE Model-D2 were the basis for loading fixture design. Sketches and calculations were used to visualize and quantify the displacements of the test specimen and loading fixtures under loading by Hampe (2012). Figure 3.4 and Figure 3.5 display the vertical displacement response of top center node of G1 and G2 for different sections. Figure 3.6 and Figure 3.7 display the radial displacement response.

The expected behavior of the test specimen is based on the results from analysis of Model-D3 (Section 2.4). The vertical and parallel displacements at the center node of the bottom flange plates, where the displacement transducers are attached, were used in planning the test instrumentation (Chapter 5). Figure 3.8 and Figure 3.9 display vertical and parallel displacements at mid span in the elastic loading range. Vertical displaced shapes of girders G1 and G2 in the elastic loading range are displayed in Figure 3.10 and Figure 3.11. Vertical and parallel displacements in the inelastic loading range are presented in Figure 3.12 and Figure 3.13. Vertical displaced shape of girders G1 and G2 in the inelastic loading range are displayed in Figure 3.14 and Figure 3.15.

In the tables and figures with results from analysis of FE models presented in this chapter and the following chapters, FE load steps 1 to 6 (FE increments 1 to 12) represent the elastic loading range. FE load steps 7 to 18 (FE increments 13 to 35) represent the inelastic loading range where the maximum load capacity is reached in FE load step 18 (FE increment 35). FE load step 19 (FE increments 36 to 50) represents post peak loading.

3.4 Loading Fixtures

The design of the loading fixtures for the test was done by Hampe (2012). The design of the loading fixtures has four main goals. The first goal is to allow loading and unloading of the test specimen in the elastic range multiple times. The second goal is to be able to load the test specimen safely beyond its maximum load capacity. The third goal is to allow the test specimen to displace without restraint from the loading fixtures so that the loading fixtures do not influence the response to the loads. The fourth goal is to keep the applied loads vertical.

The parallel plane cross section view of the loading fixture for Section A is shown in Figure 3.1. As shown in the figure, the load at Section A is applied to the mid span diaphragm. However, at Section Types B, C, and D, the load is applied to a bearing plate on top of the tube of the TFG1, as shown in Figure 3.16 through 3.18. Figure 3.16 is parallel plane cross section view of the load bearing assembly at Section A. Figure 3.17 is a parallel plane cross section view of the load bearing assembly at Section Type B (representing Section BE and BW). Figure 3.18 is a parallel plane cross section view of the load bearing assembly at Section Types C (representing Section CE and CW) and D (representing Section DE and DW).

The designs of the components of the loading fixtures are discussed in in this section. In this discussion, the term “width” refers to the dimension in the longitudinal plane, the term “length” refers to the dimension in the parallel plane, and the term “thickness” refers to the dimension in the vertical direction. A summary of the dimensions of the plates and bars of the loading fixtures is given in Table 3.1. A summary of the lengths of the HSS, the load transfer channels, the loading beam, and the half-rounds is given in Table 3.2. All steel plates used for loading rod assembly are fabricated from ASTM A572 grade 50 steel.

3.4.1 Load transfer channels and attachments

At each loading fixture, as shown in Figure 3.1, the loading rod assemblies pull down on the loading beam above the test specimen. The loading beam bears on the test specimen through the load bearing assemblies. The loading rod assemblies pull up on the load transfer channels. A standard Dywidag nut and Plate A, transfer the load from the load transfer channels to each ground anchor rod. The load transfer channels are back-to-back C12x20.7 ASTM A992 grade 50 steel channels. The load transfer channels are 2 in. apart, and are laced together with steel tie plates. The ground anchor rods and the main rods of the loading rod assemblies fit in the gap between the backs of the channels.

Figure 3.19 shows longitudinal cross section views of the south end and north end tie plates. The tie plate arrangement along the load transfer channels at each section type is shown in Figure 3.20. The figure shows that the south end tie plates and intermediate tie plates are between the ground anchor rods, and the north end tie plate is beyond the north ground anchor rod to avoid potential collision with the north loading rod assembly. The channels have stiffeners at the locations of the ground anchor rods and at the initial positions of the loading rod assemblies. The load transfer channels were braced at the ends by concrete blocks (and wooden wedges as needed). Figure 3.21 shows a plan view of the bracing (without the wooden wedges). Figure 3.22 is a photograph of the concrete blocks and wooden wedges in places for the tests.

3.4.2 Loading beams and attachments

The loading rod assemblies pull down on the loading beam, which transfers the load to the load bearing assemblies on the test specimen. The loading beam is a W10x49 (bending about its weak axis) fabricated from ASTM A992 grade 50 steel. The loading beam is 13 ft long and the mid-length is aligned with the centerline of the test specimen. Portions of the web of the loading beam are cut out so that the load bearing assemblies push up near the top of the loading beam to increase the stability provided by the load height effect. Figure 3.23 shows a photograph of a loading beam and the corresponding loading rod assemblies and load bearing assemblies.

3.4.3 Loading rod assemblies

The forces to load the test specimen are provided by jacks located within the loading rod assemblies as shown in Figure 3.24 and Figure 3.25. Figure 3.26 is a plan view of the west half of the test setup that shows the spacing between the ground anchor rods, the loading rod assemblies, and the centerline of the test specimen. Each loading fixture has two loading rod assemblies. Each loading rod assembly acts in tension. The loading rod assembly transmits this load to the load transfer channels and the loading beam through a series of plates, rods, and half-rounds that make up the loading rod assembly.

The main rod of loading rod assembly is a 1 in. diameter ASTM A193 grade B7 threaded rod. The length is approximately 6.75 ft. The main rod is put into tension when the jack pushes up against Plate C, which is held down by a nut on the main rod. As the jack pushes up on Plate C it pushes down on Plate D. Plate D distributes the load to a load cell. An oversized 1.25 in. diameter hole decreases the possibility of the main rod bearing against the side of Plate D.

The load is transferred from Plate E to Plate B by the four small rods and nuts. The small rods are 0.5 in. diameter ASTM A193 grade B7 threaded rods. Each small rod is about 3 ft. long. The small rods transfer the load to Plate B, which bears on the round surface of the half-rounds. When the jacks are re-stroked during the tests (explained in Section 6.8), a nut on the main rod above Plate B holds the loading fixture and test specimen in place. Plate B pushes down on two half-round sections that rotate with the loading beam (see Figure 3.24). The half-rounds enable the loading rod assembly to remain vertical while the loading beam rotates in the parallel plane. The half-rounds are fabricated from 4 in. diameter ASTM A193 grade B7 round bar. Two 3 in. long half-rounds are under Plate B with a space between them for the main rod. The longitudinal axis of these half-rounds is in the longitudinal plane. The loading rod assembly half-rounds bear on a 0.25 in. thick neoprene pad as shown in Figure 3.24. This material is included to “soften” the contact between the half-rounds and Plate H to permit a rotation in the longitudinal plane between the loading rod assemblies and loading beam.

The neoprene pad bears on Plate H. Plate H transfers the load from the loading rod assembly to the loading beam through welds. Plate H is attached on the bottom of the loading beam to increase stability of the loading beam from the load height effect. An extra-large hole in Plate H with diameter of 1.75 in. prevents the main rod from bearing against Plate H. The force in the main rod is transferred to the load transfer channels by Plate F. The normal force between Plate F and the load transfer channels will result in frictional forces on the contact surfaces.

The loading rod assemblies are designed assuming that they displace freely in the parallel direction in the parallel plane, and large frictional forces may prevent this. To decrease the frictional forces, Teflon is placed on the top of Plate F to reduce the friction between the load transfer channels and Plate F. The static coefficient of friction of Teflon-on-steel is about 0.04 (Serway and Jewett, 2010) compared with 0.3 for steel-on-steel (AASHTO, 2005). To minimize friction between the Teflon and the load transfer channels, a 15 in. length of the bottom of the load transfer channels was painted and greased. Figure 3.27 is a photograph of the contact between the load transfer channels and Plate F.

3.4.4 Load bearing assemblies

The load bearing assemblies transmit the load from the loading beam to the test specimen. Photographs of the load bearing assemblies are given in Figure 3.28 for Section Type B and Figure 3.29 for Section Types C and D. At each load bearing, the load is transferred from the loading beam to one or two plates. These plates bear on a half-round. The half-round bears on the top cap plate. The top cap plate bears on a 1 in. square bar, and the bottom cap is between the square bar and the HSS of the load bearing assembly. The HSS bears on a plate on top of the tube of the TFG1 (Plate G) or on top of the mid span diaphragm (Plate K). The load is transferred to the load bearing assembly through Plate J. Plate J is welded to the top of the flanges of the loading beam.

At Section A and Section Type B the half-round longitudinal axis is in the longitudinal direction and there is one Plate J. At Section Type C and Section Type D the half-round longitudinal axis is in the parallel direction and there are two Plate J spaced 4 in. apart on center. The top and bottom edges of each end of Plate J are welded to the flanges of the loading beam. At Section Type C and at Section Type D, Plate I is between the two Plate J and the half-round. Plate I transmits the load from the half-round to two Plate Js. The half-round is welded to the top cap plate to prevent relative movement. The bottom cap plate is welded to the walls of the HSS. The top cap plate bears on a 1 in. square bar. The bar is designed to act as a rotational kinematic release. As shown in Figure 3.28 and Figure 3.29, the longitudinal axis of the bar is perpendicular to the longitudinal axis of the half-round. To stabilize the square bar and cap plates during assembly of the loading fixture, crushable foam is used on both sides of the bar between the cap plates. The foam is expected to crush to allow rotations in the plane perpendicular to the longitudinal axis of the bar.

The HSS of the load bearing assembly is used to fill the distance between the bottom cap plate and the bearing plate (Plate G or Plate K) that loads the test specimen. The base of the HSS is welded to the bearing plate. The bearing plates under the HSS are Plate G on top of the TFG1 tube at Section Types B, C, and D, and Plate K on the top of the mid span diaphragm at Section A.

Table 3.1 Dimensions of plates and bars of loading fixtures (Hampe, 2012)

Part	Width (in.)	Length (in.)	Thickness (in.)
Plate A	8	5	1.5
Plate B	8.5	10	1
Plate C	5	5	0.75
Plate D	5	5	0.75
Plate E	8.5	10	2
Plate F	5	5	0.75
Plate G	12	12	1
Plate H	12	6.5	1
Plate I	2.5	6	0.75
Plate J	8.88	1.75	1.75
Plate K	8	7	0.75
1 in. Bar	1	6	1
Cap Plate	7	7	0.75
South End Tie Plate	4.5	4.5	0.25
Intermediate Tie Plate	4.5	2.75	0.25
North End Tie Plate	2	5	12
Stiffener	2.25	0.25	12

Table 3.2 Lengths of steel shapes of loading fixtures (Hampe, 2012)

Part	Length (in.)
HSS – Section A	14.75
HSS – Sections B, C, D	6.25
C12x20.7	240
W10x49	156
Loading rod assembly 4 in. diameter half-round	3
Load bearing assembly 4 in. diameter half-round	6

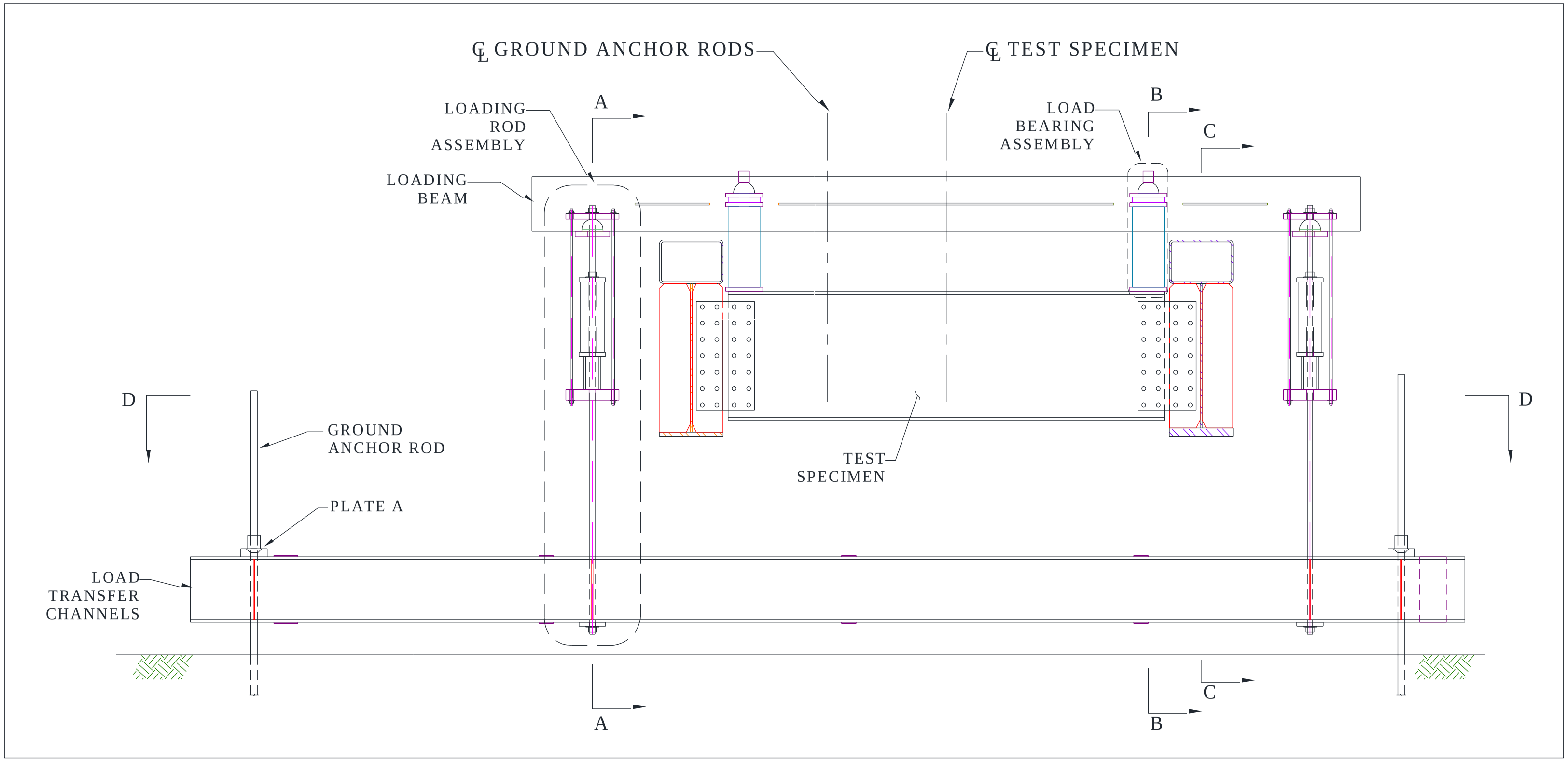

Figure 3.1 Parallel plane cross section view of test specimen and loading fixture at Section A (Hampe, 2012)

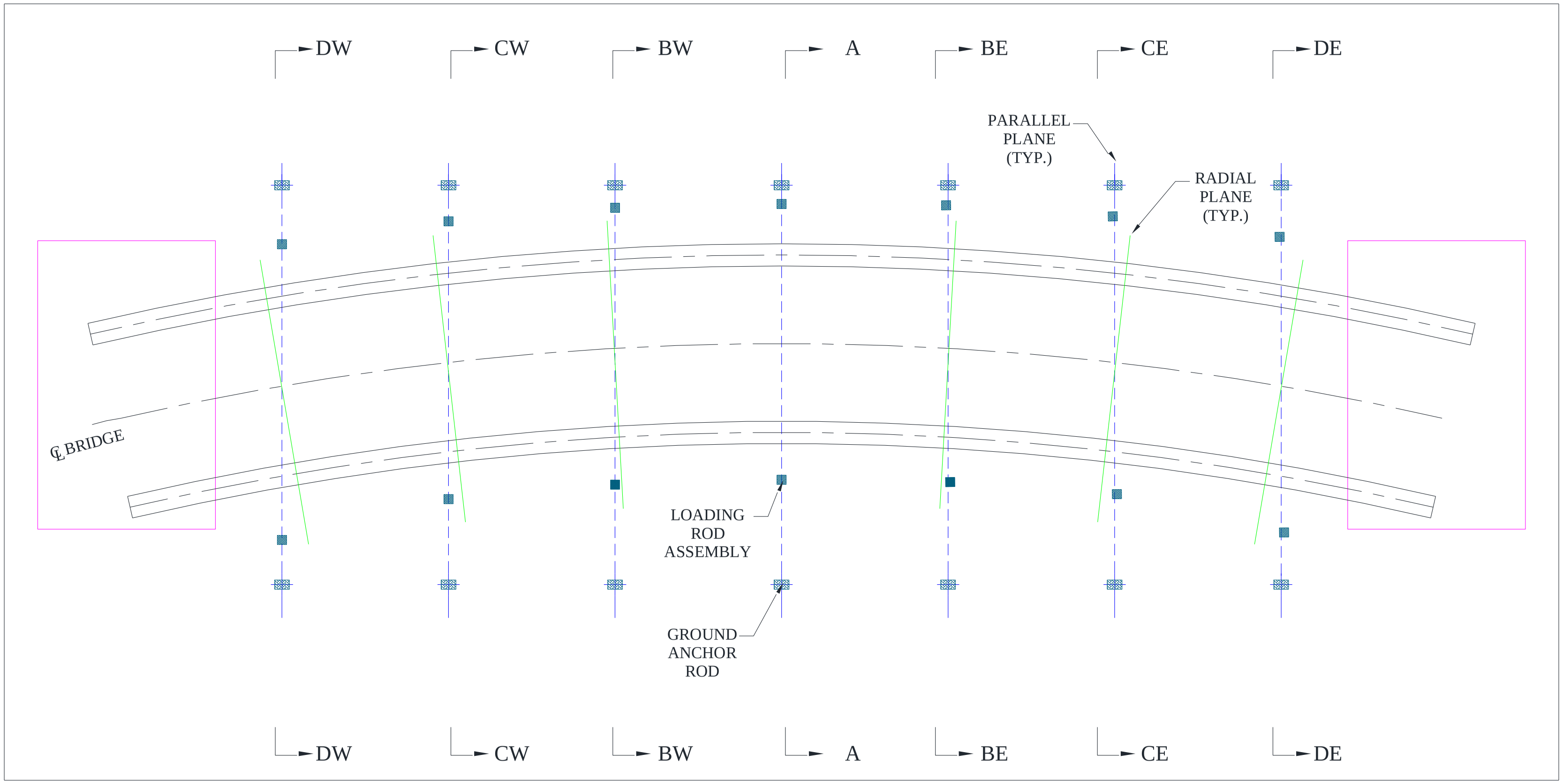

Figure 3.2 Plan view of the test specimen and position of seven parallel planes with loading fixtures

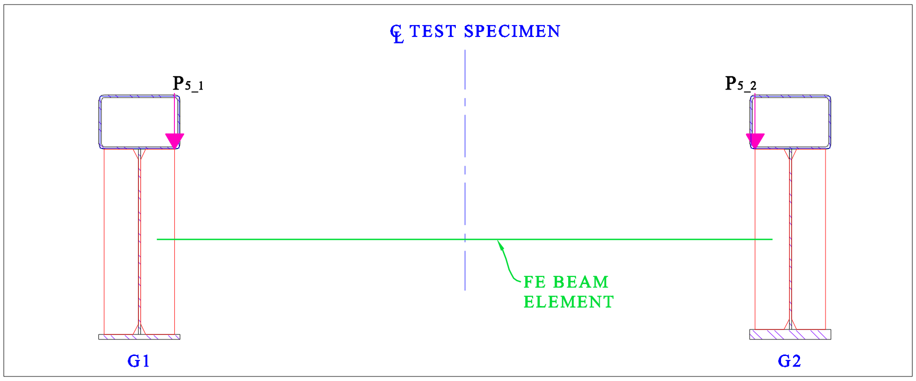

(a) Load Case 5: Applied force at Section Type A

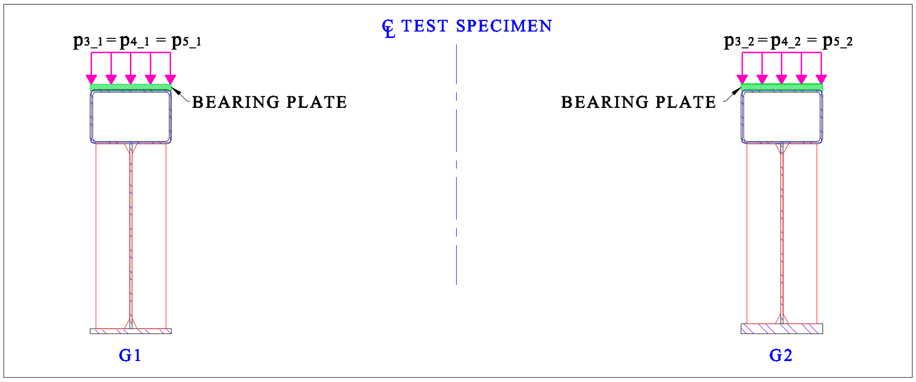

(b) Load Case 5: Applied force at Section Type B, C and D

Figure 3.3 Radial plane cross section views of applied force in model-D2 (loading case 5, Hampe, 2012)

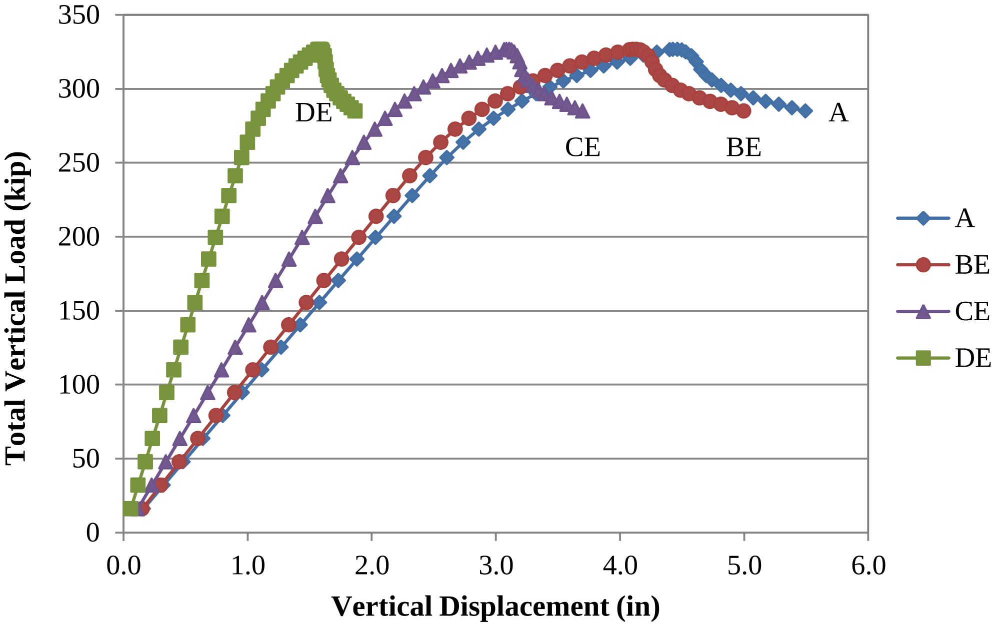

Figure 3.4 Force-vertical displacement response of top center node of G1 (Hampe, 2012)

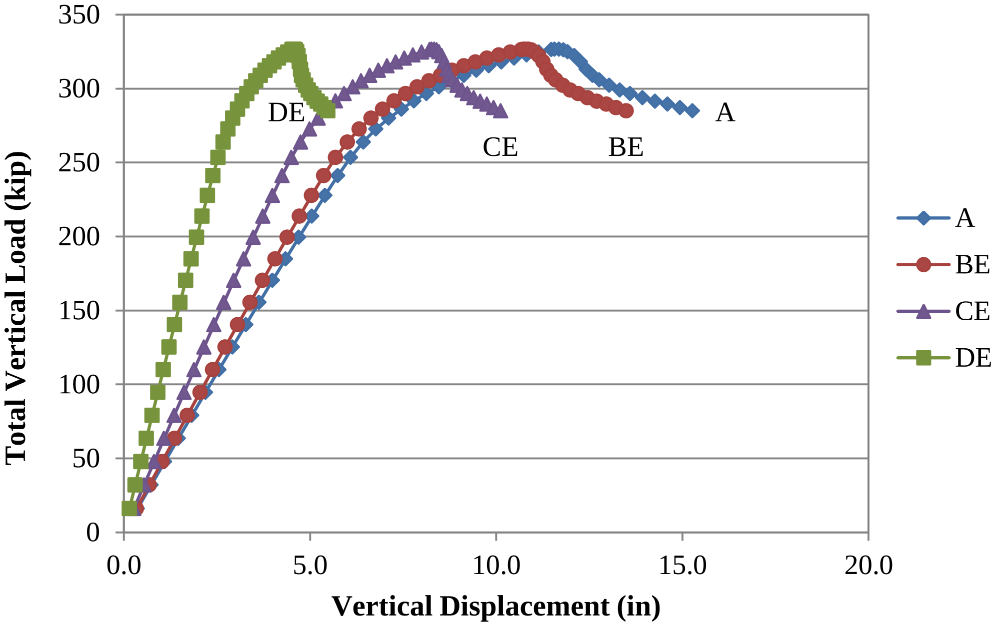

Figure 3.5 Force-vertical displacement response of top center node of G2 (Hampe, 2012)

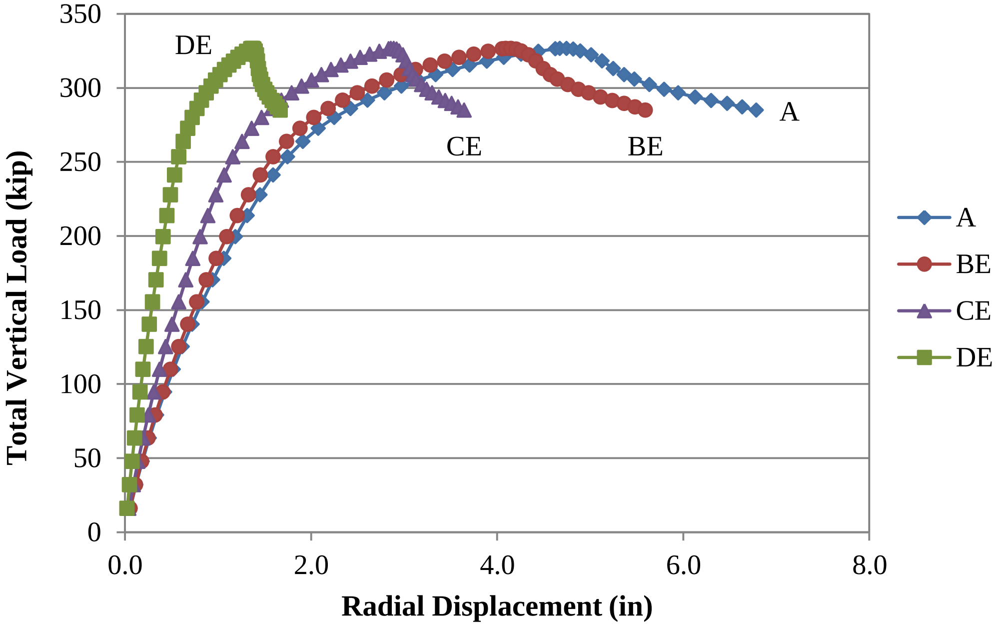

Figure 3.6 Force-radial displacement response of top center node of G1 (Hampe, 2012)

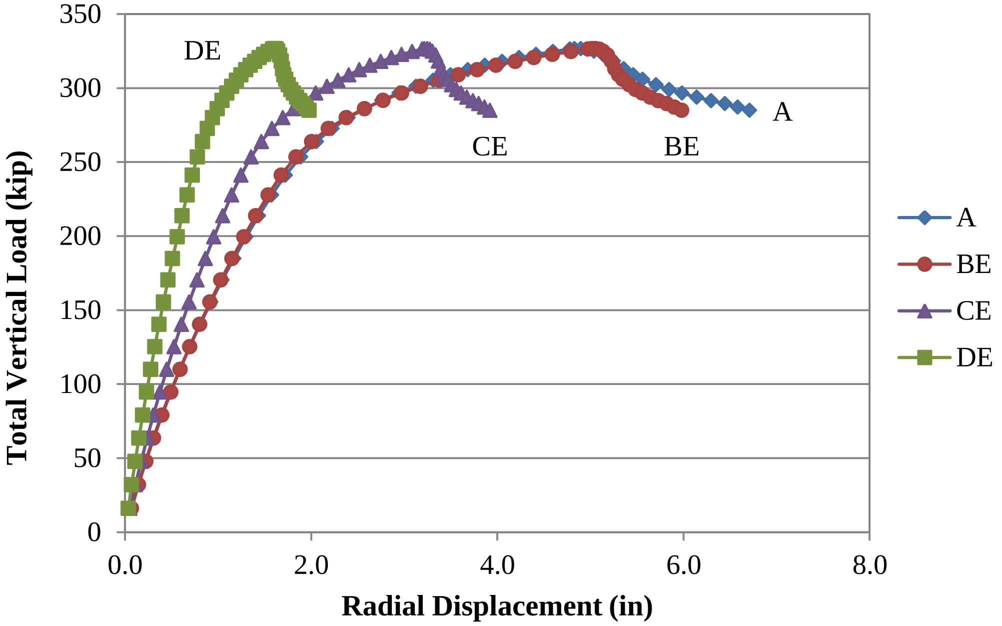

Figure 3.7 Force-radial displacement response of top center node of G2 (Hampe, 2012)

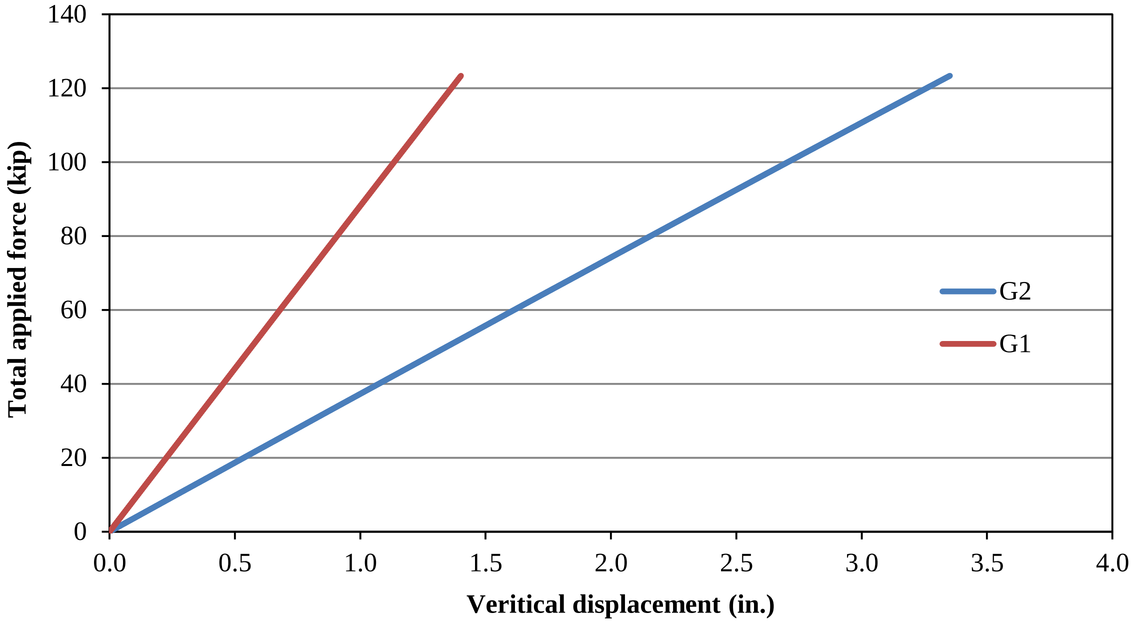

Figure 3.8 Total applied force vs. vertical displacement of bottom flange at mid span during elastic loading range (Ma, 2014)

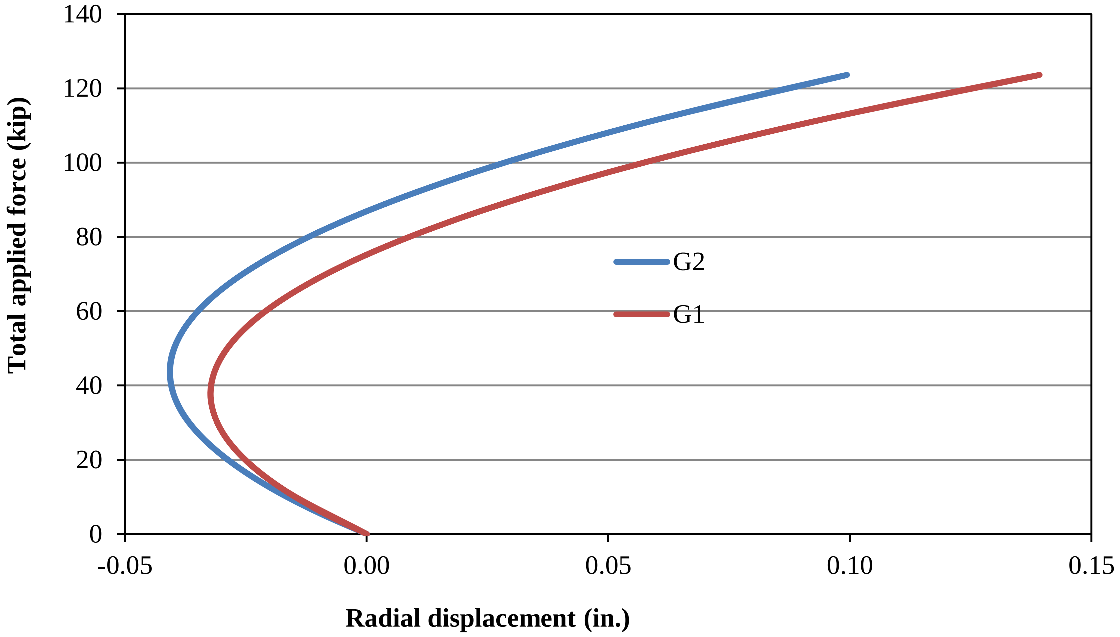

Figure 3.9 Total applied force vs. parallel displacement of bottom flange at mid span during elastic loading range (Ma, 2014)

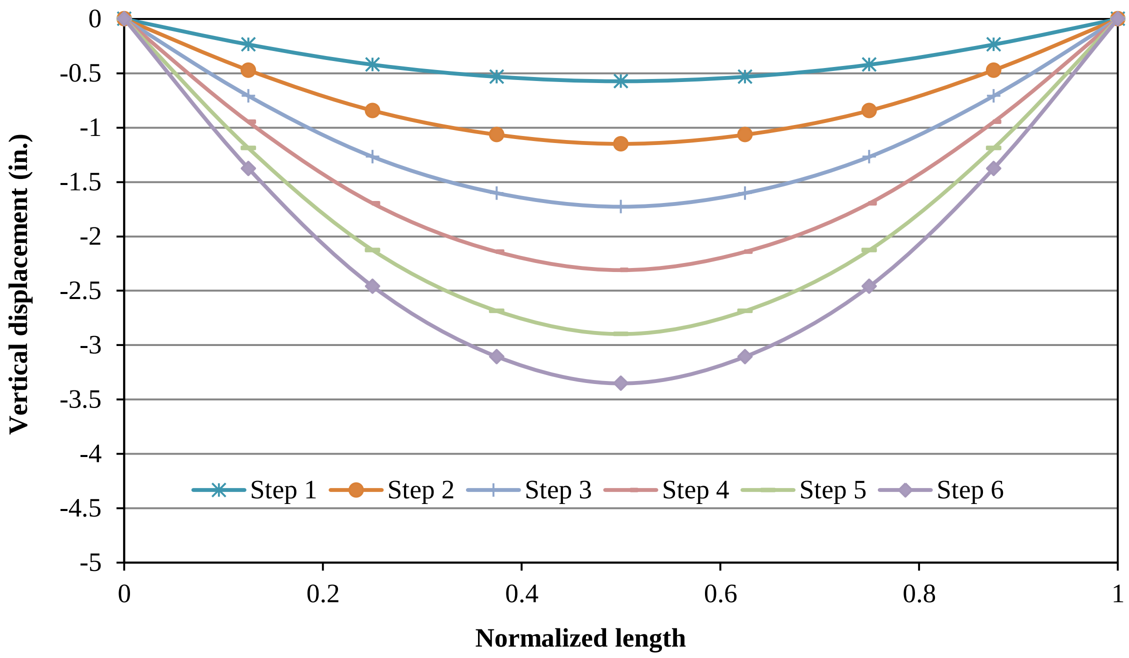

Figure 3.10 Vertical displaced shape of G2 along span during elastic loading range (Ma, 2014)

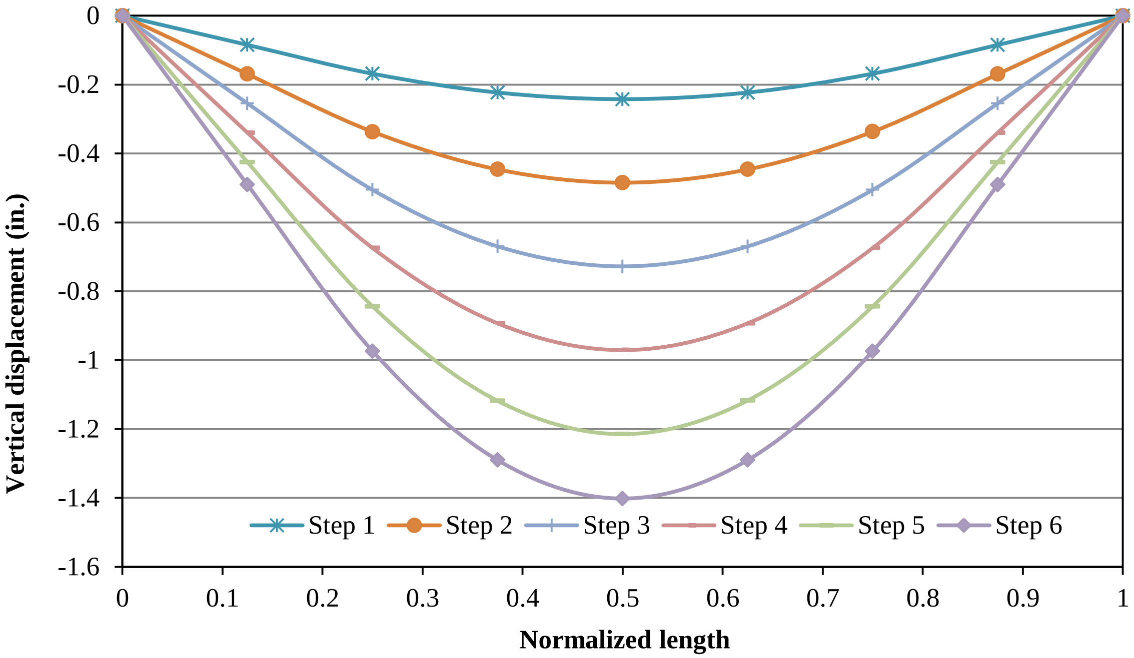

Figure 3.11 Vertical displaced shape of G1 along span during elastic loading range (Ma, 2014)

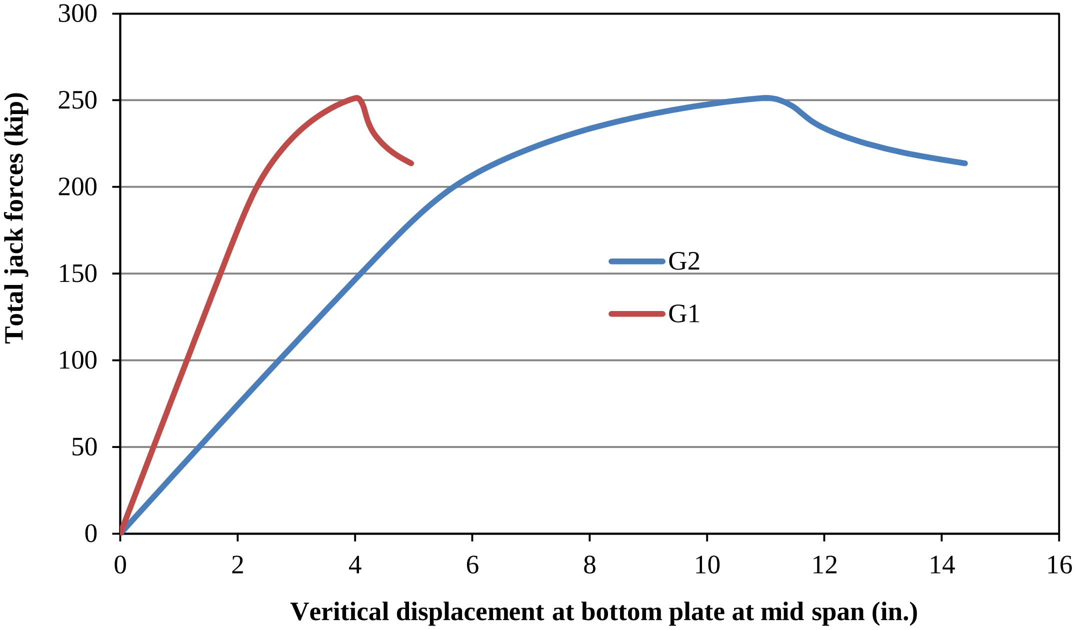

Figure 3.12 Total applied force vs. vertical displacement of bottom plate at mid span during inelastic loading range (Ma, 2014)

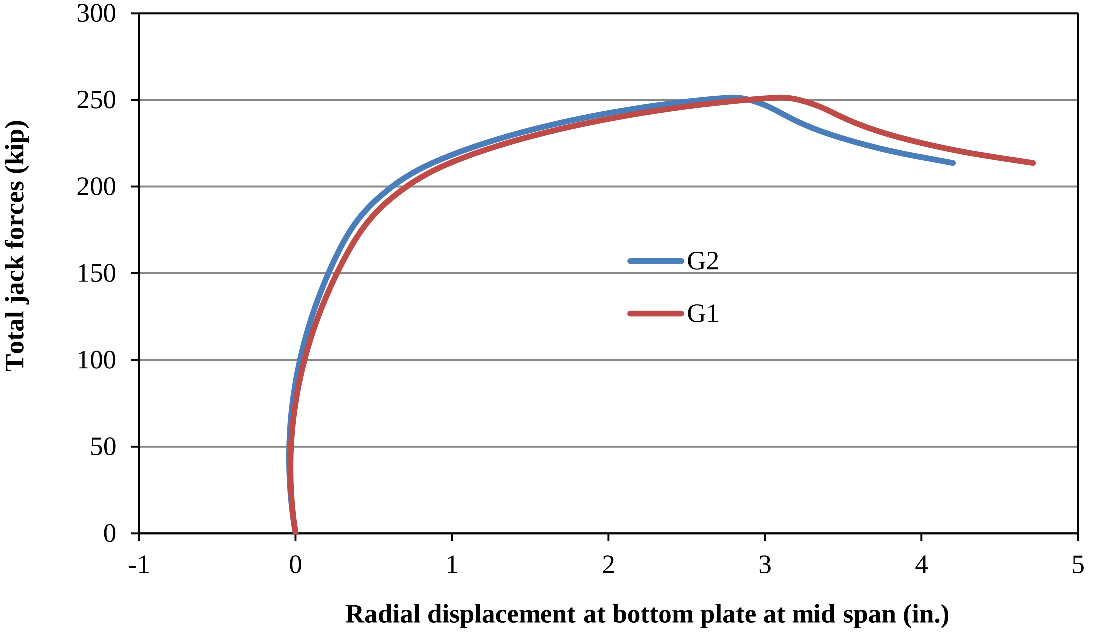

Figure 3.13 Total applied force vs. parallel displacement of bottom plate at mid span during inelastic loading range (Ma, 2014)

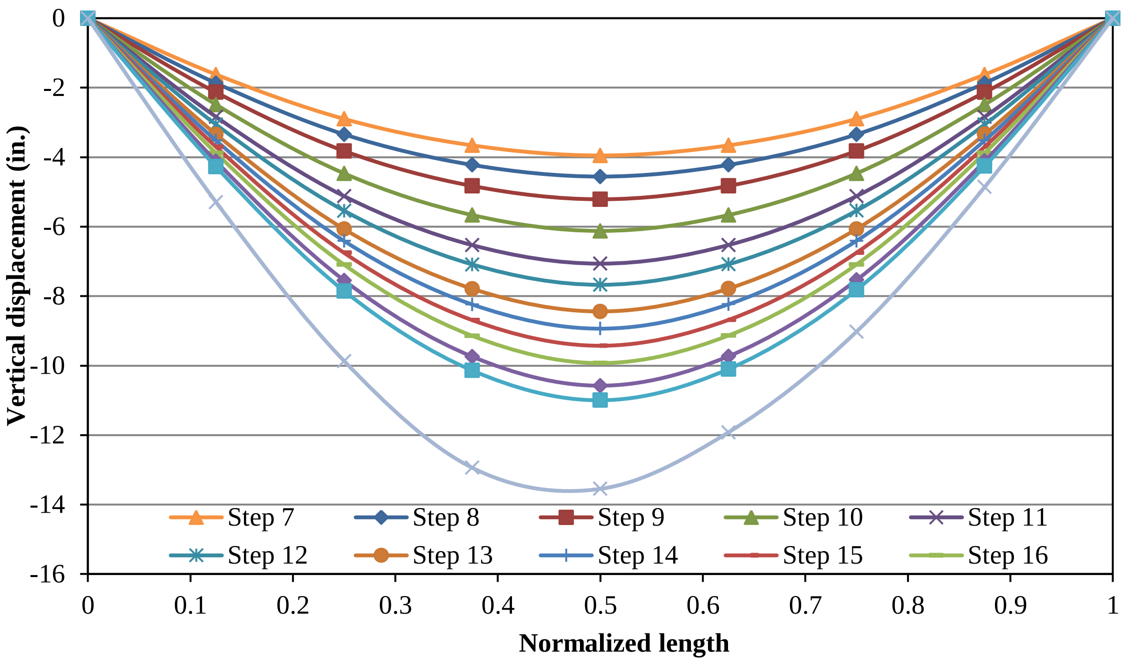

Figure 3.14 Vertical displaced shape of G2 along span during inelastic loading range (Ma, 2014)

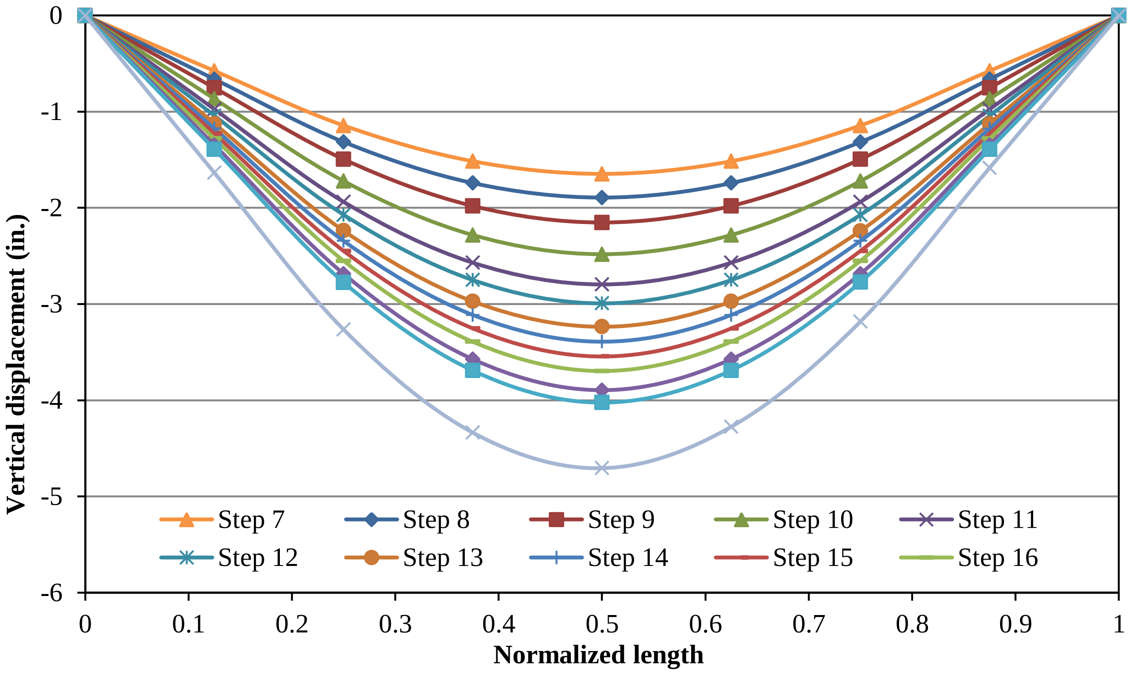

Figure 3.15 Vertical displaced shape of G1 along span during inelastic loading range (Ma,2014)

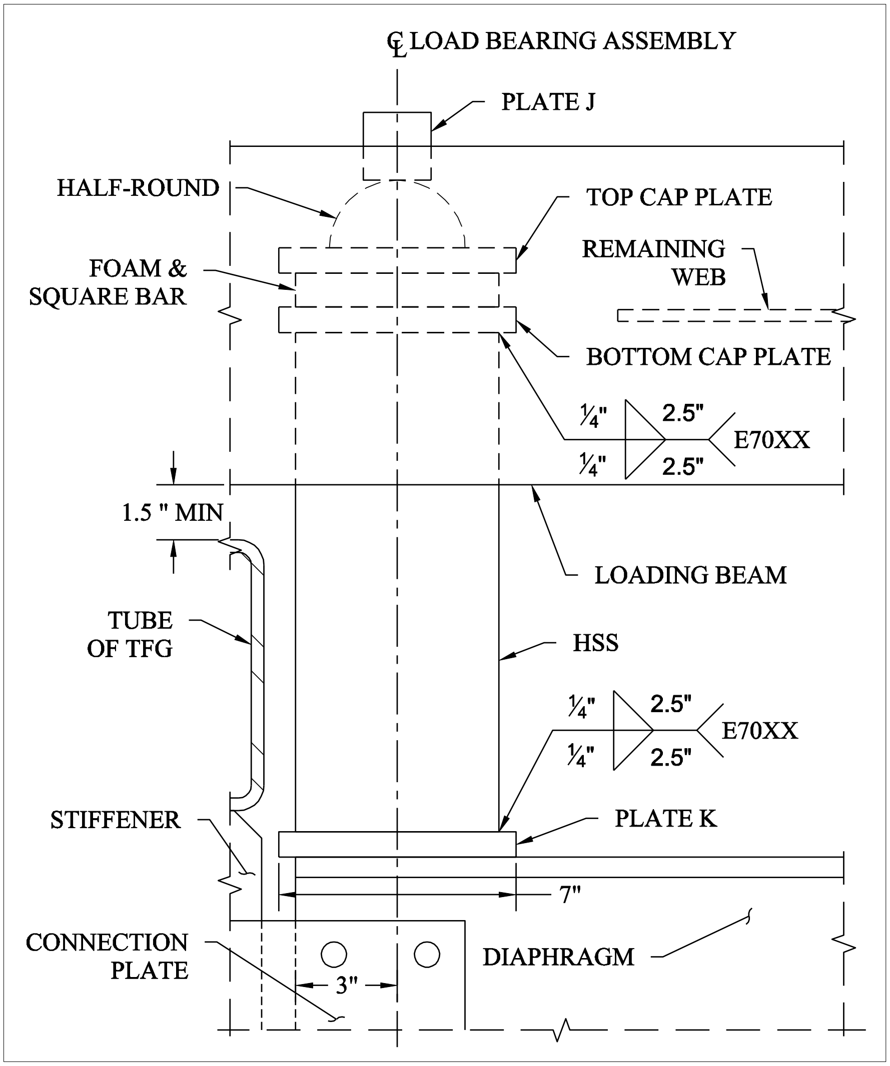

Figure 3.16 Parallel plane cross section view of load bearing assembly at Section A (Hampe, 2012)

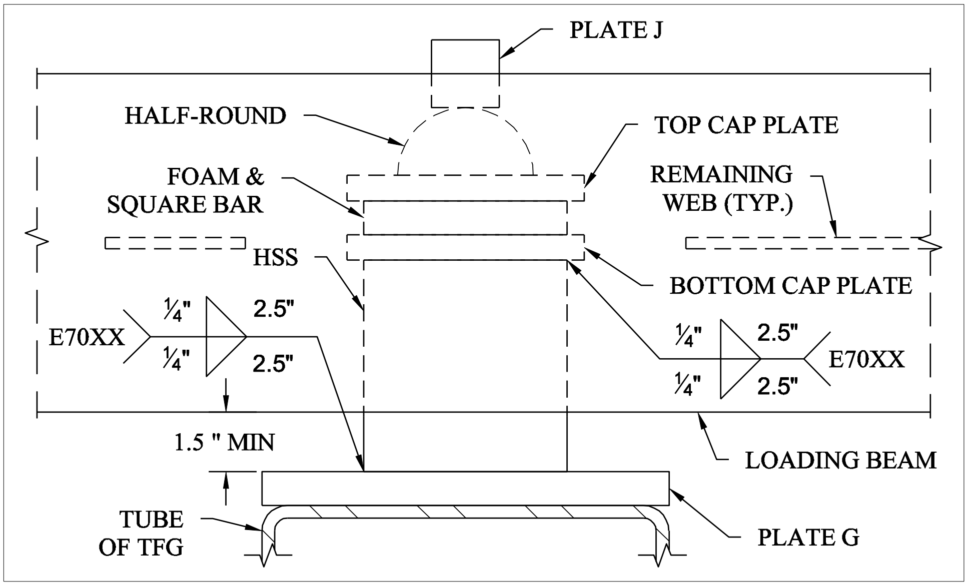

Figure 3.17 Parallel plane cross section view of load bearing assembly at Section Type B (Hampe,2012)

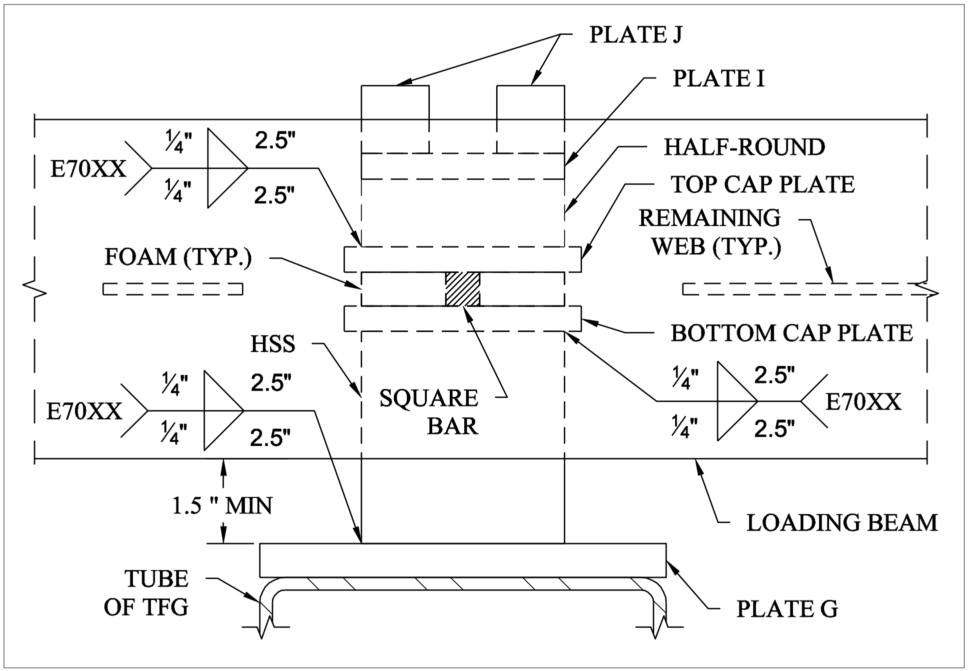

Figure 3.18 Parallel plane cross section view of load bearing assembly at Section Type C and Section Type D (Hampe, 2012)

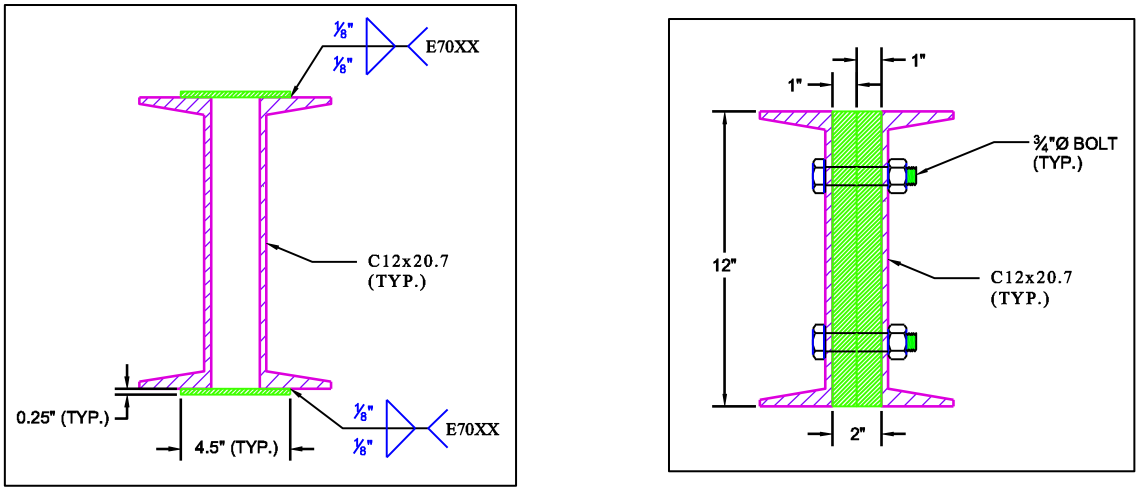

(a) Longitudinal cross section view of south end tie plate and intermediate tie plates

(b) Longitudinal cross section view of north end tie plate

Figure 3.19 South end and north end tie plates (Hampe, 2012)

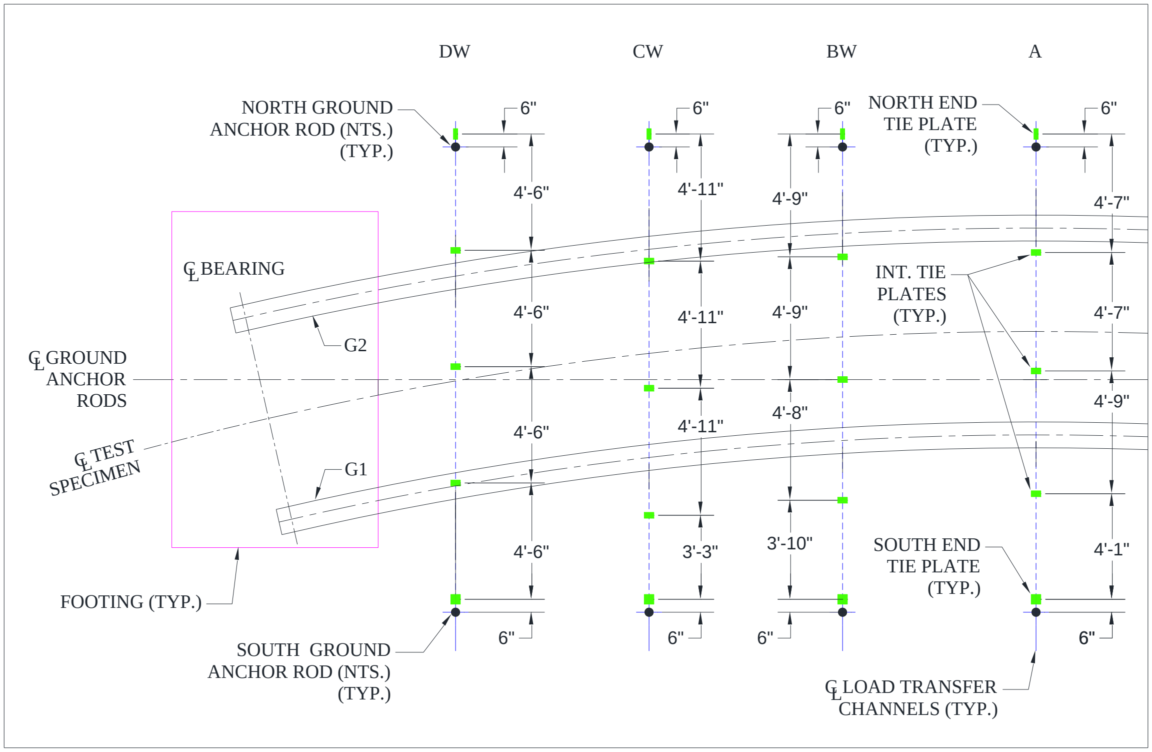

Figure 3.20 Tie plate arrangement (Hampe, 2012)

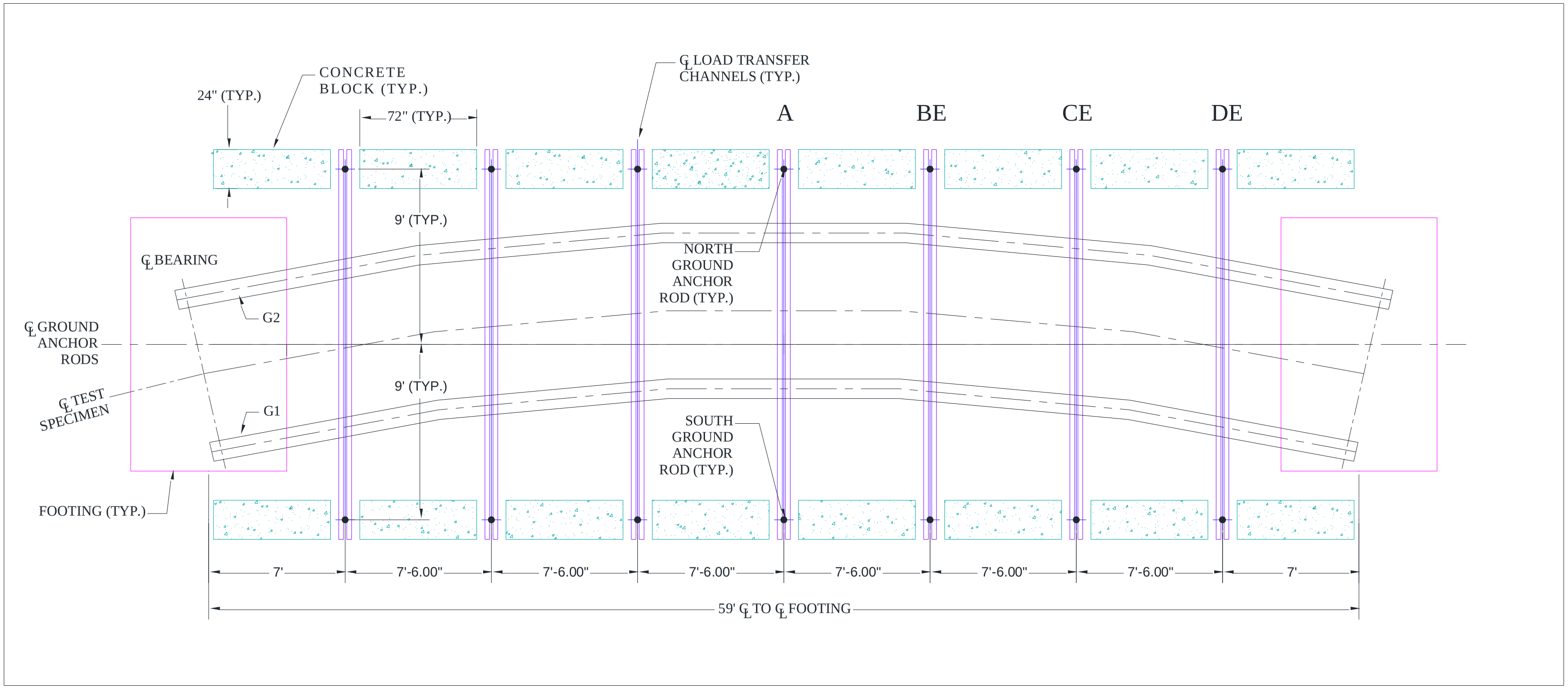

Figure 3.21 Bracing plan view (Hampe, 2012)

Figure 3.22 Photograph of concrete blocks and wooden wedges bracing load transfer channels

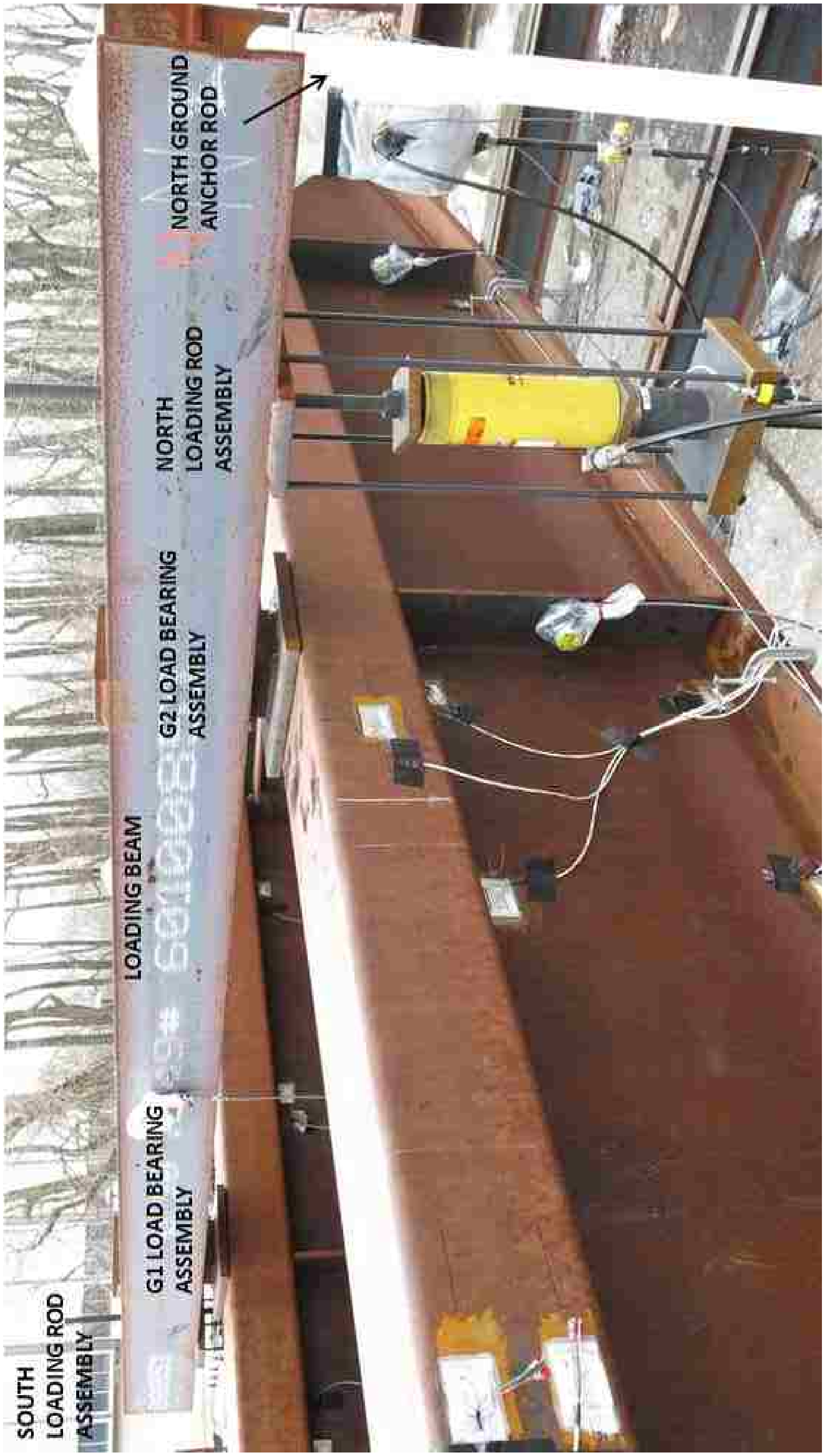
SOUTH LOADING ROD ASSEMBLY
G1 LOAD BEARING ASSEMBLY
LOADING BEAM
G2 LOAD BEARING ASSEMBLY
NORTH LOADING ROD ASSEMBLY
NORTH GROUND ANCHOR ROD

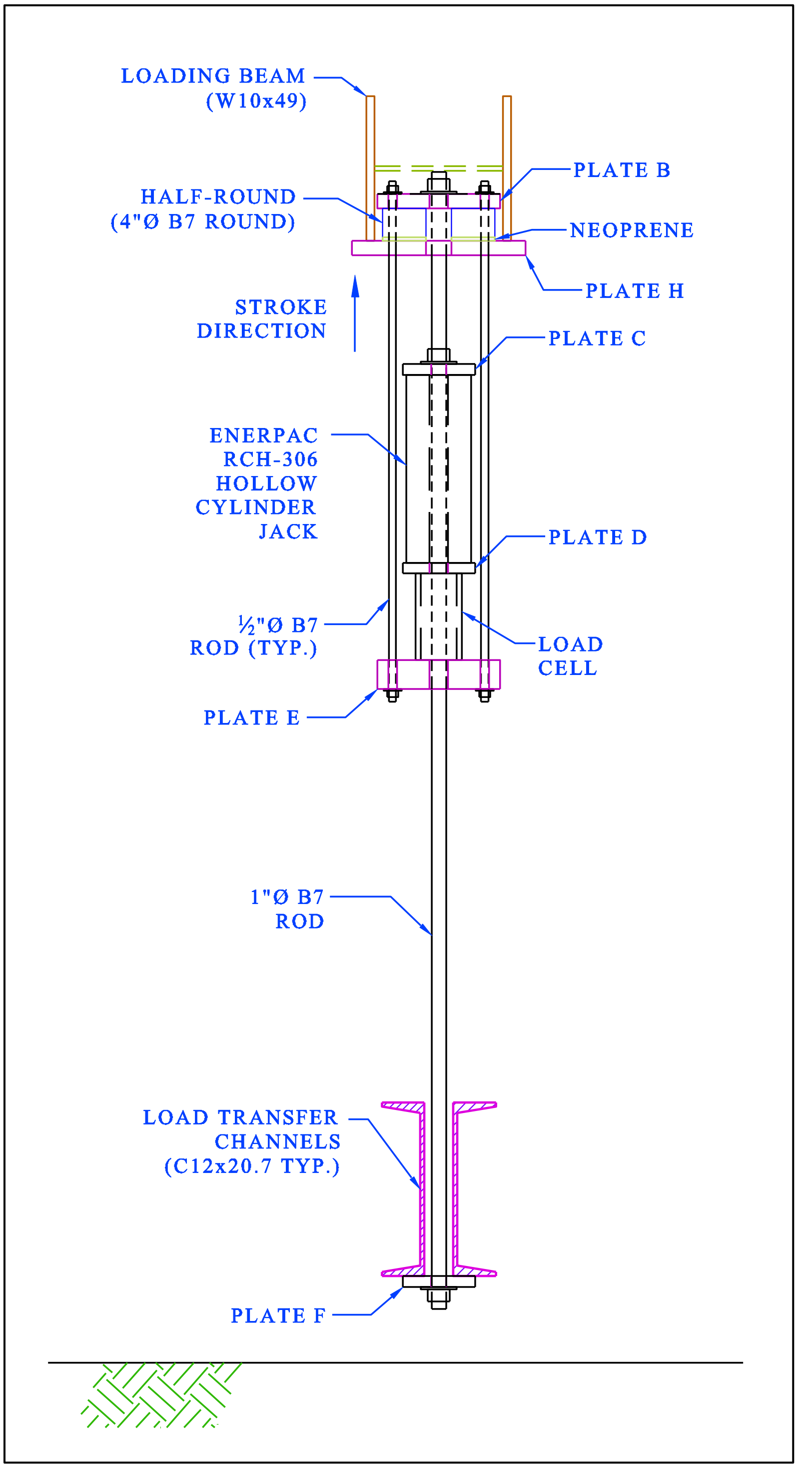

Figure 3.24 Longitudinal plane cross section view of loading rod assembly (Hampe, 2012)

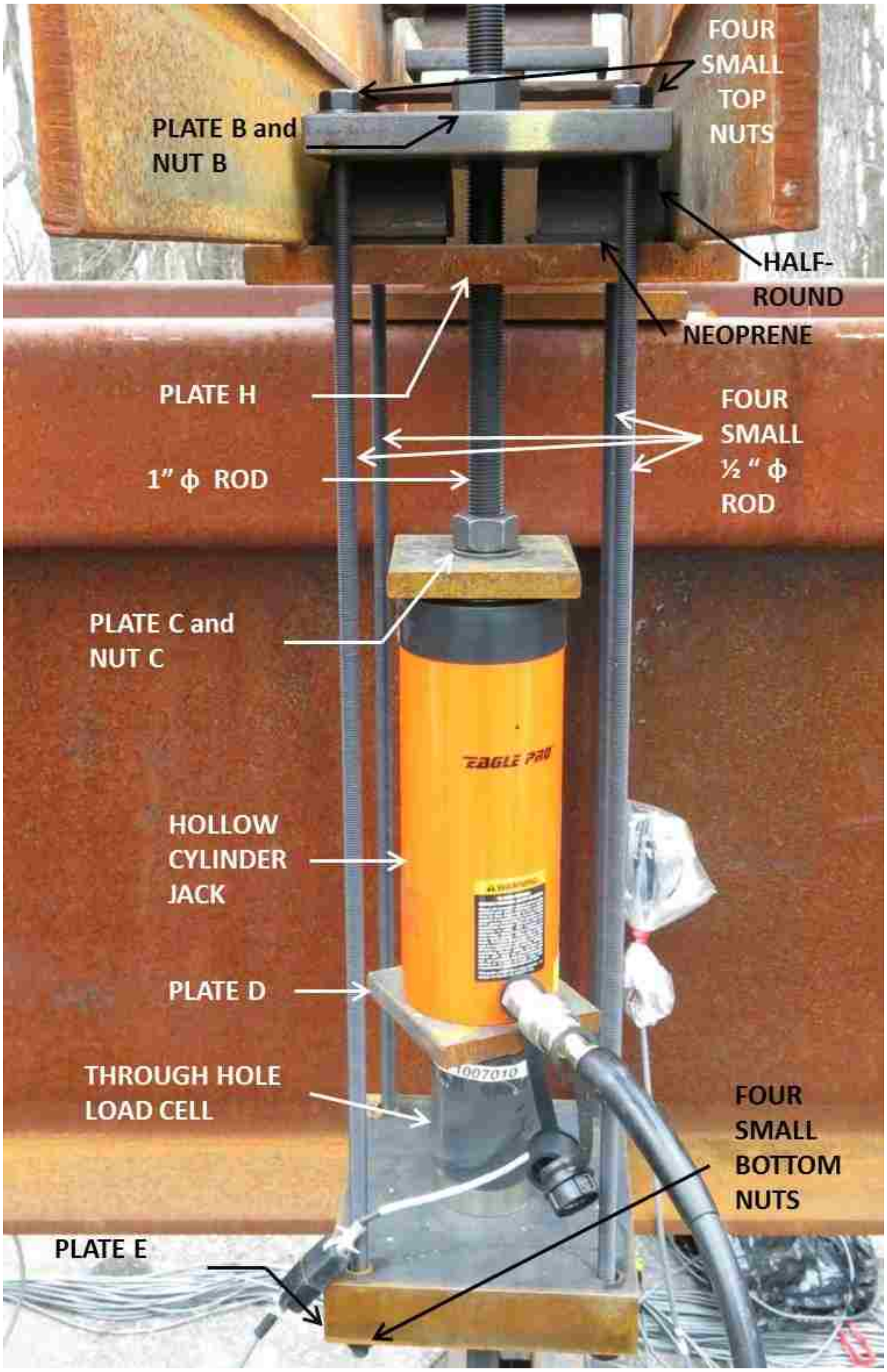

Figure 3.25 Photograph of loading rod assembly

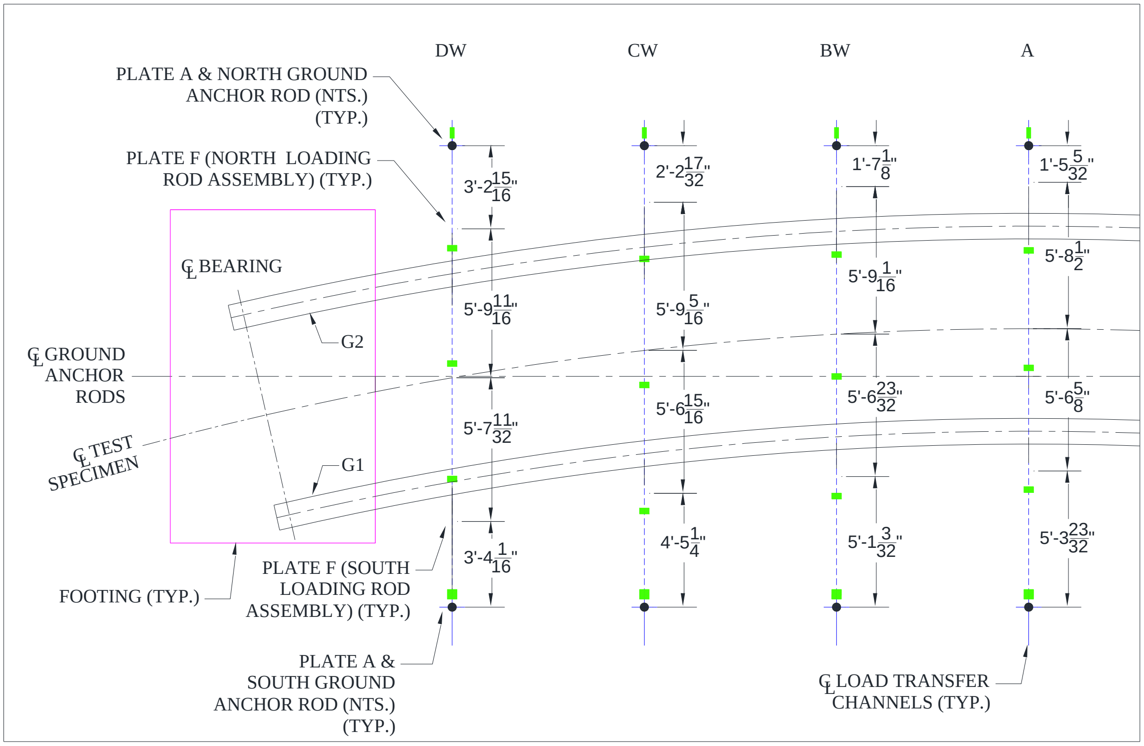

Figure 3.26 Loading rod assembly arrangement (Hampe, 2012)

(a) Photograph of bottom of loading rod assembly looking in parallel direction

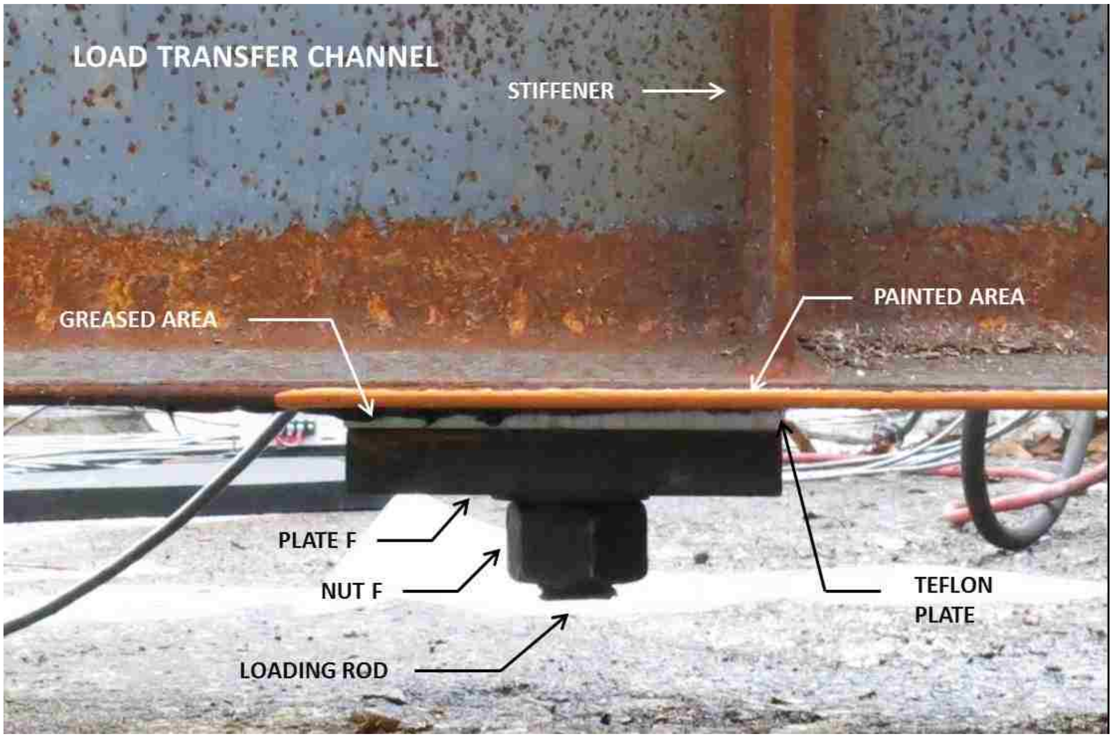

(b) Photograph of bottom of loading rod assembly looking in longitudinal direction

Figure 3.27 Photograph of loading rod assembly and load transfer channel contact

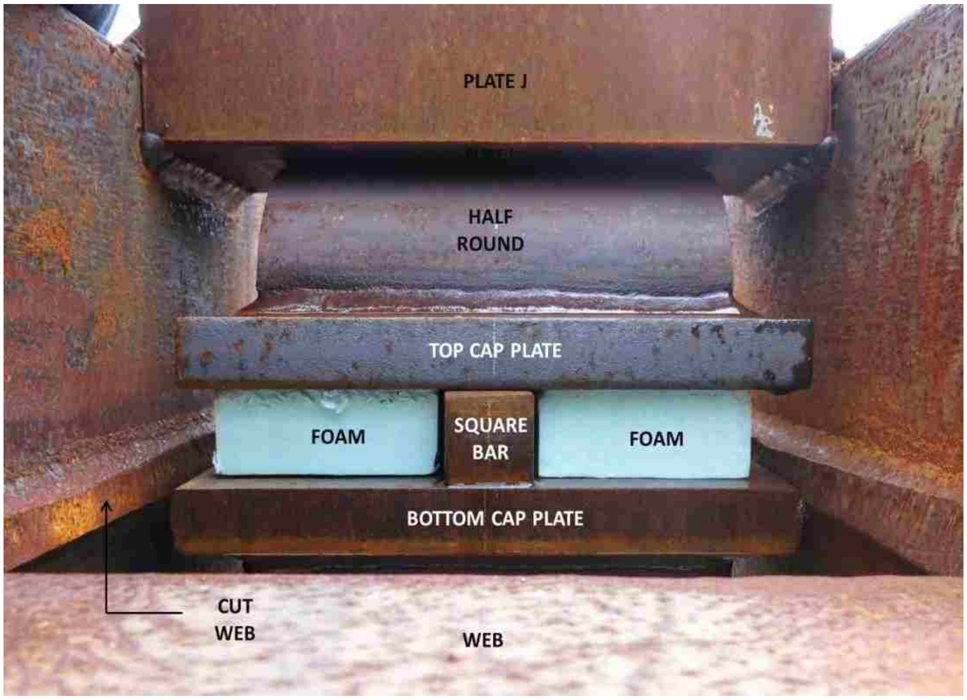

Figure 3.28 Photograph of load bearing assembly at Section Type B looking in parallel direction

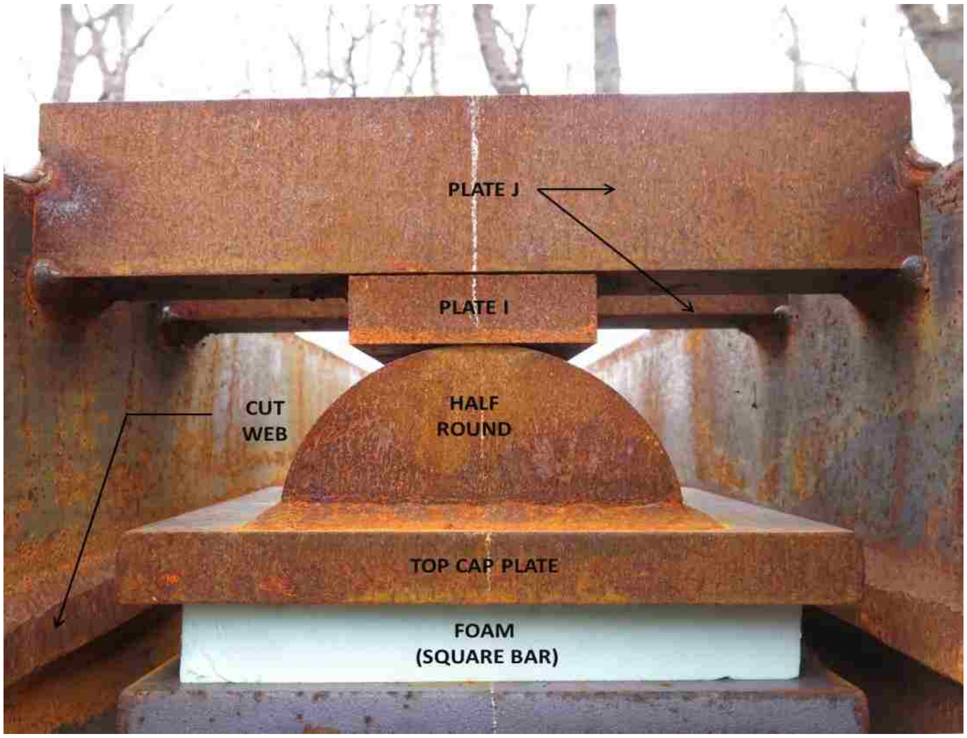

Figure 3.29 Photograph of load bearing assembly at Section Type C and Section Type D looking in parallel direction

4 BOUNDARY CONDITIONS AND BEARING ASSEMBLIES

4.1 Introduction

This chapter describes test specimen boundary conditions and the design of the bearing assemblies that were used in the test setup. Section 4.2 describes possible support types and boundary conditions that were studied. Section 4.3 describes the effect of these boundary conditions on the reaction forces and kinematics of the test specimen. Three boundary condition combinations (combinations of support types) are compared in this section and the final boundary condition combination is established for the test setup. Section 4.4 describes the concrete footings used in the test setup. Section 4.5 describes the bearing assemblies used to create the chosen boundary condition combination. Section 4.6 discusses stability conditions related to the half-rounds in the bearing assemblies. Finally, Section 4.6 explains the effects of the shim plates added to the initial bearing assembly design between the half-round and girder bottom flange.

4.2 Support Types and Boundary Condition Combinations

Three types of supports for girders G1 and G2 were used in the FE models to study the effects of different combinations of boundary conditions created by using different support types on each end of girder G1 and G2. The first type of support is a spherical roller that allows circumferential displacement, radial displacement, and rotations about all axes, and prevents vertical displacement. The second type of support is a circumferential roller that allows circumferential displacement and rotations about all axes, and prevents both radial displacement and vertical displacement. The third type of support was a pin that allowed rotations about all axes, and prevented circumferential displacement, radial displacement, and vertical displacement.

Variations on FE Model-D3 were used to study how different combinations of these three support types affect both the reaction forces and the displacements (kinematic results). Figures 4.1 (a), (b), and (c) show schematics of the three boundary condition combinations studied. For boundary condition combination bc1, the west end of G2 (G2W), the east end of G2 (G2E) and the west end of G1 (G1W) are supported by a circumferential roller; the east end of G1 (G1E) is supported by a pin support. For boundary condition combination bc2, G2W and G1W are supported by a circumferential roller and G2E and G1E are supported by a pin support. For boundary condition combination bc3, G2W and G2E are supported by a spherical roller, G1W is supported by a circumferential roller and G1E is supported by a pin support. Combination bc3 is the final support combination used in Model-D3 (Ma, 2014) to represent the boundary conditions of the test specimen during the tests.

4.3 Effect of Boundary Conditions

The boundary condition combinations were shown to affect the kinematic results and reaction forces at the bearings of the test specimen by the FE analyses. Table 4.1 presents displacements (Ui), rotations (Uri) and reaction forces (RFi) for the three boundary condition combinations. Most displacements, rotations, and vertical reaction forces are similar for the three boundary condition combinations. However, the radial reaction force (RF1) differs. The radial reaction forces develop due to the indeterminacy of the radial reactions and interactions between the girders through the end diagrams of the test specimen. For bc3 there is no radial restraint for G2W and G2E so that redundant components of the radial forces do not develop. Therefore, the radial reaction force in G1W and G1E is much smaller for bc3 than for bc1 and bc2.

To avoid instability conditions at the bearings of the test specimen considering the components of the bearing assemblies (see Section 4.6), smaller reaction forces in the radial and circumferential directions are desired. Therefore, boundary condition combination bc3 was selected for the bearings of the test specimen and used in FE Model-D3. Note that this boundary condition combination can be modeled in the FE model and is also a boundary condition combination that can be implemented in the test setup.

4.4 Bearing Footings

Figure 4.2 is a plan view of the west bearing footing. The west and east footings are approximately 10 in. thick, 8 ft. by 13 ft. concrete slabs. The depth varies to accommodate the uneven asphalt pavement of the test area and to produce a level surface for the bearings. The compressive strength of the concrete is 5 ksi and the nominal yield stress of the steel reinforcement is 60 ksi. A W14x233 reaction beam with a nominal yield stress of 36 ksi is attached to the middle of the footing and runs in a parallel plane. The footings and the reaction beams were built for previous tests of straight TFGs. The design of the footings is presented by Kim (2005). During the previous tests (Kim, 2005), each footing was subjected to 305 kip reaction forces. As shown in Figure 4.2 two 3.67 ft. long W14x176 pieces were added to the reaction beam to accommodate the locations of the bearings of the curved test specimen. There are two pairs of stiffeners along the length of the W14x233 and pairs of stiffeners along the lengths of the W14x176 pieces.

From the analysis of Model-D3, the total load on the footing when it reaches its maximum load capacity is expected to be 286 kip (including total applied force plus the self-weight of the test specimen and the superimposed dead load of the test fixtures). Note that the total reaction at each end of the test specimen is 143 kip which is much less than the total reaction of 305 kip during the previous tests (Kim, 2005).

4.5 Bearing Assemblies

This section describes the bearing assemblies used for the bearings of the test specimen. Section 4.5.1 provides an overview of the bearing assemblies. Section 4.5.2 discusses the design load and the kinematic conditions considered. Then Section 4.5.3 describes the design of the bearing assembly for each bearing. Finally Section 4.5.4 describes design of the radial restraint used at G1E and G1W.

4.5.1 Overview of bearing assemblies

All three types of supports (Section 4.2) are used in boundary condition combination, bc3. The spherical roller support allows both circumferential and radial displacements, but prevents vertical displacement. Under ideal conditions, the spherical roller support allows rotation about all three axes. Teflon plates were used instead of an actual spherical roller to avoid the potential problem of large bearing stresses between a sphere and the plate of the girder flange and bearing assembly. Using Teflon plate prevents the potential instability of a spherical roller. The Teflon plates allow radial and circumferential displacement, and rotation about the vertical axis. The coefficient of friction for Teflon is as small as 0.04, allowing the specimen to displace and rotate (about the vertical axis) freely. To get the lowest coefficient of friction, two Teflon plates were used at the bearing to provide Teflon on Teflon contact. To provide rotation about the radial axis, a half-round was used as described later. Rotation about the circumferential axis is not allowed by the combination of Teflon plates and half-round, but in the test specimen, this rotation is restrained by the end diaphragms, so there was no practical value in permitting this rotation.

The circumferential roller support allows circumferential displacement, but prevents radial and vertical displacements. Under ideal conditions the circumferential roller support allows rotations about all three axes. Teflon plates were uses to allow the circumferential displacement. To restrain the radial displacement, an additional restraint structure was designed and installed, as discussed in Section 4.5.4. This radial restraint structure also restrained rotation about vertical axis. To provide rotation about the radial axis, a half-round was used as described later. Rotation about the circumferential axis is not allowed by the combination of Teflon plates and half-round, but this rotation is restrained by the end diaphragms.

For the third type of support, the pin support, circumferential, radial, and vertical displacements are restrained; therefore Teflon plate are not used for this type of support. Under ideal conditions the pin support allows rotations about all three axes. To provide rotation about the radial axis, a half-round was used as described later. Rotation about the vertical axis is restrained by steel on steel friction force. Rotation about the circumferential axis is not allowed by the combination of steel plates and half-round, but this rotation is restrained by the end diaphragms, as mentioned earlier.

All three types of supports should ideally allow rotation about all axes. To allow rotation about the radial axis, half-rounds were included in the bearing assemblies. The half-rounds are 12 in. wide for the radial unrestrained supports and 10 in. wide for the radial restrained support. To reduce the restraint of rotation about the circumferential axis, and to keep the reaction force near the girder web during the tests, two shim plates were placed between top of each half-round and the girder flange, under the girder centerline. Section 4.7 describes the shim plates. Note that the end diaphragms provide significant restraint of the circumferential rotation as mentioned earlier, so it was not important for the bearings to permit this rotation. Finally as noted earlier, when Teflon plates are included in the bearing assembly, the rotation about the vertical axis is unrestrained. Significant rotation about the vertical axis is not expected as shown in Table 4.1. Vertical reaction forces are measured at the bearings using compression load cells. Figure 4.3 to Figure 4.6 show radial and circumferential views of the four end bearing assemblies. Figure 4.9 and Figure 4.10 are photographs of the bearing assemblies.

4.5.2 Design loads and kinematic conditions for bearing assemblies

Three load conditions are considered for design of the bearing assemblies: (1) the reactions at FE increment 35, when the test specimen reaches its maximum load capacity; (2) the conditions at FE increment 50 when the applied load has decreased but larger displacements and rotations in the test specimen have developed, which can produce larger non vertical forces at the bearings and lead to instability; (3) the conditions at FE increment 50 assuming the loading rod assemblies do not remain vertical due to friction where they are in contact with the load transfer channels. In this condition (3), the intersection of each loading beam and loading rod assembly in the parallel and longitudinal directions, but the intersection of the loading rod and load transfer channels is assumed to be restrained. Therefore, the loading rods assemblies are inclined, and the force is applied to the loading beam with parallel and longitudinal direction components.

Table 4.2 shows the anticipated inclination and corresponding non-vertical force components for this condition for each loading rod assembly. Note that the 2 in. gap within the pair of channels in the load transfer channels provides enough clearance to avoid bearing of the loading rod against the top of the load transfer channels (Hampe, 2012). The forces for the three load condition described above were multiplied by a factor of safety (FS) of 1.3 for design purposes.

4.5.3 Design of bearing assemblies

The bearing assemblies consist of copper and brass shim plates, half-rounds, Teflon plates, steel plates, and load cells to measure the vertical reaction force. The compressive reaction force from load condition (1) was considered for the design of the bearing assembly plates and half-round.

The half-rounds are placed in radial direction to allow test specimen to rotate about the radial axis at all four bearings. The half-rounds are half cylinders fabricated from 4 in. diameter ASTM A193 grade B7 round bar. At each bearing, one copper shim plate and one brass shim plate are placed between the half-round and the girder bottom flange under the centerline of the girder to keep the reaction force aligned with the web. Plate A was welded to bottom of the half-round. The width and length of Plate A are designed to match the half-round dimensions. For the bearings with Teflon plates, Teflon Plate E is glued to Plate A.

Teflon Plate F is the second Teflon plate that is glued to the top of Plate B. Teflon plate E slips on Teflon Plate F in both radial and circumferential directions. Two Teflon plates were chosen over one Teflon plate to minimize the friction force. Where Teflon is used, plate B is placed on the load cell. Note that for the pinned support type at G1E (Figure 4.6). Teflon plates are not used, so Plate A is replaced by a thicker Plate C. As shown in Figure 4.3 to Figure 4.6, a 150 kip LEBOW 3130 load cell is placed in each bearing assembly. To avoid tipping of the load cell at G1W and G2W due to circumferential displacement of the test specimen (Section 4.6), load cells are placed with a 0.5 in. initial misalignment to the east at the G1W and G2W bearings.

All steel plates used for the bearing assemblies are fabricated from ASTM A572 grade 50 steel. The dimensions of the plates are listed in Table 4.4. The term “width” refers to the dimension in the circumferential direction, the term “length” refers to the dimension in the radial direction, and the term “thickness” refers to the dimension in the vertical direction.

4.5.4 Design of radial restraint truss

For the circumferential roller support type (Section 4.2) at bearing G1W, an additional radial restraint structure is needed to prevent radial displacement. For bearing

G1E where the Teflon plates are omitted, the friction between steel Plates C and B is enough to provide the required radial reaction force, and restrain the radial displacement. However, considering the possibility of the loading rods becoming inclined in the parallel planes, which creates a larger radial reaction force (Section 4.5.2), the same truss structure designed for G1W was used at G1E. Figure 4.7 and Figure 4.8 show the restraint truss structure at the G1W and G1E bearings respectively. Figure 4.9 shows a photograph of the restraint truss structure for bearing G1E. Load condition (3) was considered for the design of the radial restraint channel.

The radial restraint truss structure consists of one restraining channel at each side of the bearing, one threaded rod to connect the two restraining channels, and two bracing angles on the north side of the bearing to transfer the radial force to the reaction beam. The restraining channels are placed symmetrically on the south and north sides of G1 and centered with the bearing assemblies in the circumferential direction. The channels are fabricated by welding two L5x3x0.5 angles made from A572 grade 50 steel welded together. A stiffener plate is welded inside of the channel. A threaded rod connecting the south and north channels, passes through the channels. To allow the threaded rod to pass through the girder web, a hole is drilled through the girder web. The size of this hole accommodates the maximum circumferential displacement from analysis of FE Model-D3.

Teflon Plate G is installed on the each restraint channel to minimize friction at the location where the channels and the bottom flange edge of G1 are in contact. Reducing this friction allows the bearing to move in the circumferential direction, and minimizes the vertical force transfer so that the vertical reaction force passes completely through the load cell. Finally two bracing L5x3x0.5 angles are welded to the north side channel to resist the radial restraining force. If G1 tends to move north at the bearing location, the north side channel restrains the girder and the reaction is transferred directly to the bracing angles. If G1 tends to move to the south at the bearing, the reaction is transferred from the south channel through connecting rod to the north channel and the bracing angles.

4.6 Instability and Tipping

The rotation of the test specimen about the radial axis has the potential to cause instability of the load cell and the associated plates of the bearing assembly. Also, tipping of the load cell (i.e., loss of contact of the base of the load cell) at the bearing should be avoided so the vertical reaction measurement is accurate. This section discusses the instability and tipping concerns. The displacements and rotations from load condition (2) were used to check instability and tipping.

The first stability concern, Stability Condition I, is the stability of test specimen on the half-rounds at the bearings. As the test specimen rotates about the radial axis at the bearings, the normal contact force between the girders and the half-rounds becomes inclined from the initial vertical direction. A static friction force develops between each girder and each half-round at the contact point. The resultant of the normal force and friction force at the contact point must be able to balance the vertical reaction at the contact point and prevent slipping of the girder on the half-round. If the inclination of a girder on a half-round becomes too large, and the maximum static friction force is fully developed but is unable to balance the total vertical reaction, slipping occurs. Table 4.5 compares the maximum rotation about the radial axis that can be balanced by the maximum static friction force with the maximum expected rotation about the radial axis from the FE Model-D3 analysis. The result shows that Stability Condition I is satisfied, and slipping of the girder on the half-round is not expected.

The second stability concern, Stability Condition II, is the stability of the shim plates on the half-rounds. Only a total shim plate thickness which is less than the radius of the half-round will be stable when the shim plates rotate due to an accidental eccentricity of the vertical load. Table 4.5 shows the total thickness of the shim plates is less than the radius of the half-round, and Stability Condition II is satisfied.

Tipping of the load cell in the end bearing assembly will affect the accuracy of the measured reaction force. Tipping of the load cell occurs when the moment produced by eccentricity of the vertical reaction causes decompression at the base of the load cell. A comparison between the stress on the base of the load cell due to the moment from an eccentric vertical reaction, with an assumed uniform bearing pressure from the vertical reaction is used to determine if tipping can occur. The circumferential displacement is not restrained for the G1W, G2W, and G2E bearings, and this displacement is the source of the vertical eccentricity.

Table 4.5 indicates the maximum allowable circumferential displacement to avoid tipping. To increase the allowable circumferential displacement, the load cells are placed with an initial 0.5 in. misalignment in the opposite direction for bearings G1W and G2W (Figure 4.3 and Figure 4.5).

4.7 Effect of Shim Plates on Half-Rounds

The shim plates between the girders of the test specimen and the half-rounds of the bearing assembly, shown in Figure 4.9 and Figure 4.10, were not in the initial bearing assembly design. However, after placing the test specimen on the initial bearing assemblies, poor contact conditions between the bottom flanges of the girders and half-rounds were observed. This lack of good contact makes the alignment of the vertical reaction force uncertain. In the FE models of the test specimen, which did not include any imperfection in the girder flange support conditions, the vertical reaction forces at the bearings tend to be concentrated at the girder webs. Table 4.6 shows the effect of misalignment of the vertical reaction forces (away from the girder webs) on the distribution of the vertical reaction forces between G1 and G2 based on FE Model-D3 analysis. The results show that only 3 in. of misalignment of the reaction force resultant from the web of the girder provides significant differences in the ratio of the vertical reaction force for G2 to the vertical reaction force for G1. To reduce the uncertainty in the contact condition, one soft (copper) shim plate and one hard (brass) shim plate were placed on top of each half-round centered on the girder web. As a result, the vertical reaction force at each bearing is more closely aligned with the girder web during the tests.

[redacted]

Table 4.2 Anticipated loading rod inclination and non-vertical force at FE increment 50

Loading rod		Inclination (degree)		Non vertical force (kip)	
		Parallel	Longitudinal	Parallel	Longitudinal
South	DW	2.110	-0.640	0.799	-0.023
	CW	3.960	-0.350	1.502	-0.131
	BW	4.950	-0.240	1.874	-0.090
	A	5.710	-0.280	2.161	-0.106
	BE	4.610	-0.210	1.745	-0.081
	CE	2.980	-0.030	1.128	-0.012
	DE	1.360	0.230	0.515	0.005
North	DW	2.560	-2.210	0.972	-0.099
	CW	5.440	-1.710	2.062	-0.644
	BW	10.160	-1.090	3.835	-0.406
	A	7.040	0.040	2.665	0.015
	BE	6.180	0.490	2.341	0.186
	CE	3.900	0.900	1.479	0.340
	DE	2.030	1.300	0.772	0.046

Table 4.3 Three load conditions considered for design of end bearing assembly

Load condition	Bearing	Reaction force (kip)			Displacement (in.)		Rotation (degree)
		RF1	RF2	RF3	U1	U2	UR1
(1) FE increment 35	G1W	0.12	0	16.6	-	-	-
	G1E	0.05	-0.07	16.7	-	-	-
	G2W	0	0	126.4	-	-	-
	G2E	0	0	126.3	-	-	-
(1) FE increment 50	G1W	1.92	0	12.2	0	-1.13	1.45
	G1E	0.18	-0.08	12.7	0	0	-1.39
	G2W	0	0	111.9	0.0008	-1.40	3.60
	G2E	0	0	111.4	-0.0001	-0.14	-3.29
(3) Inclined loading rod condition	G1W	-12.85	0	12.2	-	-	-
	G1E	-11.33	2.47	12.7	-	-	-
	G2W	0	0	111.9	-	-	-
	G2E	0	0	111.4	-	-	-

Table 4.4 Dimensions of plates of bearing assembly

Part	Width (in.)	Length (in.)	Thickness (in.)
Copper Shim Plate	2	3	0.125
Brass Shim Plate	2	3	0.375
Plate A for G1	4	10	1
Plate A for G2	4	12	1
Plate B for G1	10	10	1
Plate B for G2	10	12	1
Plate C	4	10	1.5
Bearing Plate D	17	22	2
Stiffener Plate	5	1	4
Teflon Plate E for G1	4	10	0.25
Teflon Plate E for G2	4	12	0.25
Teflon Plate F for G1	8	10	0.25
Teflon Plate F for G2	8	12	0.25
Teflon Plate G	2	0.25	2

Table 4.5 Stability and tipping conditions

Condition	Data to be checked	Maximum predicted value	Allowable value
Stability Condition I	radial rotation (UR1)	3.6 degree	5.7 degree
Stability Condition II	total thickness of shim plates	0.5 in.	2 in.
Tipping	circumferential displacement (R2)	1.4 in.	1.07 in.
Tipping (with initial misalignment)	circumferential displacement (R2)	1.4 in	1.57 in.

Table 4.6 Effect of misalignment of bearing contact point on vertical reaction force distribution based on Model-D3 analysis

Contact point position	Ratio of G2 reaction to G1 reaction
G1 contact and G2 contact aligned with web	5.14
G1 contact and G2 contact moved 3 in. toward the south	6.15
G1 contact moved 3 in. to south and G2 contact moved 3 in. to north	9.13

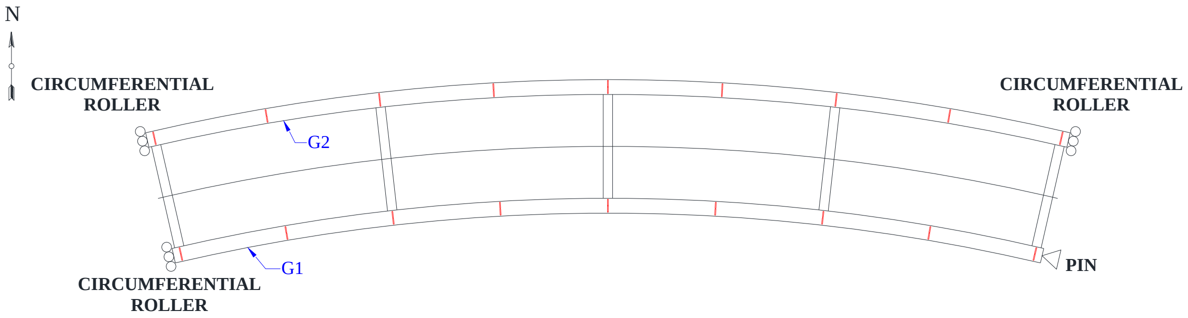

(a) bc1

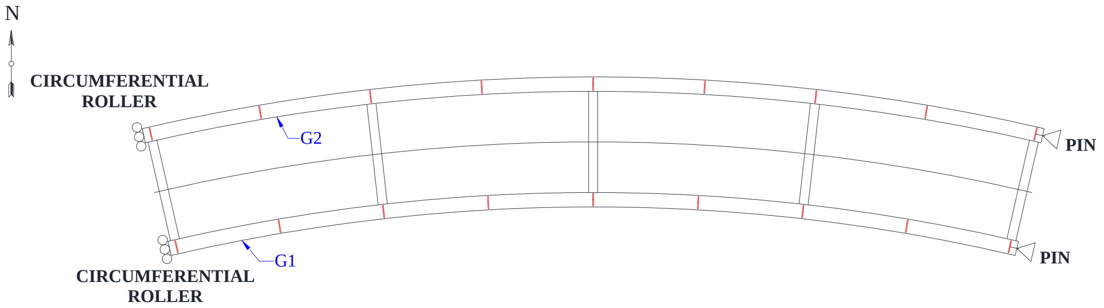

(b) bc2

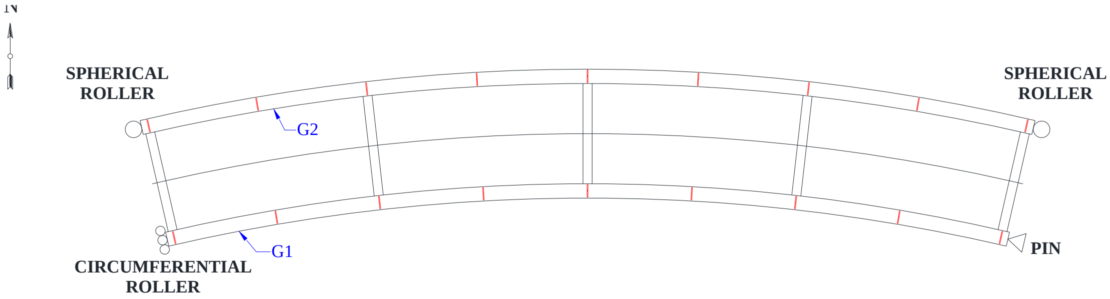

(c) bc3

Figure 4.1 Boundary condition combination studied with FE models

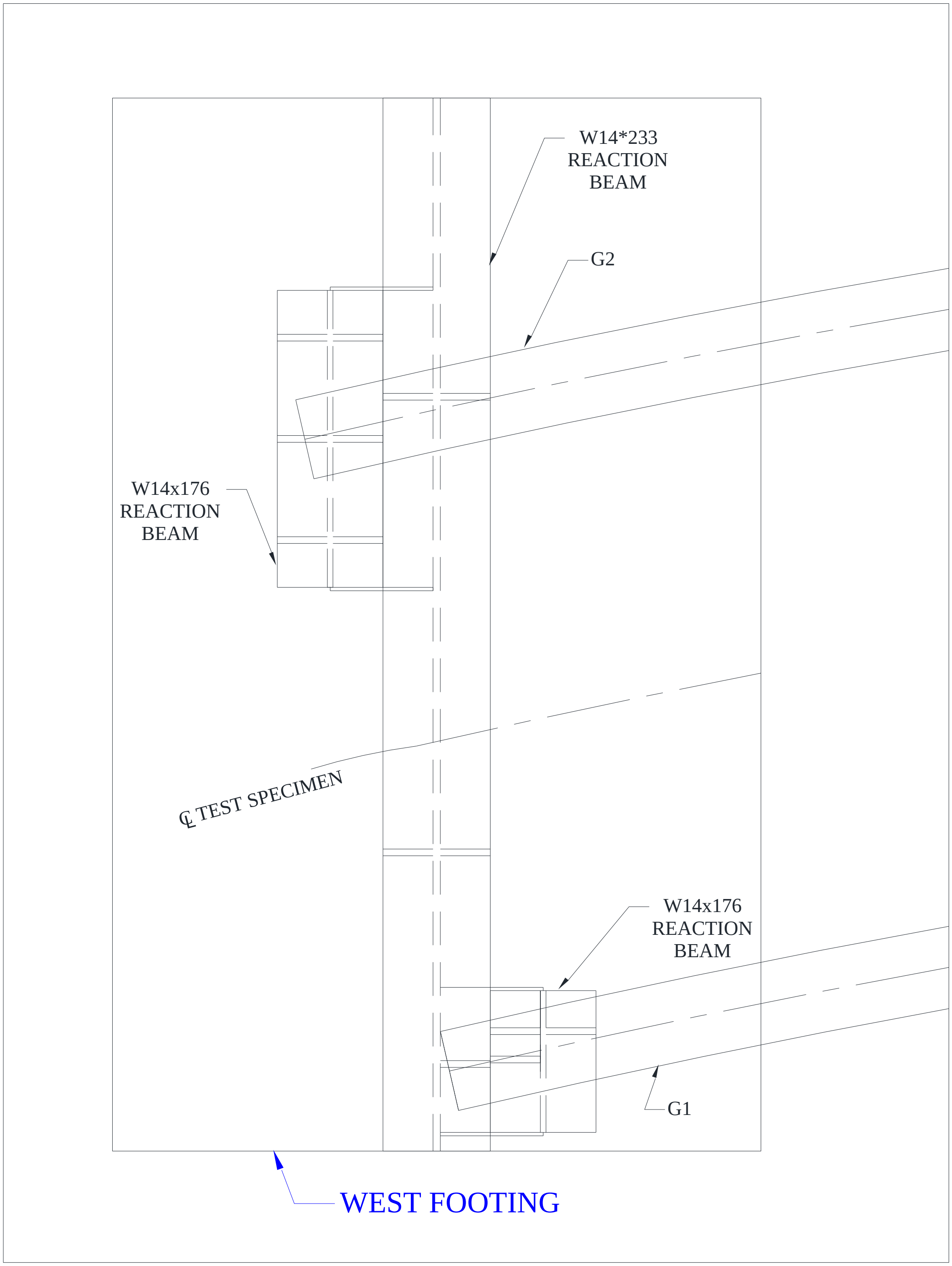

Figure 4.2 Plan view of west footing and reaction beams

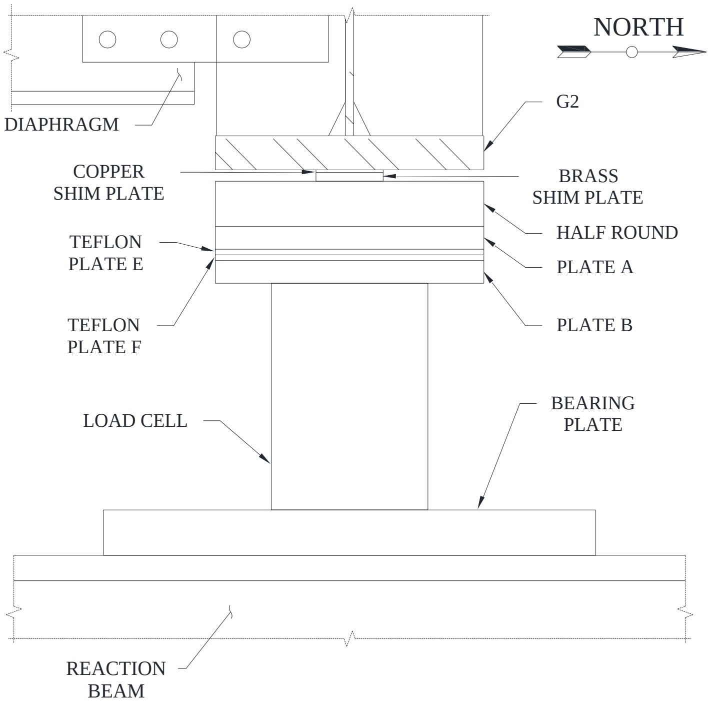

(a) Radial view

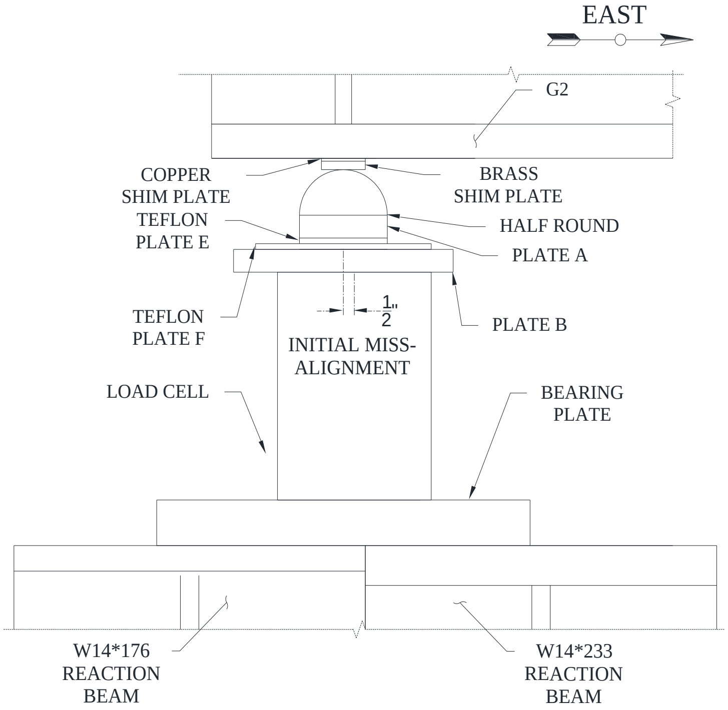

(b) Circumferential view

Figure 4.3 Radial and circumferential view of G2W bearing assembly

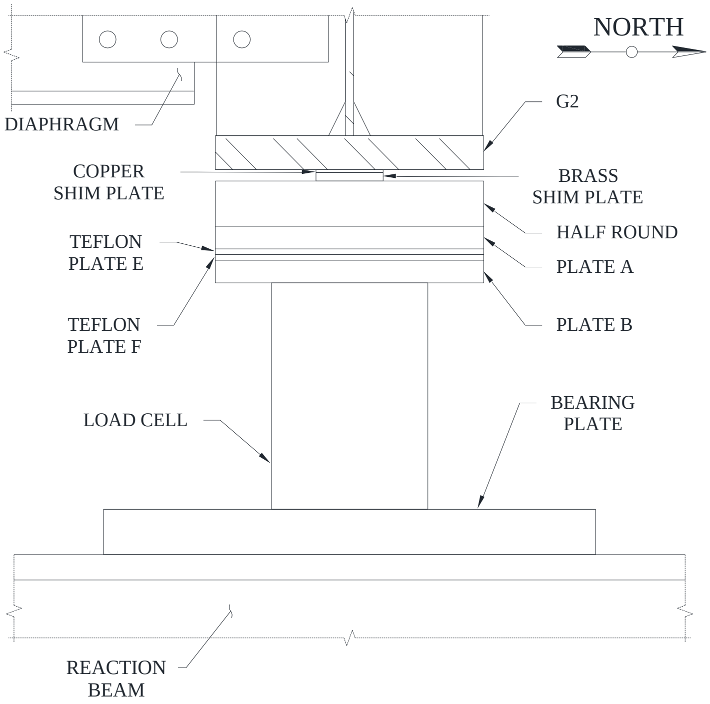

(a) Radial view

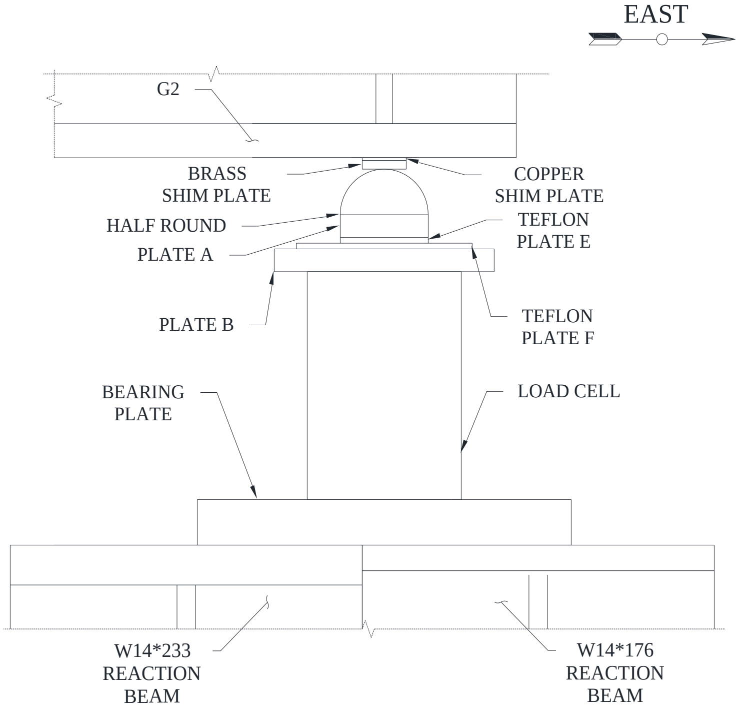

(b) Circumferential view

Figure 4.4 Radial and circumferential view of G2E bearing assembly
(Radial restraining structure is not shown for clarity)

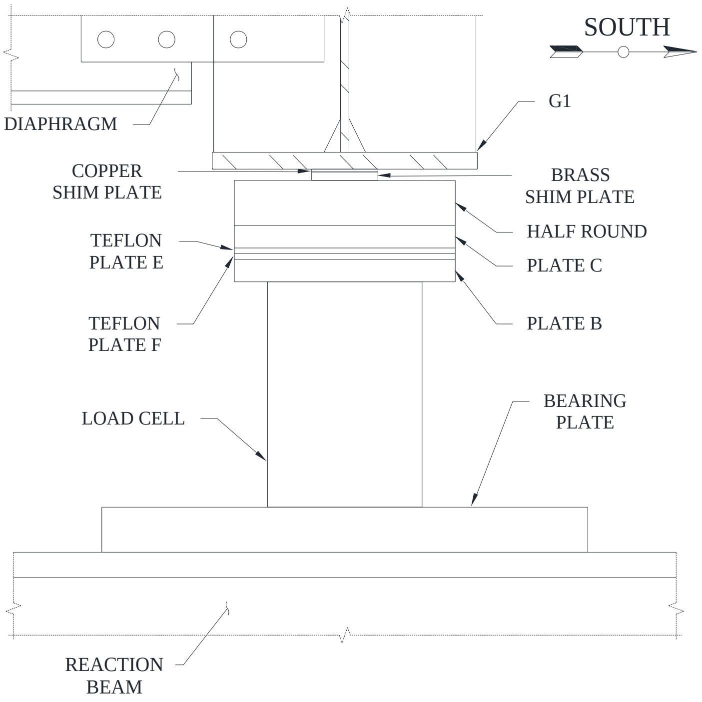

(a) Radial view

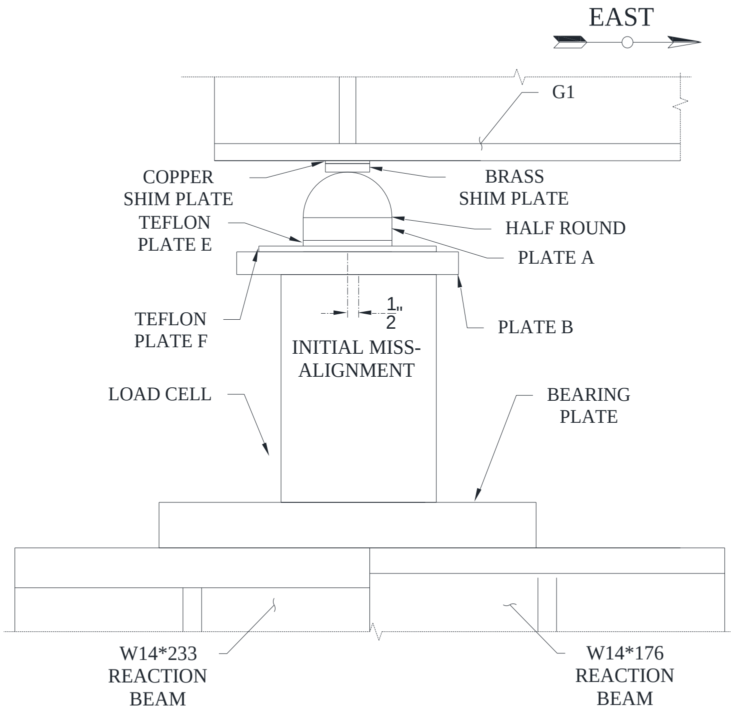

(b) Circumferential view

Figure 4.5 Radial and circumferential view of G1W bearing assembly
(Radial restraining structure is not shown for clarity)

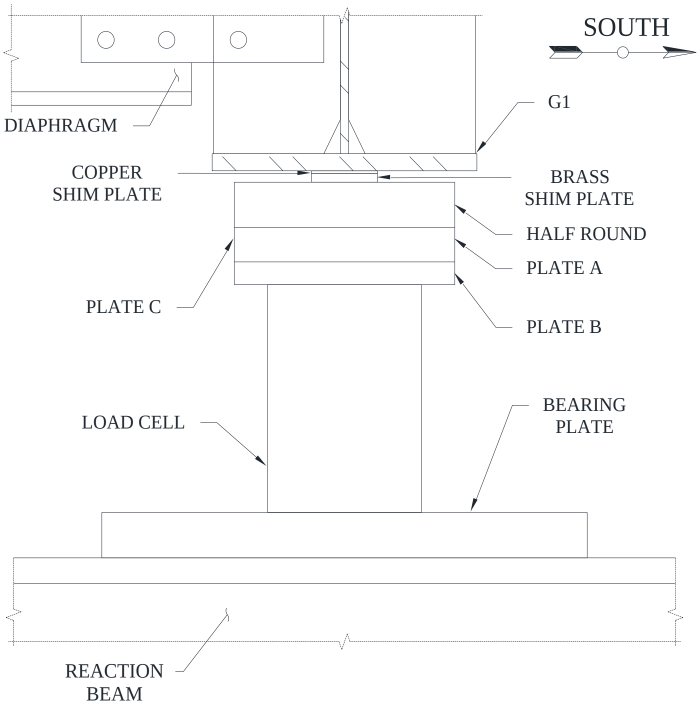

(a) Radial view

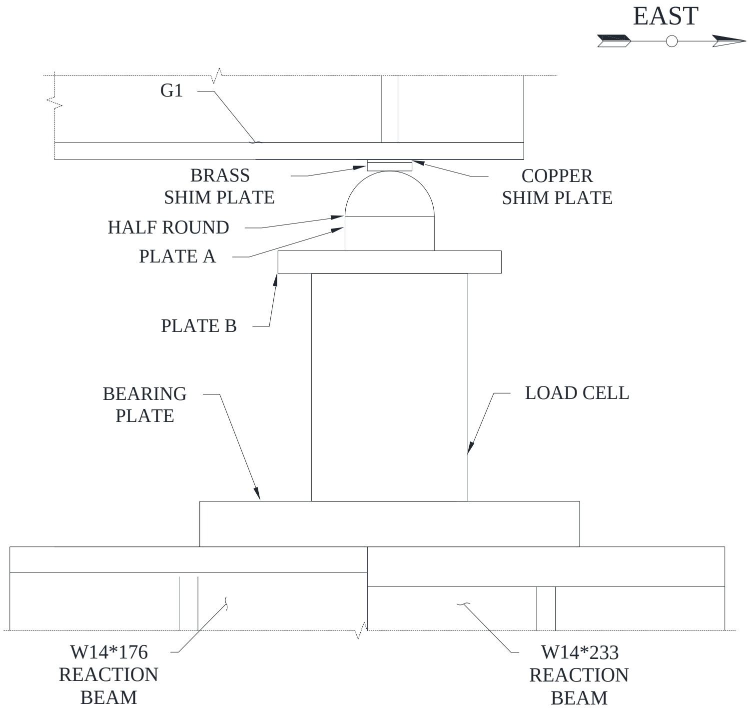

(b) Circumferential view

Figure 4.6 Radial and circumferential view of G1E bearing assembly
(Radial restraining structure is not shown for clarity)

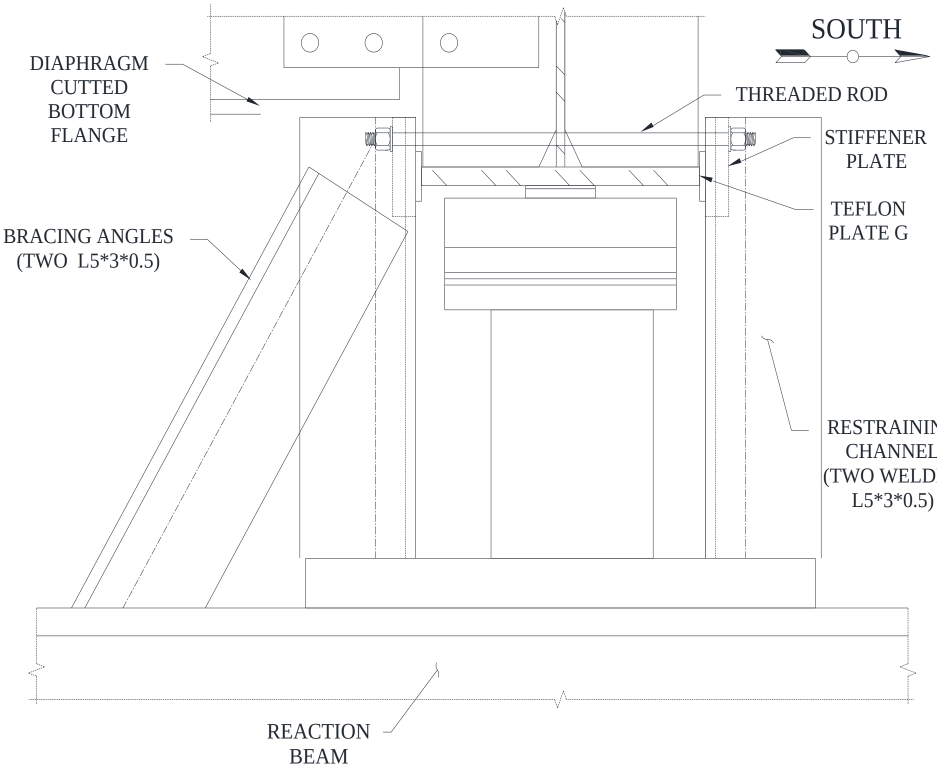

Figure 4.7 Radial restraint structure at G1W

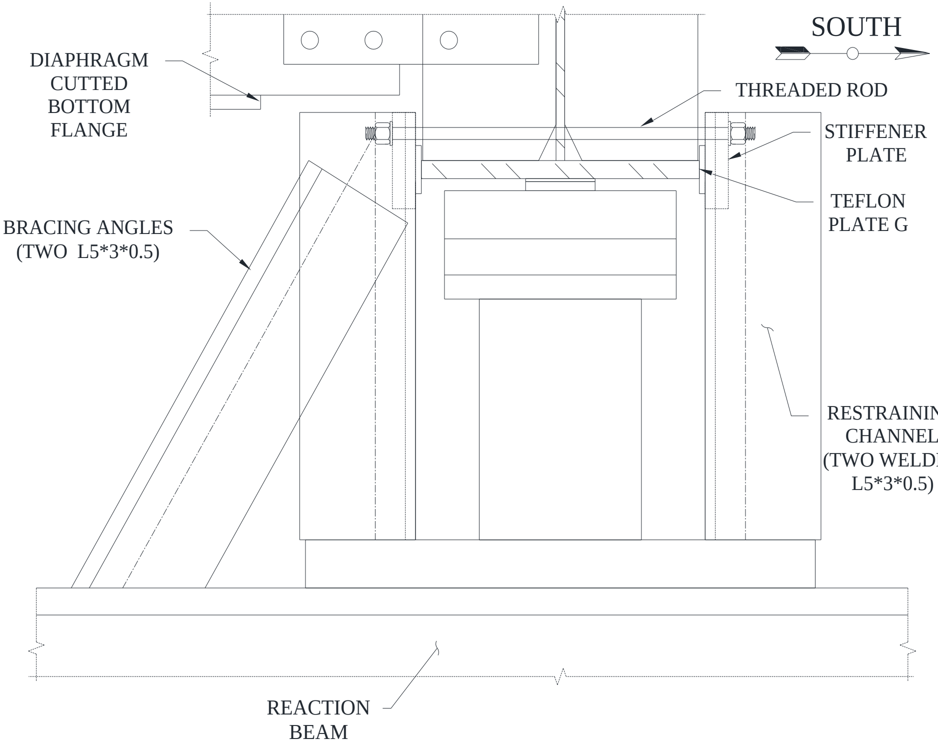

Figure 4.8 Radial restraint structure at G1E

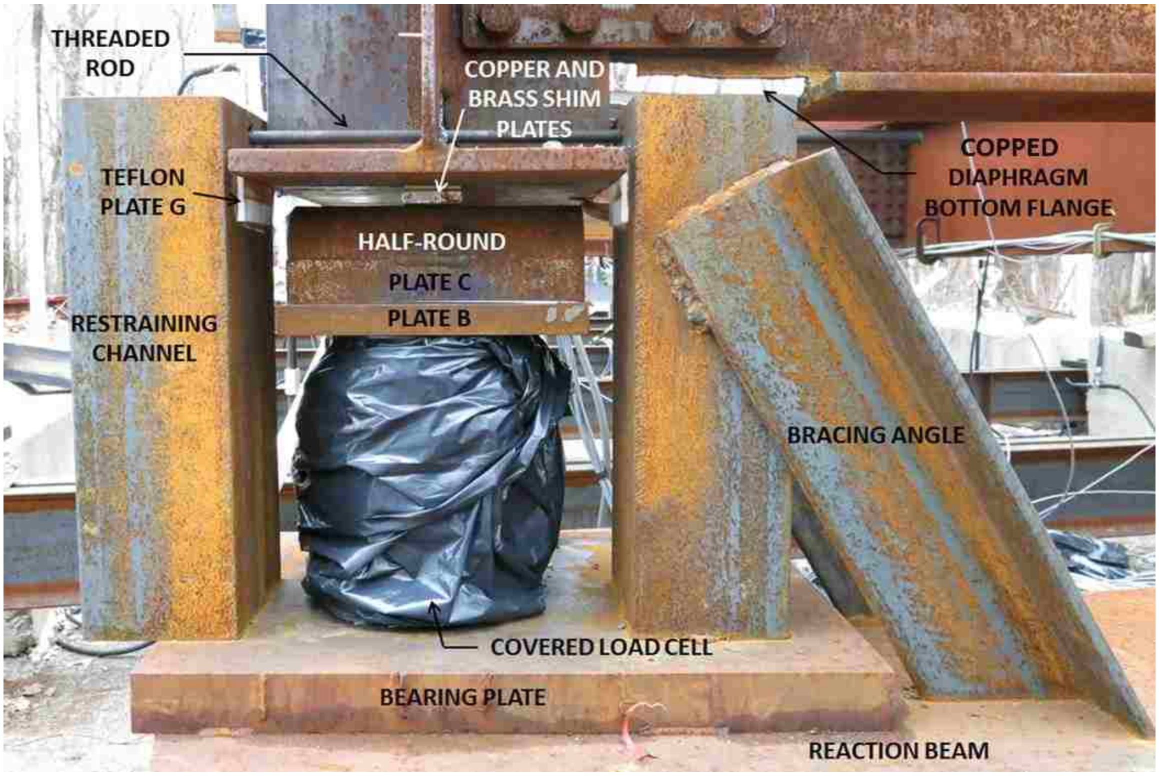

Figure 4.9 Photograph of G1E including radial restraining structure looking in circumferential direction

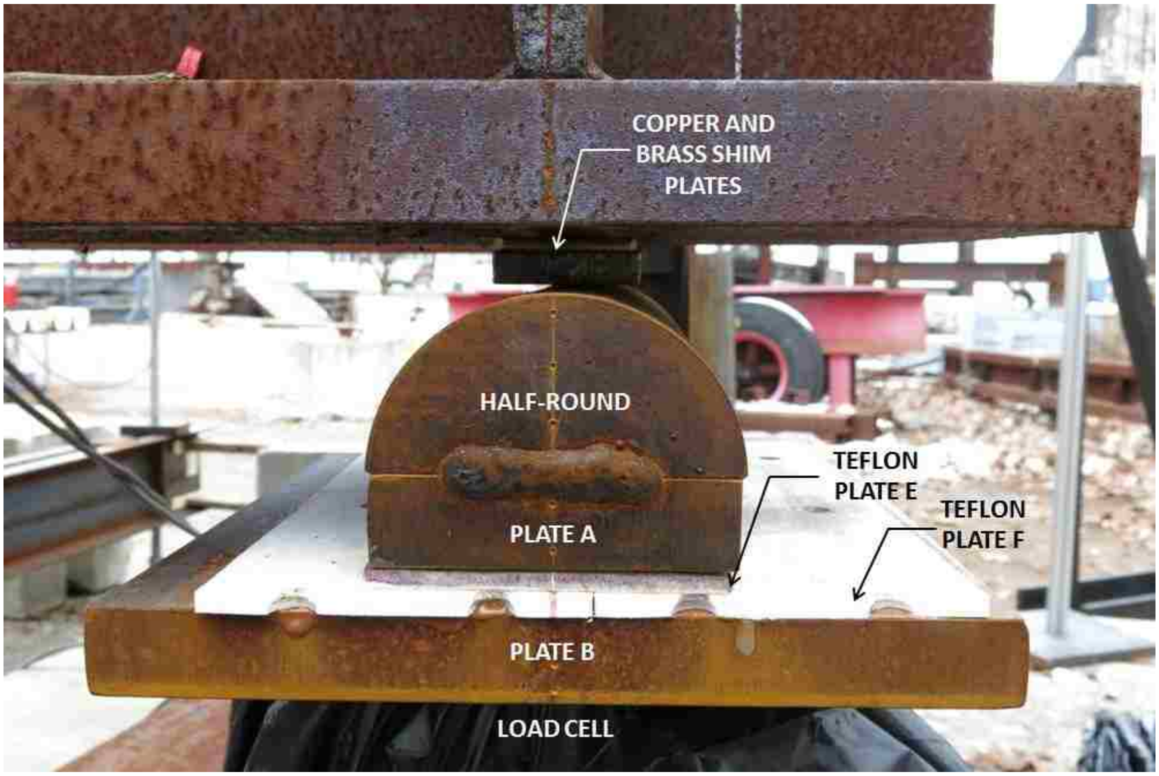

Figure 4.10 Photograph of G2W looking in radial direction

5 INSTRUMENTATION

5.1 Introduction

This chapter describes the instrumentation plan developed to measure the test specimen and loading fixture responses. Combinations of displacement, rotation, force, and strain transducers were used in the instrumentation plan to measure the responses. An instrumentation plan for one parallel plane is shown in Figure 5.1 which shows transducers attached to the test specimen and the loading fixture. Section 5.2 describes the transducers that were used to measure test specimen displacements at the bearings and at intermediate locations within the span of the test specimen, and also describes calculations needed to obtain the required displacement components from the measurements. Section 5.3 describes the rotation transducers used on the test specimen and loading fixtures. Section 5.4 describes the force transducers installed in the loading fixtures and at the bearings to measure applied forces and reaction forces, respectively. Finally, Section 5.5 describes the full bridge strain gages, uniaxial strain gages, and rosette strain gages installed on the test specimen to measure the local response.

5.2 Displacement Transducers

Displacement transducers were installed in the test setup to measure the test specimen displacements in the vertical, radial, and circumferential directions at the bearings, and in the vertical and parallel directions at the intersections of the parallel loading planes and the girders within the span of the girders (called “intermediate locations”). This section discusses the displacement transducer arrangement along with the geometric calculations needed to obtain the desired displacements from the measurements. Table 5.1, 5.2 and 5.3 present the location, name (alias), and range of these displacement transducers, as well as other details.

5.2.1 Displacements at bearings

A combination of three linear variable differential transducers (LVDTs) was used at each bearing to get the displacements in the radial, circumferential, and vertical directions. Displacements in the radial and circumferential directions are measured to evaluate the boundary conditions in comparison with the intended boundary conditions discussed in Chapter 4. Displacement in the vertical direction is measured to observe foundation settlement at the bearings. Any such foundation settlement is needed to determine the vertical deflections of the test specimen relative to the bearings from the vertical displacements measured at the intermediate locations. Table 5.1 presents the location, alias, and range of the bearing displacement transducers. Expected displacements from the analysis of FE Model-D3 (Ma, 2014) are presented in Table 5.4 for comparison.

The LVDTs at each bearing were connected to a target point on the bearing stiffener by a brass wire offset. The wire offset was used to attach the LVDT to the target point in a way that reduces the effect of displacements perpendicular to the orientation of the LVDT on the measurement by the LVDT. Figure 5.2 is a plan view of the fixtures and LVDTs used to measure displacements at the G1W bearing. Figure 5.3 (d) is a photograph of the fixtures and LVDTs for the G2W bearing. As shown, the radial and circumferential LVDTs are supported on holders attached to stand made from extruded aluminum bars and steel plates, and the vertical LVDT is supported from above by a truss structure.

5.2.2 Displacements at intermediate locations

Displacements were determined from measurements at 14 intermediate locations at the intersection of the seven interior parallel planes (A, BE, BW, CE, CW, DE and DW) with G1 and G2. A combination of one LVDT and one string potentiometer (String Pot) was used to measure the displacements at each intermediate target point. The measurements were made in the vertical direction by the String Pot and in an inclined direction by the LVDT as shown in Figure 5.3 (b) and Figure 5.3 (c), respectively. From analysis of FE Model-D3, longitudinal displacements of the test specimen were expected at the intermediate locations, however the longitudinal displacements were expected to be small at the test girder bottom flange where the displacement measurement target points are established (Figure 5.3 (a)). Therefore the longitudinal displacements were not measured. The effect of the longitudinal (out of the parallel plane) displacements on the other measurements was considered by analysis (Section 5.2.3).

At each intermediate location, a stud was welded to the bottom flange of the girder to serve as the displacement measurement target point (Figure 5.3 (a)). Therefore, there is a 2 in. vertical offset between the location on the bottom flange and the target point. The String Pot and LVDT associated with each target point were located in the parallel plane. Each String Pot was attached to a steel base plate and placed directly below target point, between the load transfer channels, on the pavement (Figure 5.3 (b)). The longitudinal displacement at the target point (estimated from the FE Model-D3 analysis) was small enough to avoid collision of the String Pot wire and the load transfer channels.

An extruded aluminum bar was placed in between the load transfer channels. The aluminum bar was attached to a steel base plate which rested on grout to level the plate. A LVDT holder that freely rotates about the longitudinal axis of the test specimen was attached to the aluminum bar (see Figure 5.3 (b)). The LVDT holder allows the LVDT to rotate in the parallel plane. As shown in Figure 5.3 (c), the LVDT was inclined in the parallel plane and attached to the target point with a brass wire offset.

5.2.3 Calculations to obtain displacement components at intermediate locations

Due to the expected large displacements at the intermediate locations of the test specimen in both vertical and parallel directions, and considering the constraints of the test setup, it was not possible to eliminate the effects of displacements in the direction perpendicular to the displacement transducers by using only wire offsets. Therefore, geometric calculations were used to obtain the vertical and parallel components of the displacements at the intermediate locations from the measured displacements.

In these calculations, the String Pot base point (P_{SP}), LVDT base point (P_{LVDT}), and target point (Q) are three vertices of a triangle as shown in Figure 5.4. The three sides of the triangular were measured initially (Table 5.5), and then calculations were applied to determine the displacement components of Q.

The String Pot base point (P_{SP}) is the tip of the String Pot rubber extension (see Figure 5.3 (b)), which the string of the String Pot rotates about due to displacement of the target point perpendicular to the string. The String Pot is placed on the pavement directly below the target point to get line $\overline{P_{SP}Q_{\iota}}$ aligned with vertical axis. The LVDT base point (P_{LVDT}) is the intersection of LVDT centerline and LVDT holder centerline. P_{LVDT} is the center of rotation for the LVDT. Q is the target point where the LVDT wire offset and the String Pot string are attached to the test setup (Figure 5.3 (a)). Figure 5.4 shows these three vertices in initial and displaced positions in space and their projection to the parallel plane, where:

Q_i = the initial position of the target point

Q_f = the displaced position of the target point

Q_f' = the projection of the displaced position of the target point to the parallel plane

L_{0_LVDT} = the distance between P_{LVDT} and Q_i

L_{0_SP} = the distance between P_{SP} and Q_i

$L_{0\_SP\_LVDT}$ = the distance between P_{LVDT} and P_{SP}

L_{LVDT} = the distance between P_{LVDT} and Q_f

L_{SP} = the distance between P_{SP} and Q_f

L_{LVDT}' = the distance between P_{LVDT} and Q_f' in the parallel plane

L_{SP}' = the distance between P_{SP} and Q_f' in the parallel plane

θ_{P_LVDT} = the angle between L_{LVDT} and L_{LVDT}'

θ_{P_SP} = the angle and between L_{SP} and L_{SP}'

As mentioned in the previous section, the longitudinal (out of the parallel plane) displacements are expected to be small enough that when L_{SP} and $\mathrm{L}_{\mathrm{LVDT}}$ are relatively large, we can assume:

$$\theta_{\mathrm{P\_LVDT}} \approx 0 \rightarrow \cos(\theta_{\mathrm{P\_SP}}) \approx 1 \tag{5.1}$$

$$\theta_{\mathrm{P\_LVDT}} \approx 0 \rightarrow \cos(\theta_{\mathrm{P\_SP}}) \approx 1 \tag{5.2}$$

And

$$\mathrm{L}_{\mathrm{SP}}{}' \approx \mathrm{L}_{\mathrm{SP}} \tag{5.3}$$

$$\mathrm{L}_{\mathrm{LVDT}}{}' \approx \mathrm{L}_{\mathrm{LVDT}} \tag{5.4}$$

Table 5.6 compares displacement components from FE Model-D3 analysis with displacement components from the geometric calculations (described later) where the effect of the out of the parallel plane displacement is neglected. Comparison of the FE displacements with the corresponding displacements from the simulation validates the assumptions. Therefore, the geometric calculations were performed in the parallel plane.

Figure 5.5 (a) shows the initial position of the vertex points in the parallel plane and defines the initial angles between the triangle sides $(\theta_{0\_Q}, \theta_{0\_SP}, \theta_{0\_LVDT})$. At each intermediate location of the test specimen, the three sides of the initial triangle were measured before the test and the results are given in Table 5.5. The corresponding initial angles are calculated from the lengths of the three sides using the law of cosines. Figure 5.5 (b) shows a displaced position of the target point in the parallel plane and the corresponding angles between the triangle sides $(\theta_{\mathrm{Q}}, \theta_{\mathrm{SP}}, \theta_{\mathrm{LVDT}})$. The updated lengths, L_{SP} and $\mathrm{L}_{\mathrm{LVDT}}$, are calculated by adding the initial lengths ($\mathrm{L}_{0\_\mathrm{SP}}, \mathrm{L}_{0\_\mathrm{LVDT}}$) to the transducers measurements ($\Delta\mathrm{L}_{\mathrm{SP}}, \Delta\mathrm{L}_{\mathrm{LVDT}}$). Since the out of parallel plane displacement is neglected, Equations 5.3 and 5.4 are used so $\mathrm{L}'_{\mathrm{SP}} = \mathrm{L}_{\mathrm{SP}}$ and $\mathrm{L}'_{\mathrm{LVDT}} = \mathrm{L}_{\mathrm{LVDT}}$. The corresponding angles are calculated from the law of cosines.

From Figure 5.5 (c), and considering line $\overline{P_{SP}Q_{\iota}}$ is aligned with the vertical axis, the displacement in the parallel direction (Δx) is calculated as follows:

$$\Delta x = \mathrm{L}_{\mathrm{LVDT}}{}' * \cos(\theta_{\mathrm{x}}) - \mathrm{L}_{0\_\mathrm{LVDT}} * \sin(\theta_{0\_\mathrm{Q}}) \tag{5.5}$$

Where

$$\theta_{\mathrm{x}} = \theta_{\mathrm{LVDT}} - (\frac{\pi}{2} - \theta_{0_{\mathrm{SP}}}) \tag{5.6}$$

Combining Equations 5.4, 5.5 and 5.6 we have:

$$\Delta x = \mathrm{L}_{\mathrm{LVDT}} * \cos\left(\theta_{LVDT} - \left(\frac{\pi}{2} - \theta_{0_{SP}}\right)\right) - \mathrm{L}_{0\_\mathrm{LVDT}} * \sin(\theta_{0\_\mathrm{Q}}) \tag{5.7}$$

Similarly from Figure 5.5 (d), and considering line $\overline{P_{SP}Q_{\iota}}$ is aligned with the vertical axis, the vertical displacement (Δy) is calculated as follows:

$$\Delta y = \mathrm{L}_{\mathrm{SP}}{}' * \cos(\theta_{\mathrm{y}}) - \mathrm{L}_{0\_\mathrm{SP}} \tag{5.8}$$

$$\theta_{\mathrm{y}} = \theta_{\mathrm{SP}} - \theta_{0\_\mathrm{SP}} \tag{5.9}$$

Combining Equations 5.3, 5.8 and 5.9 we have:

$$\Delta y = \mathrm{L_{SP}} * \cos(\theta_{\mathrm{SP}} - \theta_{0\_\mathrm{SP}}) - \mathrm{L_{0\_SP}} \tag{5.10}$$

Figure 5.6 and Figure 5.7 present the expected transducer retractions and the calculated displacement components at the mid span for G1 and G2, respectively.

5.3 Rotation Transducers

Rotation transducers (inclinometers) were installed on the test specimen and loading fixtures to measure the test specimen response and details of the loading conditions, respectively. Figure 5.8 (a), (b), and (c) shows photographs of inclinometers installed on the test specimen and loading fixtures. One inclinometer was attached to each bearing and intermediate stiffener to measure the test specimen rotation response in the radial plane (about the circumferential axis). Table 5.7 and Table 5.8 present the location, alias, and range (and other details) of these inclinometers at the bearing and intermediate stiffener locations.

The forces applied to the test specimen were provided by the jacks located within the loading rod assemblies (Section 3.4.3). Due to displacements of the test specimen, the loading rod assemblies will rotate from a vertical condition, resulting in a rotation of the applied force on the loading beam (Section 3.4.2). To measure the orientation of the applied forces, two inclinometers were attached to each loading rod to measure rotation in the parallel and longitudinal planes. Table 5.9 and Table 5.10 present the location, alias, and range of these inclinometers on the loading rods.

The forces transmitted to the test specimen during the test are reaction forces on the loading beams. The forces applied to the loading beams are the forces developed in the (inclined) loading rods. To calculate the reaction forces transmitted to the test specimen from each loading beam, the loading beam was treated as a rigid body, and one inclinometer was installed on each loading beam to measure rotation in the parallel plane (about the longitudinal axis). Calculations of the loading beam reaction forces using statics with the loading beam in the rotated position are presented in Section 7.4. Table 5.11 presents the location, alias, range of these inclinometers on the loading beams.

All inclinometers have a range of ±30˚. Based on FE Model-D3 analysis, the maximum expected rotation at all inclinometer locations does not exceed 8˚.

5.4 Force Transducers

To measure the test specimen vertical reaction forces, one Lebow-3129 (150 kip capacity) load cell was placed in each bearing assembly (Section 3.4.4). Figures 5.9 (a) and (b) show photographs of one of these reaction load cells (Lebow) on a “bench top” and covered with weather protection in the test setup.

To measure the forces applied in each loading rod assembly, one through-hole load cell with 220 kip capacity was installed in each loading rod assembly. Figures 5.9 (c) and (d) show photographs of one of these applied force through-hole load cells on a “bench top” and in the test setup. Initially, these load cells were calibrated over their full 220 kip (compression) force range. Since the maximum expected force in these load cells is much smaller than the maximum capacity of the load cells, these load cells were re-calibrated after the test over a 20 kip (compression) force range to produce a more accurate calibration factor. However, the differences between the two calibration factors were not significant and the initial calibration factors were used in the test data post processing (Chapter 7). Table 5.12 and Table 5.13 presents the location, alias, and sensor serial number (and other details) of the reaction and applied force load cells. Table 5.14 presents the calibration factors for applied force through-hole load cells based on calibration to 220 kip and to 20 kip. Figure 5.10 is a sample calibration sheet for G1DW_LC load cell.

5.5 Strain Transducers

Strain transducers (resistance strain gages) were applied to the test specimen. Strain gages arranged in full bridges, uniaxial strain gages, and rosette strain gages were used. Figure 5.12 and Figure 5.13 show strain gage locations for different sections within girder G1 and G2 where the sections are shown on the plan in Figure 5.11. Note that strain gages were installed on both the inside (south) and outside (north) of the girders. Stress and strain variations across the width and the depth of girder G2 near mid span were of interest. Therefore, more strain gages were installed near G2 mid span. Figure 5.14 shows strain gage locations near G2 mid span. Figure 5.15 shows strain gage locations for the interior diaphragms. Note that strain gages are located on both the east and west sides of the diaphragms.

As noted earlier, many of the strain gages were arranged and wired as full bridges. The full bridges were arranged to output bending moment of Sections ME, LE, KE, KW, LW, MW, IW, IE as well as on the interior diaphragms. At other sections (Section JE, JW, FM, FW, GWE, GW) the bending moment could be determined from a set of individual uniaxial strain gages. Photographs of installed strain gages are shown in Figure 5.16.

5.5.1 Full bridge strain gages

Four uniaxial strain gages were installed on the test specimen and wired in a Wheatstone full bridge to measure primary bending moment at selected sections of the test specimen, as described above. Figure 5.17 shows the moment full bridge strain gage wiring schematic. In a Wheatstone full bridge, the primary bending moment can be determined as follows (Dally and Riley, 1991):

$$M_X = X_M * V_{out} \tag{5.11}$$

$$X_M = \frac{2EI_x}{d\,S_g V_{in}} \tag{5.12}$$

Where:

M_X = the primary bending moment

V_{out} = the output voltage

X_M = the moment full bridge calibration factor

E = Young's modulus

I_x = the second moment of inertia of the girder cross section

d = the distance between two strain gages on the same side of the girder

S_g = the gage factor of the strain gages in the circuit

V_{in} = the excitation voltage

Note that the full bridge measurements of primary bending moment are only valid when the cross section is in the linear elastic range. Therefore, full bridges were used only for girder G1, the interior diaphragms and near the bearings of G2 where the cross section was expected to remain in the linear elastic range during all the tests. For girder G1, the moment diagram varies linearly between adjacent parallel plane intersections with G1, where the load is applied to G1, or interior diaphragm locations where vertical force is transmitted between G1 and the diaphragm. So two full bridge sets were used between adjacent parallel planes to obtain the moment diagram. Note that the parallel plane load fixture locations are not aligned with the diaphragm locations (see Section 2.6).

5.5.2 Uniaxial strain gages

Uniaxial strain gages were used to measure normal strains due to primary bending and flange lateral bending (warping) at selected locations. Near G2 mid span, uniaxial strain gages were installed across the width and depth of the cross section to measure primary bending normal strains and warping normal strains (Figure 5.14). As noted earlier, several strain gage combinations were installed in the same geometry as the bending moment full bridge strain gages, but wired as individual strain gages (one quarter bridge configuration) to enable the bending moment to be measured when the cross section is in the linear elastic range, and also to enable uniaxial local strains to be measured when the cross section is not in the linear elastic range.

5.5.3 Rosette strain gages

Delta rosette strain gages were used to measure the circumferential normal strain, radial normal strain, and shear strain. Rosette gages were installed at one location on top of the tube near mid span of G2 as shown in Figure 5.14 (b).

As shown in the figure, gage number 2 of delta rosette is aligned along the tangent to the circumferential direction, and gages 2 and 3 are numbered counterclockwise from gage 1. The circumferential normal strain (ε_x), the radial normal strain (ε_y), and the shear strain (γ_{xy}) are calculated as follows:

$$\varepsilon_x = \varepsilon_1 \tag{5.13}$$

$$\varepsilon_y = \frac{1}{3}[2(\varepsilon_2 + \varepsilon_3) - \varepsilon_1] \tag{5.14}$$

$$\gamma_{xy} = \frac{2}{\sqrt{3}}(\varepsilon_2 - \varepsilon_3) \tag{5.15}$$

The primary principal normal strain (ε_P) and secondary principal normal strain (ε_Q) are calculated as follows:

$$\varepsilon_{P,Q} = \frac{\varepsilon_1 + \varepsilon_2 + \varepsilon_3}{3} \pm \sqrt{[\frac{2\varepsilon_1 - (\varepsilon_2 + \varepsilon_3)}{3}]^2 + \frac{1}{3}(\varepsilon_2 - \varepsilon_3)^2} \tag{5.16}$$

Table 5.1 LVDTs to measure displacements at bearings

Section	Girder	Direction	Alias	Sensor range (in.)	Sensor serial number	Cable number
East bearing	G1	Radial	G1E_P_LVDT	± 0.5	1300000	15
		Circumferential	G1E_L_LVDT	± 0.5	27379	16
		Vertical	G1E_V_LVDT	± 0.5	27374	17
	G2	Radial	G2E_P_LVDT	± 0.5	801	19
		Circumferential	G2E_L_LVDT	± 0.5	803	20
		Vertical	G2E_V_LVDT	± 0.5	135297	21
West bearing	G1	Radial	G1W_P_LVDT	± 0.5	27378	100
		Circumferential	G1W_L_LVDT	± 1	27321	101
		Vertical	G1W_V_LVDT	± 0.5	183	102
	G2	Radial	G2W_P_LVDT	± 0.5	55515	104
		Circumferential	G2W_L_LVDT	± 1	27334	105
		Vertical	G2W_V_LVDT	± 0.5	142	106

Table 5.2 LVDTs to measure displacements at intermediate target points

Section	Girder	Alias	Sensor range (in.)	Sensor serial number	Cable number
DE	G1	G1DE_LVDT	± 2	5375	23
	G2	G2DE_LVDT	± 2	6866	24
CE	G1	G1CE_LVDT	± 3	16512	34
	G2	G2CE_LVDT	± 2	5363	35
BE	G1	G1BE_LVDT	± 3	69699	45
	G2	G2BE_LVDT	± 2	5370	46
A	G1	G1A_LVDT	± 5	57840	56
	G2	G2A_LVDT	± 2	6685	57
BW	G1	G1BW_LVDT	± 5	57841	67
	G2	G2BW_LVDT	± 2	5239	68
CW	G1	G1CW_LVDT	± 3	69697	78
	G2	G2CW_LVDT	± 2	6709	79
DW	G1	G1DW_LVDT	± 2	5338	89
	G2	G2DW_LVDT	± 2	5228	90

Table 5.3 String pots to measure displacements of intermediate target points

Section	Girder	Alias	Sensor range (in.)	Sensor serial number	Cable number
DE	G1	G1DE_SP	20	3004A	25
	G2	G2DE_SP	20	3005A	26
CE	G1	G1CE_SP	20	3000A	36
	G2	G2CE_SP	20	3001A	37
BE	G1	G1BE_SP	20	2996A	47
	G2	G2BE_SP	20	2997A	48
A	G1	G1A_SP	20	2992A	58
	G2	G2A_SP	20	2993A	59
BW	G1	G1BW_SP	20	2994A	69
	G2	G2BW_SP	20	2995A	70
CW	G1	G1CW_SP	20	2998A	80
	G2	G2CW_SP	20	2999A	81
DW	G1	G1DW_SP	20	3002A	91
	G2	G2DW_SP	20	3003A	92

Table 5.4 FE prediction of displacements at bearings at FE increment 50

Section	Girder	FE displacement (in.)		
		Radial	Circumferential	Vertical
East Bearing	G1	0	0	0
	G2	-0.0001	-0.140	0
West Bearing	G1	0	-1.130	0
	G2	0.0008	-1.400	0

Table 5.5 Initial distance between String Pot reference points, LVDT reference points and test specimen target points

Section	Girder	L_{0_SP} (in.)	L_{0_LVDT} (in.)	$L_{0\_SP\_LVDT}$ (in.)
DE	G1	39.88	33.31	37.25
	G2	37.63	46.63	49.81
CE	G1	38.56	44.34	47.81
	G2	36.13	34.00	38.38
BE	G1	39.44	39.63	43.56
	G2	37.00	38.88	42.81
A	G1	39.31	34.13	38.25
	G2	37.31	38.88	42.38
BW	G1	40.06	39.81	43.19
	G2	38.00	39.63	43.06
CW	G1	40.75	34.56	37.63
	G2	38.19	40.06	44.00
DW	G1	41.94	40.13	43.13
	G2	39.06	26.31	30.38

Table 5.6 FE intermediate target point displacements based on Model-D3 analysis at FE increment 50, and obtained displacement component from geometric calculations where effect of out of plane displacement is neglected

Section	Girder	FE displacement (in.)		Simulated transducers final length (in.)		Simulated extension of transducers (in.)		Corresponding displacement (in.)	
		δx	δy	L_{SP}	L_{LVDT}	ΔL_{SP}	ΔL_{LVDT}	Δx	Δy
DE	G1	-1.572	0.540	38.31	32.09	-1.57	-1.23	-1.572	0.540
	G2	-4.785	0.799	32.85	46.12	-4.78	-0.50	-4.785	0.799
CE	G1	-3.155	1.811	35.45	41.63	-3.11	-2.71	-3.154	1.811
	G2	-8.888	1.790	27.30	33.26	-8.83	-0.74	-8.887	1.791
BE	G1	-4.235	2.932	35.33	35.37	-4.11	-4.25	-4.234	2.932
	G2	-11.772	2.418	25.35	38.70	-11.65	-0.17	-11.770	2.420
A	G1	-4.660	3.581	34.84	28.90	-4.47	-5.23	-4.658	3.580
	G2	-13.450	3.133	24.07	39.09	-13.24	0.21	-13.446	3.135
BW	G1	-4.300	3.397	35.93	35.03	-4.14	-4.78	-4.296	3.394
	G2	-12.902	3.053	25.29	39.69	-12.71	0.07	-12.898	3.056
CW	G1	-3.242	2.511	37.60	30.79	-3.15	-3.77	-3.236	2.506
	G2	-9.839	2.447	28.46	40.00	-9.73	-0.06	-9.832	2.451
DW	G1	-1.626	1.163	40.34	38.38	-1.60	-1.75	-1.619	1.158
	G2	-5.270	1.122	33.82	24.35	-5.24	-1.96	-5.261	1.131

Table 5.7 Inclinometers to measure cross section rotation about circumferential axis of test specimen at intermediate stiffener locations

Section	Girder	Alias	Sensor range (degree)	Sensor serial number	Cable number
DE	G1	G1DE_ROT	± 30	T19	32
	G2	G2DE_ROT	± 30	T21	33
CE	G1	G1CE_ROT	± 30	T10	43
	G2	G2CE_ROT	± 30	T12	44
BE	G1	G1BE_ROT	± 30	T24	54
	G2	G2BE_ROT	± 30	TB1-1	55
A	G1	G1A_ROT	± 30	TB5-1	65
	G2	G2A_ROT	± 30	TB5-2	66
BW	G1	G1BW_ROT	± 30	TB4-2	76
	G2	G2BW_ROT	± 30	TB4-3	77
CW	G1	G1CW_ROT	± 30	21030093	87
	G2	G2CW_ROT	± 30	31610162	88
DW	G1	G1DW_ROT	± 30	21030314	98
	G2	G2DW_ROT	± 30	31610079	99

Table 5.8 Inclinometers to measure cross section rotation about circumferential axis of test specimen at bearing stiffener locations

Section	Girder	Alias	Sensor range (degree)	Sensor serial number	Cable number
East Bearing	G1	G1EE_ROT	± 30	T5	18
	G2	G2EE_ROT	± 30	T7	22
West Bearing	G1	G1EW_ROT	± 30	T1	103
	G2	G2EW_ROT	± 30	T3	107

Table 5.9 Inclinometers to measure rotation in south loading rod assemblies

Section	Direction	Alias	Sensor range (degree)	Sensor serial number	Cable number
DE	Parallel	DESP_ROT	± 30	T9	27
	Longitudinal	DESP_ROT	± 30	T11	28
CE	Parallel	CESP_ROT	± 30	T23	38
	Longitudinal	CESP_ROT	± 30	T23	39
BE	Parallel	BESP_ROT	± 30	T14	49
	Longitudinal	BESP_ROT	± 30	T16	50
A	Parallel	ASP_ROT	± 30	TB1-2	60
	Longitudinal	ASL_ROT	± 30	TB1-3	61
BW	Parallel	BWSP_ROT	± 30	TB5-3	71
	Longitudinal	BWSP_ROT	± 30	TB2-1	72
CW	Parallel	CWSP_ROT	± 30	TB6-1	82
	Longitudinal	CWSP_ROT	± 30	TB6-2	83
DW	Parallel	DWSP_ROT	± 30	31370138	93
	Longitudinal	DWSP_ROT	± 30	21030316	94

Table 5.10 Inclinometers to measure rotation in north loading rod assemblies

Section	Direction	Alias	Sensor range (degree)	Sensor serial number	Cable number
DE	Parallel	DENP_ROT	± 30	T13	29
	Longitudinal	DENP_ROT	± 30	T15	30
CE	Parallel	CENP_ROT	± 30	T4	40
	Longitudinal	CENP_ROT	± 30	T6	41
BE	Parallel	BENP_ROT	± 30	T18	51
	Longitudinal	BENP_ROT	± 30	T20	52
A	Parallel	ANP_ROT	± 30	TB3-1	62
	Longitudinal	ANL_ROT	± 30	TB3-2	63
BW	Parallel	BWNP_ROT	± 30	TB2-2	73
	Longitudinal	BWNP_ROT	± 30	TB2-3	74
CW	Parallel	CWNP_ROT	± 30	TB6-3	84
	Longitudinal	CWNP_ROT	± 30	31610066	85
DW	Parallel	DWNP_ROT	± 30	82850072	95
	Longitudinal	DWNP_ROT	± 30	31610080	96

Table 5.11 Inclinometers to measure rotation of loading beams about longitudinal axis

Loading beam	Alias	Sensor range (degree)	Sensor serial number	Cable number
DE	DELB_ROT	± 30	T17	31
CE	CELB_ROT	± 30	T8	42
BE	BELB_ROT	± 30	T22	53
A	ALB_ROT	± 30	TB3-3	64
BW	BWLB_ROT	± 30	TB4-1	75
CW	CWLB_ROT	± 30	31610093	86
DW	DWLB_ROT	± 30	21030315	97

Table 5.12 Reaction Lebow load cells in bearing assemblies

Section	Girder	Alias	Sensor model	Sensor serial number
East Bearing	G1	E_G2_LC	Lebow-3129 load cell	677
	G2	E_G1_LC		680
West Bearing	G1	W_G2_LC		679
	G2	W_G1_LC		678

Table 5.13 Applied force through-hole load cells installed in loading rod assemblies

Section	Loading rod	Alias	Sensor model	Sensor serial number
DE	S	G1DE_LC	Through-hole 220 kip load cell	100709
	N	G2DE_LC		990905
CE	S	G1CE_LC		100715
	N	G2CE_LC		100708
BE	S	G1BE_LC		100712
	N	G2BE_LC		100713
A	S	G1A_LC		100711
	N	G2A_LC		100707
BW	S	G1BW_LC		100710
	N	G2BW_LC		100705
CW	S	G1CW_LC		100716
	N	G2CW_LC		100706
DW	S	G1DW_LC		990903
	N	G2DW_LC		100717

Table 5.14 Calibration factor for applied force through-hole load cells, based on calibration to 220 kip and 20 kip compression load

Section	Serial number	Calibration factor (kip/V)		Difference (%)
		Calibrated to 220 kip	Calibrated to 20 kip	
G1DW	990903	6.935	6.804	-1.888
G1CW	100716	6.933	6.962	0.421
G1BW*	100710	6.997	-*	-*
G1A	100711	6.961	6.967	0.097
G1BE	100712	6.942	7.009	0.955
G1CE	100715	6.933	6.887	-0.664
G1DE	100709	6.936	6.890	-0.670
G2DW	100717	6.953	6.788	-2.366
G2CW	100706	6.946	6.878	-0.966
G2BW	100705	6.931	7.066	1.948
G2A	100707	6.916	6.895	-0.298
G2BE	100713	7.012	6.934	-1.101
G2CE	100708	6.928	6.894	-0.485
G2DE	990905	6.979	6.852	-1.823

* G1BW load cell was damaged during the 20 kip calibration after tests

Table 5.15 Moment full bridge strain gage plan

Girder	Section	Alias	Calibration factor (kip-in/mV)
G1	ME	G1_MEW_MF	1035
		G1_MEE_MF	1035
	LE	G1_LEW_MF	1035
		G1_LEE_MF	1035
	KE	G1_KEW_MF	1035
		G1_KEE_MF	1035
	KW	G1_KWW_MF	1035
		G1_KWE_MF	1035
	LW	G1_LWW_MF	1035
		G1_LWE_MF	1035
	MW	G1_MWW_MF	1035
		G1_MWE_MF	1035
G2	IW	G2_IWW_MF	1010
	IE	G2_IEE_MF	1010
Diaphragm	East Diaphragm	Dia_E_MF	185
	Middle Diaphragm	Dia_M_MF	185
	West Diaphragm	Dia_W_MF	185

Table 5.16 Uniaxial and rosette strain gage plan

Girder	Section	Alias	Type
G1	J-J	G1_JE_WTI	Uniaxial - EA
		G1_JE_WTO	Uniaxial - EA
		G1_JE_WBI	Uniaxial - EA
		G1_JE_WBO	Uniaxial - EA
		G1_JW_WTI	Uniaxial - EA
		G1_JW_WTO	Uniaxial - EA
		G1_JW_WBI	Uniaxial - EA
		G1_JW_WBO	Uniaxial - EA
		G1_JM_TWI	Uniaxial - EA
		G1_JM_TWO	Uniaxial - EA
		G1_JM_TFI	Uniaxial - EA
		G1_JM_TFO	Uniaxial - EA
		G1_JM_WBI	Uniaxial - EA
		G1_JM_WBO	Uniaxial - EA
G2	IE	G2_IEW_WBI	Uniaxial - EA
		G2_IEWE_WBO	Uniaxial - EA
	HE	G2_HE_WBI	Uniaxial - EA
		G2_HE_WBO	Uniaxial - EA
	GE	G2_GE_TWI	Uniaxial - EA
		G2_GE_TWO	Uniaxial - EA
	HW	G2_HW_WBI	Uniaxial - EA
		G2_HW_WBO	Uniaxial - EA
G2	GW	G2_GWE_WTI	Uniaxial - EA
		G2_GWE_WTO	Uniaxial - EA
		G2_GWE_WBI	Uniaxial - EA
		G2_GWE_WBO	Uniaxial - EA
		G2_GW_WTI	Uniaxial - EA
		G2_GW_WTO	Uniaxial - EA
		G2_GW_WBI	Uniaxial - EA
		G2_GW_WBO	Uniaxial - EA
		G2_GW_TWI	Uniaxial - EP
		G2_GW_TWO	Uniaxial - EP

Table 5.16 Uniaxial and rosette strain gage plan (continued)

Girder	Section	Alias	Type
G2	F-F	G2_FM_R1	Rosette -EA
		G2_FM_R2	Rosette -EA
		G2_FM_R3	Rosette -EA
		G2_FM_TFO	Uniaxial - EP
		G2_FM_TWI	Uniaxial - EP
		G2_FM_TWO	Uniaxial - EP
		G2_FM_TBFI	Uniaxial - EP
		G2_FM_TBFO	Uniaxial - EP
		G2_FM_WTI	Uniaxial - EA
		G2_FM_WTO	Uniaxial - EA
		G2_FM_WBI	Uniaxial - EA
		G2_FM_WBO	Uniaxial - EA
		G2_FM_PTI	Uniaxial - EA
		G2_FM_PTO	Uniaxial - EA
		G2_FM_PBI	Uniaxial - EA
		G2_FM_PBO	Uniaxial - EA
		G2_FMW_TWO	Uniaxial - EP
		G2_FME_TWO	Uniaxial - EP
		G2_FW_WTI	Uniaxial - EA
		G2_FW_WTO	Uniaxial - EA
		G2_FW_WBI	Uniaxial - EA
		G2_FW_WBO	Uniaxial - EA
		G2_FWW_TWTO	Uniaxial - EP
		G2_FWW_TWBO	Uniaxial - EP

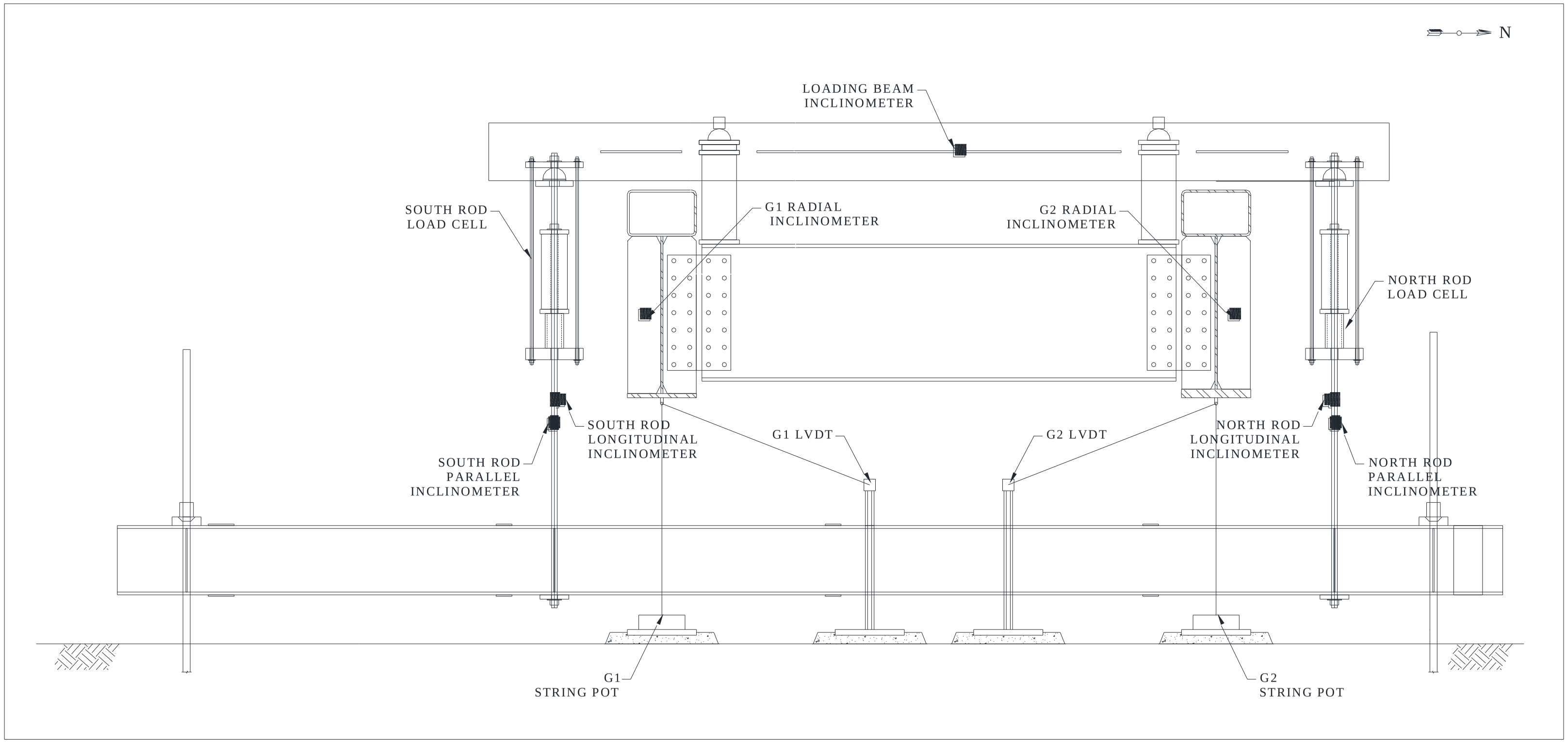

Figure 5.1 Typical instrumentation for parallel planes (A, BE, BW, ...)

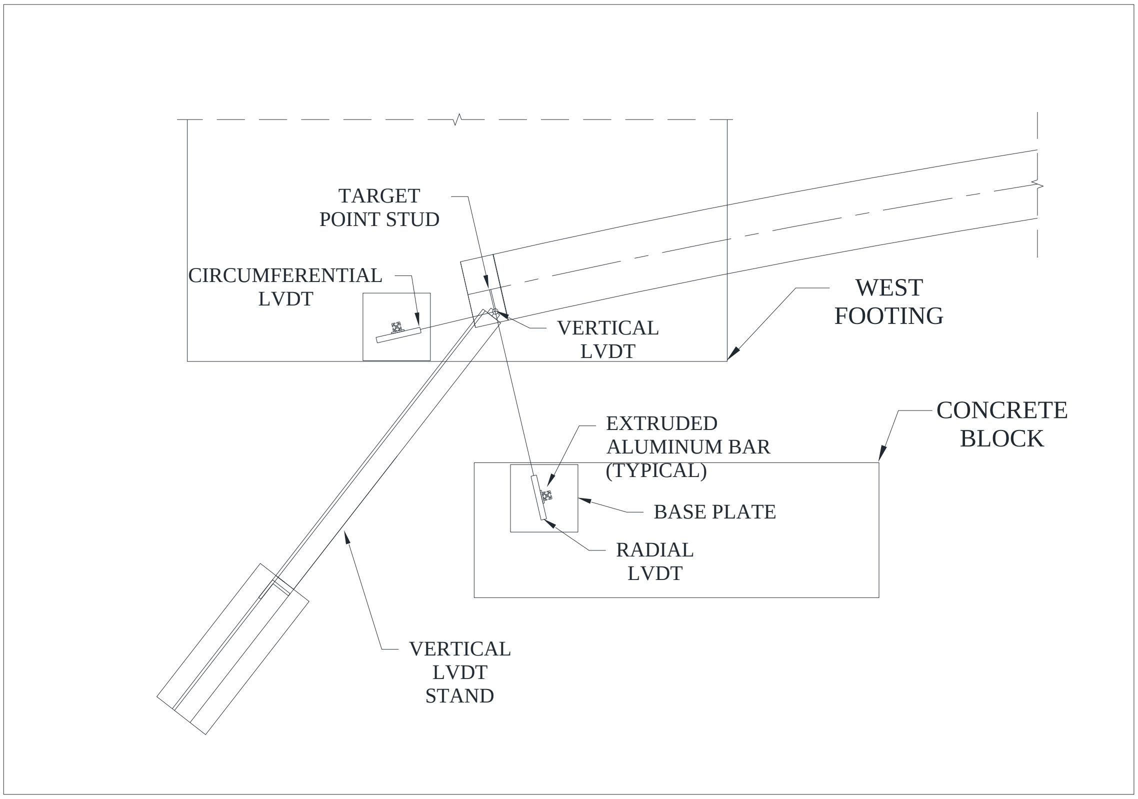

Figure 5.2 Fixtures and LVDTs to measure bearing displacements in three directions for G1W

(a) Intermediate target point located 1 in. below the bottom flange

(b) String Pot placed between load transfer channels

Figure 5.3 Transducers to measure displacements of test specimen

(c) LVDT to measure displacements of intermediate point installed on extruded aluminum bar stand

(d) Three LVDTs to measure displacement of G2W bearing

Figure 5.3 Transducers to measure displacements of test specimen (continued)

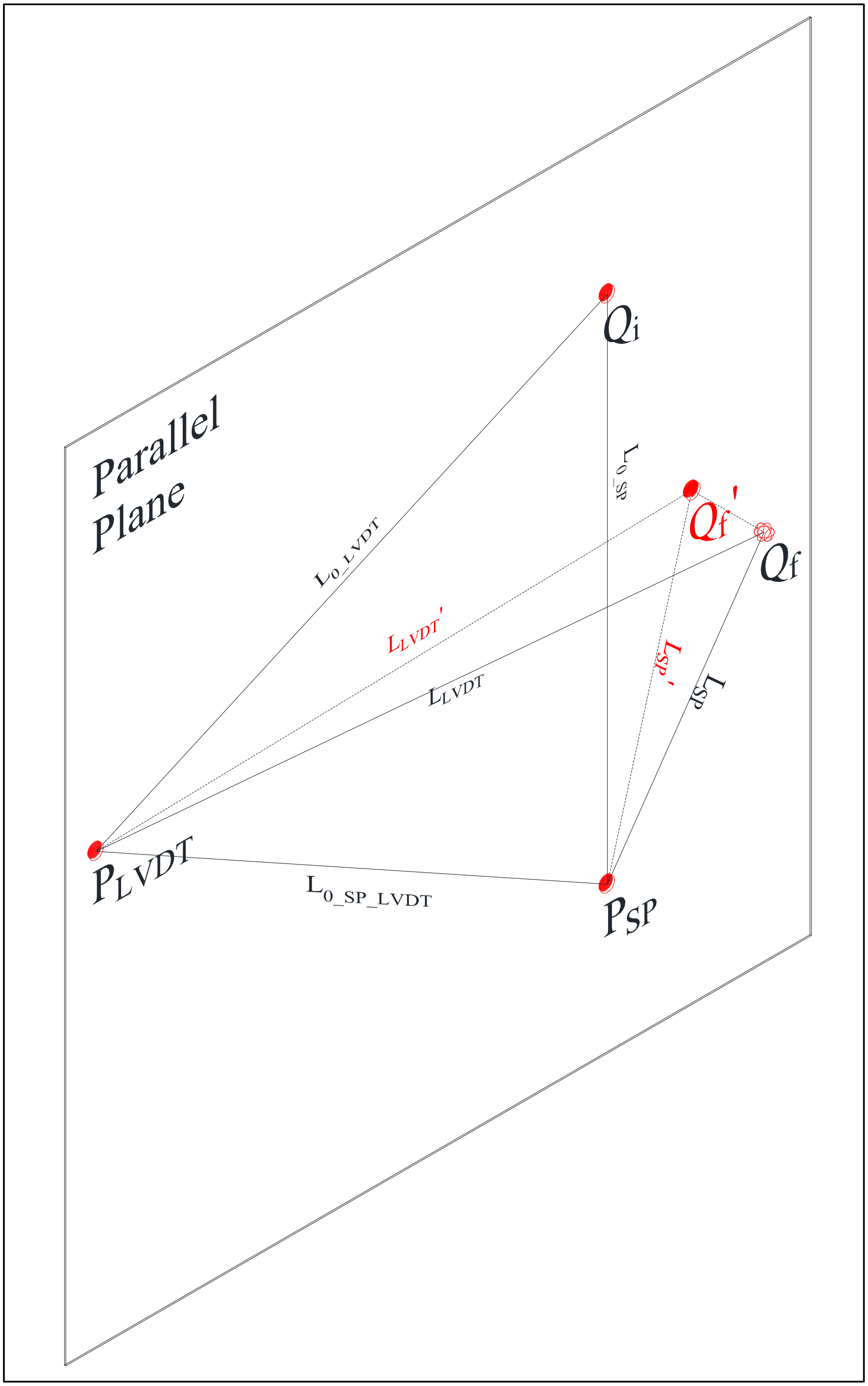

Figure 5.4 Position of displaced target point in space and its projection to parallel plane

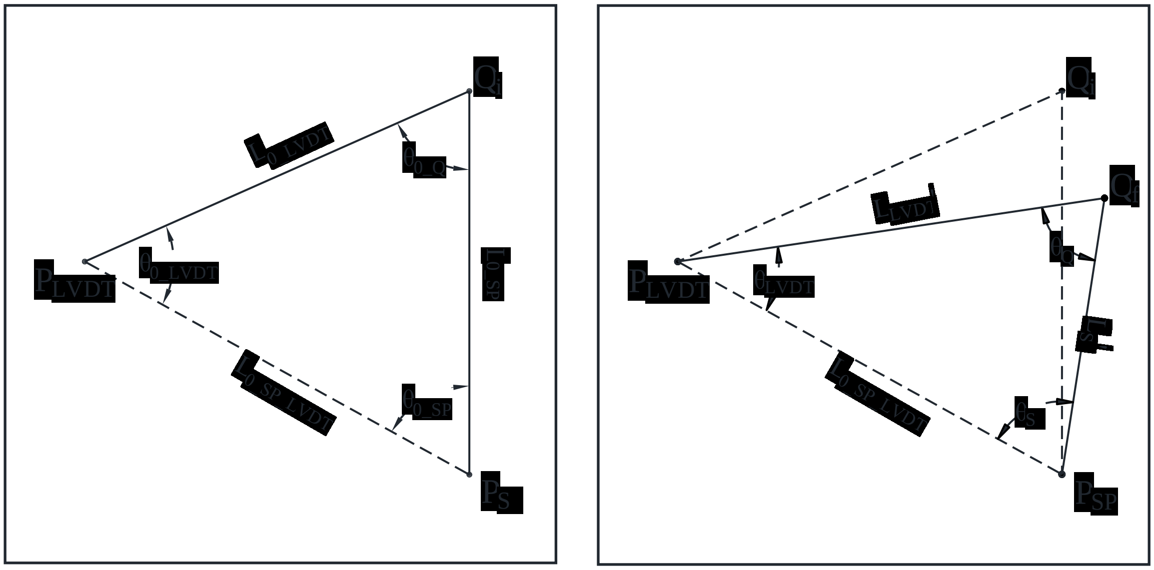

(a) Initial position (b) Position for any given step

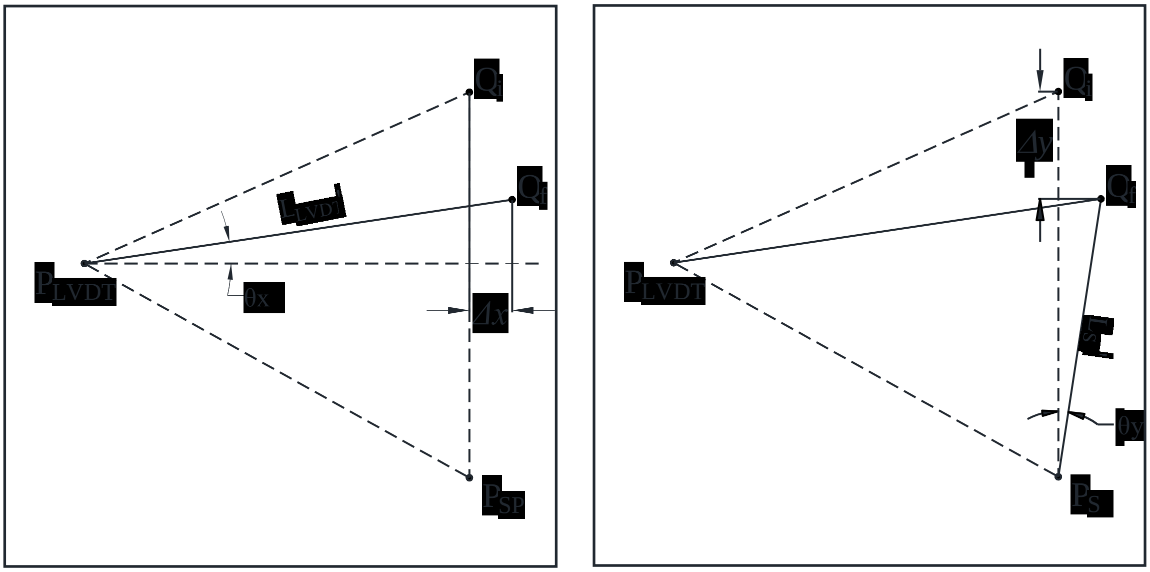

(c) Parallel displacement (d) Vertical displacement

Figure 5.5 Geometric calculations to obtain parallel and vertical displacement components from displacement transducer results

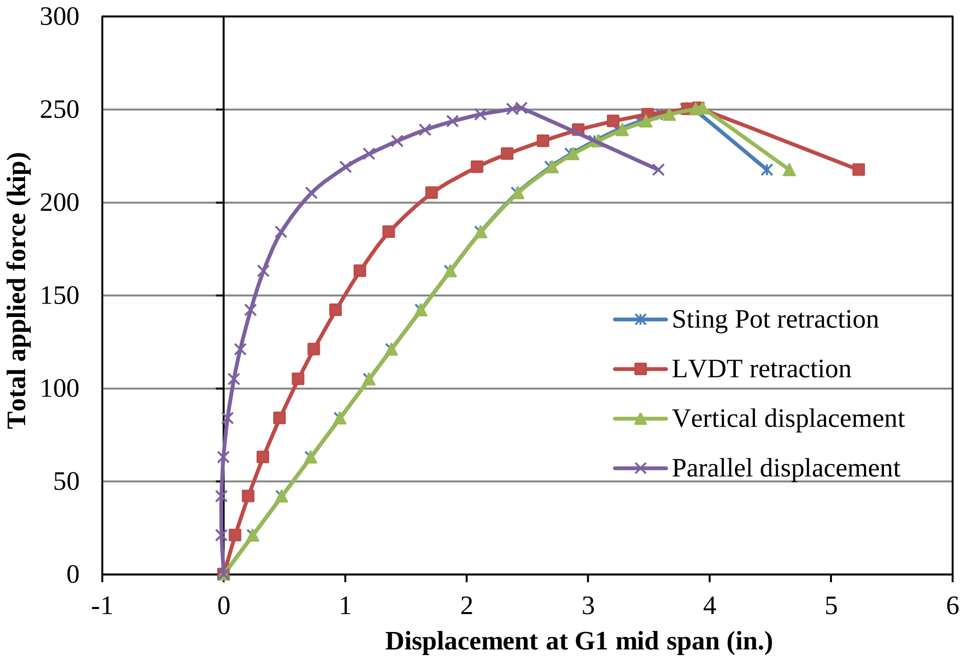

Figure 5.6 Expected girder displacements and transducer retractions at mid span of G1

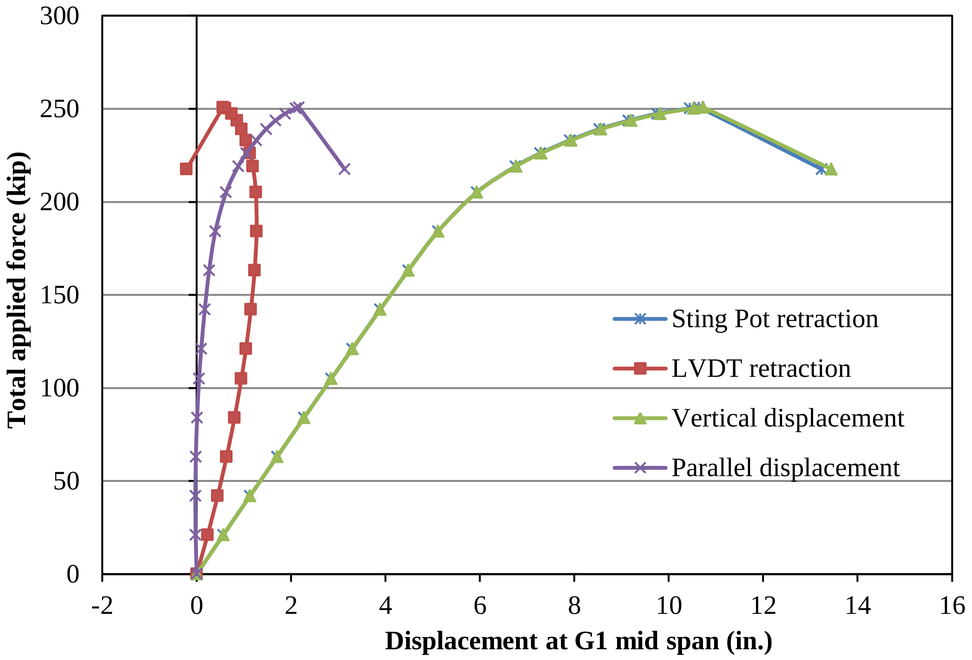

Figure 5.7 Expected girder displacements and transducer retractions at mid span of G2

(a) Inclinometer attached to stiffener to measure test specimen rotation in radial plane

(b) Inclinometers attached to loading rod to measure rotation in parallel and longitudinal planes

(c) Inclinometer attached to loading beam to measure rotation in parallel plane

Figure 5.8 Transducers to measure rotation of test specimen and loading fixtures

(a) Lebow-3129 load cell (Lebow, 2006)

(b) Reaction Lebow-3129 covered by weather protection cover in bearing assembly

(c) Applied force through-hole load cell

(d) Applied through-hole load cell in loading rod assembly

Figure 5.9 Transducers to measure forces in test setup

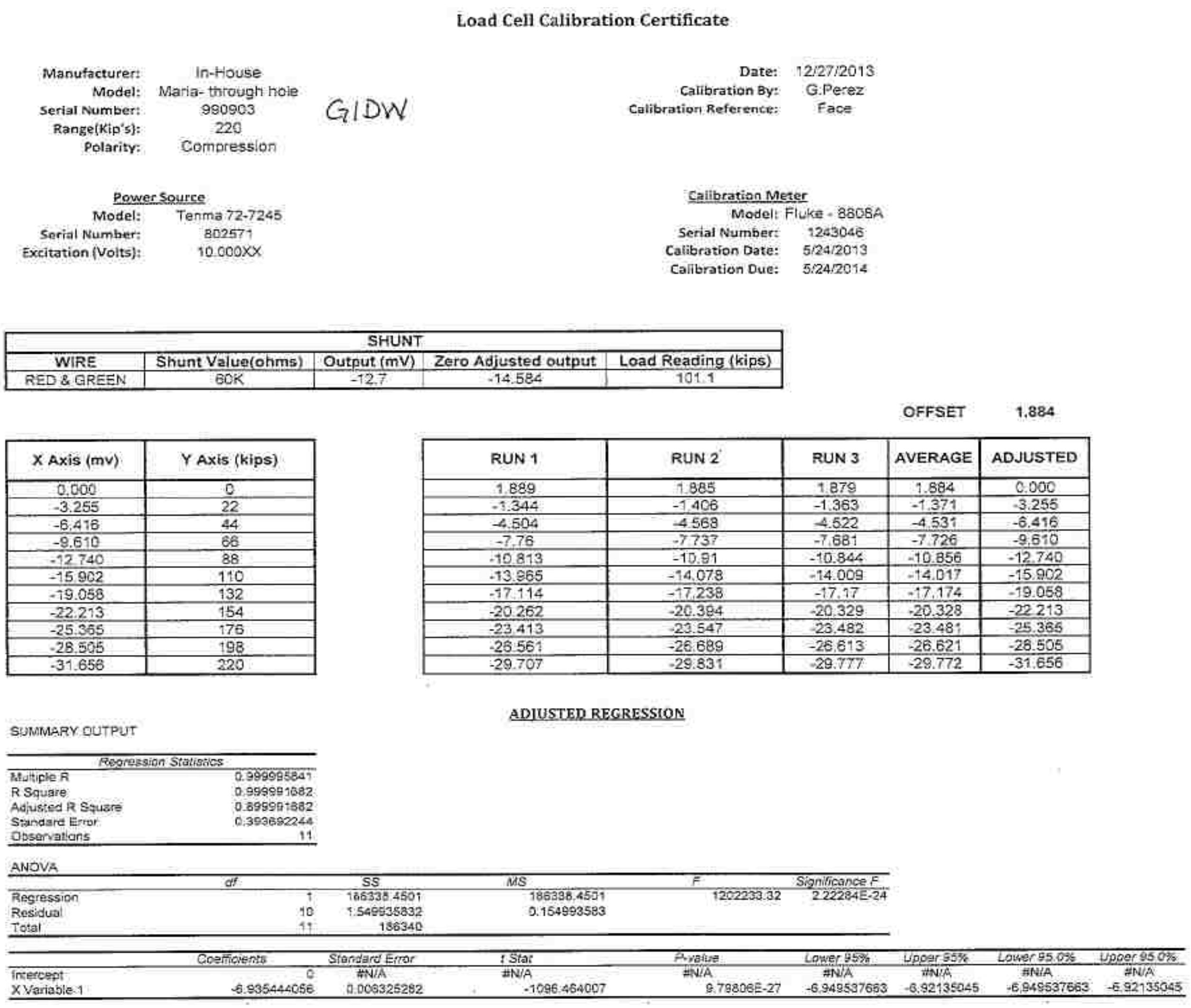

Load Cell Calibration Certificate

Manufacturer: In-House
Model: Maria- through hole
Serial Number: 990903
Range(Kip's): 220
Polarity: Compression

GIDW

Date: 12/27/2013
Calibration By: G.Perez
Calibration Reference: Face

Power Source
Model: Tenma 72-7245
Serial Number: 802571
Excitation (Volts): 10.000XX

Calibration Meter
Model: Fluke - 8808A
Serial Number: 1243046
Calibration Date: 5/24/2013
Calibration Due: 5/24/2014

SHUNT				
WIRE	Shunt Value(ohms)	Output (mV)	Zero Adjusted output	Load Reading (kips)
RED & GREEN	60K	-12.7	-14.584	101.1

OFFSET 1.884

X Axis (mv)	Y Axis (kips)
0.000	0
-3.255	22
-6.416	44
-9.610	66
-12.740	88
-15.902	110
-19.058	132
-22.213	154
-25.365	176
-28.505	198
-31.656	220

RUN 1	RUN 2	RUN 3	AVERAGE	ADJUSTED
1.889	1.885	1.879	1.884	0.000
-1.344	-1.406	-1.363	-1.371	-3.255
-4.504	-4.568	-4.522	-4.531	-6.416
-7.76	-7.737	-7.681	-7.726	-9.610
-10.813	-10.91	-10.844	-10.856	-12.740
-13.965	-14.078	-14.009	-14.017	-15.902
-17.114	-17.238	-17.17	-17.174	-19.058
-20.262	-20.394	-20.329	-20.328	-22.213
-23.413	-23.547	-23.482	-23.481	-25.365
-26.561	-26.689	-26.613	-26.621	-28.505
-29.707	-29.831	-29.777	-29.772	-31.656

ADJUSTED REGRESSION

SUMMARY OUTPUT

Regression Statistics	
Multiple R	0.999995841
R Square	0.999991682
Adjusted R Square	0.899991682
Standard Error	0.393692244
Observations	11

ANOVA

	df	*SS*	*MS*	*F*	*Significance F*
Regression	1	186338.4501	186338.4501	1202233.32	2.22284E-24
Residual	10	1.549935832	0.154993583		
Total	11	186340			

	Coefficients	*Standard Error*	*t Stat*	*P-value*	*Lower 95%*	*Upper 95%*	*Lower 95.0%*	*Upper 95.0%*
Intercept	0	#N/A	#N/A	#N/A	#N/A	#N/A	#N/A	#N/A
X Variable 1	-6.935444056	0.006325282	-1096.464007	9.79806E-27	-6.949537663	-6.92135045	-6.949537663	-6.92135045

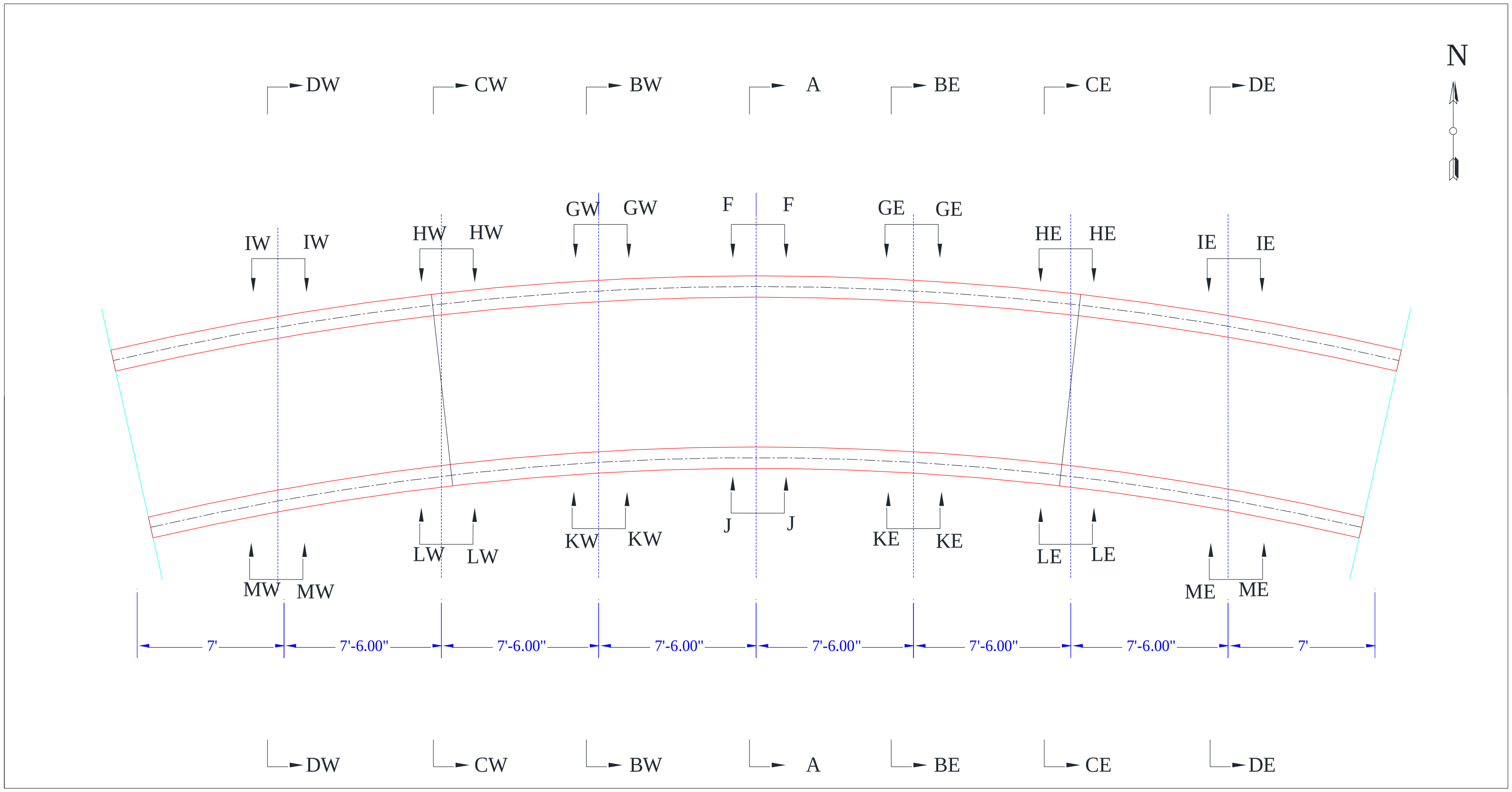

Figure 5.11 Plan view of test specimen showing sections used for strain gage planning

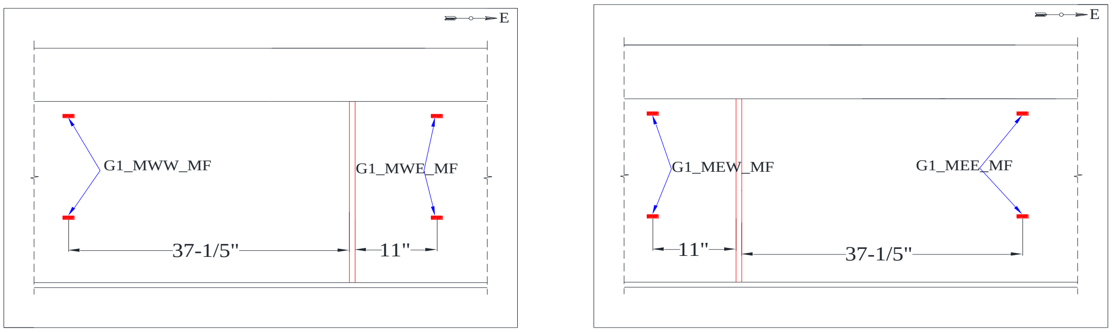

(a) Section MW

(b) Section ME

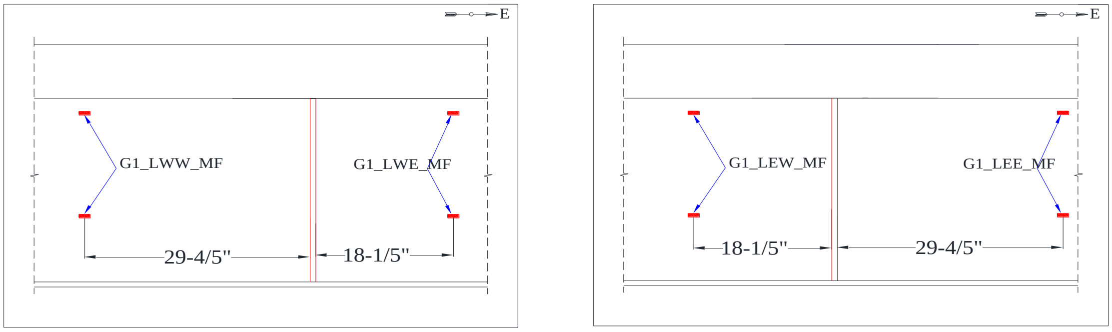

(c) Section LW

(d) Section LE

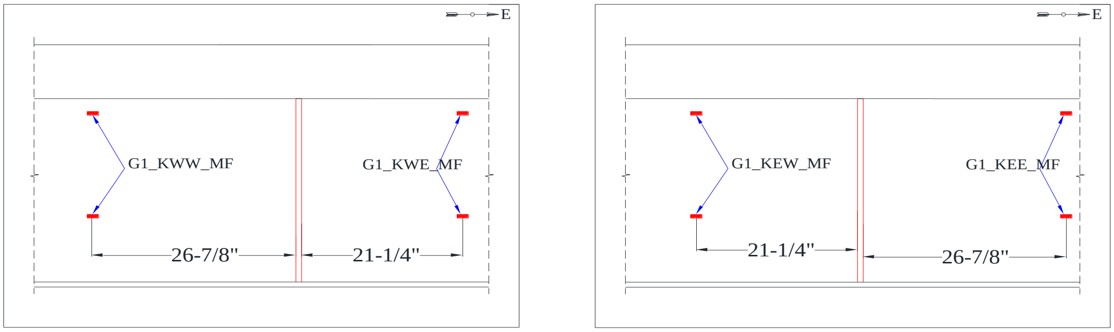

(e) Section KW

(f) Section KE

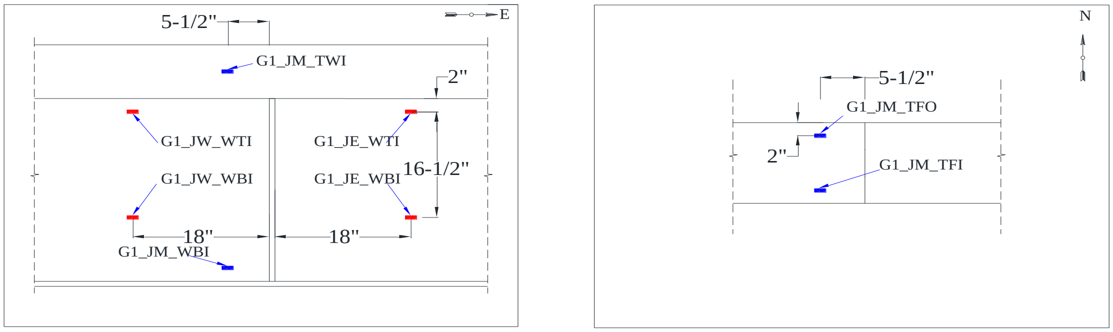

(g) Section J

(h) Top view at Section J

Figure 5.12 Strain locations in G1 at sections indicated in Figure 5.11

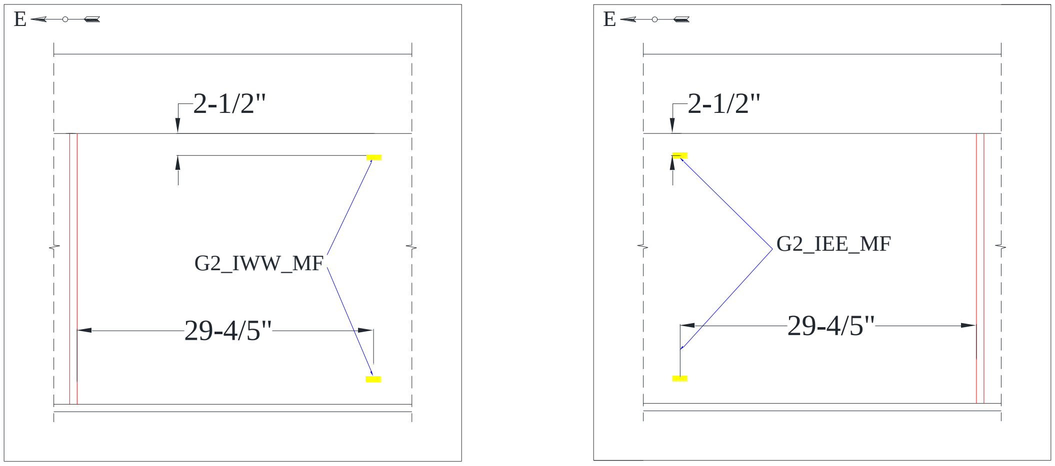

(a) Section IW (b) Section IE

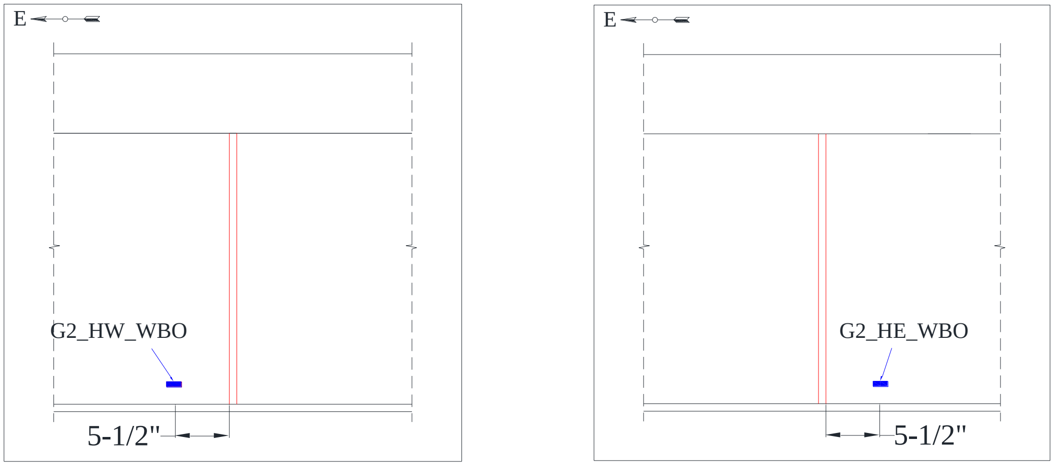

(c) Section HW (d) Section HE

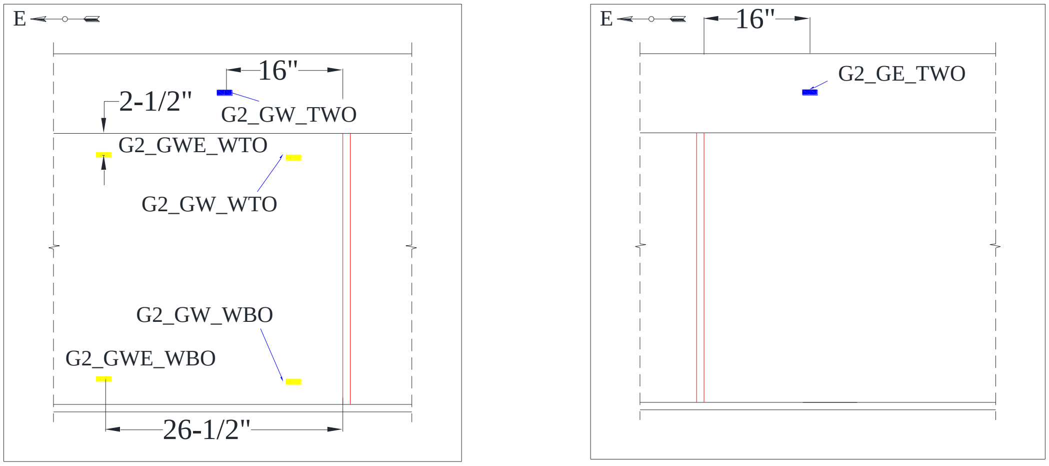

(e) Section GW (f) Section GE

Figure 5.13 Strain gage locations in G2 at sections indicated in Figure 5.11 (mid span strain gages shown in Figure 5.14)

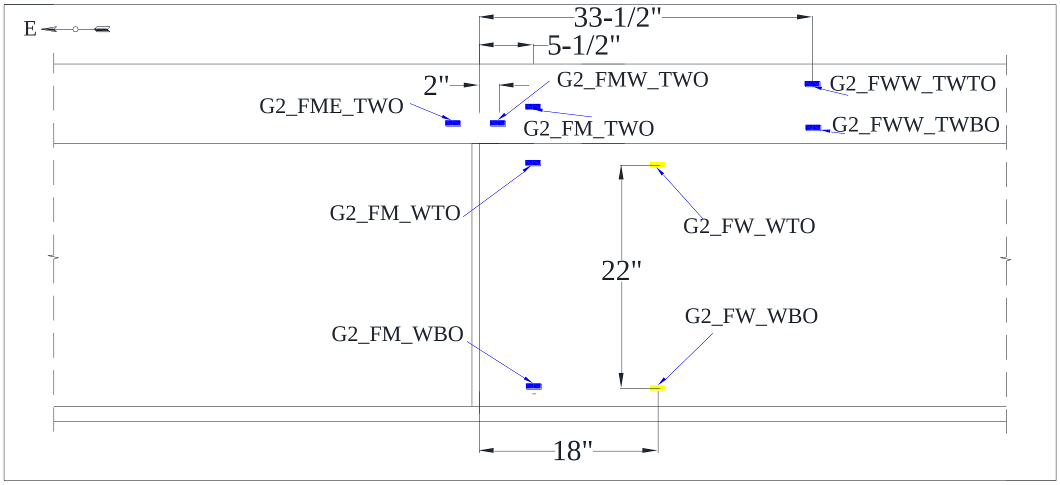

(a) Side view at Section F

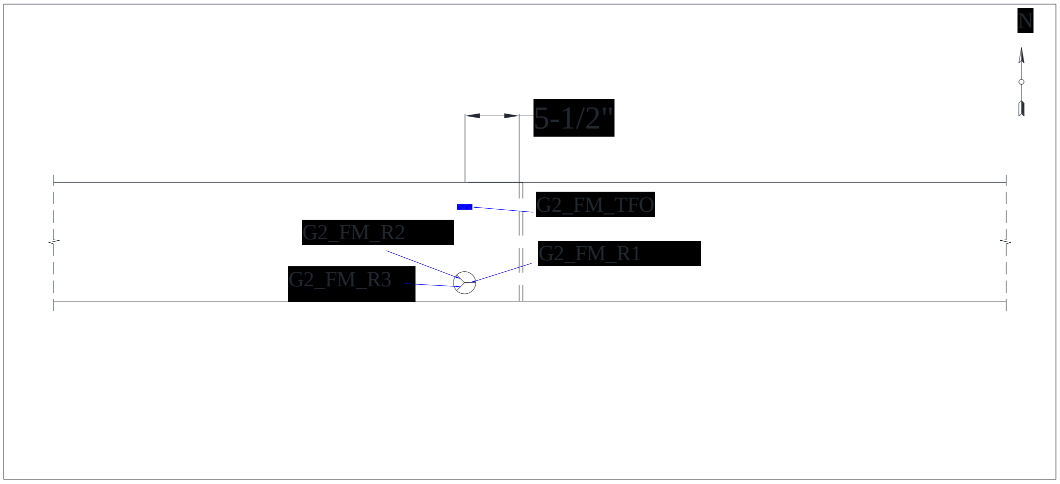

(b) Top view at section F

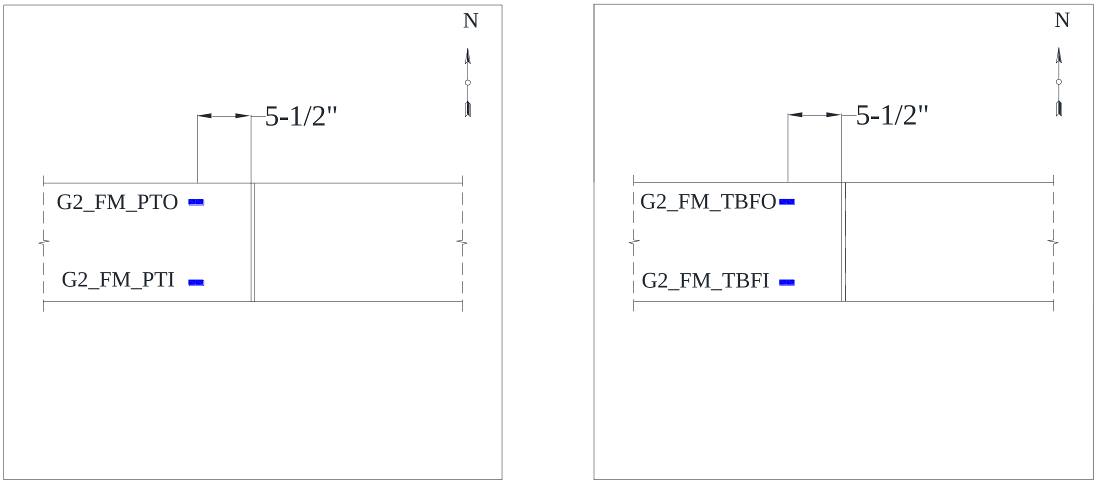

(c) Top view of bottom flange at Section F (d) Bottom view of top tube at Section F

Figure 5.14 Strain gage locations near mid span of G2 (Section F of Figure 5.11)

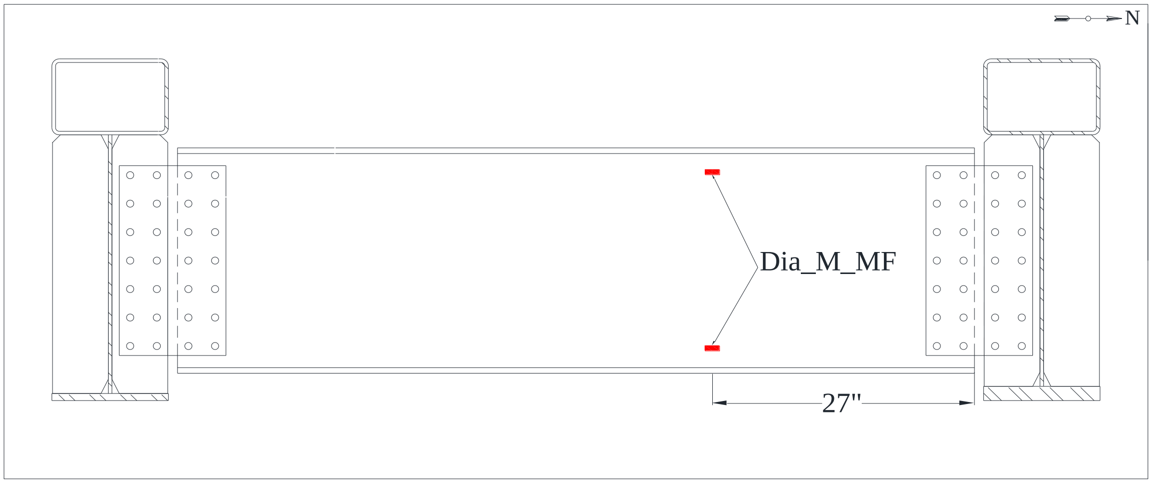

(a) Mid span interior diaphragm (full bridge) strain gages

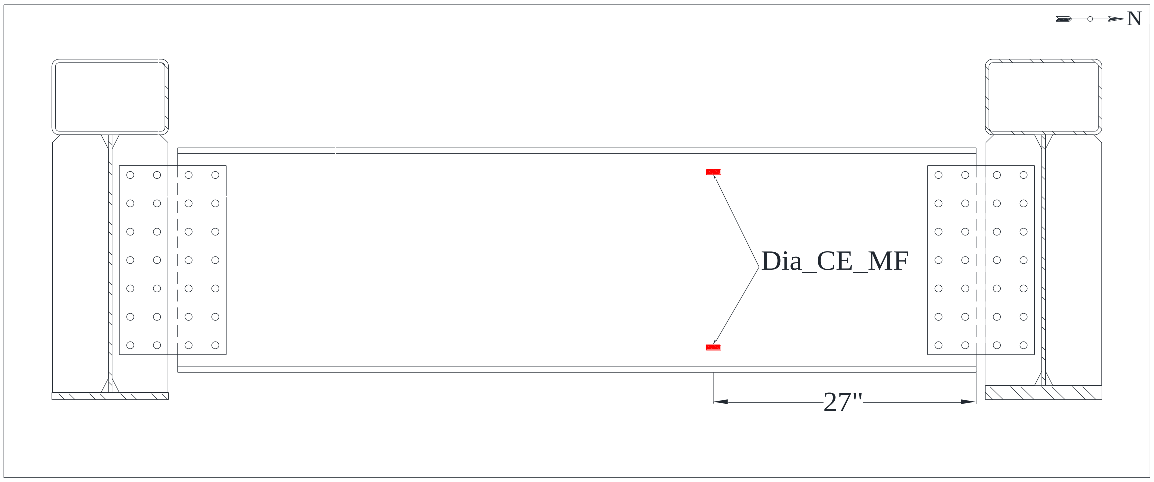

(b) East interior diaphragm (full bridge) strain gages

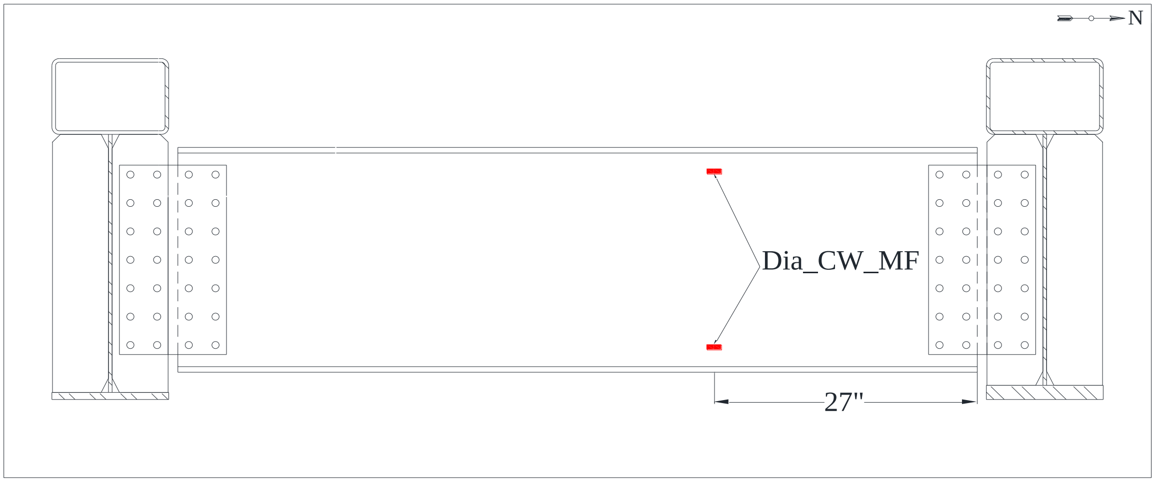

(c) West interior diaphragm (full bridge) strain gages

Figure 5.15 Strain gage locations for interior diaphragms

(a) Bending moment full bridge strain gages on girder web

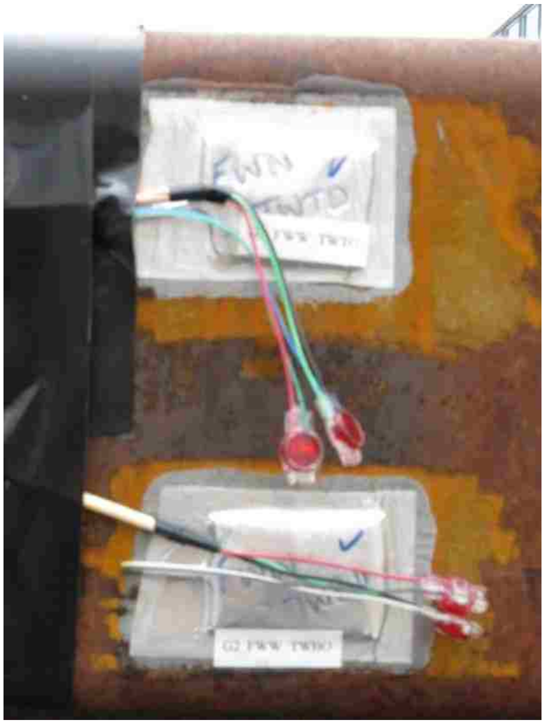

(b) Uniaxial strain gages on girder tube

(c) Photograph of installed strain gages at Section G2_FM facing outside of curvature

Figure 5.16 Strain gages attached to test specimen to measure bending moment and strain

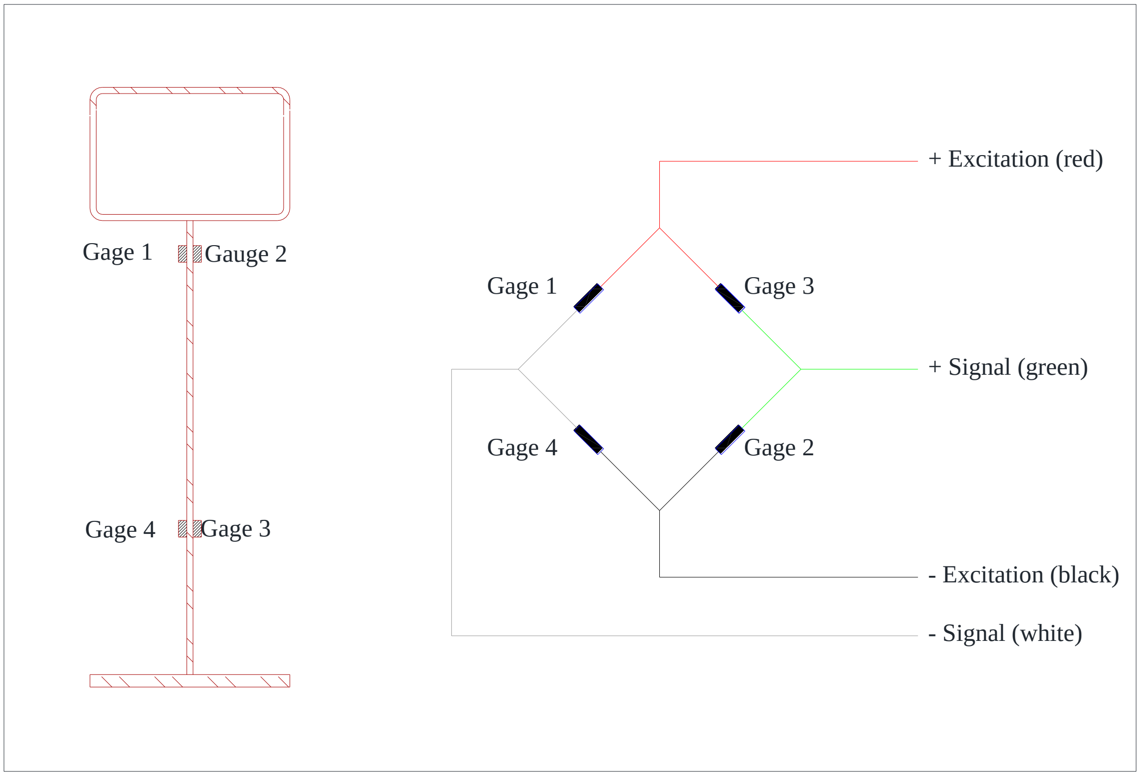

Figure 5.17 Moment full bridge wiring schematic

6 TEST PROCEDURE

6.1 Introduction

This chapter describes the procedure used for the tests, including the initial test plan and adjustments made while testing was in progress. Two types of tests were conducted: elastic loading and inelastic loading tests. Section 6.2 describes the elastic test plan and Section 6.3 describes the inelastic test plan. Hydraulic loading equipment used to provide the loads during the test is discussed in Section 6.4. Section 6.5 discusses the data acquisition (DAQ) system and the sampling methods used to collect and monitor the test data. The test control plan is discussed in Section 6.6.

Loading or unloading the test specimen involves snugging and loosening different nuts in the loading rod assembly (discussed in Section 3.4.3). The initial steps in the testing procedures and the jack re-stroking plan, including nut snugging and loosening, are discussed in Section 6.7 and Section 6.8 respectively.

6.2 Elastic Test Plan

Three cycles of elastic testing were planned to check various transducers in the instrumentation plan, and to develop experience with the jack re-stroking process, as well as to collect data on the test specimen response in the elastic range. In all three elastic cycles, the test specimen was loaded to the factored Constructability limit state load (Chapter 2.4) which is less than the expected elastic limit of the test specimen. Table 6.1 presents the initial test loading plan for a typical elastic cycle. The test results for the last of the three elastic cycles are presented in Table 6.2. Load steps 1 to 6 are to simulate elastic loading up to the factored Constructability limit state load; unloading is applied from load steps 6U to 1U after step 6. Force control (Section 6.6) was used to conduct the elastic tests. The displacements given in Table 6.1 are from analysis of FE Model-D3 (Ma, 2014). Force increments for the jacks in the north and south loading rod assemblies of the Section A (mid span) loading fixtures were used to control each load step. It was expected that the same force would develop in all loading rod assemblies (because all jacks on the north side were pressurized from one pump and all jacks on the south side were pressurized from another pump). However, Table 6.2 indicates that the average force over all the loading rod assemblies is less than the force in the Section A loading rod assemblies where the applied force is controlled (see Section 6.4). This result suggests that due to friction and the hose lengths, the jacks at Section A (closest to the pumps) developed larger forces than the other jacks.

6.3 Inelastic Test Plan

The test specimen was loaded up to (and beyond) the maximum load capacity in the inelastic test. Table 6.3 shows the initial test plan for the inelastic test. When the total applied force is close to the test specimen load capacity, the increase in displacement will be significantly greater than the increase in force. Therefore, different combinations of displacement control and force control were planned for different test stages of the test (Section 6.6). Also, large displacements were expected (based on results from FE Model-D3 given in Chapter 3) and jack re-stroking was required (Section 6.8). In Table 6.3, planned load steps 1 to 6 represent loading in the elastic range, planned load steps 7 to 18 represent loading in the inelastic range to the maximum load capacity. Planned load step 19 is post peak loading, where larger displacements are expected as the force carried by the test specimen decreases. The force and displacement data given in Table 6.3 is from FE Model-D3. The actual inelastic test plan (data during the inelastic test) is presented in Table 6.4. In Table 6.4, actual load steps 1 to 6 represent loading in the elastic range, the maximum load capacity of the test specimen is reached in actual load step 14, and actual load step 17 is the final post peak load step.

6.4 Hydraulic System and Equipment

As discussed in Chapter 6, the load for the tests was provided by fourteen hydraulic jacks. A series of hydraulic hoses and manifolds connected the jacks to hydraulic pumps. Figure 6.1 shows the hydraulic system plan, and hydraulic equipment is shown in Figure 6.2. As shown in these figures, two separate hydraulic pumps were used in the test setup. Two similar ENERPAC ZE3 hydraulic electric pumps were used. Based on the availability of jacks, one set of seven hydraulic jacks was installed in the south loading rod assemblies, and one set of different jacks was installed in the north loading rod assemblies. Eagle Pro Tools ESH 306 hollow core cylinders with a 30 ton capacity at a maximum pressure of 10 ksi were used in the south loading rod assemblies. Enerpac RCH-326 hollow core cylinders with a 30 ton capacity at a pressure of 10 ksi were used in the north loading rod assemblies. All jacks have an approximate stroke of 6.1 in. To accommodate the required larger vertical displacements (total stroke) at the north jack locations (discussed in Section 6.3.2), a jack re-stroking plan was developed (Section 6.8). Since one hydraulic pump provides oil at the same pressure to one set of seven hydraulic jacks, it was assumed that all jacks supplied by one pump would apply the same force. However, due to friction in the hydraulic jacks, hydraulic hoses, and the different lengths of the hoses, the force provided by the jacks was not perfectly uniform across all jacks (see Section 7.4).

6.5 Data Acquisition (DAQ) System

Two similar CR9000X data loggers, DAQ1 and DAQ2 were used to collect the test data. All force and strain transducers (89 channels) were connected to DAQ1, and all displacement and rotation transducers were connected to DAQ2 (93 channels). A metal box was installed at the test setup to protect the DAQ systems from the weather. Figure 6.3 (a) shows a photograph of the DAQ monitoring desk located in the ATLSS van which was parked near the test setup. Figure 6.4 (a) and (b) show photographs of the metal protective box containing the wired DAQ systems.

A zero reference point for data recorded by the DAQ1 and DAQ2 systems was established just before the tests were started, after the loading fixtures were completely assembled. In this condition, the test specimen self-weight and weight of the loading fixtures, including the weight of the load bearing assemblies, loading rod assemblies and load transfer channels were applied to the test specimen. This initial load at the start of the tests is called the "total dead load" on the test specimen. To provide some understanding of the effect of the total dead load, Figure 6.5 shows the load versus mid span vertical displacement of G2 under components of the total dead load from analysis of FE Model-D3.

Manual readings of the reaction load cells were made during the test fixture assembly (before the DAQ systems were in place) and are presented in Table 6.5. The total dead load condition is equivalent to the established zero reference point for the tests.

Two different sampling rates of 1/3 Hz and 2 Hz were used to collect the test data. The 1/3 Hz sampling rate was used to sample data constantly from the beginning of the test to the end of the test, including any pauses in the test. The 2 Hz rate was used to sample data only when loading by the hydraulic jacks was in progress and did not include jack re-stroking and other pauses. Figure 6.6 compares data from the two sampling routines for an elastic test.

6.6 Test Control

A combination of force control and displacement control was used to control loads during the tests. The controller controlled the oil flow from the hydraulic pumps. Two String Pots at the G1 and G2 mid span (G1A_SP and G2A_SP) and two load cells in the south and north loading rod assemblies (SA_LC and NA_LC) in the loading fixture at Section A were used as feedback to the controller. The control equipment was located in a rented van parked near the test setup. Figure 6.3 (b) shows a photograph of the desk used for the load control equipment (controller).

The control plan consisted three control phases as shown in Figure 6.7 (a). In phase I, force control was used and the force increments specified for the north loading rod assembly at Section A with feedback from load cell NA_LC were used to control the north hydraulic pump. To get the same force in the south and north hydraulic jacks, the south hydraulic pump was controlled to make the force feedback from the south load cell (SA_LC) equal to the force feedback from NA_LC.

In the inelastic range, when the total applied load is close to the test specimen capacity, the increment of displacement for each load step is significantly more than the increment of force. Therefore, a mixed control plan of force control and displacement control was implemented in phase II of the test control plan. Displacement increments specified for the mid span displacement of G1 with feedback from the vertical String Pot (G1A_SP) were used to control the south hydraulic pump. The north hydraulic pump was controlled to make the force feedback from NA_LC equal to the feedback from SA_LC.

Since the hydraulic pump valves were one sided, meaning that it was not possible to accurately control the oil flow under reversal, there was some doubt about how effectively the phase II control plan would work for the post peak range of test specimen behavior when the applied force decreases, as the vertical displacement and jack stroke increase. Therefore, phase III of the test control plan was proposed for post peak loading conditions. In this phase, vertical displacement increments for the G1 and G2 mid span, with vertical displacement feedback from String Pots G1A_SP and G2A_SP, would be used to control the south and north loading pumps, respectively. There is no force feedback in phase III, and the north and south jacks would have different levels of force during this part of the inelastic test. It was observed during the inelastic test that control plan phase II performed well for the post peak loading and there was no need to switch to control plan phase III as shown in Figure 6.7 (b). Figure 6.7 (a) shows the proposed control plan with data from FE Model-D3. Figure 6.7 (b) shows the actual control plan used in the inelastic test with data from the test. Control plan phase I was used for the elastic tests.

6.7 Pretesting

To check the functionality of the hydraulic loading equipment, pretesting was performed after the loading fixtures and hydraulic equipment were assembled. Loading or unloading the test specimen involves snugging and loosening different nuts in the loading rod assembly. Figure 6.8 show a longitudinal view of the loading rod assembly including different plates and nuts. A photograph of the upper part of the loading rod assembly is shown in Figure 6.9. The nut condition during loading stages of a test is shown in Figure 6.10. Figure 6.11 shows the pretesting instructions. In the pretesting procedure, Nut C is loosened and is not in contact with the jack (see Figure 6.12), so plate C can move upward freely and the jack stroke and retraction can be checked without developing a force in the loading rod assembly.

6.8 Re-stroking of the Jacks

As discussed earlier in Section 6.4, the hydraulic jack stroke is about 6.1 in. so jack re-stroking was necessary to provide larger vertical displacements of the test specimen. After re-stroking, the jacks can continue to be used to load the test specimen. Figure 6.13 shows instructions for jack re-stroking.

To re-stroke the jacks, Nut B on the main rod above Plate B is snugged to hold the loading fixture and test specimen in place. Then Nut C above Plate C is loosened to take the jack out of contact with Plate C. The jack is completely retracted in the next step. Then, Nut C is snugged again to put the jack in contact. Finally, Nut B is loosened and Nut C carries the force. Figure 6.15 (a) to (d) shows the different stages in the jack re-stroking process.

The total loading rod assembly retraction (‘vertical displacement of jacks”) was calculated based on FE Model-D3 analysis and the loading fixture kinematics (discussed in 3.4). Three jack re-stroking operations were included in the initial loading plan for the inelastic test. Figure 6.14 show the corresponding load steps for jack re-stroking. The total loading rod assembly retraction and jack stroke position after each re-stroking is presented in Table 6.6. Note that re-stroking is not required for the jacks in the south loading rod assemblies.

Table 6.1 Initial elastic test loading plan

Test stage	Planned load step	Increment force (kip)				Total applied force (kip)	Vertical displacement (in.)	
		Target	Mid span south rod	Mid span north rod	Average for all rods		G1 mid span	G2 mid span
Elastic loading	1	1.5	1.5	1.5	1.5	21	0.24	0.56
	2	1.5	1.5	1.5	1.5	42	0.35	1.13
	3	1.5	1.5	1.5	1.5	63	0.72	1.70
	4	1.5	1.5	1.5	1.5	84	0.96	2.27
	5	1.5	1.5	1.5	1.5	105	1.20	2.85
	6	1.15	1.15	1.15	1.15	121.1	1.38	3.30
Unloading	6U	-1.15	-1.15	-1.15	-1.15	105	1.20	2.85
	5U	-1.5	-1.5	-1.5	-1.5	84	0.96	2.27
	4U	-1.5	-1.5	-1.5	-1.5	63	0.72	1.70
	3U	-1.5	-1.5	-1.5	-1.5	42	0.35	1.13
	2U	-1.5	-1.5	-1.5	-1.5	21	0.24	0.56
	1U	-1.5	-1.5	-1.5	-1.5	0	0.00	0.00

Table 6.2 Actual elastic test loading plan

Test stage	Actual load step	Increment force (kip)				Total applied force (kip)	Vertical displacement (in.)	
		Target	Mid span south rod	Mid span north rod	Average for all rods		G1 mid span	G2 mid span
Elastic loading	1	1.5	1.41	1.42	1.07	15.0	0.17	0.47
	2	1.5	1.49	1.48	1.30	33.3	0.39	0.99
	3	1.5	1.47	1.49	1.47	53.9	0.64	1.58
	4	1.5	1.48	1.47	1.42	73.9	0.88	2.17
	5	1.5	1.49	1.53	1.40	93.5	1.12	2.77
	6	1.15	1.4	1.35	1.33	112.0	1.35	3.34
Unloading	6U	-1.15	-1.38	-1.42	-1.02	97.8	1.19	2.90
	5U	-1.5	-1.46	-1.37	-1.36	78.8	0.96	2.33
	4U	-1.5	-1.52	-1.52	-1.40	59.2	0.73	1.76
	3U	-1.5	-1.47	-1.5	-1.40	39.6	0.50	1.19
	2U	-1.5	-1.48	-1.5	-1.42	19.8	0.26	0.60
	1U	-1.5	-1.38	-1.38	-1.41	0.0	0.01	0.03

Table 6.3 Initial inelastic test loading plan

Phase	Planned load step	Increment force (kip)				Total applied force (kip)	Target String Pot retraction (in.)		Vertical displacement (in.)	
		Target	Mid span south rod	Mid span north rod	Average for all rods		G1A	G2A	G1A	G2A
I	1	1.5*	1.5	1.5	1.5	21			0.24	0.56
	2	1.5*	1.5	1.5	1.5	42			0.35	1.13
	3	1.5*	1.5	1.5	1.5	63			0.72	1.7
	4	1.5*	1.5	1.5	1.5	84			0.96	2.27
	5	1.5*	1.5	1.5	1.5	105			1.2	2.85
	6	1.15*	1.15	1.15	1.15	121.1			1.38	3.3
	7	1.5*	1.5	1.5	1.5	142.1			1.62	3.89
	8	1.5*	1.5	1.5	1.5	163.1			1.87	4.48**
	9	1.5*	1.5	1.5	1.5	184.1			2.12	5.11
	10	1.5*	1.5	1.5	1.5	205.1			2.42	5.94
	11	1*	1	1	1	219.1			2.7	6.77
	12	0.5*	0.5	0.5	0.5	226.1			2.88	7.3
	13	0.5*	0.5	0.5	0.5	233.1			3.08	7.93**
II	14					239.1	3.25*		3.28	8.57
	15					243.7	3.43*		3.48	9.22
	16					247.4	3.61*		3.68	9.87**
III	17					250.3	3.8*	10.44*	3.88	10.52
	18					250.8	3.85*	10.64*	3.94	10.73
	19					217.6	4.45*	13.24*	4.66	13.45

*	Measurement for control
**	Jack re-stroking
Phase I	Force control
Phase II	Mixed control
Phase III	Displacement control

Table 6.4 Actual inelastic test loading plan

Phase	Actual load step	Increment force (kips)				Total applied force (kips)	Target String Pot retraction (in)		Vertical displacement (in)	
		Target	Mid span south rod	Mid span north rod	Average for all rods		G1A	G2A	G1A	G2A
I	1	1.5^{*}	1.44	1.44	1.1	15.0			0.18	0.50
	2	1.5^{*}	1.52	1.51	1.40	34.6			0.42	1.04
	3	1.5^{*}	1.43	1.44	1.49	55.4			0.66	1.63
	4	1.5^{*}	1.49	1.50	1.44	75.5			0.91	2.21
	5	1.5^{*}	1.49	1.49	1.44	95.6			1.16	2.80
	6	1.5^{*}	1.40	1.39	1.35	114.6			1.39	3.36
	7	1.5^{*}	1.48	1.49	1.44	134.8			1.67	4.07^{**}
	8	1.5^{*}	1.50	1.50	1.37	154.0			1.95	4.79
	9	1.5^{*}	1.48	1.48	1.44	174.1			2.26	5.60
	10	1.5^{*}	1.52	1.52	1.47	194.8			2.64	6.69
	11	1^{*}	0.99	1.00	0.95	208.1			2.90	7.45^{**}
II	12					214.7	3.10^{*}		3.09	8.05
	13					222.7	3.31^{*}		3.31	8.78
	14					225.3	3.51^{*}		3.53	9.64
	15					212.1	3.66^{*}		3.66	10.57^{**}
	16					193.6	3.90^{*}		3.93	11.84
	17					155.4	4.39^{*}		4.47	14.91

*	Measurement for control
**	Jack re-stroking
Phase I	Force control
Phase II	Mixed control
Phase III	Displacement control

Table 6.5 Reaction force at bearings during loading fixture assembly

Loading condition	Reaction force (kip)				
	G1E	G1W	G2E	G2W	Total
Self-weight (0-S)	1.52	1.55	8.29	8.53	19.89
After addition of the loading beams	1.92	2.11	10.60	10.65	25.28
After addition of main loading rods and load transfer channels *	2.63	2.70	12.98	12.67	30.98
Final dead load condition (0-F) **					33.39

* Loading rod assemblies are not fully assembled at this point

** Weight of complete loading rod assemblies are calculated from the geometry of the parts and are added to previous data

Table 6.6 Loading rod assembly retraction and jack re-stroke plan

North loading rod assembly	Re-stroke 1 after step 8		Re-stroke 2 after step 13		Re-stroke 3 after step 16	
	Jack stroke (in.)	Total assembly retraction (in.)	Jack stroke (in.)	Total assembly retraction (in.)	Jack stroke (in.)	Total assembly retraction (in.)
A	5.07	5.07	4.03	9.09	1.58	10.68
BE	4.75	4.75	3.75	8.49	1.47	9.96
BW	4.75	4.75	3.77	8.51	1.49	10.00
CE	3.77	3.77	2.83	6.60	1.09	7.69
CW	3.77	3.77	2.85	6.62	0.59	7.21
DE	2.21	2.21	3.82	3.82	0.59	4.41
DW	2.14	2.14	3.69	3.69	0.58	4.28

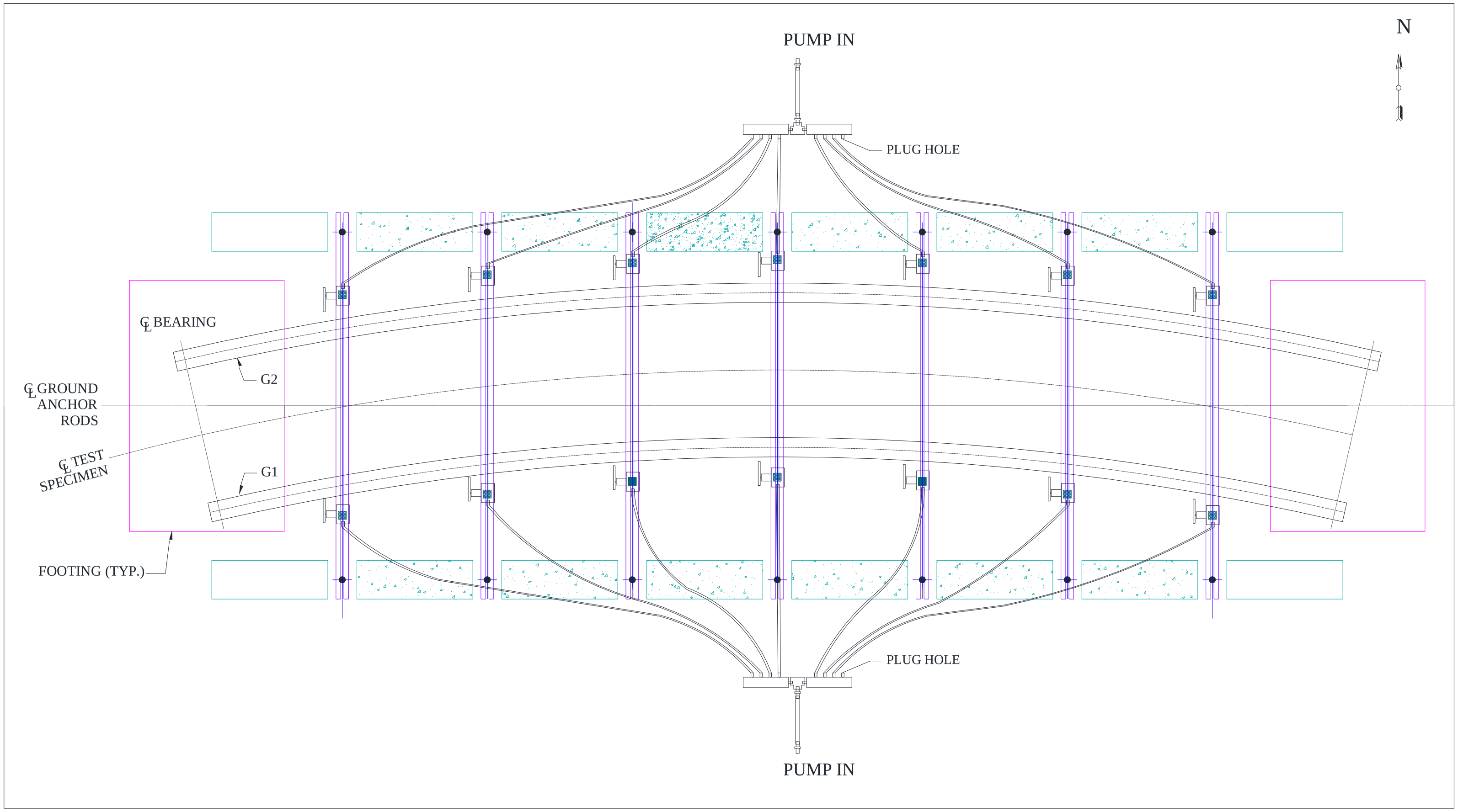

Figure 6.1 Hydraulic system plan

(a) ENERPAC ZE3 hydraulic electric pump

(b) Eagle Pro Tools ESH-306 (c) Enerpac RCH-326

Figure 6.2 Hydraulic equipment

(a) DAQ monitoring desk

(b) Control equipment desk

Figure 6.3 Control and DAQ monitoring equipment in vans

(a) Protective metal box

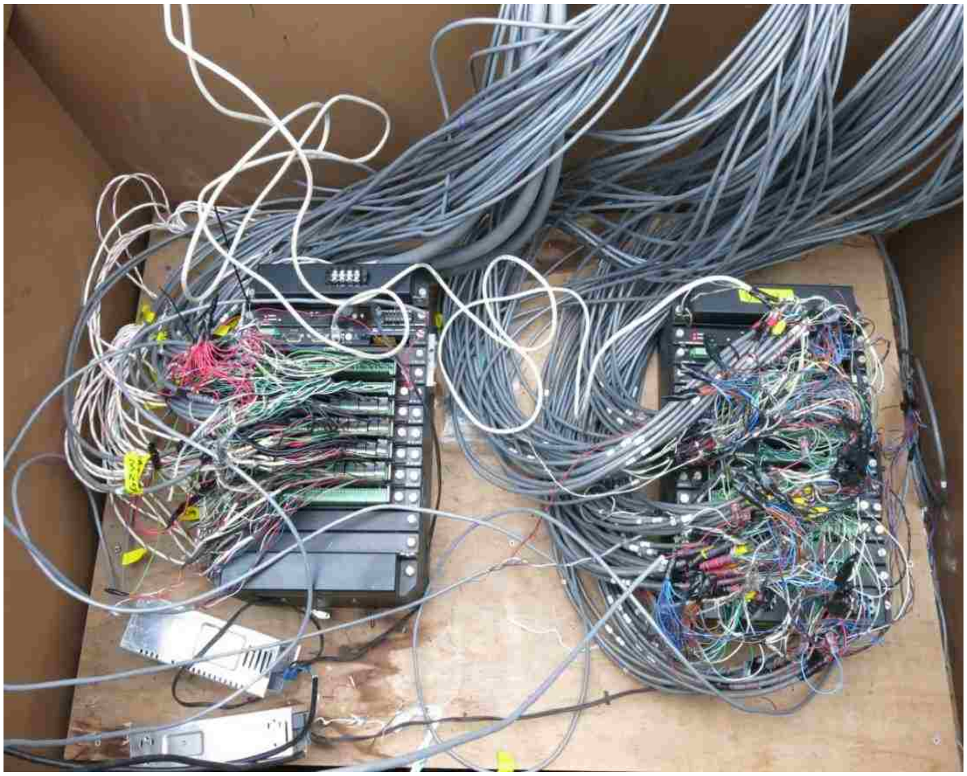

(b) DAQ wiring inside protective metal box

Figure 6.4 Data acquisition system equipment

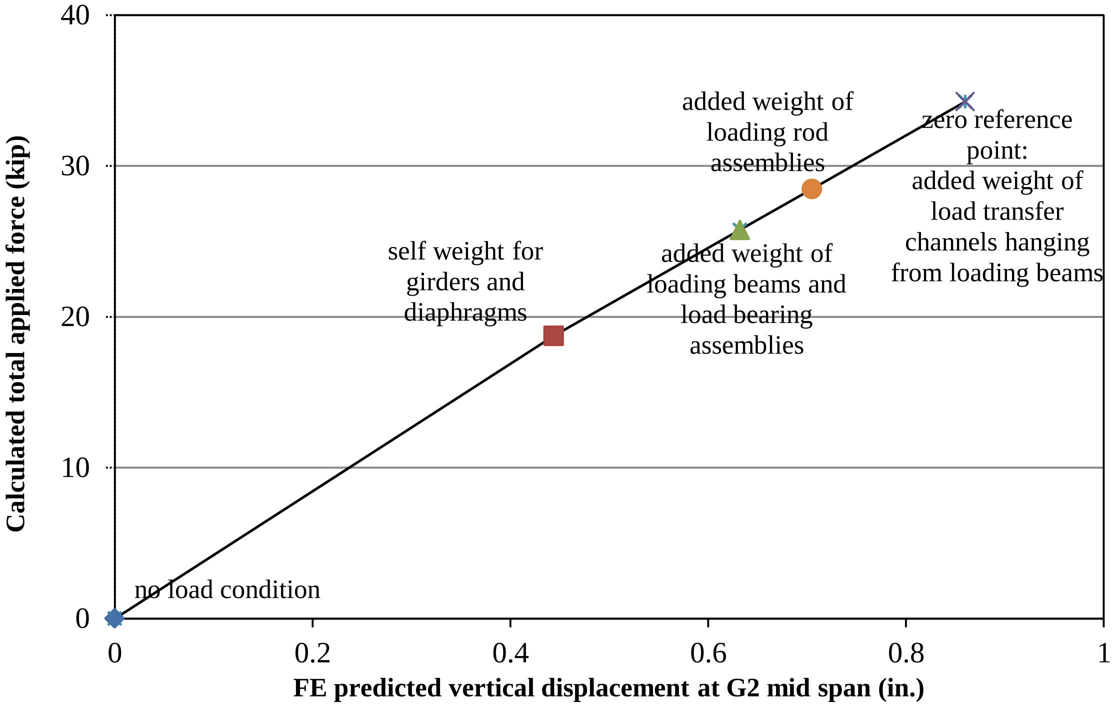

Figure 6.5 Established zero reference point to modify all DAQ readings

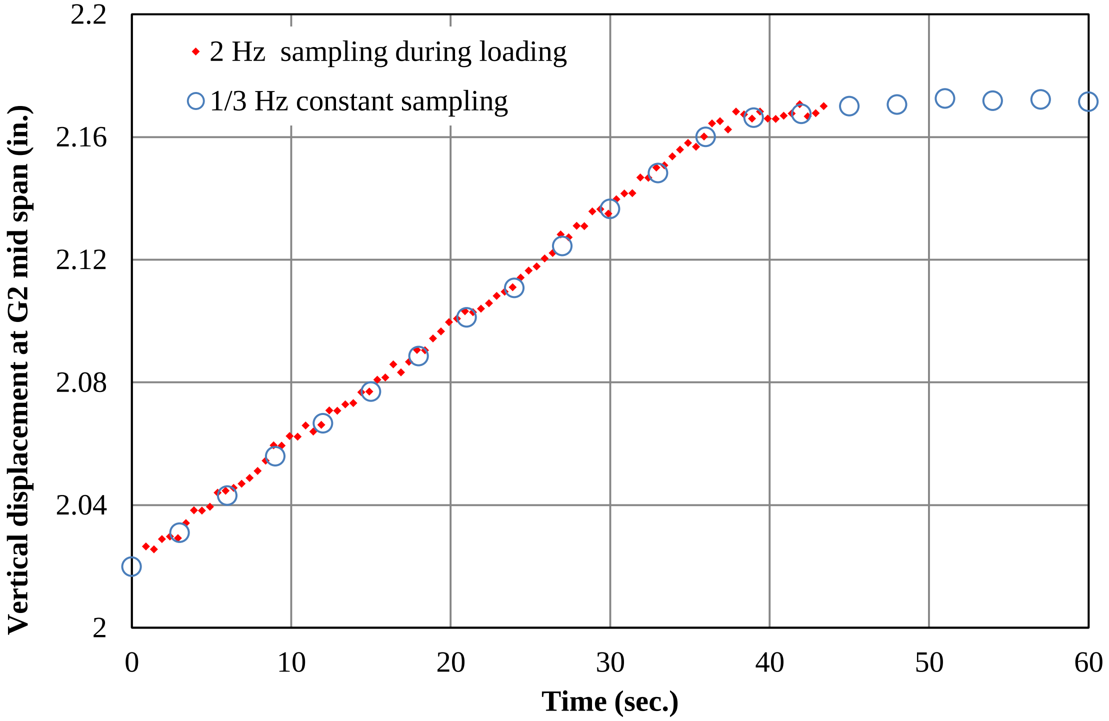

Figure 6.6 “2 Hz” costume sampling during loading and “1/3 Hz” constant sampling results in the elastic test

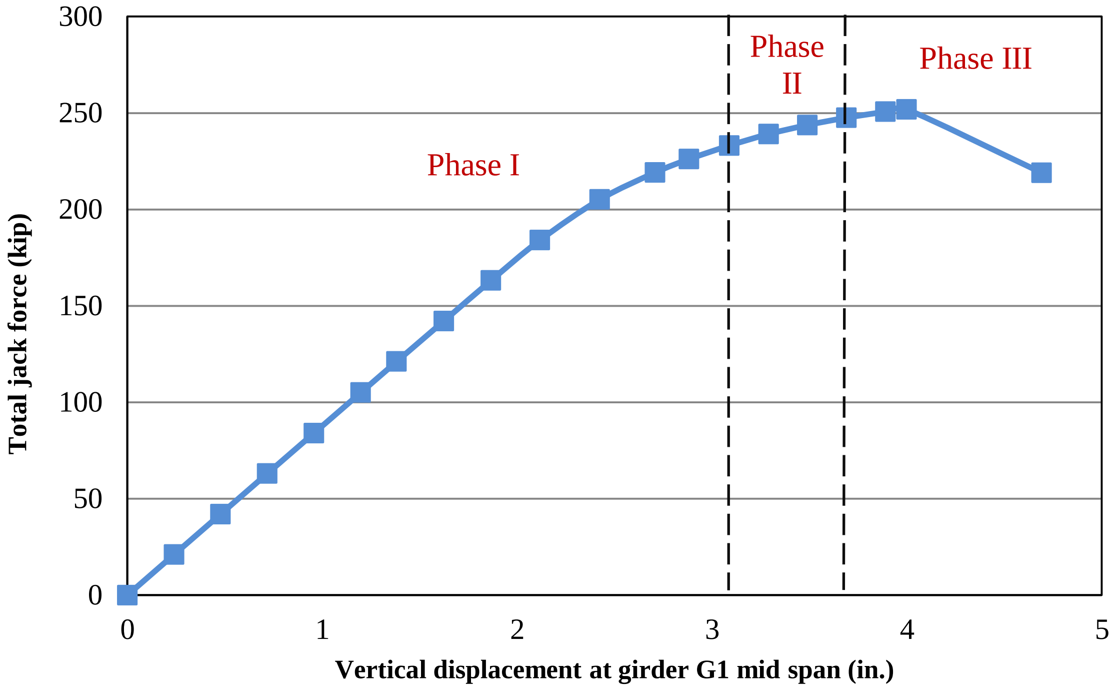

(a) Initial control plan with respect to vertical displacement at girder G1 mid span

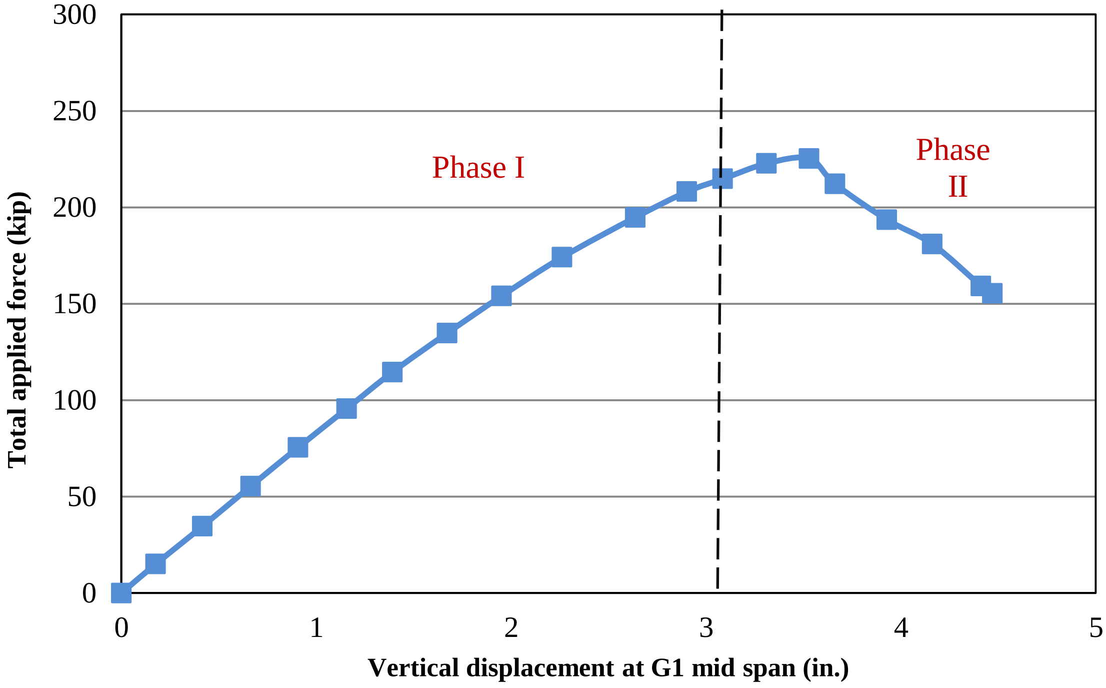

(b) Actual control plan with respect to vertical displacement at G1 mid span

Figure 6.7 Three phases of control plan for inelastic test

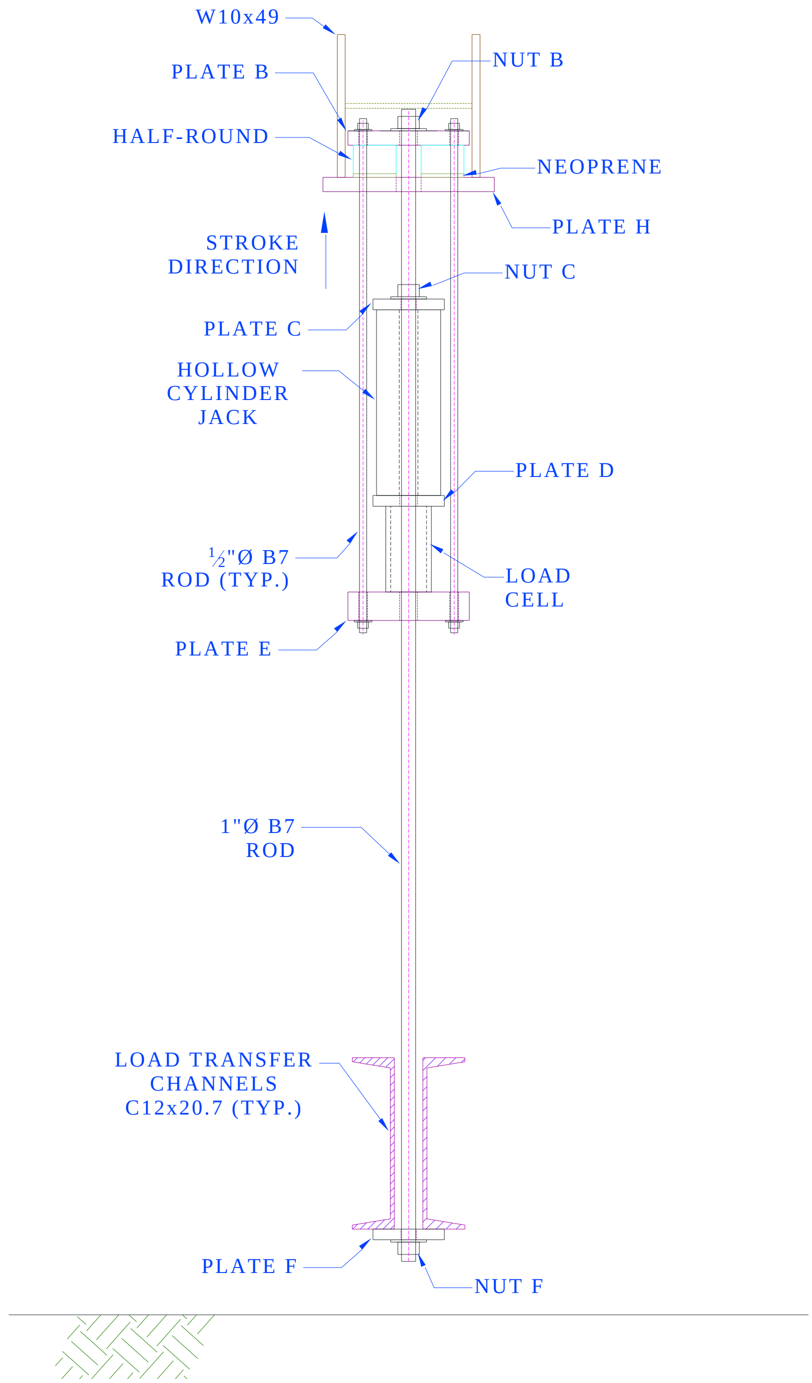

Figure 6.8 Longitudinal view of loading rod assembly

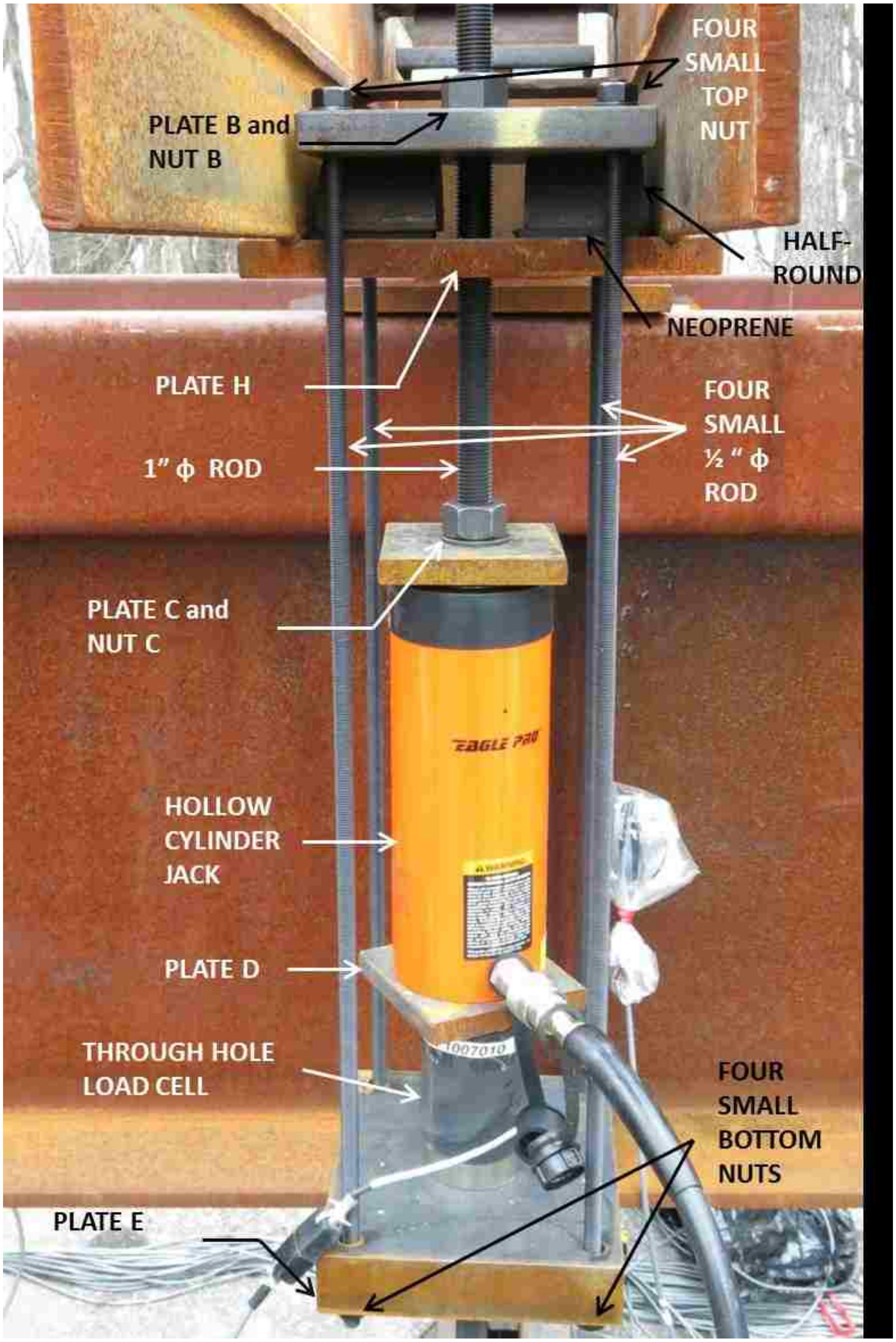

Figure 6.9 Photograph of upper part of loading rod assembly

(a) Snug four small top nuts and loosen Nut B

(b) Snug Nut C

(c) Snug four small bottom nuts

Figure 6.10 Nut condition during loading stages of test

Pretesting Procedure	
P-1	Make sure **Nut C** is 1 to 2 in. from the **Plate C**
P-2	Apply 1.0 kip on each jack to check the jack is working
P-3	Retract the jacks
P-4	Make **Nut C** snug to **Plate C**
P-5	Put data acquisition system in recording mode

Figure 6.11 Pretesting procedure

Figure 6.12 Nut C position during pretesting

Jack Re-stroking Procedure	
R-1	Make **Nut B** snug
R-2	Loosen **Nut C**
R-3	Retract the jacks
R-4	Make **Nut C** snug at **Plate C** and loosen **Nut B**;
R-5	Check and continue

Figure 6.13 Jack re-stroking procedure

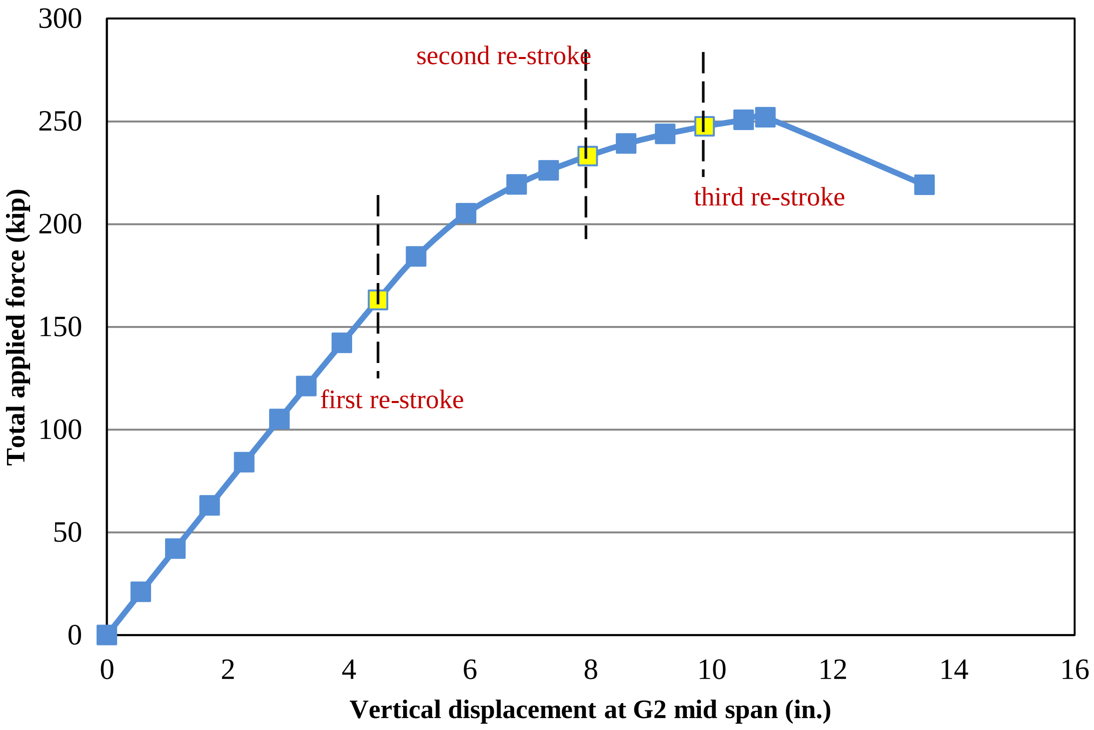

Figure 6.14 Initial re-stroking plan shown with respect to G2 mid span vertical displacement

(a) Jack stroke before re-stroking (b) Nut B is snugged and nut C is loosened

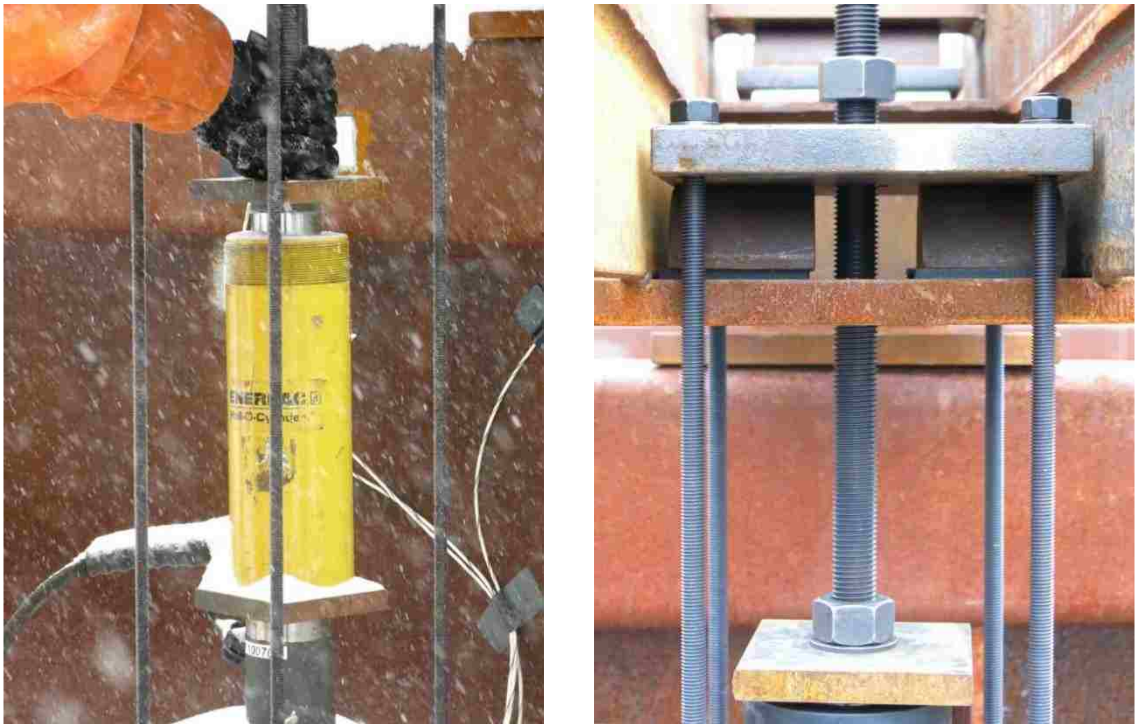

(c) Retracting jack (d) Position of Nut C and B after re-stroking

Figure 6.15 Position of jack stroke, nuts and plates during jack re-stroking process

7 TEST RESULTS

7.1 Introduction

In this chapter, the results from the elastic and inelastic tests are presented and discussed. Section 7.2 briefly presents results from the first elastic cycles. Section 7.3 is an overview of the inelastic test results. Section 7.4 presents the measured applied force from hydraulic jacks and the force transferred to the girders through the loading beams. Section 7.5 presents reaction forces at four end bearing assemblies and compares them with applied forces. Vertical and parallel components of displacement at the intermediate locations are presented in Section 7.6. Cross section rotations at the intermediate stiffeners are then presented in Section 7.7. Section 7.8 presents the primary bending moment along the span of G1 and G2, obtained from full bridge wired strain gages or individual quarter bridges. The variation of the normal strains along the width, depth, and length of the test specimen is presented in Section 7.9. Obtained shear strains and principle strains from the set of rosette strain gages are presented in Section 7.10. Finally Section 7.11 describes the inelastic test failure mode.

7.2 Elastic Test Results

As discussed in Section 6.2, three cycles of elastic testing were performed to check various transducers in the instrumentation plan, and to develop experience with the jack re-stroking process, as well as to collect data on the test specimen response in the elastic range. Figure 7.1 and Figure 7.2 show the total applied force versus vertical displacement of G1 at mid span for the first elastic test, and the second elastic test. Figure 7.3 and 7.4

show the same for the G2 mid span. The figures show that it was likely that there were residual stresses in the test specimen before the first elastic test, that were eliminated by the first elastic test loading and unloading cycle. The second elastic test shows no significant effect from residual stresses.

7.3 Overview of Inelastic Test Results

As discussed in Section 6.3, the test specimen was loaded to (and beyond) the maximum load capacity in the inelastic test. Figure 7.5 shows a photograph of the test specimen before the start of the inelastic test. A photograph of the test specimen at the final loading step of the inelastic test (load step 17) is shown in Figure 7.6. Vertical deflection and cross section rotation are noticeable in the figure 7.6.

A zero reference point for the inelastic test was established just before the inelastic test was started. The initial load at the start of the tests is called the “total dead load” on the test specimen. Actual load steps 1 to 6 represent loading in the elastic range, the maximum load capacity of the test specimen is reached in actual load step 14, and actual load step 17 is the final post peak load step.

7.4 Applied Forces from Hydraulic Jacks

As discussed in Section 6.4, due to friction in the hydraulic jacks and the different lengths of the hoses in the hydraulic system, the force provided by the jacks was not uniform (i.e., not the same for all jacks). Each hydraulic jack force was recorded by the applied force through-hole load cell in each loading rod assembly (see Section 5.4). Table

7.1 presents the measured force in each loading rod assembly. The orientation of each loading rod assembly in the parallel and longitudinal planes was measured by rotation transducers (see Section 5.3). Table 7.2 presents the loading rod assembly orientations and the corresponding force components at a post peak load step (i.e., at actual load step 17, beyond the point of maximum load capacity).

Each loading beam was treated as a rigid body and its rotation was recorded to perform the required statics calculations to determine the reaction forces between the loading beam and load bearing assemblies on G1 and G2. The loading beam was treated as simply supported beam where the half-rounds of the load bearing assemblies are the supports and the tops of the half-rounds of the loading rod assemblies are the locations where the loading rod assembly forces are applied. Note that the tops of the half-rounds were used in the static calculations to prevent the need to consider concentrated applied moments and reaction moments in the calculations. Figure 7.7 (a) shows the loading beam at the initial position, and the location of the loading rod assemblies and the load bearing assemblies.

Figure 7.7 (b) shows a free-body diagram of the loading beam when it is subjected to a rotation in parallel plane. The parallel and vertical components of applied forces from the north loading rod assembly (J_N_x and J_N_y) and the south loading rod assembly (S_N_x, S_N_y) are calculated based on magnitude of the applied forces (measure by the through-hole load cells) and the orientation of the applied force (measured by the rotation transducers attached to the loading rods). The longitudinal components of the applied forces were relatively small (see Table 7.2), and were neglected in the calculations.

The forces were transformed to the local coordinate system shown in Figure 7.7 (c), which is rotated from the global coordinate system by the loading beam rotation (measured by the loading beam rotation transducers during the tests). The loading beam is determinate in the Y direction, but is indeterminate in the X direction. The Y direction component and X direction component of the reaction force are the normal force and the frictional force between Plate J and the half-round. To solve the indeterminacy problem, it was assumed that the frictional force is the same for the south and north load bearing assemblies (i.e., R_G1_X and R_G2_X are equal). This assumption was tested by varying R_G1_X or R_G2_X up to the maximum frictional force (f_{s_max}) that could be reached (based on the normal force and assumed coefficient of friction of 0.3) to investigate the possible consequences of this assumption. No significant change in the results was observed.

Finally, the reaction forces are transformed to the global coordinate system and vertical and parallel components were determined. Table 7.3 presents loading beam rotation and corresponding reaction forces at the post peak load step (actual load step 17). The forces in the table are the reactions acting on the loading beam and are positive toward the north in the parallel direction, positive toward the west in the longitudinal direction, and positive upward in the vertical direction.

The forces applied onto the top of load bearing assemblies are equal and opposite (in sign) to those in Table 7.3. Table 7.4 and Table 7.5 list these forces, applied to the top of the load bearing assemblies, for each actual load step, for G1 and G2 respectively. The forces in the Table 7.4 and 7.5 are applied to the top of load bearing assemblies and are positive toward the north in the parallel direction, positive toward the west in the longitudinal direction, and positive upward in the vertical direction.

To obtain the reaction force at the top of the girders, the height of the load bearing assemblies and the rotation of the girders should be considered (see Figure 7.7 (d)). Figure 7.7 (e) shows a free body diagram of a load bearing assembly where the reaction moment is also developed at the contact surface with the top of the girder.

7.5 Reaction Forces

As discussed in Section 5.4, one compressive load cell was placed in each bearing assembly to record the reaction force. The modified total reaction force from the four bearings is compared with total applied force (the total of the applied forces for all the jacks) in Figure 7.8. The modified total reaction force equals the total reaction force minus the weight of the test specimen and test fixtures. In Figure 7.8, the forces are plotted versus the mid span vertical displacement of G2. The difference between the two forces is, as expected, negligible which validates the force measurements. Figure 7.9 shows the distribution of reaction forces between the bearings. Note that the reaction forces are modified based on the established zero reference point for the inelastic test and do not include the total dead load.

7.6 Displacements

Table 5.1 to Table 5.3 list each transducer used to measure the test specimen displacement response with the corresponding identifier (alias). As discussed in Section

5.2, geometric calculations are required to obtain vertical and lateral displacement components at the intermediate locations. Table 7.6 presents the displacement transducer data and the calculated displacement components for G2 at the mid span target point (G2A) at different load steps during the inelastic test up to and beyond the maximum load capacity.

Figure 7.10 shows the total applied force versus vertical displacements of G1 and G2 at mid span during the inelastic test. Parallel displacements of G1 and G2 at mid span are presented in Figure 7.11. Figure 7.12 and Figure 7.13 show the displacement at the target points in parallel planes BE and BW for girder G1 and G2 in the vertical and parallel directions, respectively. Displacements in parallel planes CE and CW are shown in Figure 7.14 and Figure 7.15, and displacements in parallel planes DE and DW are shown in Figure 7.16 and Figure 7.17. The String Pot at parallel plane CW for girder G1 did not work properly and the vertical and parallel displacements are not presented in the figures for this location. The LVDTs at parallel plane CE for G1, at parallel plane DE for G2, and at parallel plane DW for G2 did not work properly and parallel displacements are not presented in the figures for these locations. Since String Pot retractions were not large for these locations, the difference between String Pot retractions and modified vertical displacements are negligible, so String Pot retractions were presented in the figures to represent vertical displacements.

Figure 7.18 and Figure 7.19 shows vertical displacements at three load steps during the inelastic test along the span of G1 and G2, respectively. In the figures, the normalized span length represents the relative distance between the west and east bearings, and 0 represents the east bearing and 1 represents the east bearing. Note that the displacements shown in the tables and figures are positive toward the north in the parallel direction, positive toward the west in the longitudinal direction, and positive upward in the vertical direction.

7.7 Cross Section Rotations

Table 5.5 listed each transducer used to measure the test specimen cross section rotation response with the corresponding identifier (alias). Section 5.3 explains that the rotation transducers are attached to the bearing and intermediate stiffeners, and provide cross section rotation in the radial planes, about the circumferential axis.

Figure 7.20 shows the cross section rotations at mid span of G1 and G2 during the inelastic test. Cross section rotations at stiffeners near planes BE and BW are shown in Figure 7.21, near planes CE and CW are shown in Figure 7.22, and near planes DE and DW are shown in Figure 7.23. Figure 7.24 and Figure 7.25 show the cross section rotation in the radial planes at three load steps in the inelastic test along the span of G1 and G2, respectively. The cross section rotation is positive for a right hand rotation along the westward circumferential axis.

7.8 Primary Bending Moments

Strain transducers arranged in full bridges were used to calculate the primary bending moment in the test specimen as discussed in Section 5.4. Also as mentioned, in Section 5.4, the primary bending moment can be calculated from uniaxial strain gages not wired into a full bridge. Since there is no force applied to G1 between parallel planes BW and A (as well as BE and A), the moment diagram is linear between BW and A. The primary bending moment was calculated from strain gages located between parallel planes BW and A (at Sections KW, JW, and JM as defined in Section 5.4), and least squares fit line was passed through these primary bending moment values as shown in Figure 7.26 for actual load step 6. This line was extrapolated to estimate the primary bending moment of G1 at mid span. The primary bending moment at mid span of G2 was obtained by static calculations, considering the applied forces, the reaction forces and estimated moment at mid span of G1. Note that the primary bending moment was obtained at Section KWE from a full bridge, at Section JW from four single strain gages, and at Section JM from two single strain gages and the expected location of the neutral axis. Also, note that the region near mid span of G1 remains elastic during the inelastic test. From the estimated moment at mid span of G1, the primary bending moment at mid span of G2 was obtained by static calculations, considering the applied forces, and the reaction forces.

In Figure 7.27, the modified primary bending moment carried by each girder, and the sum of the modified primary bending moments carried by both girders are plotted versus total applied force. Figure 7.28 and Figure 7.29 show the FE results and test data for the primary bending moment diagram along the spans of G1 and G2, respectively. The primary bending moment from the FE analysis (Ma, 2014) was obtained by integrating the stresses at two sections between two consecutive parallel planes. Then, linear extrapolation was used to find the primary bending moment at the two corresponding parallel plane sections. The bending moment within the small length between the interior diaphragms (on radial planes R-CE and R-CW) and the location of the applied load in parallel planes CE and CW is not included in the figures (see Section 2.6).

Figure 7.28 and Figure 7.29 include test data for the moment diagram for actual load step 6. For G1 (Figure 7.29) the test data is shown for the full bridge locations and where the primary bending moment could be determined from individual strain gages. For G2 (Figure 7.29), the test data is shown for a few locations between Section A and Section BW (obtained from individual strain gages) and west of Section DW and east of Section DE (obtained from full bridges). The FE results for G2 are very close to the test data. The FE results for G1 are approximately 15% larger than the test data over the entire span. Near the mid span, the difference in bending moment for G1 and G2 is approximately 400 kip-in and 200kip-in. However, the bending moment carried by G2 is much larger than G1 and the difference in bending moment is less than 3% for G2.

7.9 Normal Strains

Uniaxial strain gages were installed across the width and depth of the cross section to measure the normal strain due to the primary bending moment and lateral bending moment. Figure 7.30 is a cross section view of section FM of G2 which shows the installed strain gages. Figure 7.31 to Figure 7.37 shows the normal strains at various locations across the width and depth of G2 at cross section FM (Section 8.4.2) during the inelastic test. In all figures, positive normal strain means tension and negative normal strain means compression. Note that the steel yield strain is approximately 2000 micro-strain for tubes and approximately 1800 micro-strain for the webs and flange plates, based on tensile coupon tests. The figures indicate that top tube is almost fully yielded at section FM, however the web bottom and bottom flange are not yielded and the section was not fully plastic at failure. Note that due to top flange lateral bending, the inside tube web did not yielded, as shown in Figure 7.2.3.

Figure 7.38 shows normal strains near mid span of G1 (Section JM) at the tube wall and top of the tube. The strain results indicates that the strains in girder G1 is always less than the yield strain and G1 remained in the elastic range during the inelastic range. Figure 7.39 shows the normal strain from strain gages arranged (but not wired) in a full bridge at Section JE during the inelastic test.

Normal strain results at the G2 tube outside wall between Section BW and BE are shown in Figure 7.40. Figure 7.41 shows normal strain results for the tube inside wall at same region. The strain gages at the outside and inside of the tube were placed at the same depth in the cross section. Therefore, they are expected to have same level of strain from primary bending moment. On the other hand, lateral bending of the tube flange produces opposite contributions to the strain at the tube inside wall and outside wall. Figure 7.42 shows the average normal strain at the tube wall. The average strain of the tube inside wall and outside wall is close to the expected primary bending moment strain. Figure 7.43 shows the difference between normal strains at the tube outside wall and inside wall. The difference in the normal strain of the tube outside wall and inside wall is similar to the expected flange lateral bending moment strain.

7.10 Shear Strains

One set of rosette strain gages was installed on the top of the tube of G2 near mid span to measure shear strain, normal strains, and principal strains. Required calculations to obtain these strain results are discussed in Section 5.5.3. Figure 7.44 shows rosette strain gage data during the inelastic test. The calculated normal strains, shear strain, and principal strains during the inelastic test are presented in Figure 7.45, Figure 7.46 and Figure 7.47, respectively. Note that the installed rosette strain gages have limited capacity to measure large strains after yielding.

7.11 Failure Mode

Local buckling of the tubular flange of G2 occurred after the mid span section yielded. The local buckling occurred between parallel planes A and BE, at a location about 50 in. east from mid span and 3.5 in. east from the location of welded splice between tube sections made in the fabrication shop. From FE analysis (Ma, 2014), the primary bending moment is almost constant between the two adjacent parallel planes, and the lateral bending moment is expected to be almost constant near the location of the buckling. Figure 7.48 is a photograph of the local buckling in the tubular flange of G2 between parallel planes A and BE. More photographs of the buckled region are shown in Chapter 8.

Actual load step 14 is the load step when the maximum load capacity is reached. At this load step, the total applied force is 225 kip, and including the total dead load, the load capacity is 260 kip. The modified primary bending moment about the radial axis at mid span carried by G2 is 20100 kip-in. The maximum primary bending moment including the total dead load is 23200 kip-in.

[redacted]

Table 7.2 Orientation of loading rod assemblies and corresponding force components for post peak load condition (actual load step 17)

Loading fixture	Loading rod	Loading rod rotation (degree)		Jack applied force (kip)		
		Parallel plane	Longitudinal plane	Vertical	Parallel	Longitudinal
A	S	3.23	0.42	-11.20	-0.63	-0.08
	N	3.12	-1.11	-11.35	-0.62	0.22
B_E	S	4.12	0.46	-10.54	-0.76	-0.08
	N	2.68	0.00	-12.15	-0.57	0.00
B_W	S	4.69	0.02	-11.41	-0.94	0.00
	N	-2.89	-0.90	-11.22	0.57	0.18
C_E	S	1.75	-0.69	-10.32	-0.32	0.13
	N	2.27	1.84	-12.10	-0.48	-0.39
C_W	S	3.02	0.09	-9.74	-0.51	-0.01
	N	3.20	-1.63	-11.17	-0.62	0.32
D_E	S	2.39	-0.35	-11.30	-0.47	0.07
	N	2.61	2.40	-10.12	-0.46	-0.42
D_W	S	2.16	-0.51	-9.68	-0.37	0.09
	N	2.19	-1.64	-10.97	-0.42	0.31

Table 7.3 Loading beam reaction forces at actual load step 17

Loading fixture	loading beam rotation (degree)	Reaction force at G1 (kip)			Reaction force at G2 (kip)		
		Vertical	Parallel	Longitudinal	Vertical	Parallel	Longitudinal
A	6.32	10.53	0.59	0.07	12.01	0.66	0.07
B_E	6.87	9.60	0.51	-0.04	13.09	0.82	-0.04
B_W	5.24	10.91	0.74	0.09	11.73	0.76	0.09
C_E	4.70	9.52	0.28	-0.13	12.89	0.52	-0.13
C_W	3.75	9.04	0.49	0.15	11.87	0.65	0.15
D_E	2.64	11.16	0.49	-0.18	10.26	0.44	-0.18
D_W	2.24	9.07	0.35	0.20	11.59	0.44	0.20

[redacted]

[redacted]

Table 7.6 Displacement transducer data and calculated displacement components for G2 at mid span (target point G2A) during inelastic test

Load step	Extension of transducer (in.)		Transducer length (in.)		Displacement components (in.)	
	ΔL_{SP}	ΔL_{LVDT}	L_{SP}	L_{LVDT}	Δx	Δy
1	-0.50	-0.13	36.81	38.75	0.07	-0.50
2	-1.04	-0.26	36.27	38.62	0.13	-1.04
3	-1.63	-0.44	35.68	38.44	0.16	-1.63
4	-2.21	-0.62	35.10	38.26	0.18	-2.21
5	-2.80	-0.79	34.51	38.09	0.20	-2.80
6	-3.36	-0.95	33.95	37.93	0.21	-3.36
7	-4.07	-1.14	33.24	37.74	0.23	-4.07
8	-4.79	-1.31	32.52	37.57	0.27	-4.79
9	-5.60	-1.46	31.71	37.42	0.32	-5.60
10	-6.68	-1.66	30.63	37.22	0.38	-6.69
11	-7.45	-1.79	29.86	37.09	0.42	-7.45
12	-8.04	-1.86	29.27	37.02	0.46	-8.05
13	-8.77	-1.97	28.54	36.91	0.48	-8.78
14	-9.63	-2.05	27.68	36.83	0.53	-9.64
15	-10.56	-2.03	26.75	36.85	0.67	-10.57
16	-11.82	-1.81	25.49	37.07	1.01	-11.84
17	-14.85	-1.25	22.46	37.63	1.70	-14.91

[redacted]

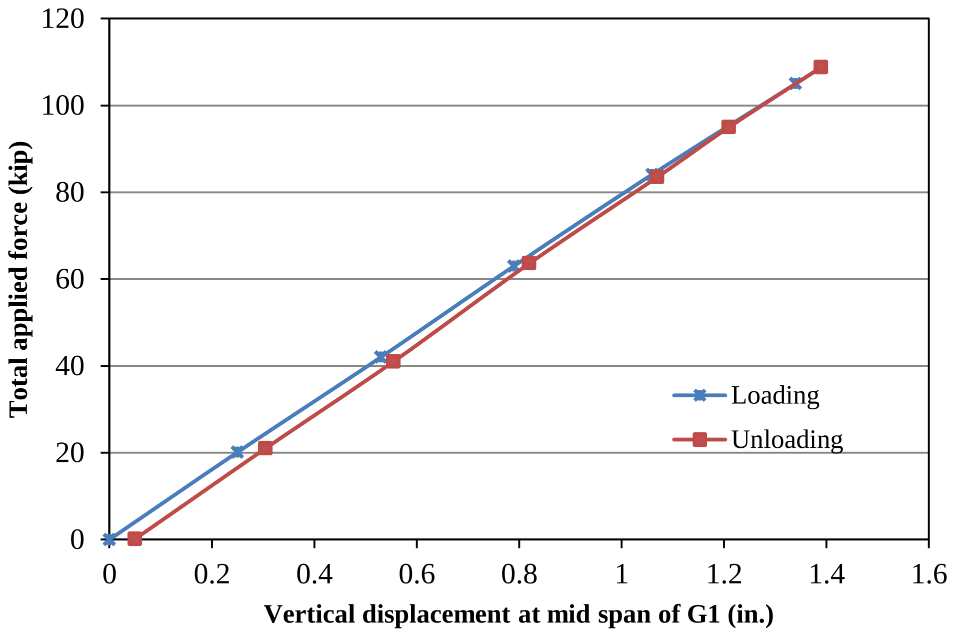

Figure 7.1 Total applied force versus vertical displacement at mid span of G1 during the first elastic test

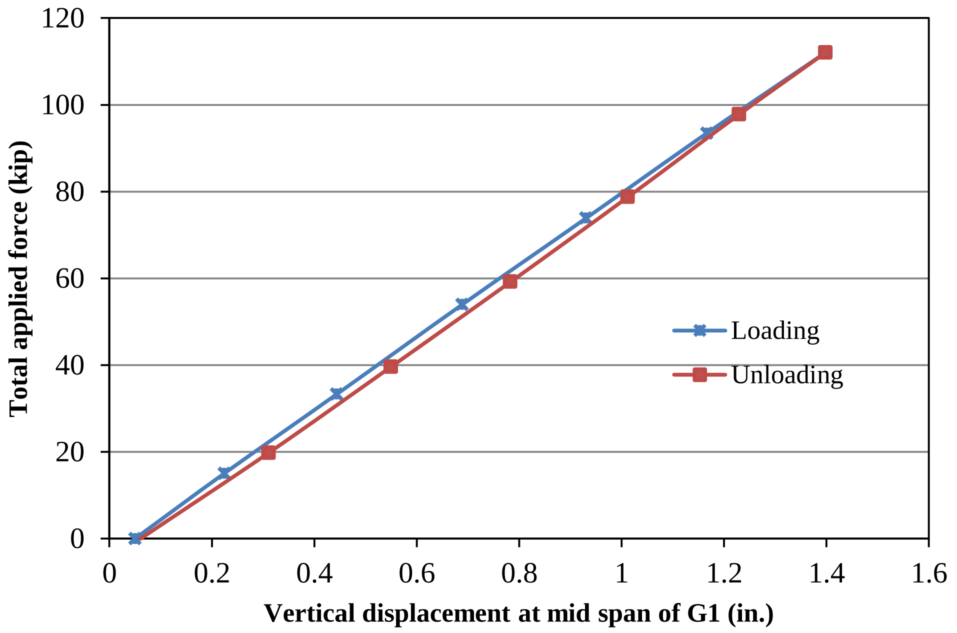

Figure 7.2 Total applied force versus vertical displacement at mid span of G1 during the second elastic test

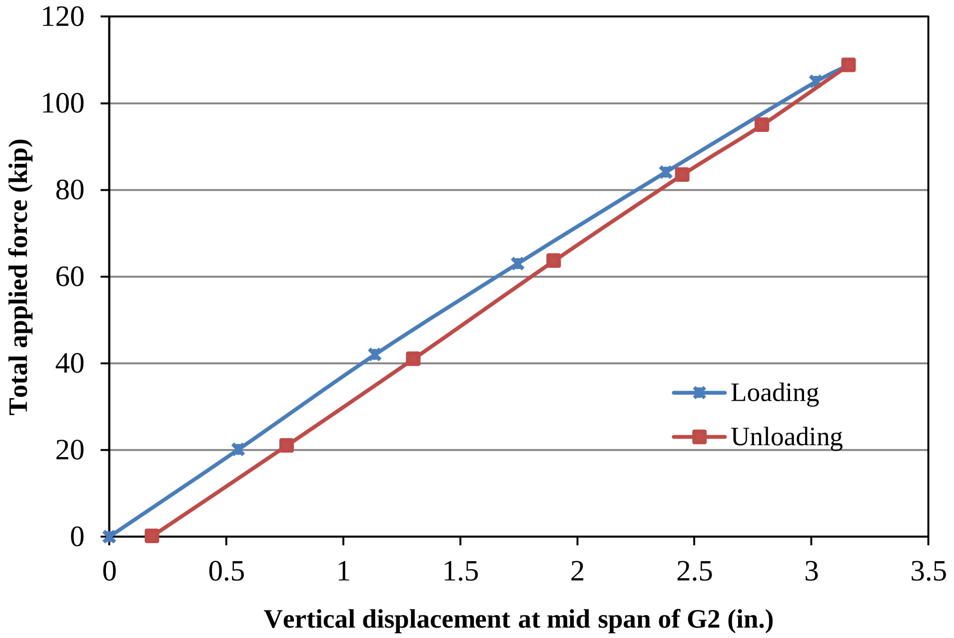

Figure 7.3 Total applied force versus vertical displacement at mid span of G2 during the first elastic test

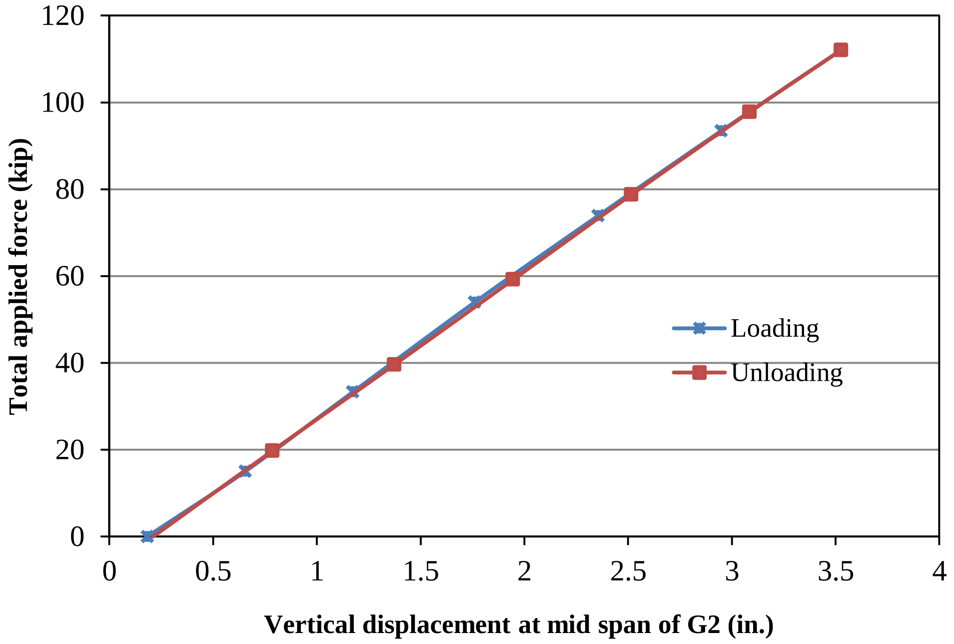

Figure 7.4 Total applied force versus vertical displacement at mid span of G2 during the second elastic test

Figure 7.5 Test specimen condition at start of the inelastic test

Figure 7.6 Test specimen condition at load step 17 of the inelastic test

(a) Loading beam at initial position

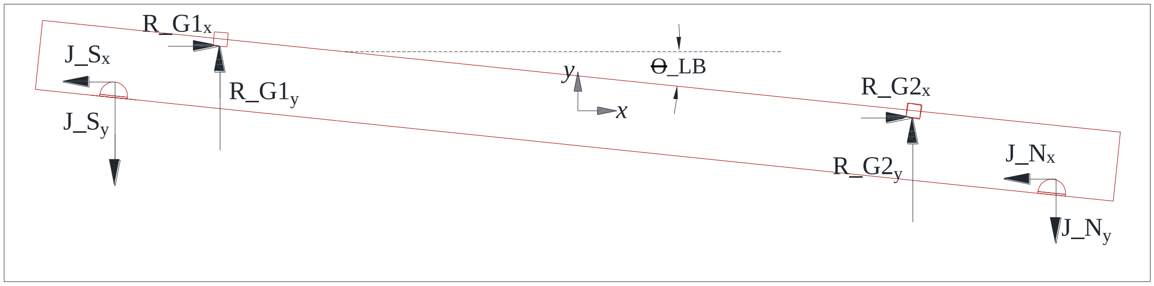

(b) Loading beam free body diagram in global coordinate system at displaced position

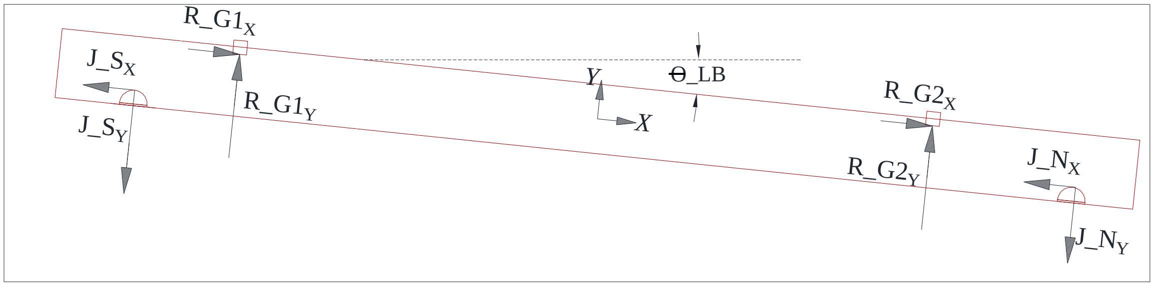

(c) Loading beam free body diagram in local coordinate system at displaced position

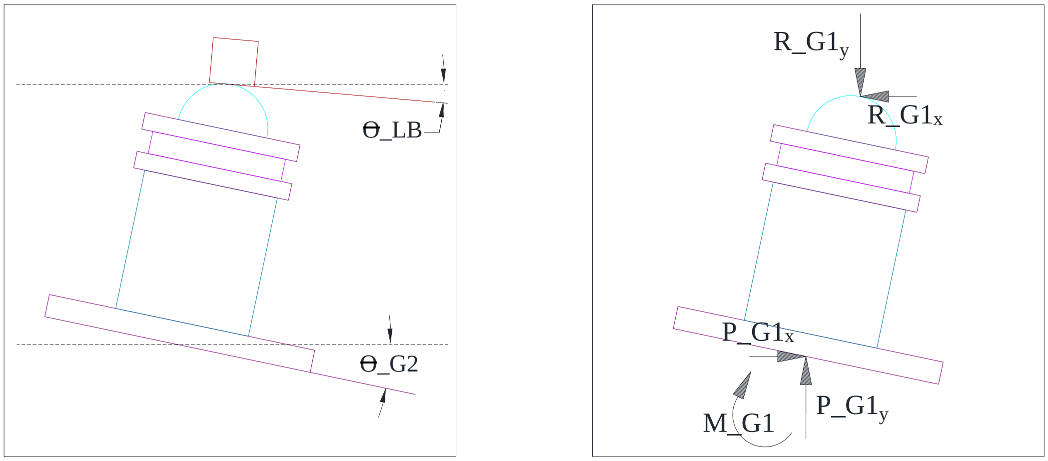

(d) Load bearing assembly at displaced position

(e) Load bearing assembly free body diagram at displaced position

Figure 7.7 Statics of loading beam showing transfer of jack forces to girders

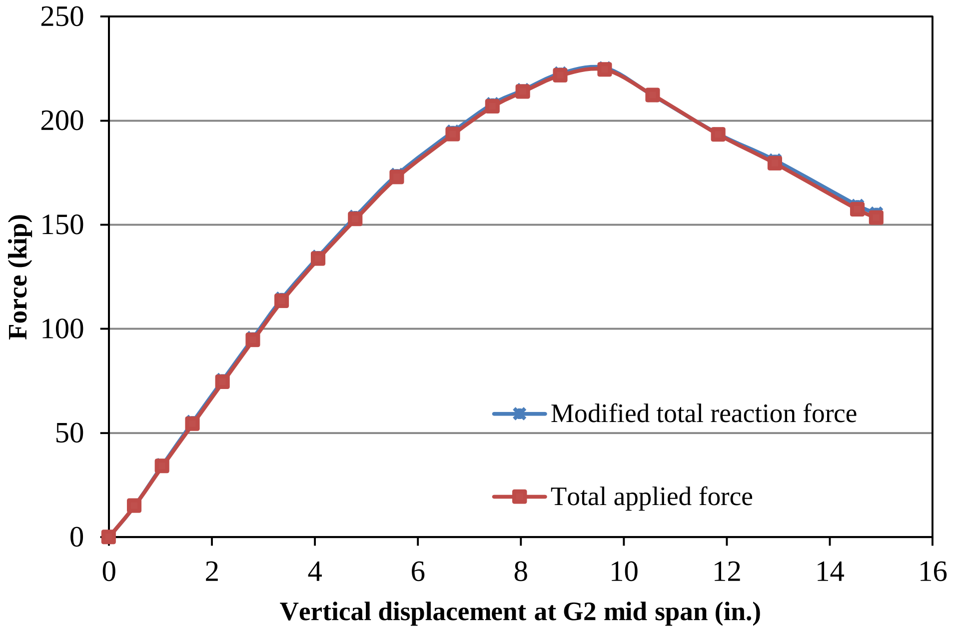

Figure 7.8 Modified total reaction force and total applied force versus vertical displacement at mid span G2 during inelastic test

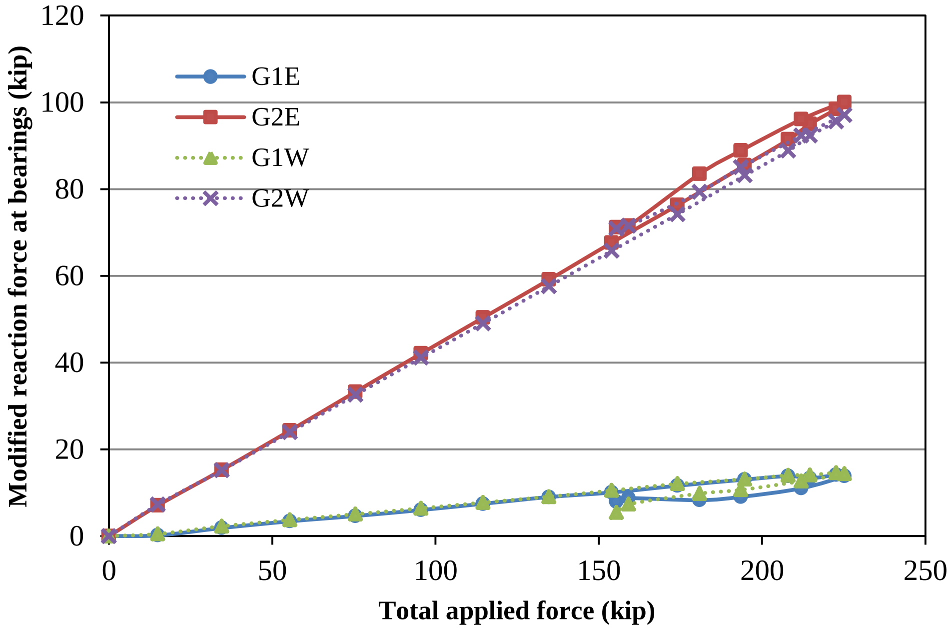

Figure 7.9 Modified reaction force at each bearing

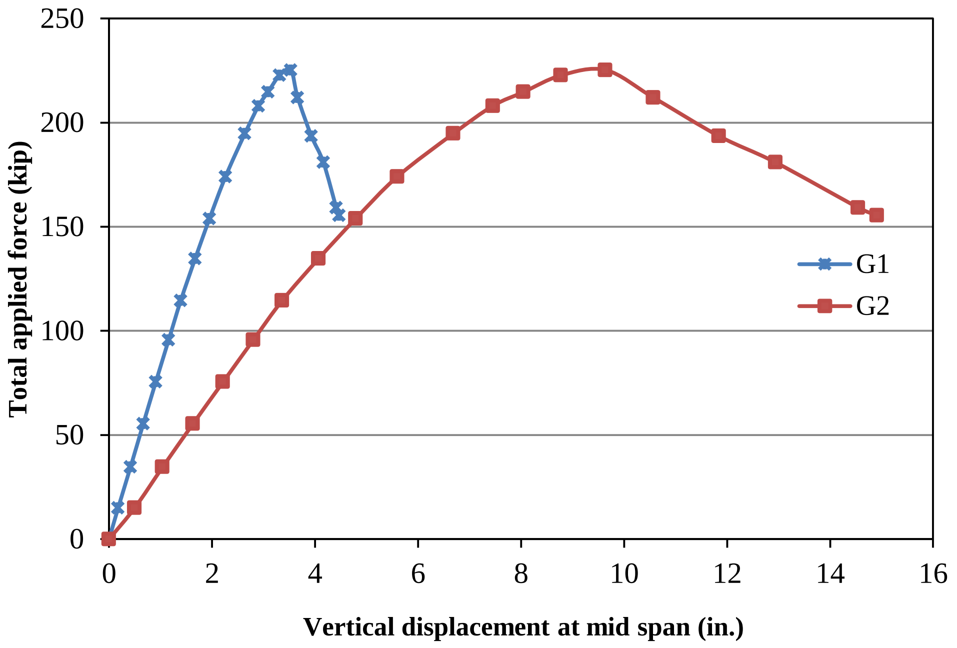

Figure 7.10 Vertical displacements at mid span of G1 and G2 during inelastic test

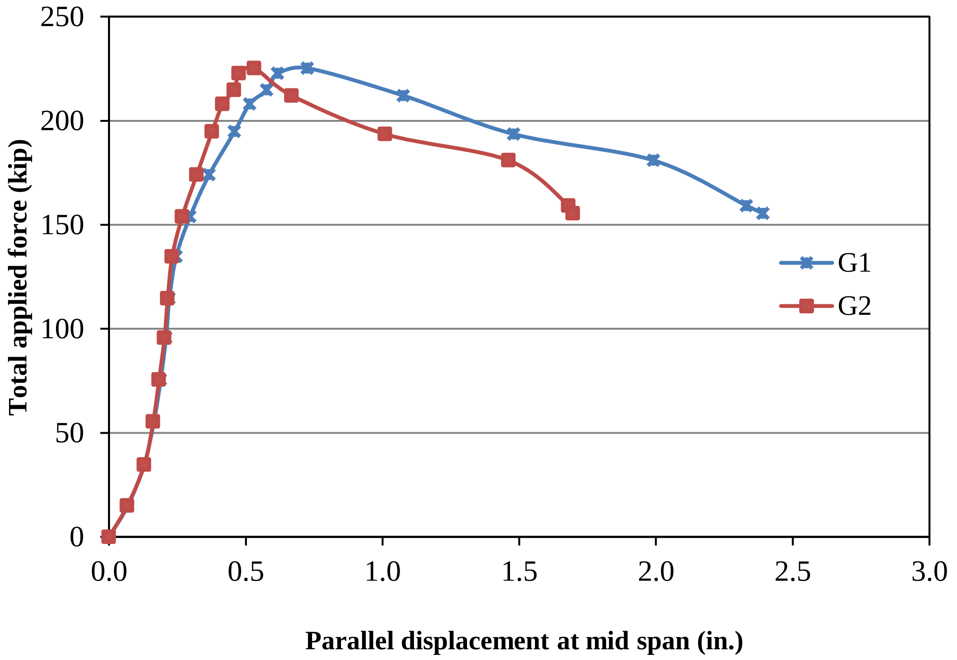

Figure 7.11 Parallel displacements at mid span of G1 and G2 during inelastic test

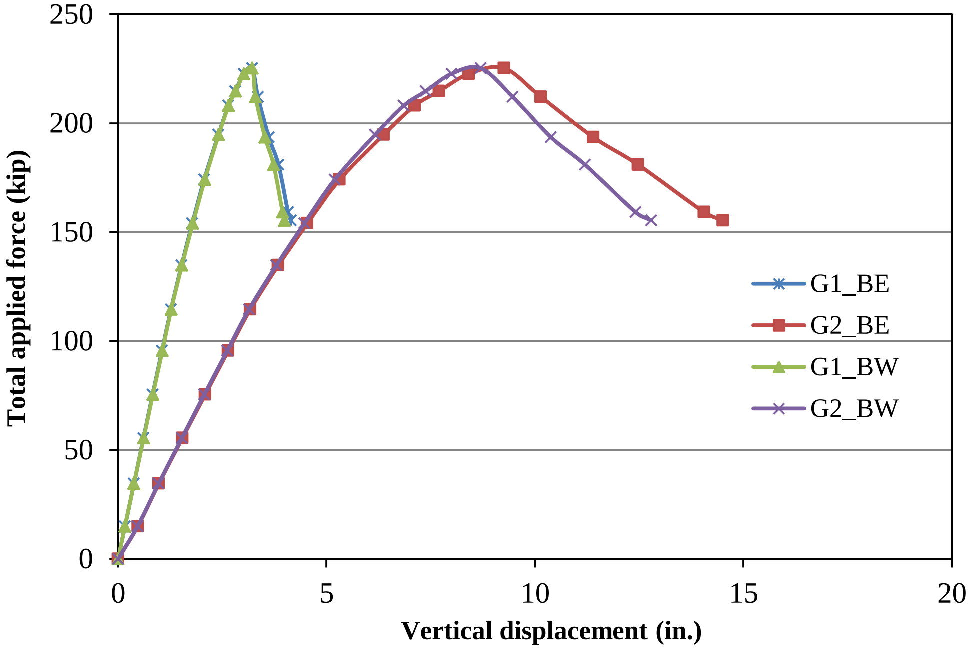

Figure 7.12 Vertical displacements in planes BE and BW during inelastic test

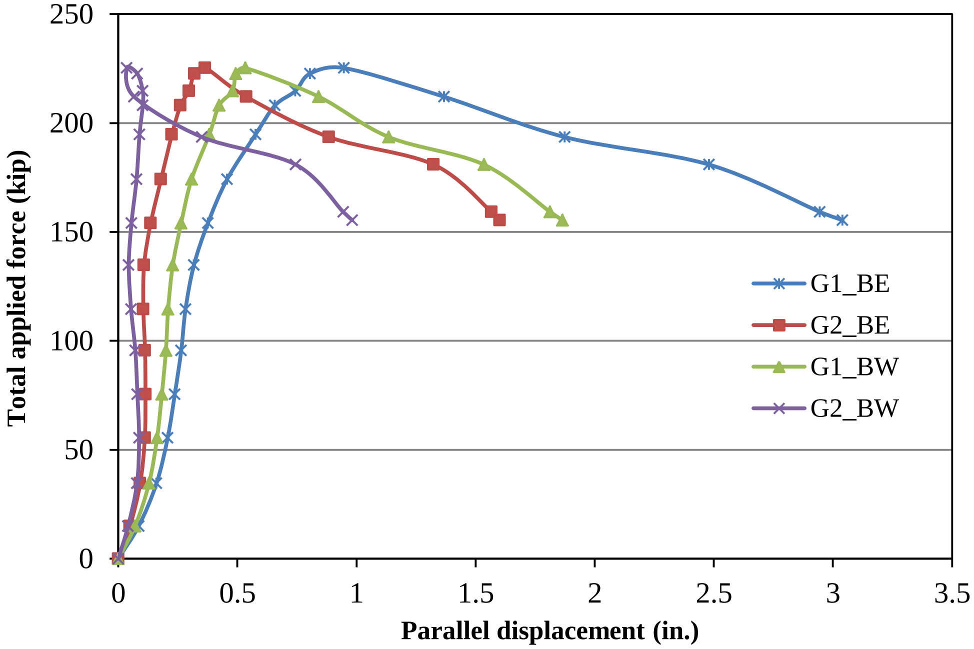

Figure 7.13 Parallel displacements in planes BE and BW during inelastic test

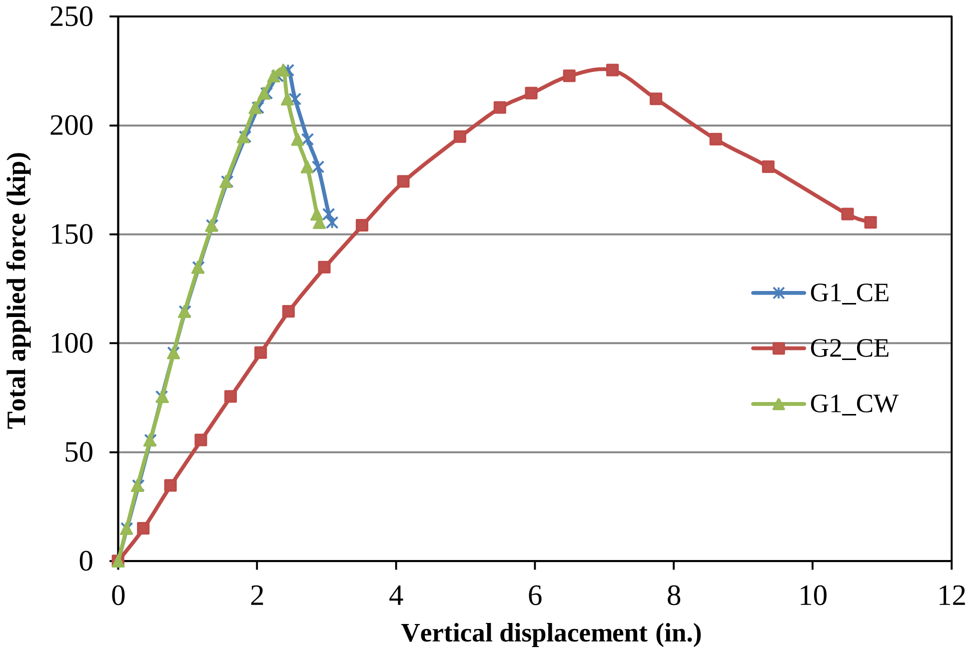

Figure 7.14 Vertical displacements in planes CE and CW during inelastic test

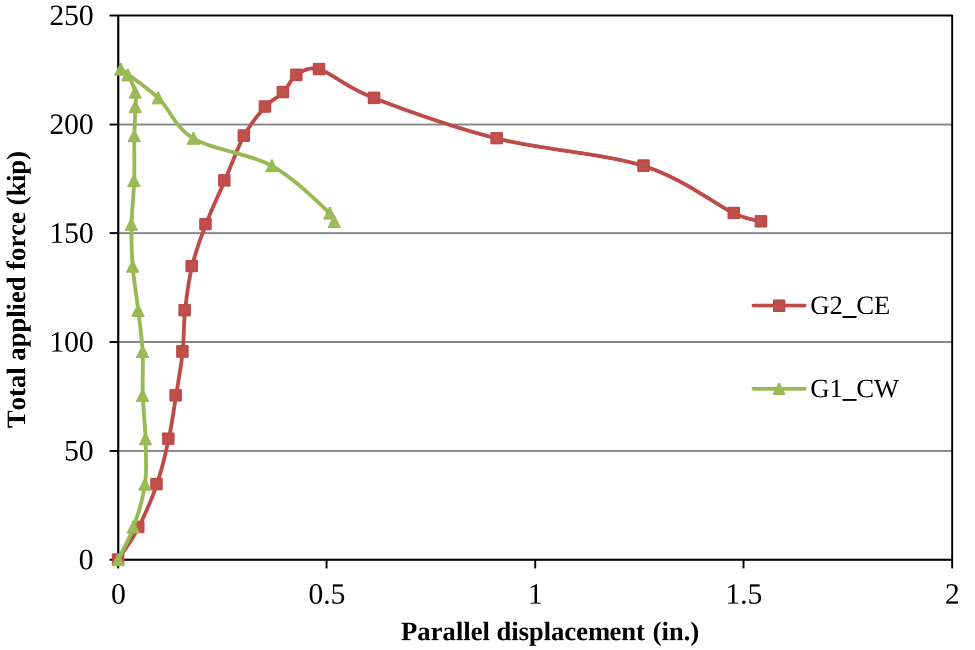

Figure 7.15 Parallel displacements in planes CE and CW during inelastic test

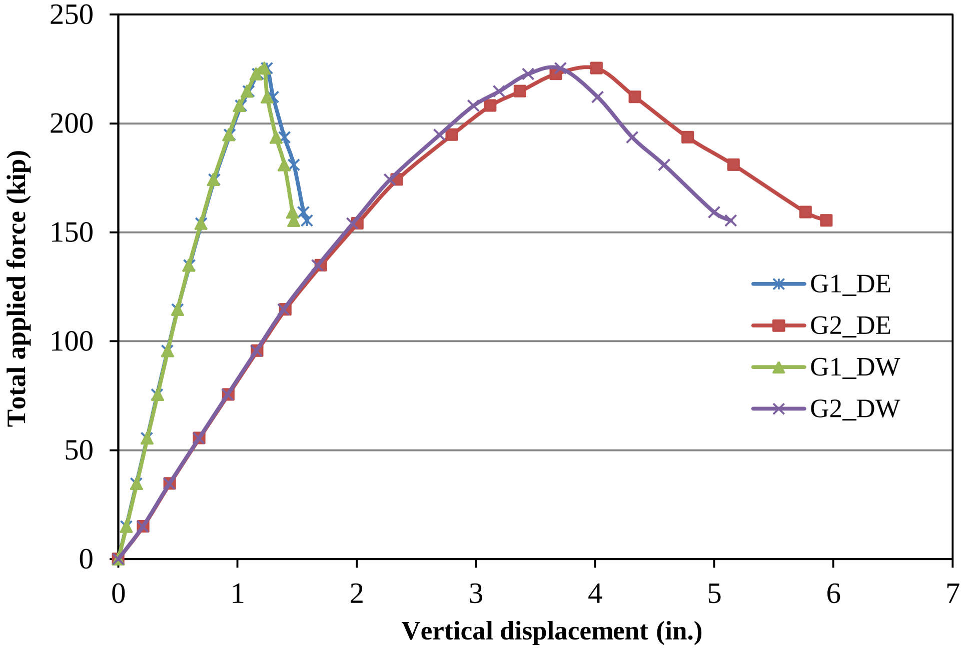

Figure 7.16 Vertical displacements in planes DE and DW during inelastic test

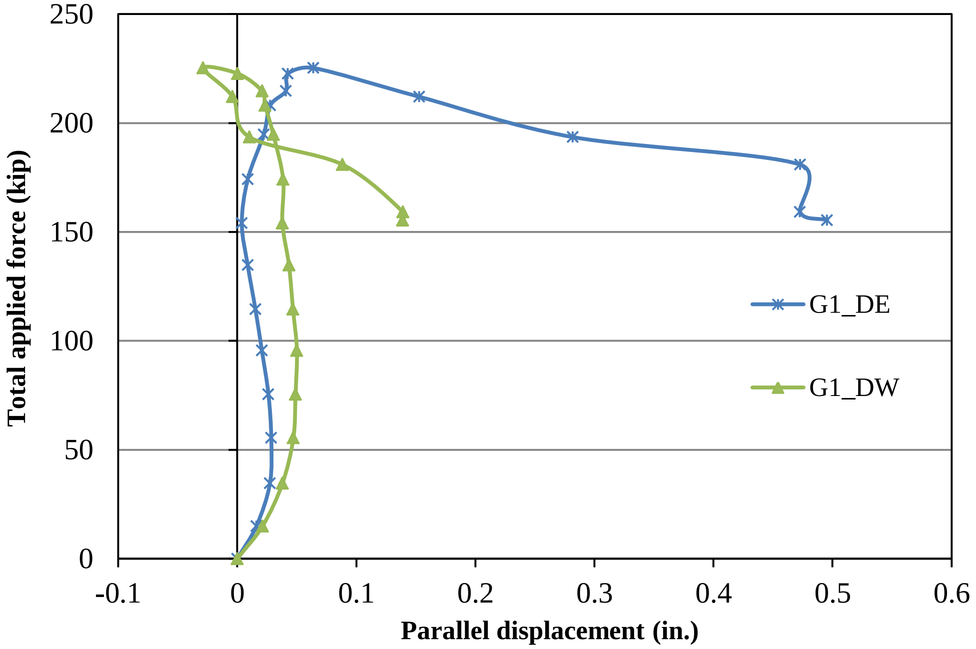

Figure 7.17 Parallel displacements in planes DE and DW during inelastic test

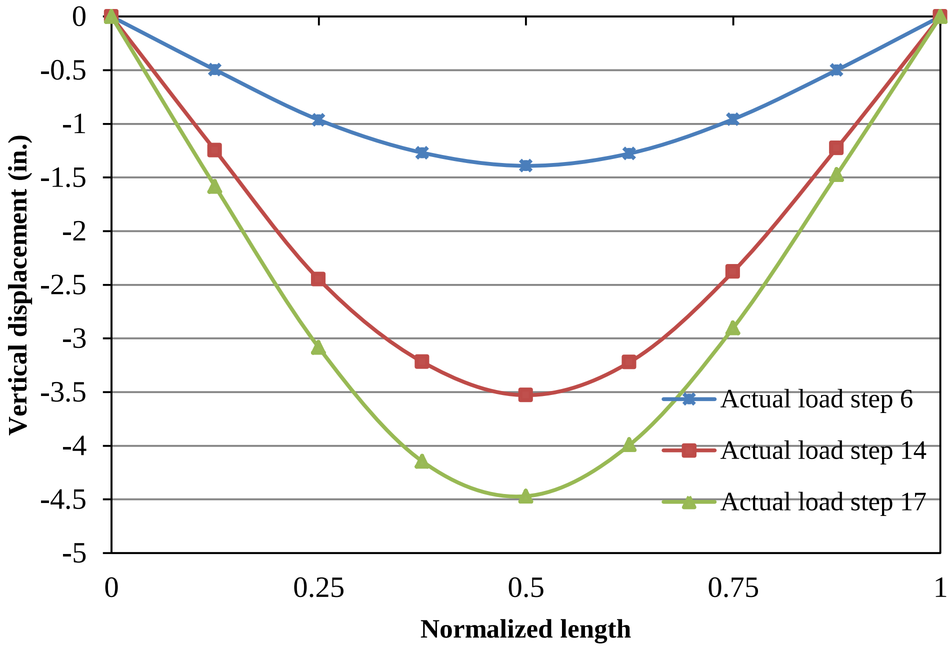

Figure 7.18 Vertical displacements along span of G1 for different actual load steps during inelastic test

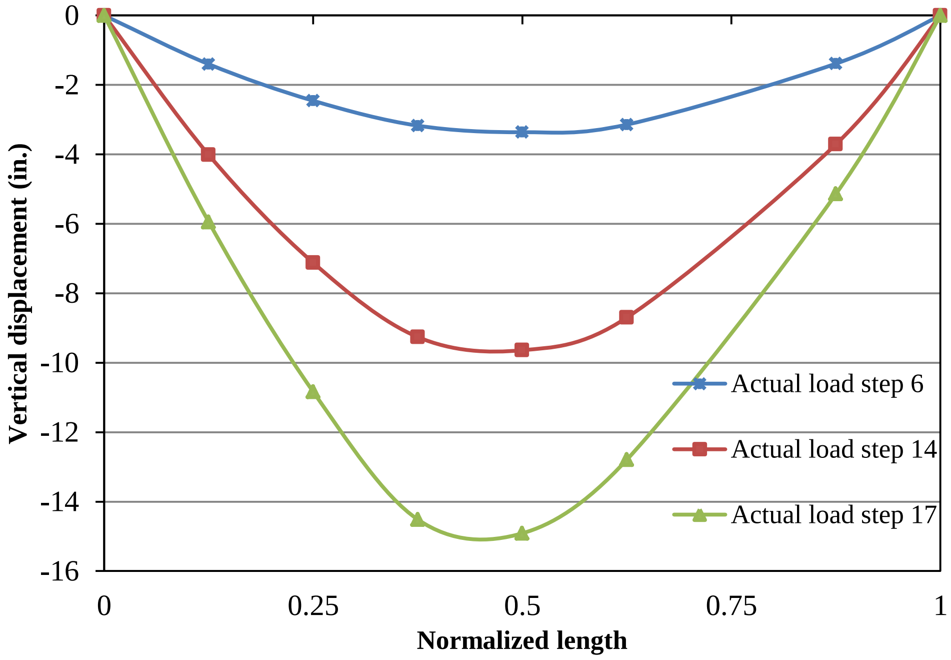

Figure 7.19 Vertical displacements along span of G2 for different actual load steps during the the inelastic test

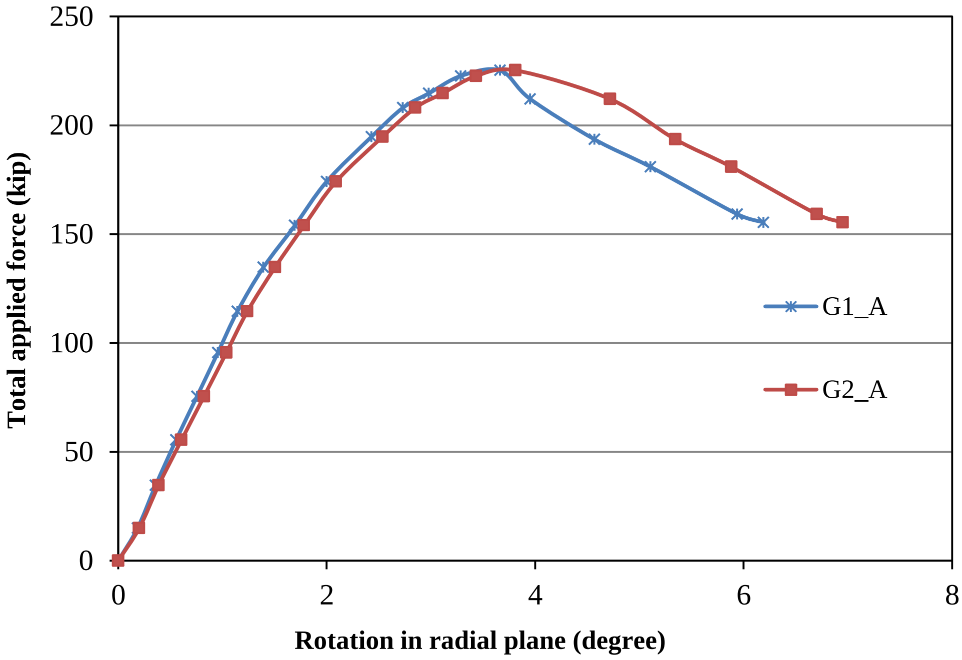

Figure 7.20 Cross section rotation at mid span during inelastic test

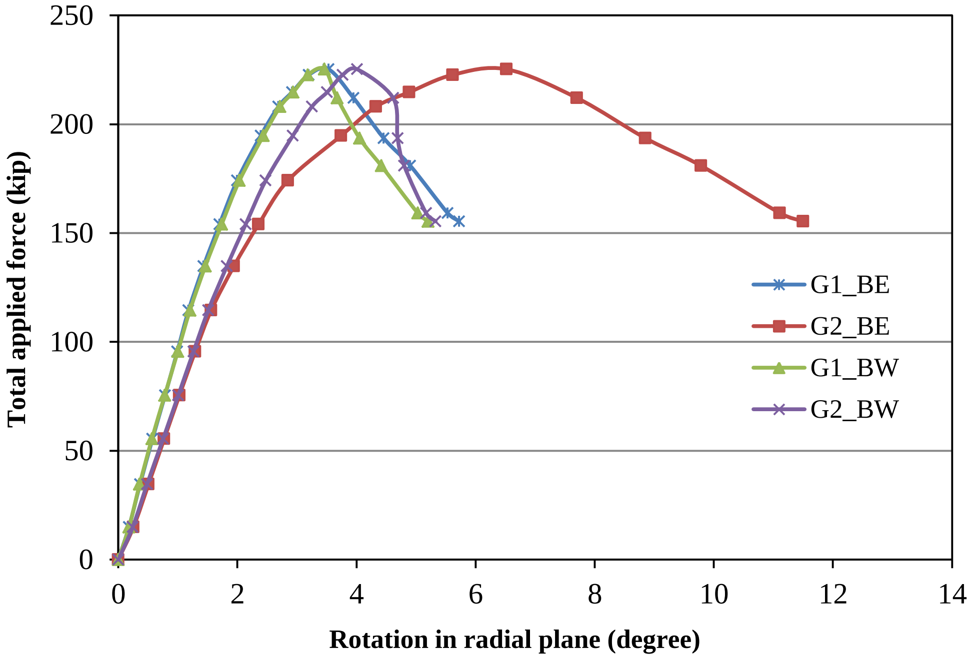

Figure 7.21 Cross section rotation at intermediate stiffeners near planes BE and BW during inelastic test

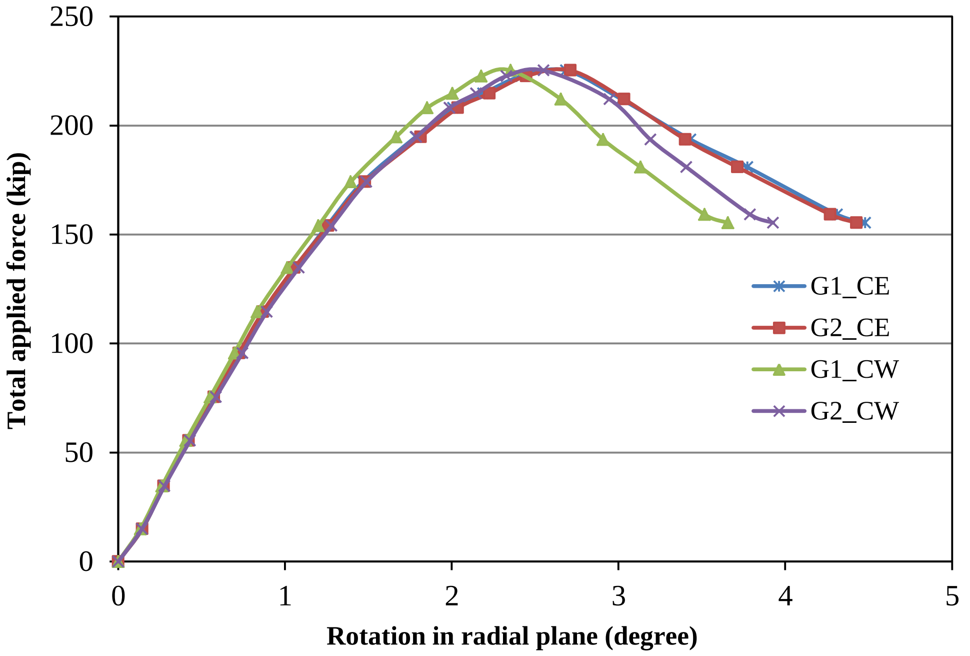

Figure 7.22 Cross section rotation at intermediate stiffeners near planes CE and CW during inelastic test

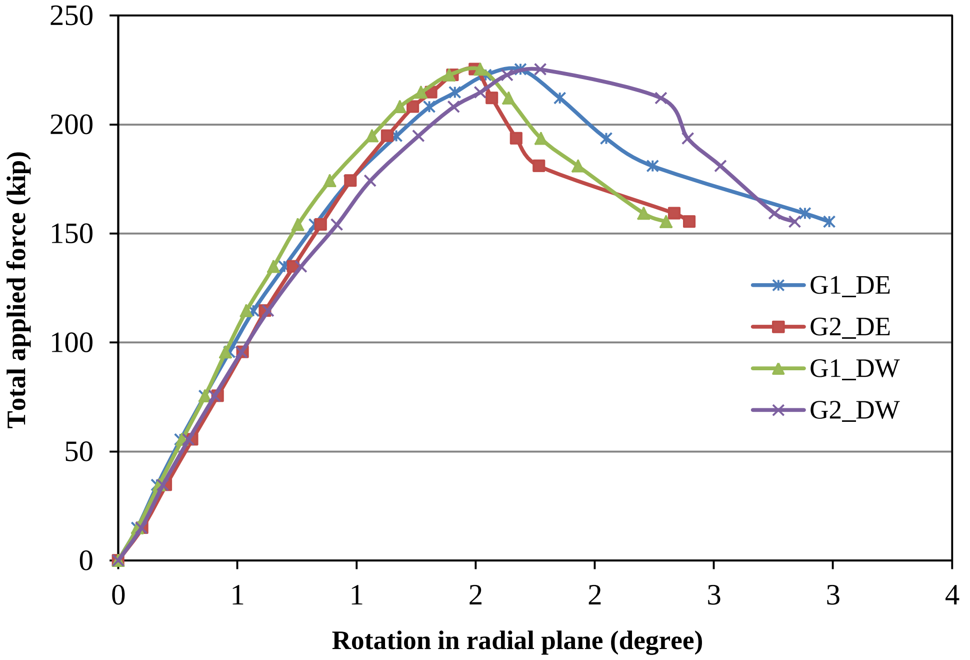

Figure 7.23 Cross section rotation at intermediate stiffeners near planes DE and DW during inelastic test

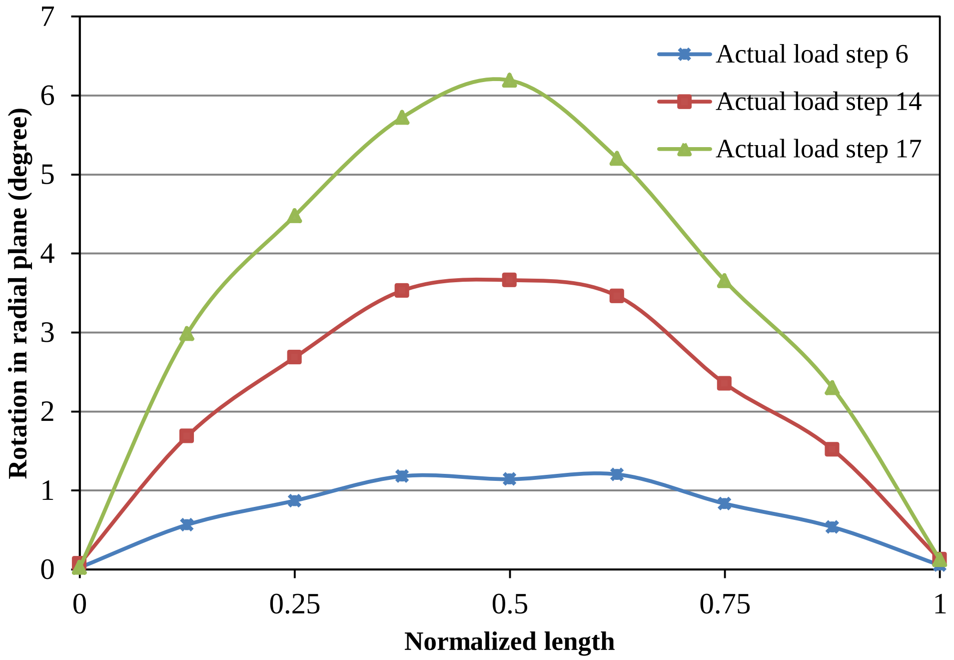

Figure 7.24 Cross section rotation in radial planes along span of G1 for different actual load steps during inelastic test

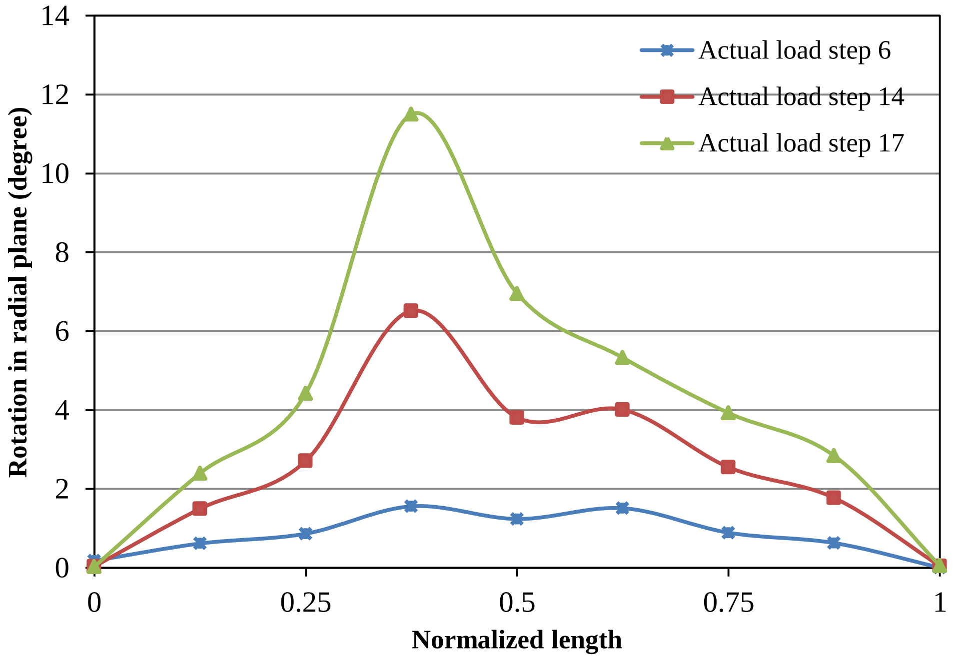

Figure 7.25 Cross section rotation in radial planes along span of G2 for different actual load steps during inelastic test

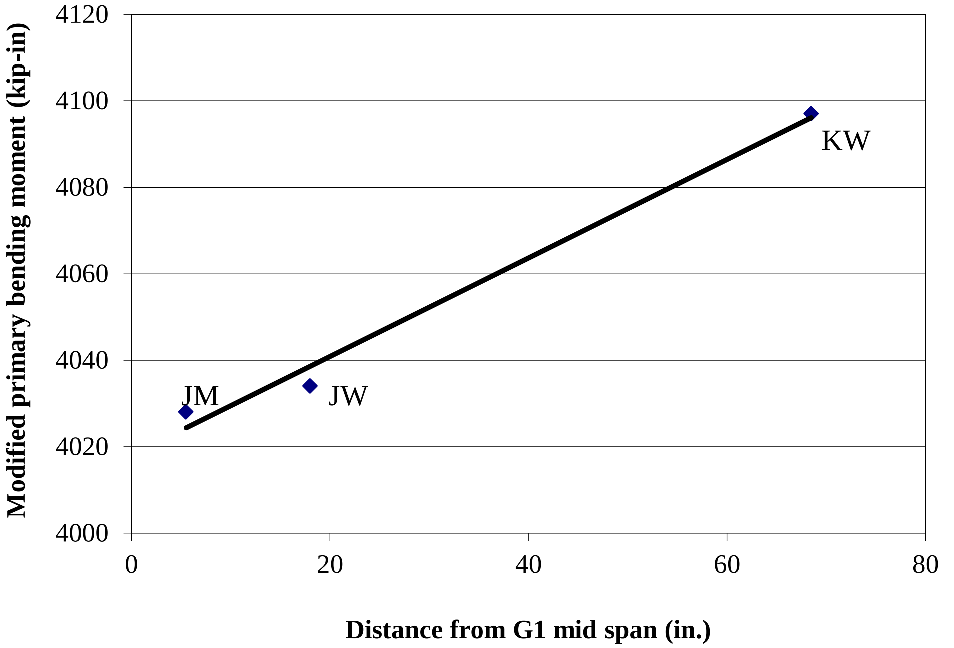

Figure 7.26 Line through primary bending moment data points near mid span of G1 for actual load step 6

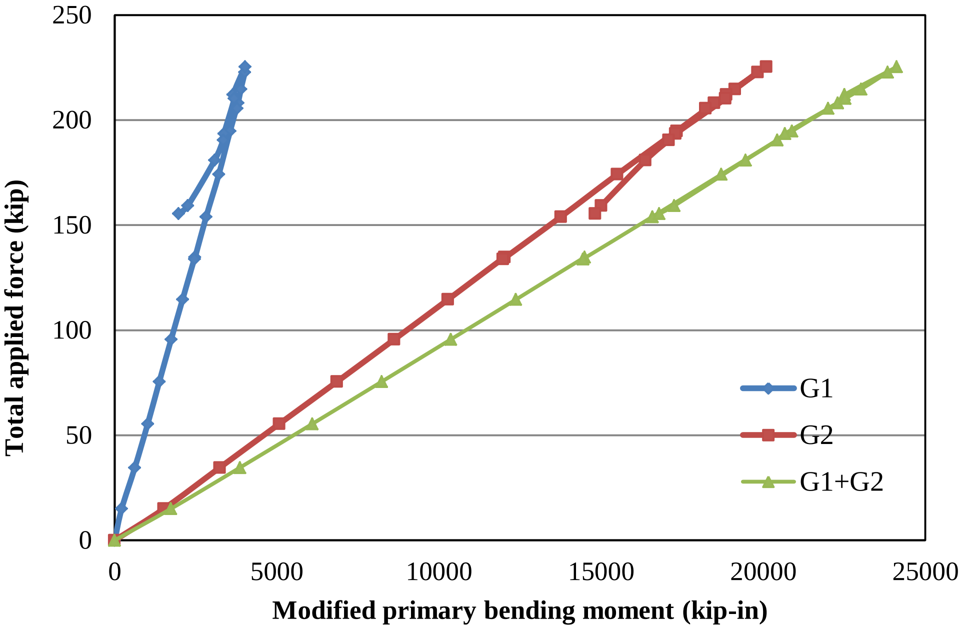

Figure 7.27 Primary bending moment at mid span of G1 and G2

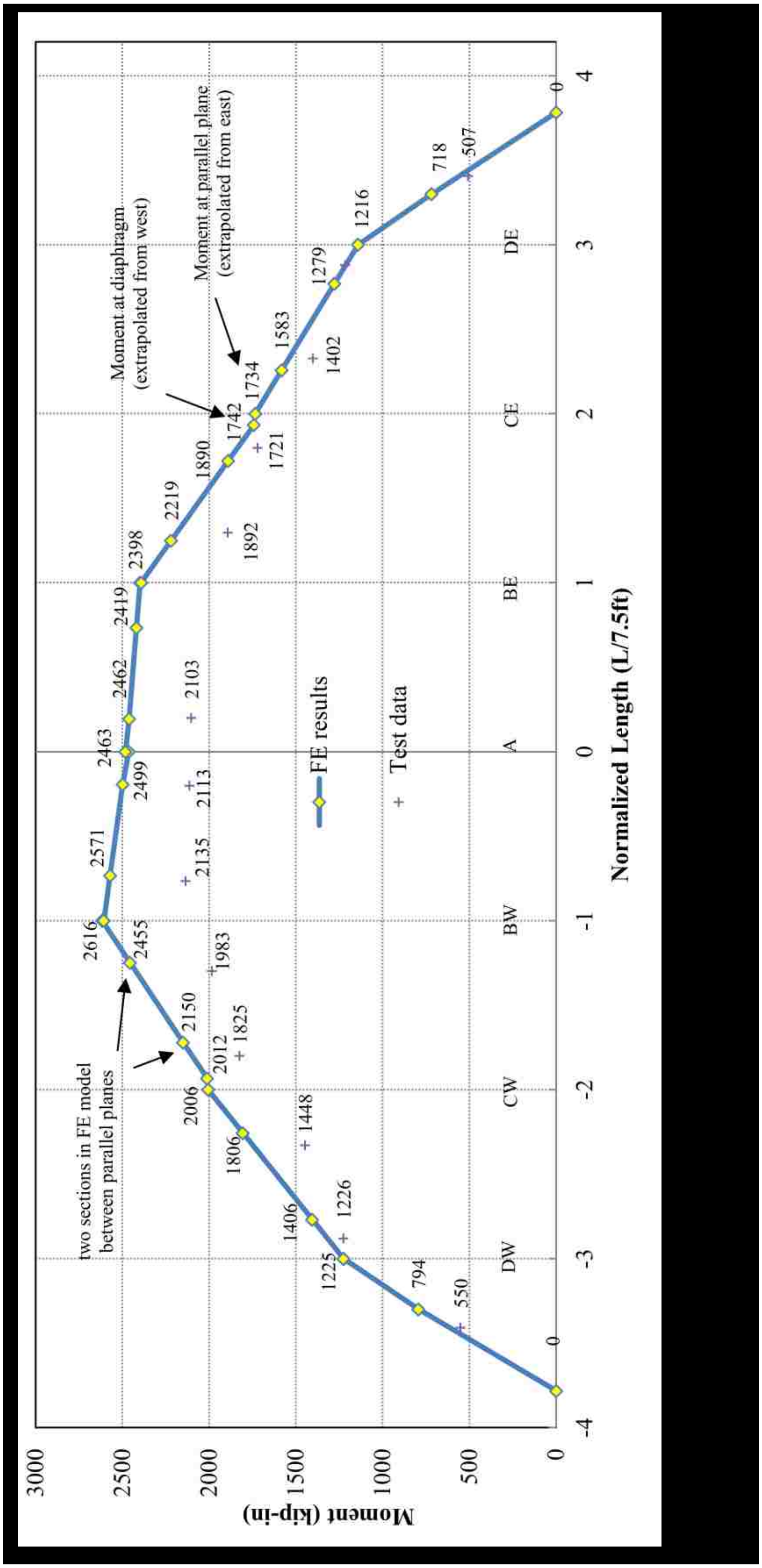
Moment (kip-in)
0
500
1000
1500
2000
2500
3000
Normalized Length (L/7.5ft)
-4
-3
-2
-1
0
1
2
3
4
DW
CW
BW
A
BE
CE
DE
FE results
Test data
two sections in FE model between parallel planes
Moment at diaphragm (extrapolated from west)
Moment at parallel plane (extrapolated from east)
0
794
550
1225
1406
1226
1806
1448
2006
2012
1825
2150
2455
1983
2616
2571
2135
2499
2113
2463
2462
2103
2419
2398
2219
1892
1890
1742
1721
1734
1583
1402
1279
1216
718
507
0

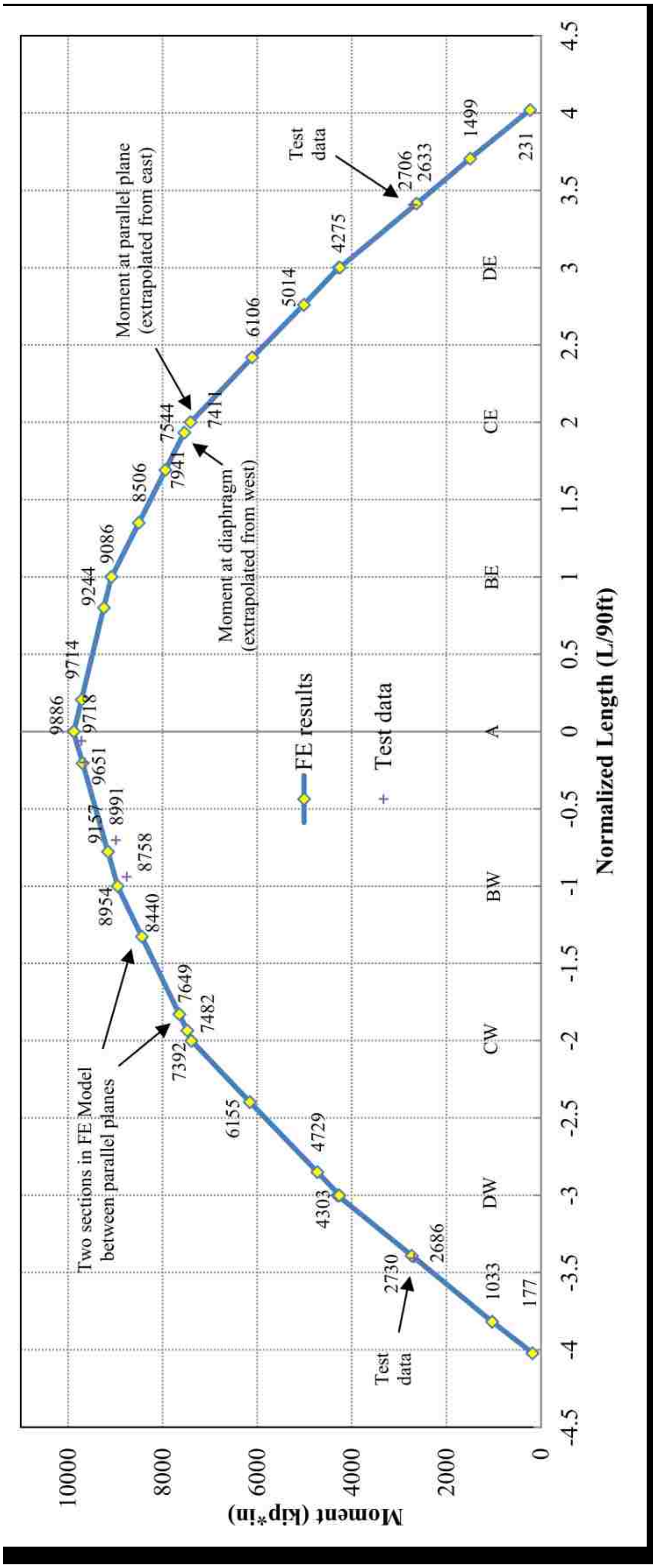

Moment (kip*in)
0
2000
4000
6000
8000
10000
Normalized Length (L/90ft)
-4.5
-4
-3.5
-3
-2.5
-2
-1.5
-1
-0.5
0
0.5
1
1.5
2
2.5
3
3.5
4
4.5
DW
CW
BW
A
BE
CE
DE
FE results
Test data
Test data
Test data
Two sections in FE Model between parallel planes
Moment at parallel plane (extrapolated from east)
Moment at diaphragm (extrapolated from west)
177
1033
2730
2686
4303
4729
6155
7392
7482
7649
8440
8954
8758
9157
8991
9651
9886
9718
9714
9244
9086
8506
7941
7544
7411
6106
5014
4275
2706
2633
1499
231

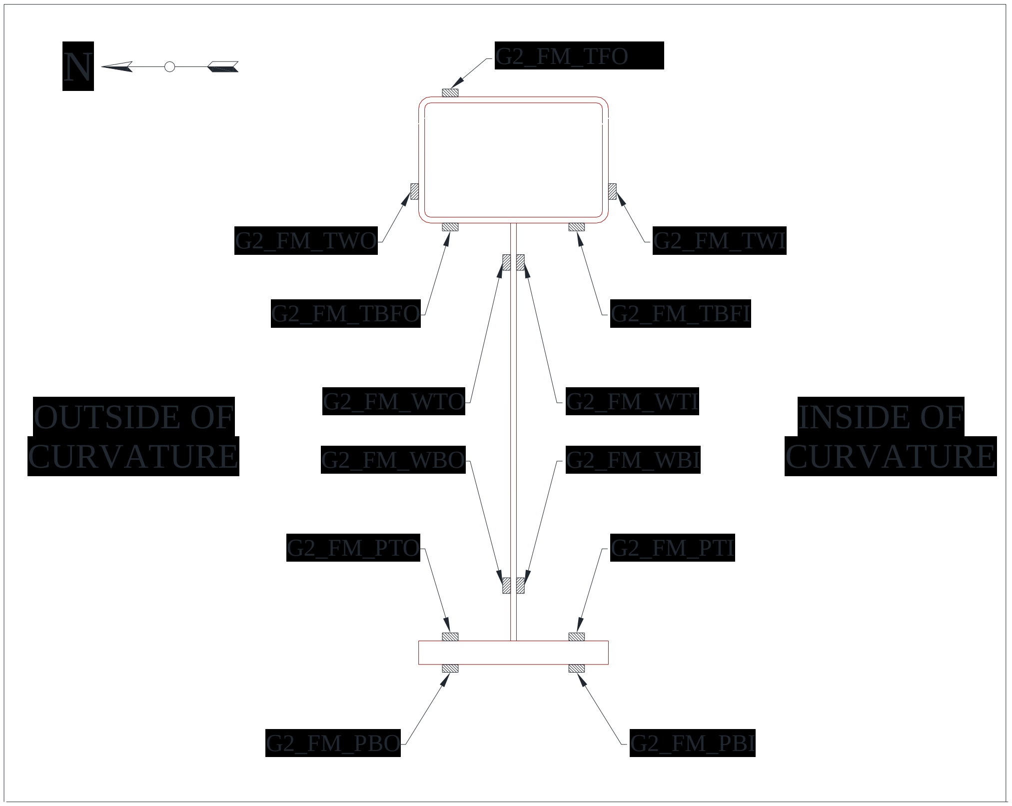

Figure 7.30 Uniaxial strain gages at Section FM of G2

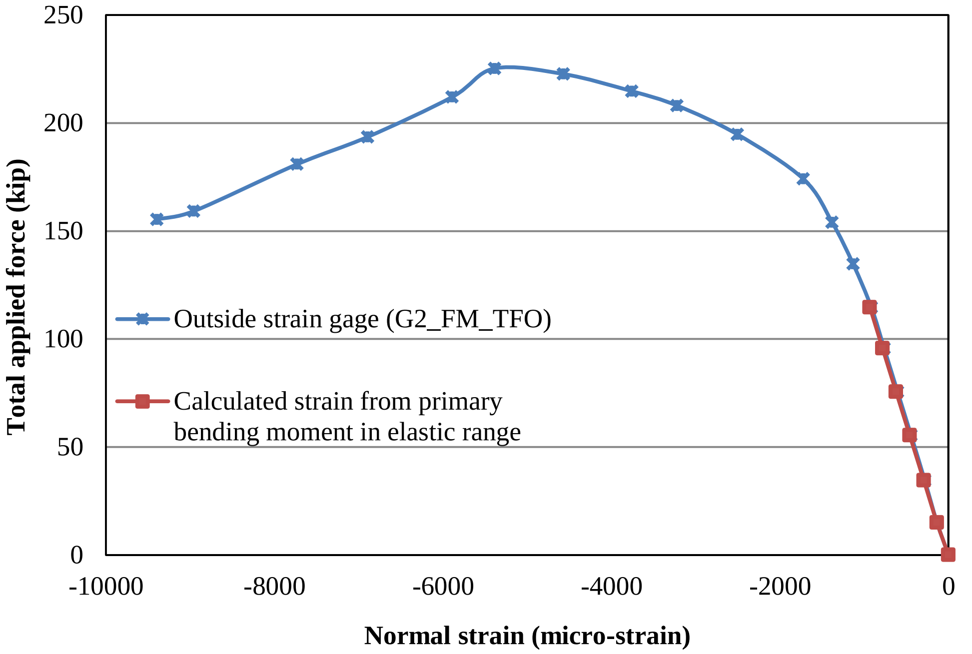

Figure 7.31 Normal strain at top of tube at Section FM during inelastic test

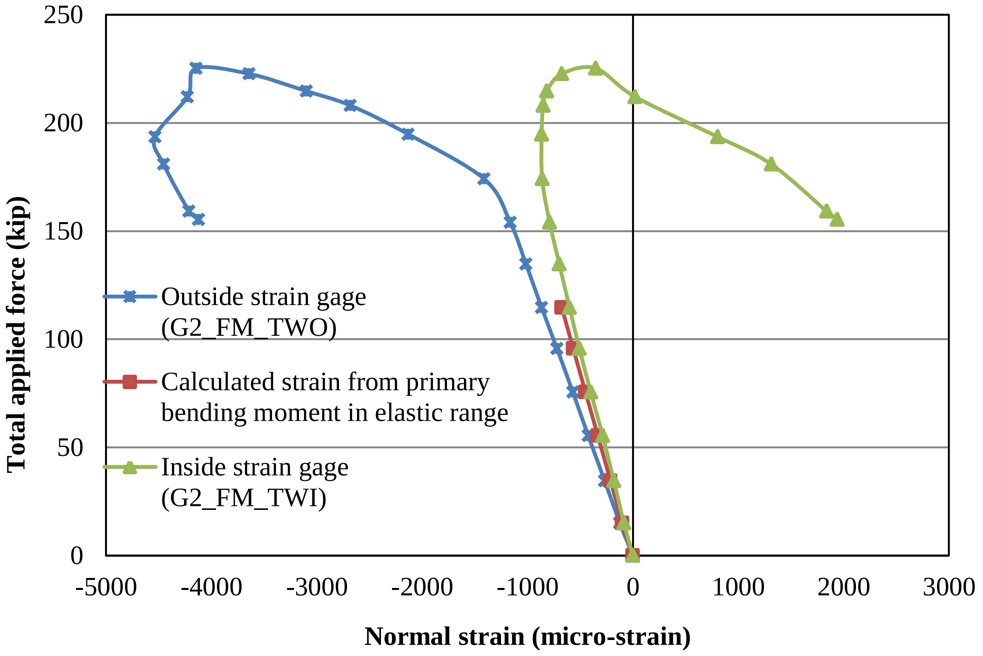

Figure 7.32 Normal strain at tube web at Section FM during inelastic test

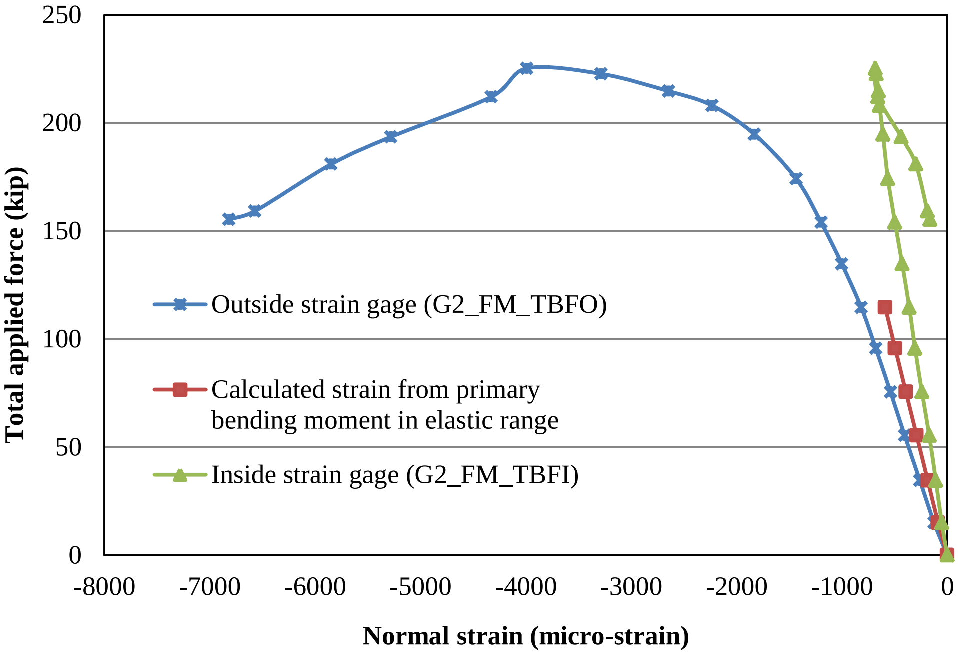

Figure 7.33 Normal strain at tube bottom at Section FM during inelastic test

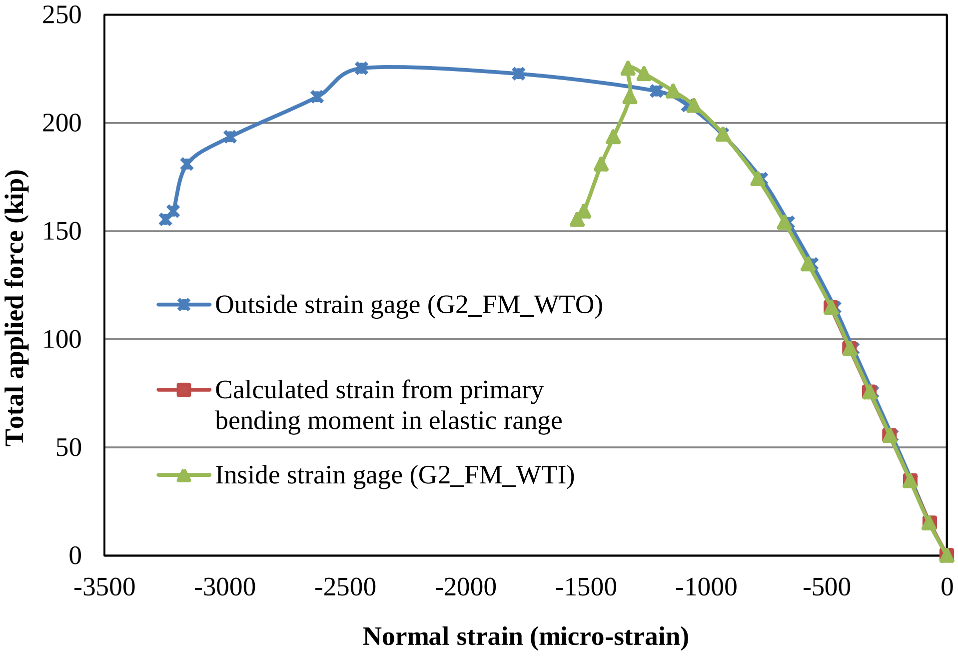

Figure 7.34 Normal strain at web top at Section FM during inelastic test

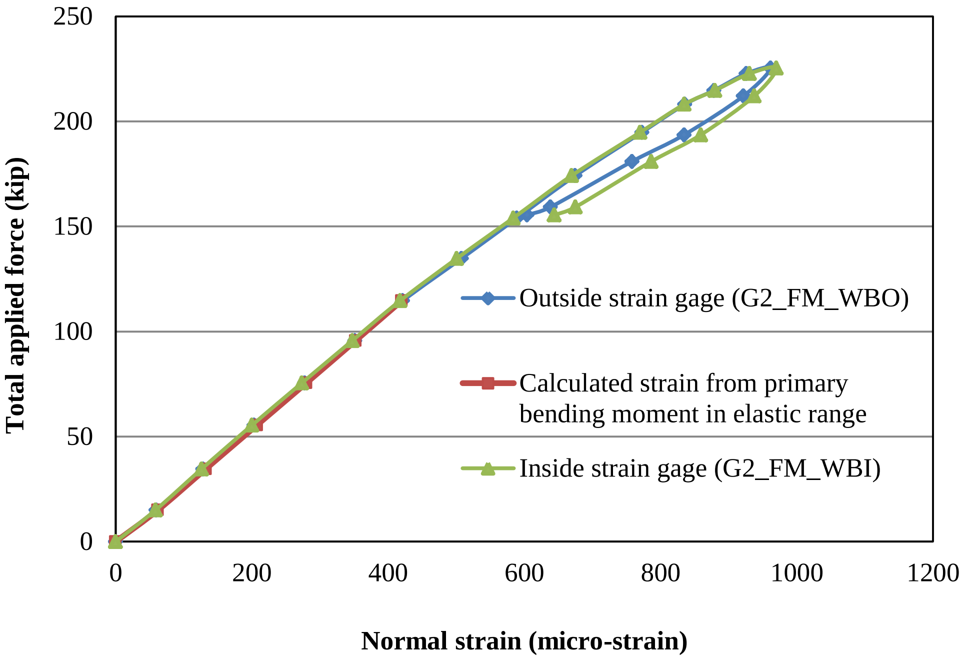

Figure 7.35 Normal strain at web bottom at Section FM during inelastic test

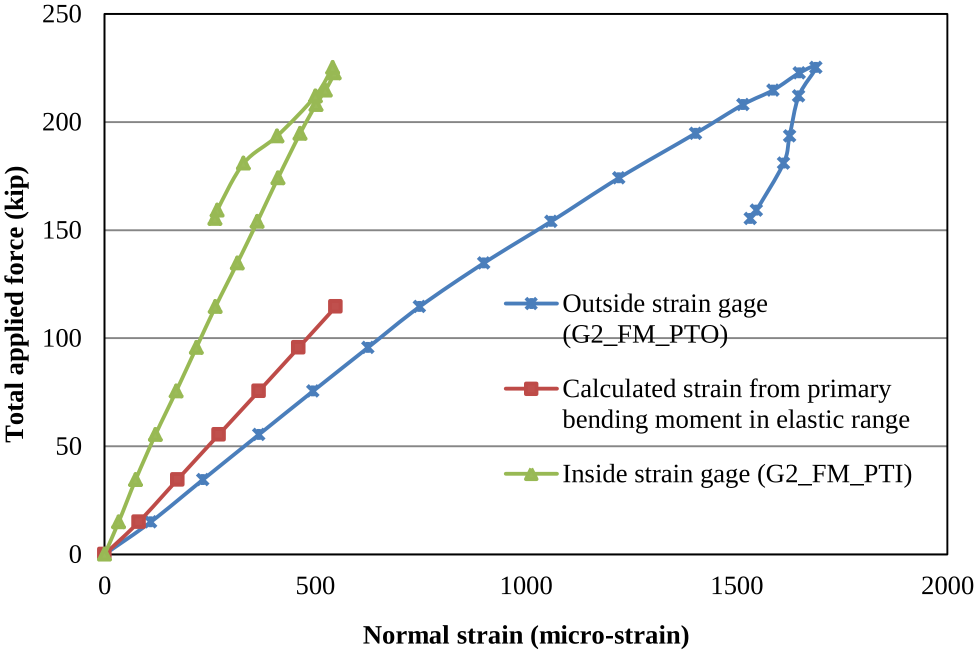

Figure 7.36 Normal strain at top surface of bottom flange at Section FM during inelastic test

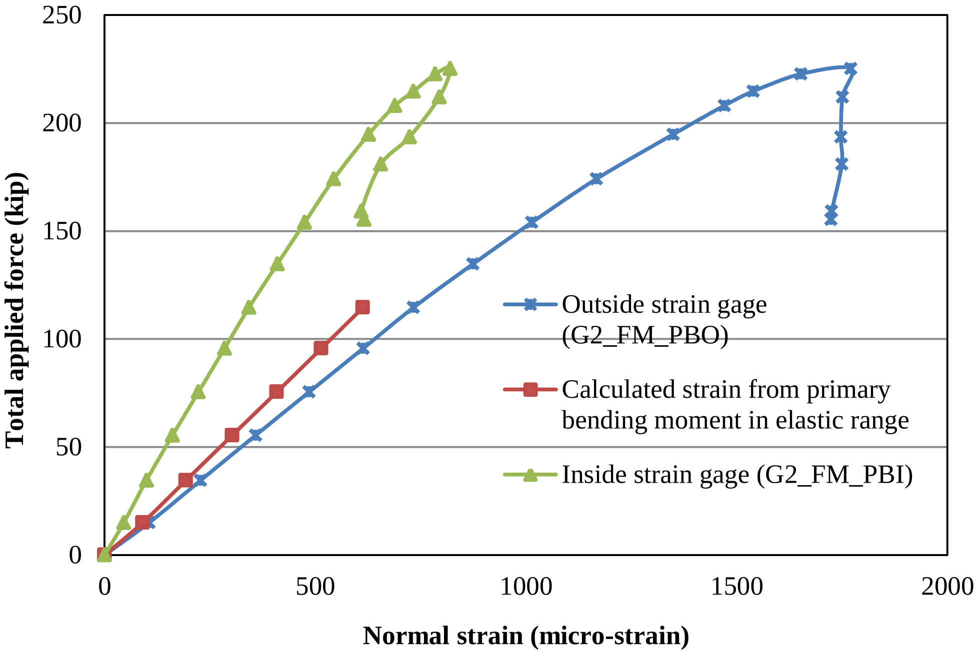

Figure 7.37 Normal strain test results at bottom surface of bottom flange at Section FM during inelastic test

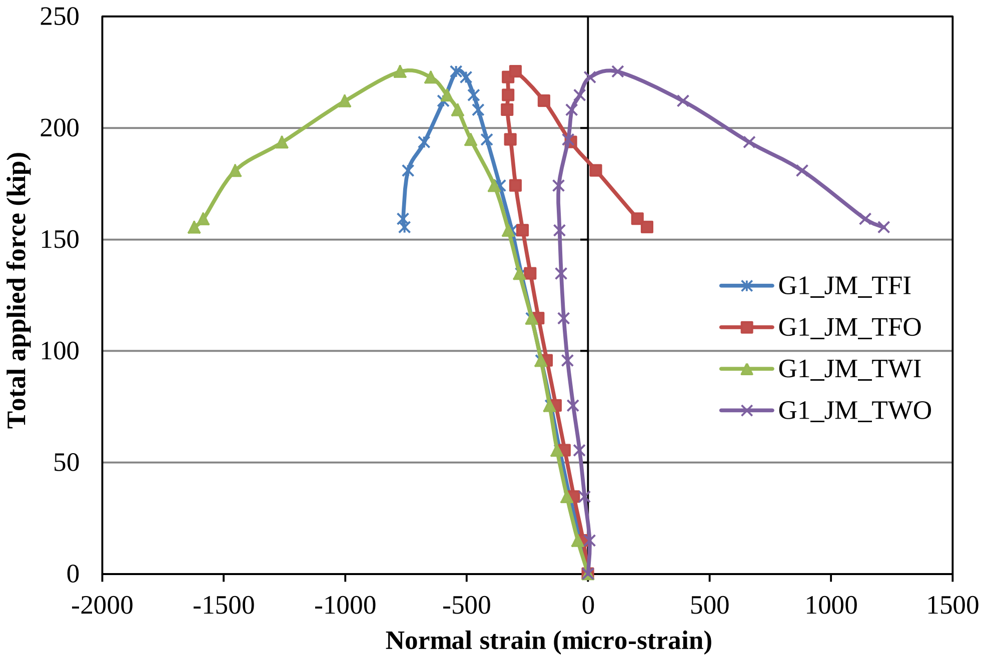

Figure 7.38 Normal strain test results at tube wall and top at Section JM during inelastic test

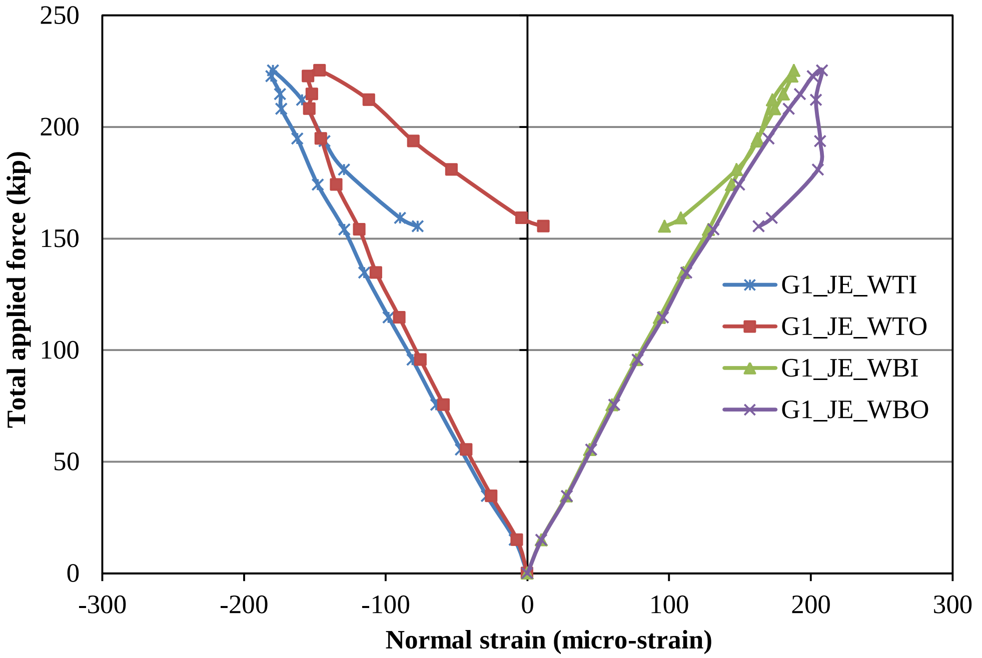

Figure 7.39 Normal strain test results at web top and bottom at Section JE during inelastic test

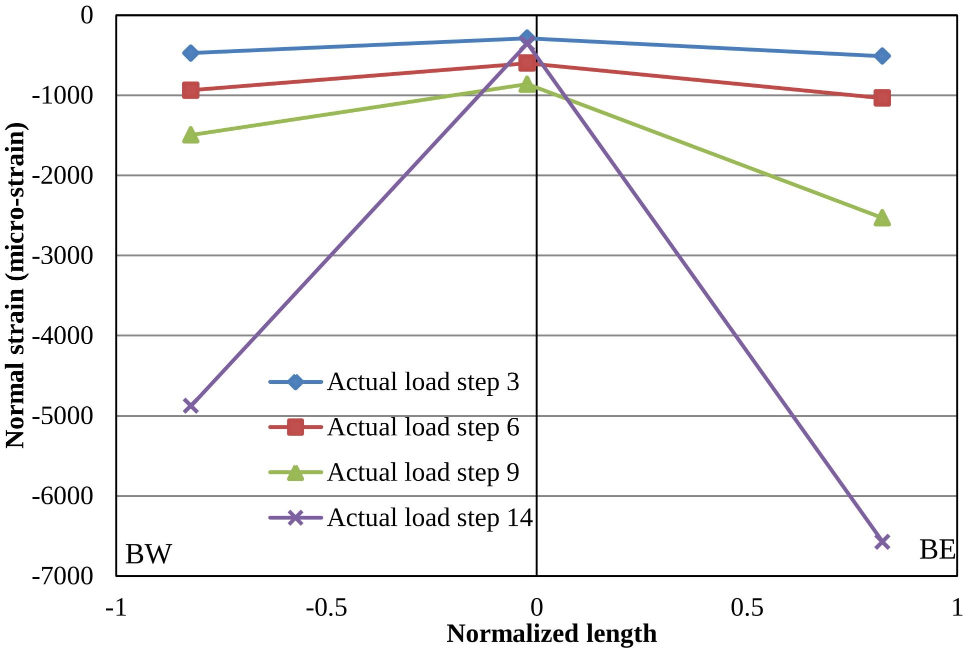

Figure 7.40 Normal strain test results at G2 tube outside wall between Section BW and BE during inelastic test

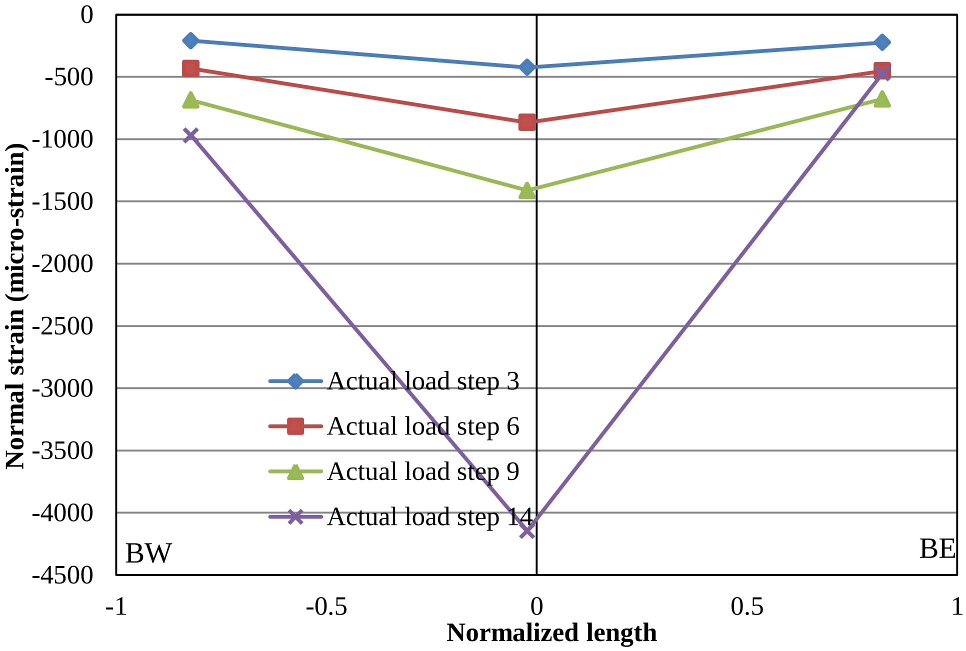

Figure 7.41 Normal strain test results at G2 tube inside wall between Section BW and BE during inelastic test

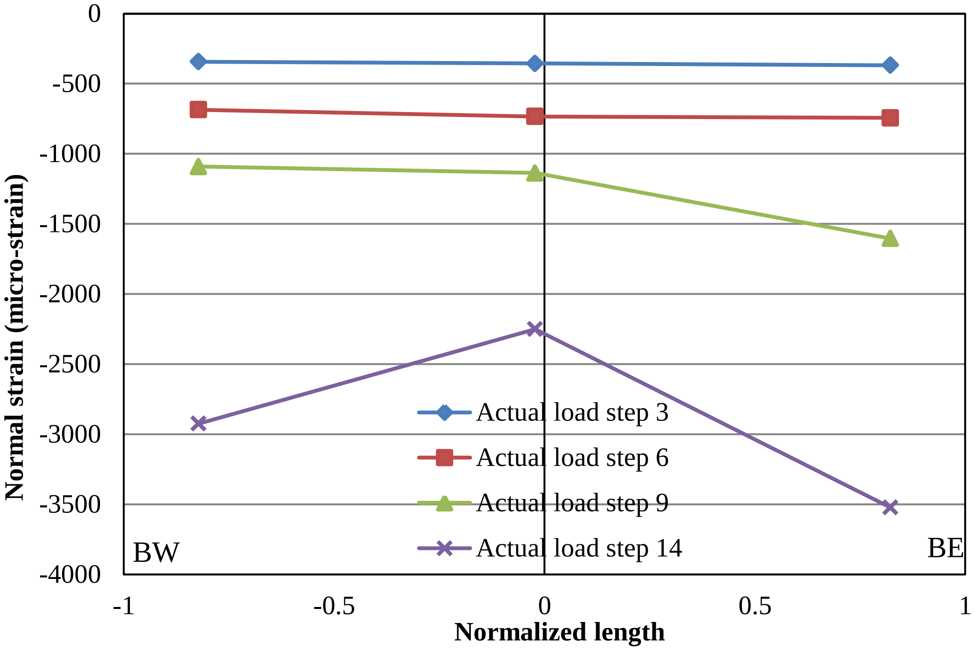

Figure 7.42 Average normal strain at the outside and inside of the G2 tube between Section BW and BE during inelastic test

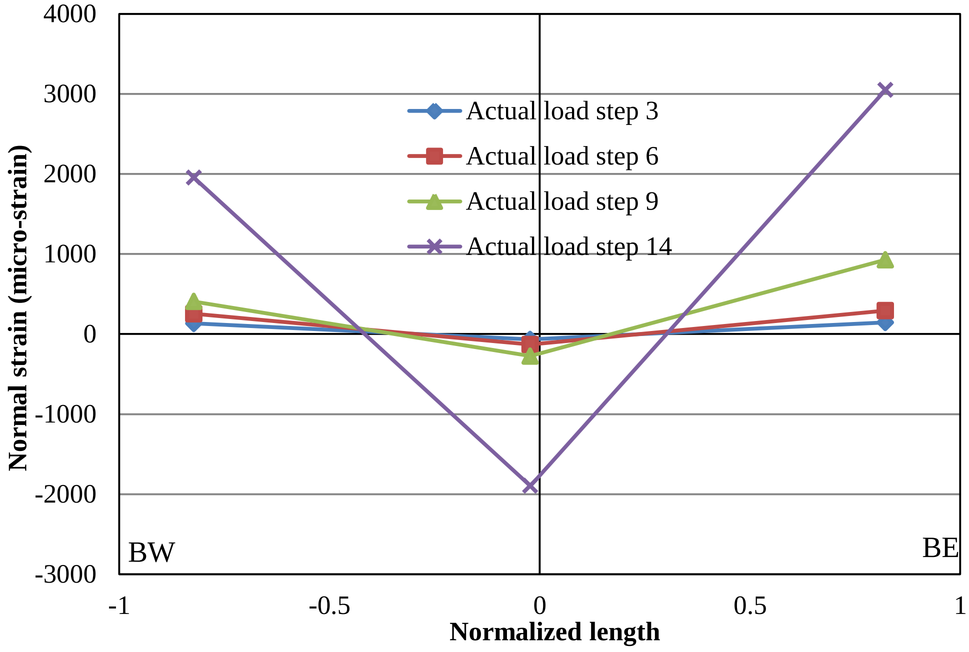

Figure 7.43 Difference between normal strain at outside and inside of G2 tube between Section BW and BE during inelastic test

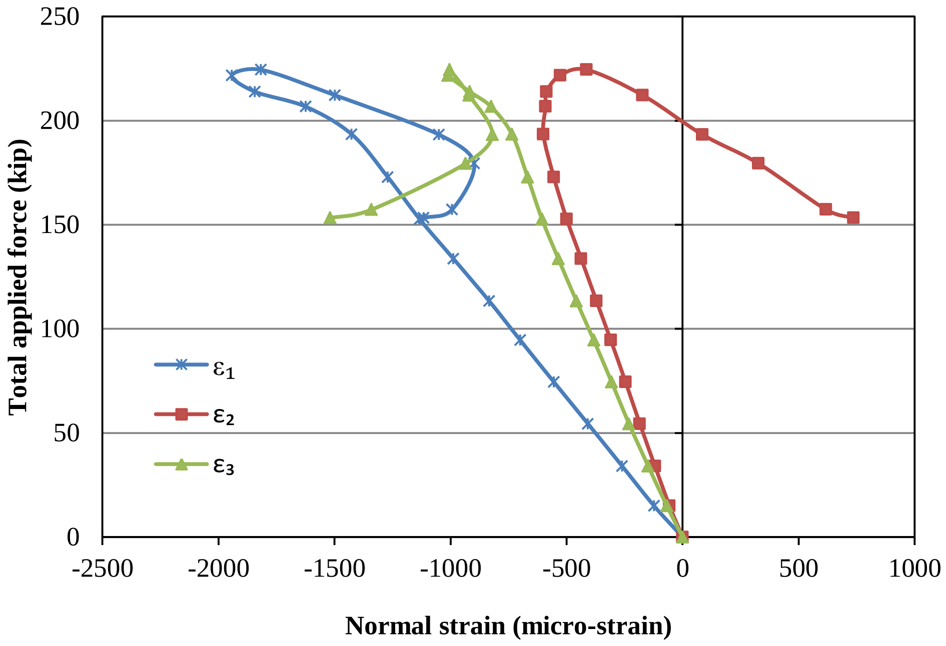

Figure 7.44 Strain data from installed rosette strain gages during inelastic test

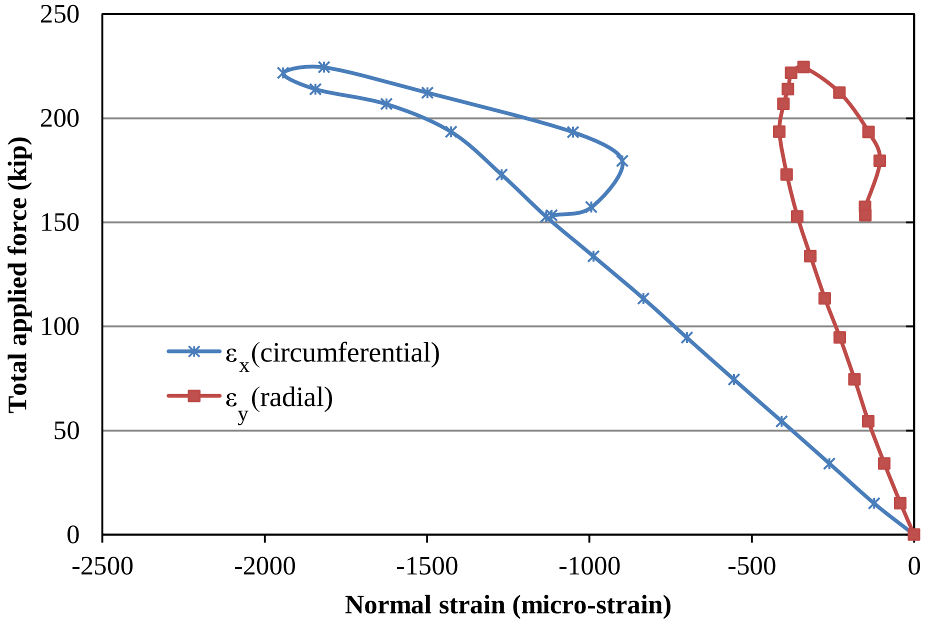

Figure 7.45 Calculated normal strains from rosette strain gage data during inelastic test

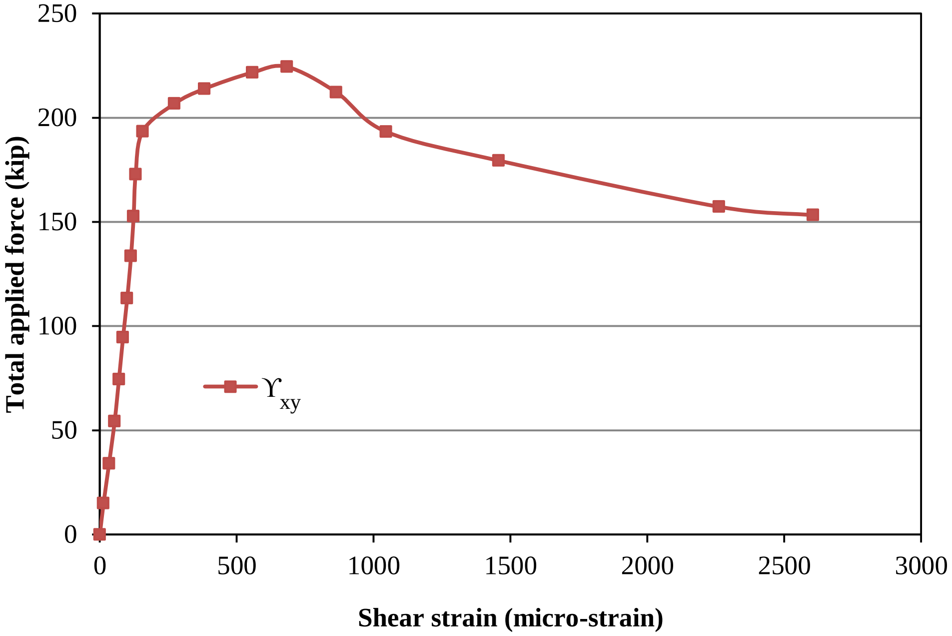

Figure 7.46 Calculated shear strain from rosette strain gage data during inelastic test

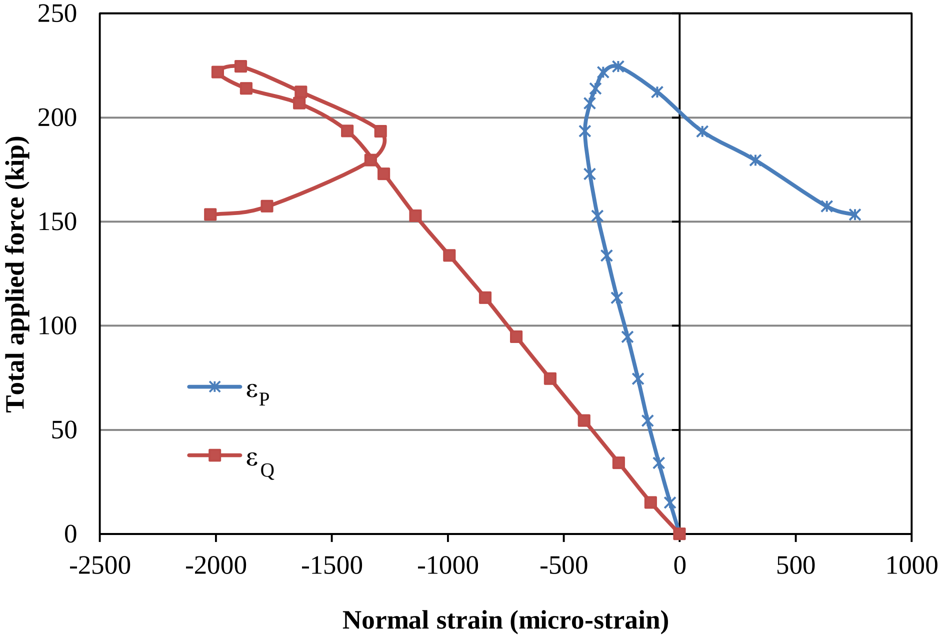

Figure 7.47 Calculated principal strains from rosette strain gage data during inelastic test

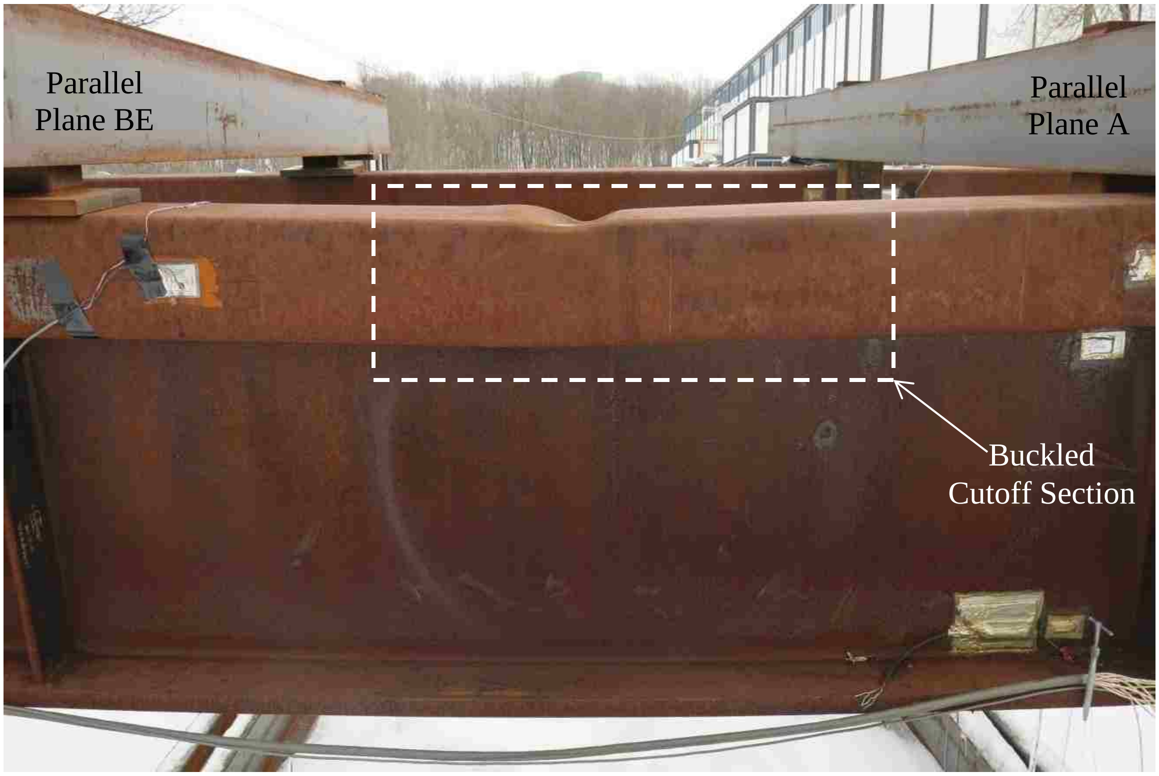

Figure 7.48 Location of local buckled region in test specimen looking from outside of curvature

8 MATERIAL TESTING

8.1 Introduction

This chapter describes material tests performed on samples removed from the test specimen after the tests on the test specimen were completed. Four different sections were cut from the test specimen. These sections were in regions of the test specimen that did not yield during the tests. Tensile coupons were machined from the material in these sections, and tested, as discussed in Section 8.2. Section 8.3 discusses the tensile test procedure and resulting material properties. Another section was cut from the test specimen which included the local buckled region. Section 8.4 presents the observations of the local buckling from this section. A metallography process was used on samples from the local buckled section to examine the tube splice welding. These results are discussed in Section 8.5.

8.2 Tensile Coupon Manufacture

To obtain the actual material properties of the test specimen steels, tensile coupons were machined from sections cut from the test specimen. Figure 8.1 shows the locations of the cutoff sections. Two inverted T shaped sections were cut from the bottom flange and web of girder G1 and G2 at regions that did not yield during the tests of the test specimen. As discussed earlier, two individual tubes were spliced together to make the top flange tube for each girder. One section was cut from the east side and one section was cut from the west side of G2 to provide tensile coupons from the west and east tubes of G2. Figure 8.2 (a) and (b) shows two sections (labeled tube2 and flange1 and web1) cut from the test specimen. Photographs of two sections are displayed in Figure 8.3 (a) and (b).

Six tensile coupons were manufactured from each tube, from inside and outside of the tube top plates, webs, and bottom plate. Two tensile coupons were manufactured from each web section. Two tensile coupons were manufactured from each bottom flange section. The coupons are “dog-bone” shaped specimens that have a narrower width at the center, in accordance with the ASTM E8 standard (ASTM, 2013). Figure 8.4 shows the typical tensile coupon geometry. Figure 8.5 shows the location and identification of the tensile coupons. Geometric properties of coupons are presented in Table 8.1. Figure 8.6 is a photograph showing a side view of the tensile coupons from different sections with different thickness. Figure 8.7 is a plan view photograph of typical tensile coupon.

8.3 Tensile Tests

The tensile coupons were aligned and gripped in the SATEC 600K universal testing machine crossheads. An extensometer was used which consisted of two aluminum parts, attached to the coupon, with 8 in. between the parts, as shown in Figure 8.8. Two extensometer LVDTs measured the relative displacement of the two attached aluminum parts. The readings from the LVDTs are averaged and divided by the gage length (8 in.) to determine the strain. The coupons were pulled to failure in tension by the SATEC machine. The tensile stress is obtained by dividing the force measured by SATEC machine load cell by the initial cross section area of the coupon. Figure 8.8 shows the tensile coupon and attached extensometer in the SATEC machine before the test. Figure 8.9 shows the tensile coupon after the test.

The loading of the coupon was interrupted three times after the coupon yielded and before the strain hardening initiated to determine the static yield stress based on SSRC Technical Memorandum no. 7: Tension Testing (Ziemian, 2010). Figure 8.10 (a) shows the full stress-strain curve for coupon 15, which had no significant residual stress and has a flat yielding curve (called “Type A” in SSRC Technical Memorandum no. 7). A close view of the stress-strain curve near the yielding region is presented in Figure 8.10 (b). The static yield stress for a Type A stress-strain curve is the average of the stress at the low points at the loading interruptions. Figure 8.11 (a) shows full stress-strain curve for coupon 16, where the residual stress effect is noticeable resulting in a rounded yielding curve (called “Type B” in SSRC Technical Memorandum no. 7). A close view of the stress-strain curve near the yielding region is presented in Figure 8.11 (b). The static yield stress for a Type B stress-strain curve is the stress at the intersection of 0.2 % offset line and a least squares line fit to the low points at the three loading interruptions. The material properties from the tensile coupon tests are listed in Table 8.2 for each coupon.

8.4 Buckled Cutoff Section

As discussed in Section 7.11, local buckling of the tubular top flange of G2 occurred after the mid span section yielded. The buckling occurred at a location between parallel planes A and BE. The local buckle is located about 45 in. east of the mid span and about 3.5 in. east of the tube splice location. Figure 8.12 shows the location of local buckled region on the test specimen. As indicated in the figure, a section of the local buckled region was cut from the test specimen for more detailed observations. Figure 8.13 to Figure 8.16 shows different views of the local buckled section. Since local buckling occurred at a region close to the splice location, and significant geometric imperfection and misalignment were expected at the splice location, different samples at the splice location, were removed from local buckled section. Figure 8.17 shows the locations of the samples. Several samples, samples 2,3,4,5 and 6, were cut so that they included the splice in the sample. These samples included the thickness variations along the length of the tube as it passes from the east side to the west side of the splice location. These thickness variations were measured and summarized in Table 8.3. Note that the samples were noticeably distorted buckled material and it was not possible to measure the thickness accurately at those locations.

8.5 Metallography

To study the tube splice welding and to observe possible misalignment of the spliced tubes, a metallography process was performed on the samples shown in Figure 8.17. First, the surface layers of the sample that were damaged by cutting were removed by grinding. The samples were ground with three different wet silicon carbide papers (40 grit, 160 grit, and 400 grit) on rotating disk (Figure 8.18). A finer grit paper was used at each stage to remove the scratches from the previous coarser paper. Then the samples were etched by acid to reveal the base and weld metals. Figure 8.19 shows sample 4 after the metallography. Misalignment of the tubes at the splice location is discernible. Also it can be seen that some base metal was removed by grinding the outer surface of the tube during the process of fabricating the splice, which resulted in a thinner tube section near splice location.

Table 8.1 Geometric properties of tensile coupons

Coupon Number	Average thickness (in.)	Average width (in.)	Area (in.^{2})	Out of flatness	
				mm	in.
1	0.353	1.516	0.535	0.8	0.033
2	0.352	1.516	0.533	1.7	0.067
3	0.351	1.509	0.530	0.3	0.012
4	0.352	1.509	0.531	0.7	0.028
5	0.356	1.510	0.537	0.2	0.008
6	0.355	1.520	0.539	1.3	0.051
7	0.351	1.517	0.532	0.6	0.024
8	0.351	1.514	0.531	2.2	0.087
9	0.350	1.515	0.531	0.3	0.012
10	0.349	1.518	0.530	0.5	0.020
11	0.356	1.514	0.538	0.7	0.028
12	0.355	1.507	0.535	1.9	0.075
13	0.383	1.510	0.579	-	-
14	0.385	1.521	0.586	-	-
15	0.755	1.505	1.137	-	-
16	0.754	1.506	1.136	-	-
17	0.384	1.513	0.580	-	-
18	0.383	1.510	0.578	-	-
19	1.526	1.510	2.304	-	-
20	1.526	1.509	2.303	-	-

Table 8.2 Material properties from the tensile coupon tests

Coupon Number	Static yield stress (ksi)	Ultimate strength (ksi)	Elongation (%)
1	58.0	74.0	18.6
2	55.3	67.1	21.8
3	49.4	67.7	24.8
4	53.0	66.6	22.0
5	53.1	66.1	22.1
6	56.1	66.4	21.4
7	61.7	75.7	14.4
8	62.5	76.7	15.2
9	54.1	73.8	16.5
10	62.6	74.8	17.4
11	58.4	73.2	17.4
12	64.0	77.3	13.6
13	52.4	73.5	23.9
14	58.1	74.0	21.6
15	51.1	76.8	22.7
16	50.8	76.9	22.7
17	51.7	73.2	23.5
18	53.5	75.4	21.7
19	54.7	83.8	25.0
20	54.2	83.8	15.3

Table 8.3 Thickness variation within the samples

Measurement location			Test sample thickness (in.)		
			Sample 2	Sample 3	Sample 4
West side of splice	1 in. from splice	North (T*)	0.3512	0.3538	0.3299
		South (B**)	0.3417	0.3418	0.3262
		average	0.3465	0.3478	0.3281
	0.5 in. from splice	North (T)	0.3536	0.3517	0.3143
		South (B)	0.3393	0.3361	0.3084
		average	0.3465	0.3439	0.3114
	0.25 in. from splice	North (T)	0.3537	0.3831	0.3105
		South (B)	0.3278	0.3404	0.3021
		average	0.3408	0.3618	0.3063
East side of splice	1 in. from splice	North (T)	0.3483	0.3352	0.3828
		South (B)	0.3456	0.3428	0.4182
		average	0.3470	0.3390	0.4005
	0.5 in. from splice	North (T)	0.3471	0.3457	0.3696
		South (B)	0.3486	0.3428	0.3641
		average	0.3479	0.3443	0.3669
	0.25 in. from splice	North (T)	0.3485	0.3549	0.3472
		South (B)	0.3483	0.3446	0.3431
		Average	0.3484	0.3498	0.3452

* T = North is top side for sample 4
** B =South is bottom side for sample 4

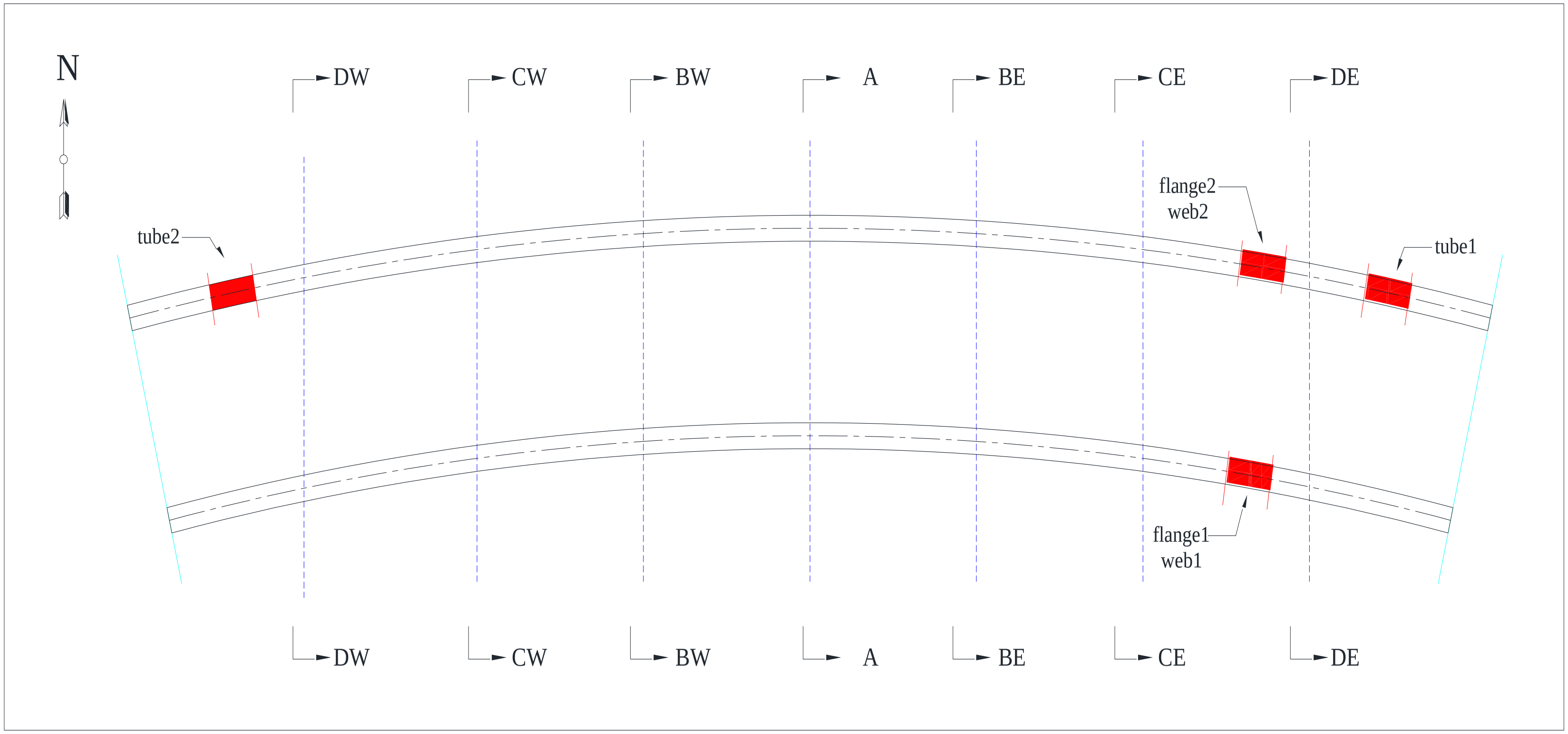

Figure 8.1 Locations of sections cut for tensile coupons

(a) Tube2

(b) Flange1 and web1

Figure 8.2 Sections cut from test specimen

(a) Tube2

(b) Flange2 and web2

Figure 8.3 Sections cut for tensile coupons

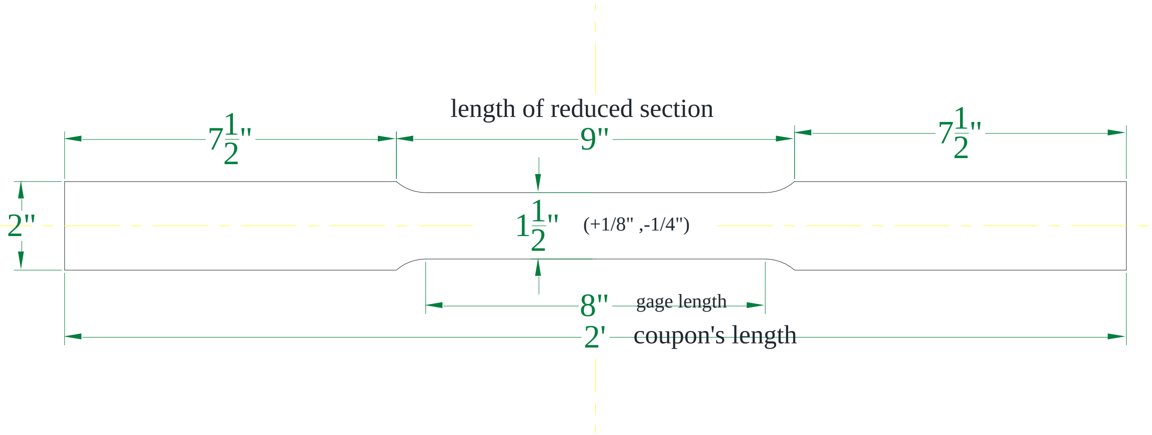

Figure 8.4 Typical tensile coupon geometry

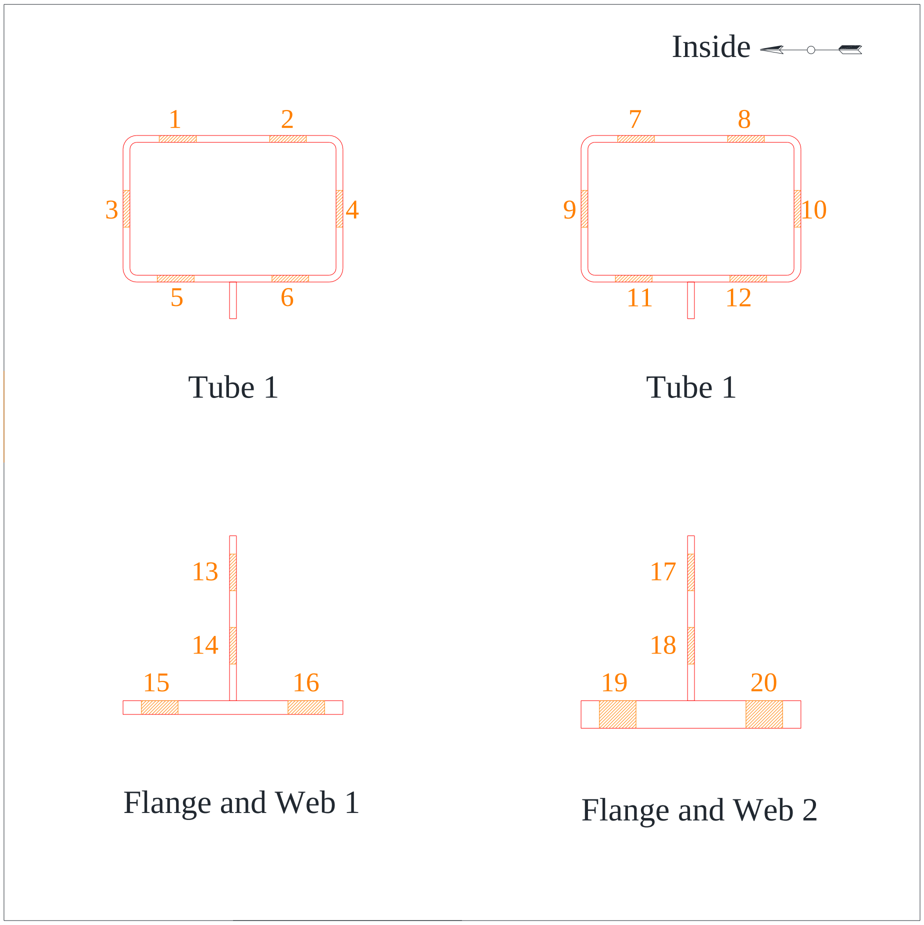

Figure 8.5 Locations of tensile coupons from cutoff sections

Figure 8.6 Side view of tensile coupons (from top to bottom: G2 bottom flange, G1 bottom flange, G2 web and G2 tube)

Figure 8.7 Plan view of typical tensile coupon

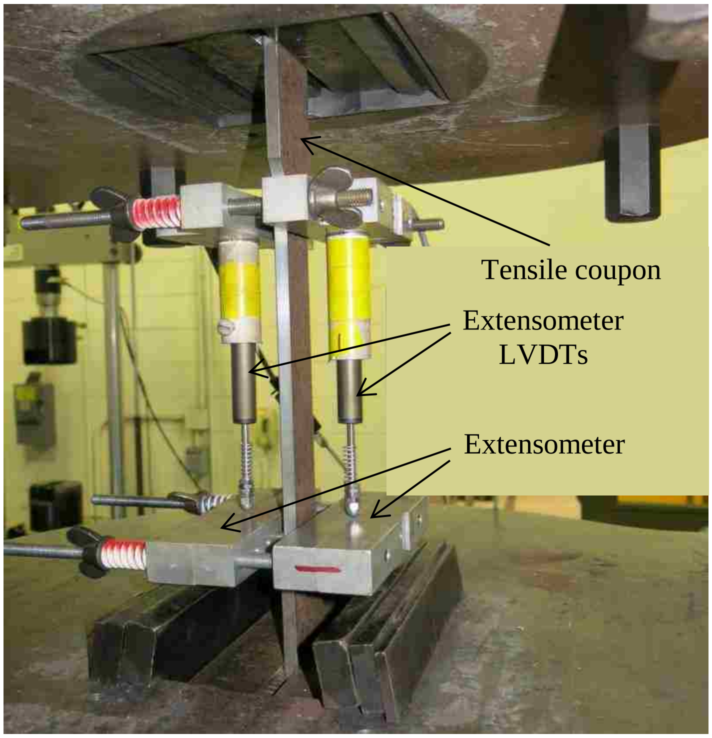

Figure 8.8 Extensometer placed in SATEC machine

Figure 8.9 Tensile coupon after fracture

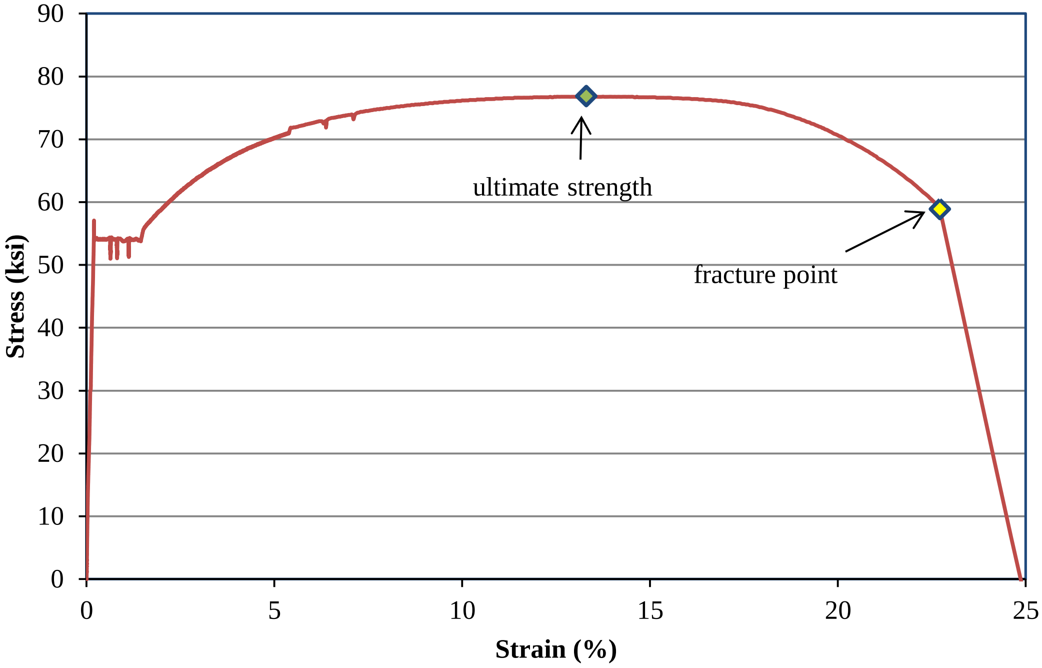

(a) Full stress-strain curve

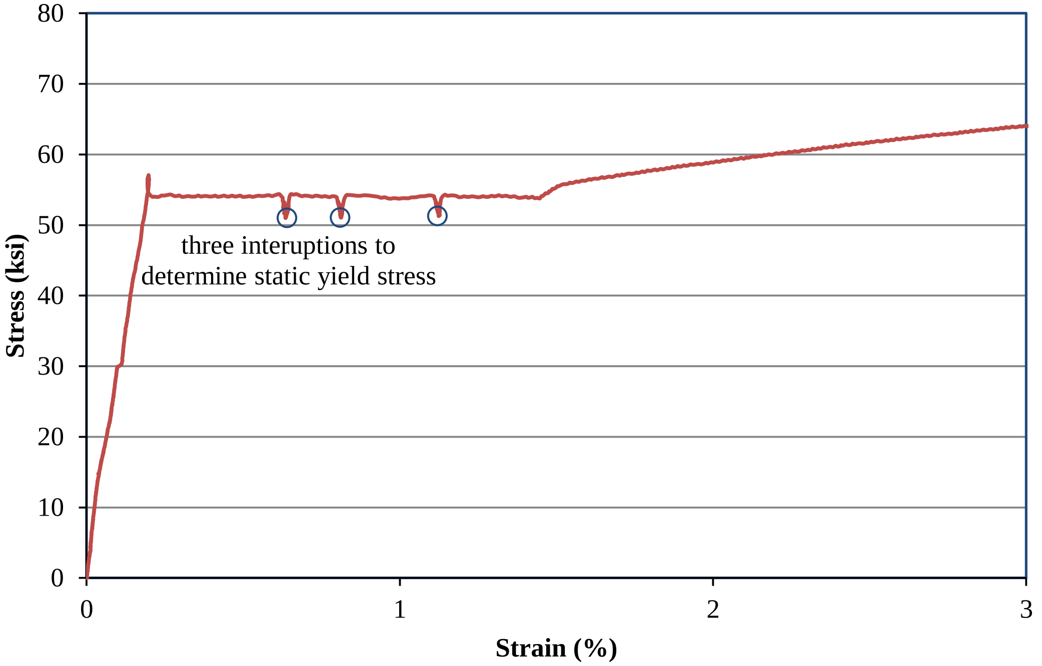

(b) Stress-strain curve near yielding region

Figure 8.10 Stress-strain curve for coupon test 15 with no significant residual stress

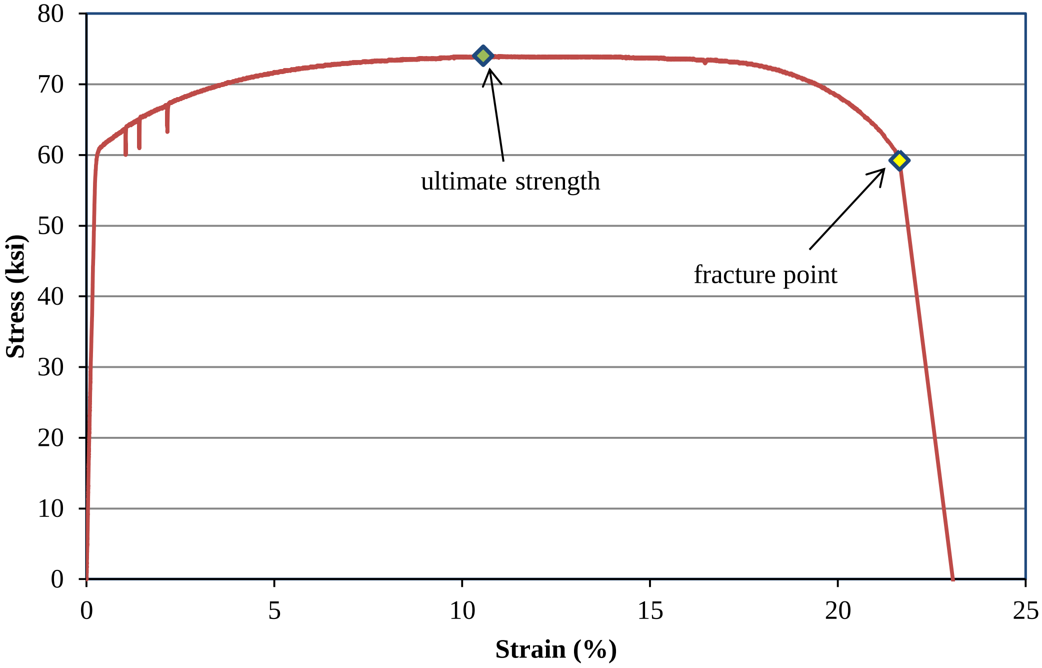

(a) Full stress-strain curve

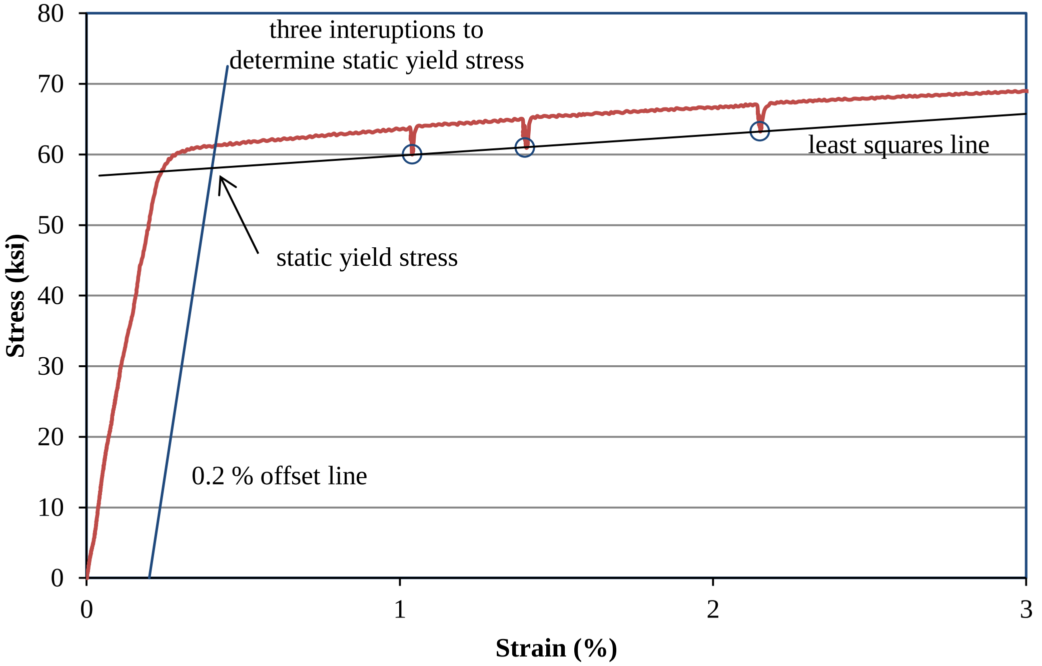

(b) Close view of stress-strain curve at yielding region

Figure 8.11 Stress-strain curve for coupon test 14 with significant residual stress

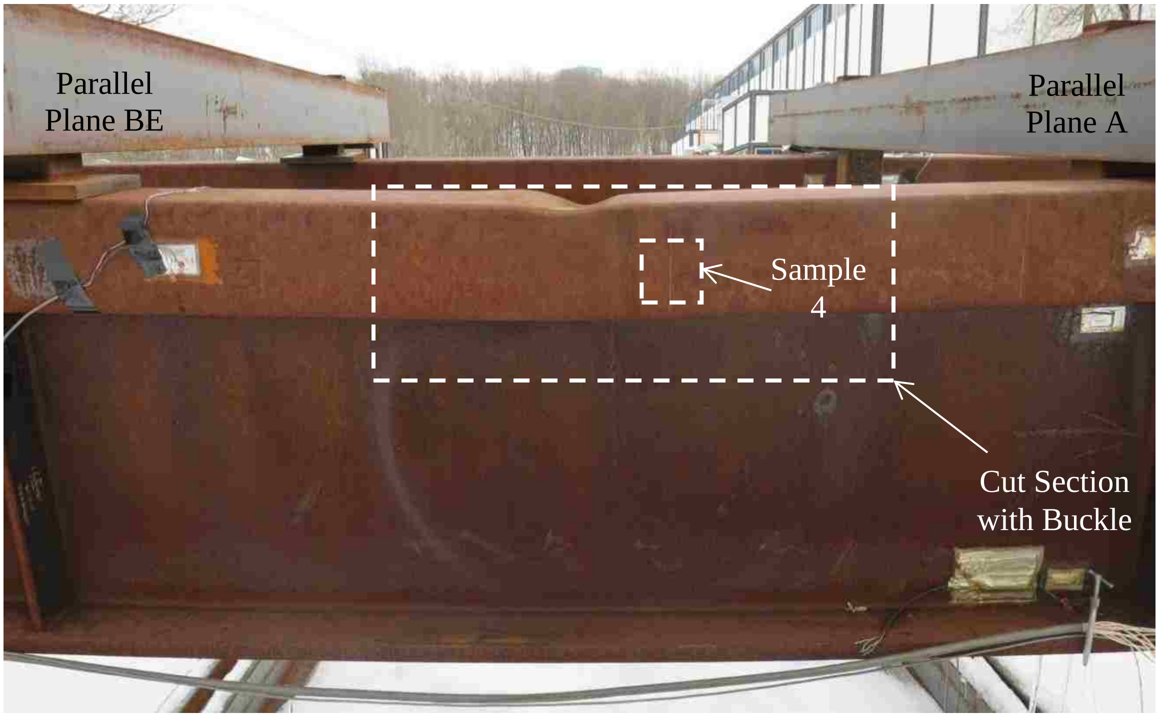

Figure 8.12 Location of local buckled region of the test specimen looking from the outside of the curvature

Figure 8.13 Buckled section looking from the inside of the curvature

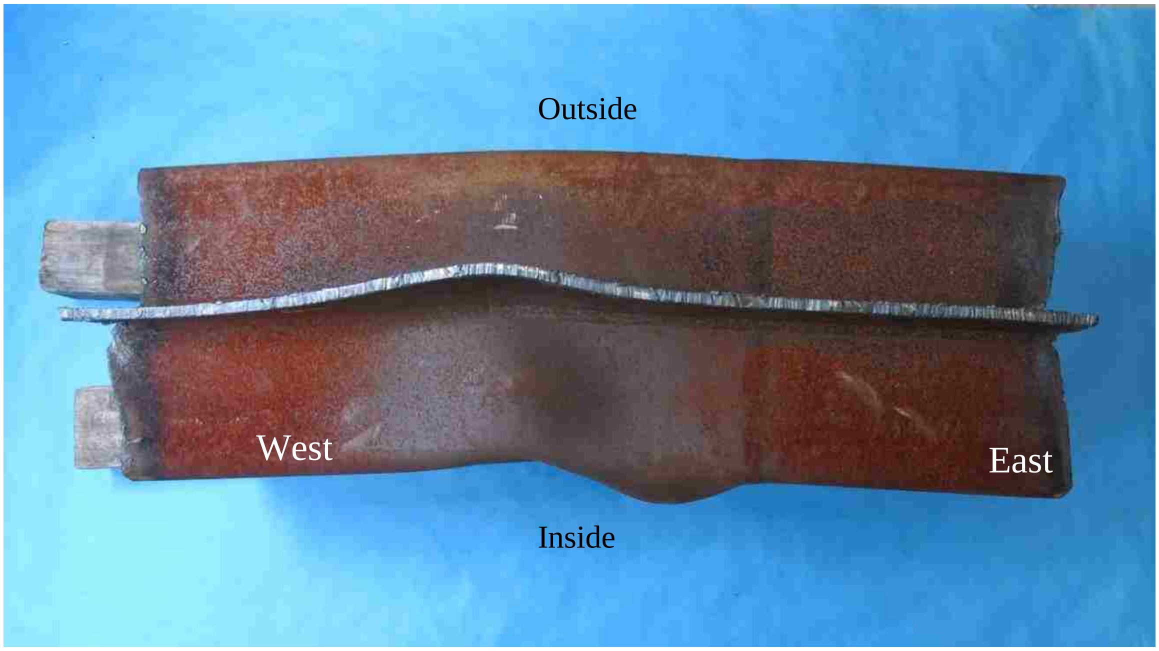

Figure 8.14 Buckled section looking from bottom

Figure 8.15 Buckled section looking from top

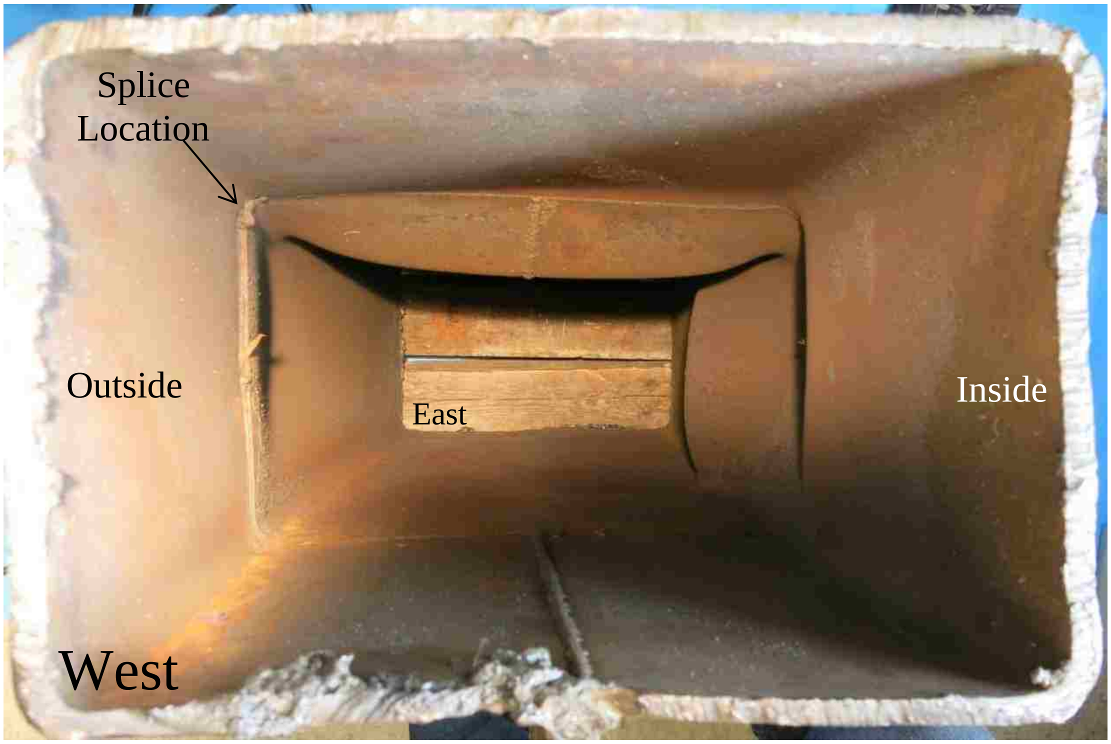

Figure 8.16 Buckled section looking from inside of tube

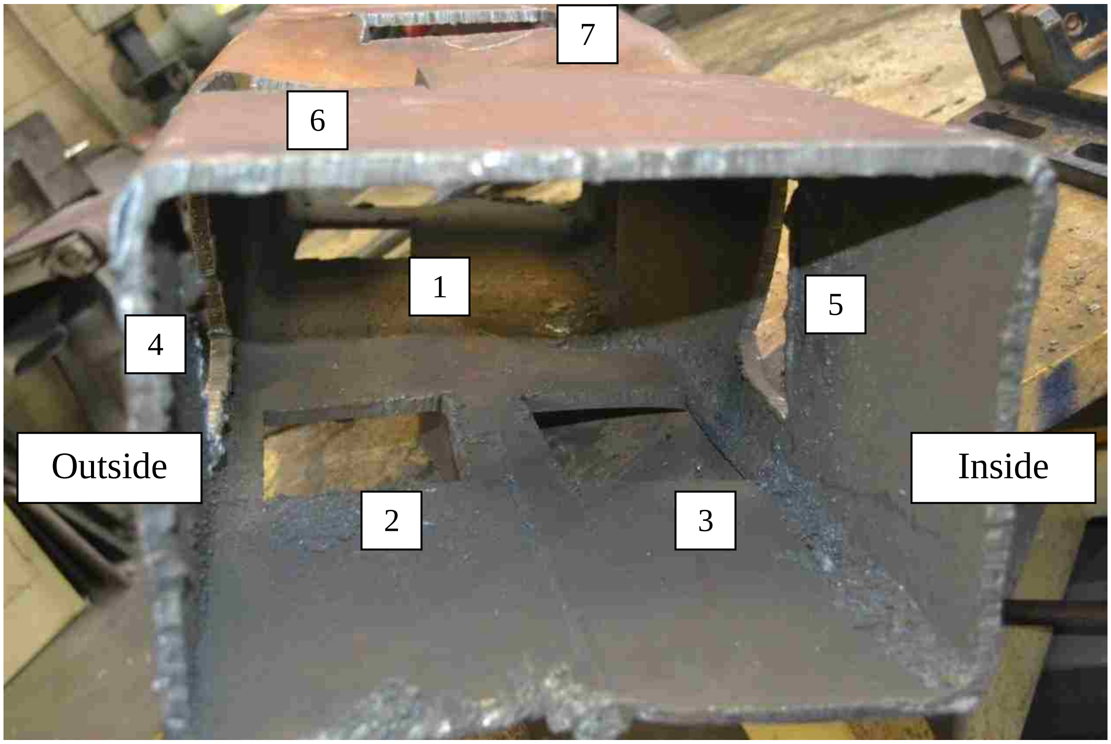

Figure 8.17 Location of samples cut from buckled section

Figure 8.18 Grinding process during the metallography

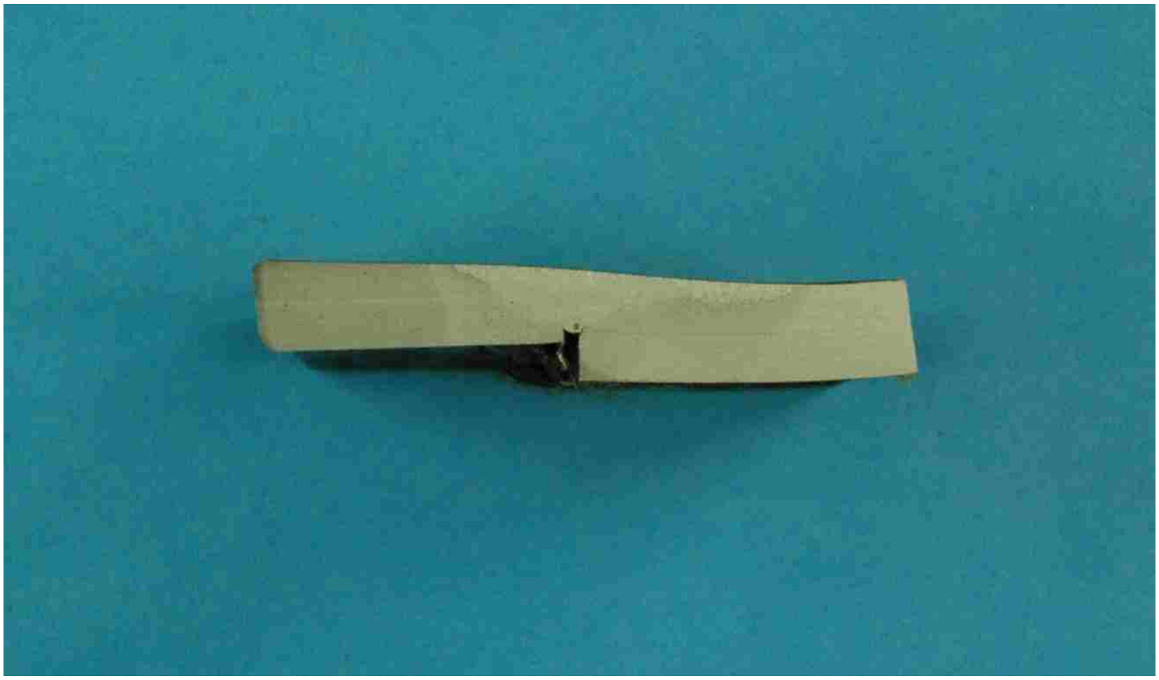

(a) Photograph of etched side of sample 4

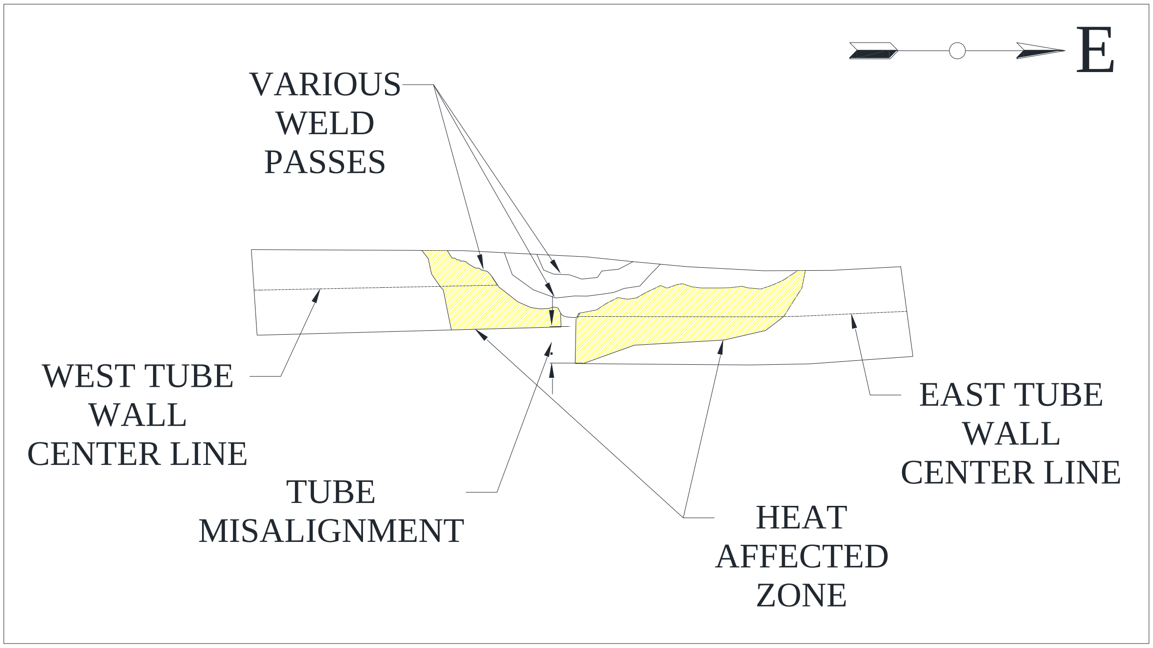

(b) Details of etched side of sample 4

Figure 8.19 Tube misalignment at splice location for sample 4 after metallography

9 SUMMARY AND CONCLUSION

9.1 Summary

Tubular flange girders (TFGs) are an innovative I-shaped steel bridge girder proposed for horizontally curved bridge systems. The I-shaped TFG has a tube flange rather than a conventional flat plate flange for one or both flanges. In this study a type of tubular flange girder, called TFG1, with a rectangular hollow steel tube as the top flange and a flat plat as the bottom flange was studied. The close section of the tube provides significant torsional stiffness and strength to the section while the open I shape provides significant flexural stiffness and strength. A full-size curved two-girder bridge with TFG1s and the corresponding two-thirds scale test specimen were designed by Ma (2014) and Putnam (2011) based on AASHTO Load and Resistance Factor Design Bridge Design Specifications (2004) and TFG design recommendations by Dong (2008). The full-size bridge has a 90 ft span, and a curvature ratio (span length over curvature radius) of 0.45. The scaled test specimen has same curvature ratio, but all dimensions are scaled by two-thirds. This thesis reviewed the design of the test setup and loading fixtures (Hampe, 2012) and presented instrumentation and loading plans for the tests. This thesis also presented the test results and complimentary material test results.

First, the procedure for design of the full-size and scaled two-TFG1 bridge system was reviewed and the corresponding design limit states from AASHTO (2010) were summarized. Then the information on test setup location and layout was presented.

Second, the expected behavior of the test specimen based on analysis of FE models (Ma, 2014) was presented. This expected behavior was the basis for the design of the loading fixtures (Hampe, 2012) which was also reviewed in this thesis. Then, the effect of the boundary conditions on behavior of the test specimen was discussed and the final design of the bearing assemblies for the test setup was described.

Third, the instrumentation plan developed for measuring the loading conditions and test specimen behavior was described, and the geometric calculations to obtain the required displacement components were presented. Then the loading plan, including the control plan and jack re-stroking plan were discussed. The instrumentation and test procedures were planned with a focus on the conditions of the inelastic test, which loads the test specimen up to and beyond the maximum load capacity.

Finally, the tests results were presented, including measured test data and processed test results. The test specimen material properties from tests of tensile coupons fabricated from the test specimen materials were also presented. The geometric imperfections of the tube at the tube splice location within the local buckled region of girder G1 from the test specimen were also presented.

9.2 Major Findings

The following findings are obtained from the work presented in this thesis:

- The design criteria for curved steel I-shaped girders based on the AASHTO LRFD Bridge Design Specifications (AASHTO, 2004 and 2010), recommended by Dong and Sause (2008), can be effectively used to design curved steel TFG1 bridge systems. This thesis focused on criteria for the Constructibility limit state under the deck placement conditions.

- The kinematics and design forces for the test fixtures were predicted with sufficient accuracy by the FE results from Model-D2 so that the test fixtures performed well, even though the kinematic requirements for the test fixture were challenging. The test fixtures remained stable during the tests. Similarly, the bearing assemblies, designed using FE results from Model-D3, performed well during the tests.
- Although the loading rod assemblies in the test fixtures did not remain completely vertical during the tests, the inclination of the loading rod assembly and corresponding non-vertical force component were not significant.
- The combination of displacement transducers used to measure displacements of the test specimen at locations within the span, and the associated geometric calculations worked well to enable the vertical and parallel components of the displacements to be determined.
- Strain gages provided good results for the normal strain variation over the depth and width of the TFG1 cross sections, especially for inelastic strains at the mid span of G2 of the test specimen.

9.3 Conclusions

The following conclusions are drawn from the study presented in this thesis:

- The FE analysis predicted the test specimen and loading fixture kinematic response with sufficient accuracy. Loading fixtures successfully loaded the test specimen up to (and beyond) the maximum capacity using fourteen concentrated loads.

- The bearing assemblies provided the expected boundary condition combinations for the test specimen. The half-rounds allowed rotation about the radial axis, Teflon plates allowed circumferential and radial displacements, and radial restraint prevented radial displacements as intended.
- The loading equipment and the load control plan used for the tests of the curved two-TFG1 test specimen were successful for loading the test specimen in the elastic range, inelastic range, and beyond the maximum load capacity. However, the fourteen concentrated loads were not as uniform in magnitude as intended.
- The instrumentation plan was successful in measuring test specimen and loading fixture response during the tests. The large displacements of the test specimen and the complex test setup did not interfere with the instrumentation.
- The geometric imperfections caused by the tube splice welding appears to have affected the failure mode and contributed to the local buckling.
- The design criteria based on the AASHTO LRFD Bridge Design Specifications (AASHTO, 2004 and 2010) used in this study can be used effectively to design curved steel TFG1 bridge systems.

9.4 Future Work

The following recommendations are made for further analytical and experimental research:

- The test results should be used to further validate FE models and the design criteria used to design the curved TFG1 test specimen.
- Complimentary FE models should be developed to consider the geometric imperfections and actual loads applied in the loads.
- A complete welding procedure should be developed for splicing the tubes as needed for curved TFG girders.

REFERENCES

AASHTO (2004, 2010) AASHTO LRFD Bridge Design Specifications. American Association of State Highway and Transportation Officials, Washington, D.C.

AISC (2005) Steel Construction Manual, 13th Edition. American Institute of Steel Construction, Inc., Chicago, IL.

ASTM Standard E8 (2013) "Standard Test Methods for Tension Testing of Metallic Materials," ASTM International, West Conshohocken, PA.

Dong, J., Sause, R. (2008a) "Flexural strength of tubular flange girders," Journal of Constructional Steel Research, 65, 622-630.

Dong, J., Sause, R. (2008b) "Analytical Study of Horizontally Curved Hollow Tubular Flange Girders." ATLSS Report 08-15, ATLSS Engineering Research Center, Lehigh University, Bethlehem, PA.

Dong, J., Sause, R. (2010a) "Finite Element Analysis of Curved Steel Girders with Tubular Flanges," Engineering Structures, 32, 319-327.

Dong, J., Sause, R. (2010b) "Behavior of Hollow Tubular-Flange Girder Systems for Curved Bridges," Journal of Structural Engineering, 136, 174-182.

Hampe (2012) "Analysis and Design of Test Setup and Loading Fixtures for Horizontally Curved Tubular Flange Girder Test Specimen." M.S. Thesis, Department of Civil and Environmental Engineering, Lehigh University, Bethlehem, PA.

Kim, B.G., Sause, R. (2005a) "High Performance Steel Girders with Tubular Flanges." ATLSS Report 05-15, ATLSS Engineering Research Center, Lehigh University, Bethlehem, PA.

Kim, B.G., Sause, R. (2005b) "High Performance Steel Girders with Tubular Flanges," International Journal of Steel Structures, 5, 253-263.

Kim, B.G., Sause, R. (2008) "Lateral Torsional Buckling Strength of Tubular Flange Girders," Journal of Structural Engineering, ASCE, 134, 902-910.

Ma, H.Y, (2014) "Analytical and Experimental Study on Horizontally Curved Bridges with Tubular Top Flange Girders," Ph.D. Dissertation, Department of Civil and Environmental Engineering, Lehigh University, Bethlehem, PA.

Putnam E. (2010). "Design, Experimental, and Analytical Study of a Horizontally Curved Tubular Flange Girder." M.S. Thesis, Department of Civil and Environmental Engineering, Lehigh University, Bethlehem, PA.

Sause R. (2012). "Innovative Steel Bridge Girders with Tubular Flanges." IABMAS 2012, Proceedings of the 6th International Conference on Bridge Maintenance, Safety, and Management, Stresa, Lake Maggiore, Italy, July 8-12, 2012.

Sause R., Dong J. (2008). "Finite-element analysis of curved hollow tubular flange girders." Proceedings, 25th Annual International Bridge Conference, Pittsburgh, PA, USA.

Sause R., Ma H., Mahvashmohammadi K., (2014). “Design, Analysis, and Tests of Steel Tubular Flange Girder (TFG) System for Curved Highway Bridges” ATLSS Report 14-x, ATLSS Engineering Research Center, Lehigh University, Bethlehem, PA.

Sause R., Ma H., Putnam E., Dong J. (2009). “Update on Curved Girders with Tubular Flanges.” Summer Meeting of the American Iron and Steel Institute Bridge Task Force, Baltimore, MD, August 12-14, 2009.

Sause R., Kim B.G., Wimer M.R. (2008). “Experimental Study of Tubular Flange Girders.” Journal of Structural Engineering, 134, 384-392.

Serway R. A., Jewett J. W. (2010) Physics for Scientists and Engineers, Volume 1, 8th Edition. Cengage Learning, Belmont, CA.

Wassef, W.G., Ritchie, P.A., Kulicki, J.M. (1997) “Girders with Corrugated Webs and Tubular Flanges – An Innovative Bridge System,” In Proceedings, 14th Annual Meeting, International Bridge Conference, Pittsburgh, PA, 425-432.

Ziemian, R. D. (ed) (2010) Appendix B: Technical Memoranda of Structural Stability Research Council, in Guide to Stability Design Criteria for Metal Structures, Sixth Edition, John Wiley & Sons, Inc., Hoboken, NJ

VITA

Kourosh Mahvashmohammadi, son of Zohreh Torabi and Ahmadreza Mahvashmohammadi, was born on March 6, 1989 in Isfahan, Iran. In June 2012, Kourosh earned a bachelor of science in Civil Engineering from Sharif University of Technology (SUT) in Tehran, Iran. Kourosh began his graduate studies in the Department of Civil and Environmental Engineering at Lehigh University in Bethlehem, PA in August 2012. He will receive his Master of Science of Structural Engineering in September 2014.